# Toward an operationnal single photon source based on semiconductor nanowires

Thibault Cremel

## To cite this version:

Thibault Cremel. Toward an operationnal single photon source based on semiconductor nanowires. Optics [physics.optics]. Université Grenoble Alpes, 2016. English. NNT : 2016GREAY064 . tel-01592076

HAL Id: tel-01592076
https://theses.hal.science/tel-01592076

Submitted on 22 Sep 2017

Communauté
UNIVERSITÉ Grenoble Alpes

# THÈSE

Pour obtenir le grade de

**DOCTEUR DE LA COMMUNAUTÉ UNIVERSITÉ GRENOBLE ALPES**

Spécialité : **Physique**

Arrêté ministériel : 7 août 2006

Présentée par

## Thibault CREMEL

Thèse dirigée par **Kuntheak KHENG** et
codirigée par **Edith Bellet-Amalric**

préparée au sein du **Laboratoire NanoPhysique et Semiconducteur (NPSC) du CEA-Grenoble**
dans **l'École Doctorale de Physique.**

# Vers une source de photons uniques opérationnelle à base de nanofils semiconducteurs

Thèse soutenue publiquement le **08 Novembre 2016**,
devant le jury composé de :

**Valia Voliotis**
Professeure, CNRS-Université Pierre et Marie Curie, Paris, Rapportrice.
**Frank Glas**
Directeur de recherche, C2N, CNRS, Université Paris-Sud, Université Paris-Saclay, Marcoussis, Rapporteur.
**Christophe Couteau**
Professeur assistant, CNRS-Université de Technologie de Troyes, Examinateur.
**Benoît Boulanger**
Professeur, CNRS-Université Grenoble Alpes, Grenoble, Président.
**Edith Bellet-Amalric**
Ingénieure CEA, INAC, Grenoble, Co-Directrice de thèse.
**Kuntheak KHENG**
Professeur, Université Grenoble Alpes, INAC, Grenoble, Directeur de Thèse.

*Le bonheur est là, blotti, patient, endormi au creux de l'instant. Il attend que ton regard volage se pose enfin sur lui.*

Pascale Verger

# Acknowledgments

This work has been performed at the Commissariat à l'Energie Atomique (CEA) at Grenoble in the newly renamed PHELIQS (PHotonique, ELectronique et Ingénierie QuantiqueS) department, more precisely within the mixed CEA-CNRS NanoPhysics and Semiconductors (NPSC).

First of all, I express my deepest gratitude to my main PhD supervisor Kuntheak Kheng for his deep knowledge in Physics, for teaching me to be more pedagogical and for transmitting me the *way of the logical path*. I am particularly grateful for the confidence and freedom he gave me, while keeping a critical eye throughout the PhD. I would also like to thank him for sending me an email during my Master 1 internship at Cornell University to expose this PhD proposal. This passionating subject on single-photon sources gave me the strength to politely decline PhD opportunities at Cornell and carry out the research exposed in this manuscript with confidence.

A very warm thank you to Edith Bellet-Amalric for accepting to be my co-supervisor after my first year of PhD, for teaching me the art of the epitaxial growth and to keep calm during the MBE sample transfers. With her expertise in X-ray diffraction and molecular beam epitaxy, it has been a pleasure to share her optimism, her experimental experience and all the nice moments we spent together.

I also thank Benoît Boulanger for presiding my PhD jury and for lauching the EOS SFO Alpes student Club that I co-directed during these past two years. I also deeply thank Valia Voliotis and Frank Glas for accepting to report this manuscript. I greatly appreciated the original view they provided on this work. Many thanks also to Christophe Couteau for accepting to be part of my PhD jury.

In addition, I wish to thank the epitaxial team composed of Edith Bellet-Amalric, Regis André, Yann Genuist, Didier Boilot, Joël Cibert, Serge Tatarenko for accepting to teach me epitaxial growth even if it was not planned at the beginning of the PhD. Besides, I kindly thank Martine Den Hertog and Catherine Bougerol for the TEM characterizations provided in this manuscript.

I would also like to thank the whole Nanostructures and Semiconductor (NPSC) group for the enjoyable moments and discussions we had, especially Joël Bleuse for teaching me how to be in charge of a photoluminescence setup, for sharing his deep experimental skills and experience; Jean Dussaud for his intensive three months help to create the optical lab security report at the very beginning of the PhD to start measuring the luminescence of the samples; Yoann Cure for sharing his deep knowledge about computational simulations, life and technical skills and Régis André for his typewriting advice :-), his very sharp mind, technical skills and amazing critical ideas. It has also been a pleasure to share his enjoyable sense of humor.

I express my gratitude to Gilles Nogues for introducing me to Comsol and for all the enlightening discussions we shared, Laurent Cagnon for providing me support during the Atomic Layer Deposition and the enjoyable movies discussions we shared; to Eric Robin and Nicolas Mollard for teaching me how to efficiently get nice images on a SEM and our fruitful collaboration; to Thierry Crozes, Sébastien Dufresnes, Bruno Fernandez, Thierry Fournier, Gwénaëlle Julie et Jean-François Motte for their warm technical support in the NanoFab clean-room. I am also very grateful to Alberto Artioli and Petr Stepanov for their help at the beginning of my PhD during microphotoluminescence experiments, Le Si Dang for asking me eye-opening questions, Jean-Michel Gerard, Henri Mariette, Alexia Auffèves and Jean-Philippe Poizat for the photonic and semiconductors courses they provided me during my Master 2 program and the enjoyable discussions we had, Joël Eymery, Dmitry Aldakov, Julien Claudon, Hervé Boukari, Bruno Daudin, Bruno Gayral, Christophe Durand, Moïra Hocevar and Eva Monroy for the pleasant conversations we shared.

I offer special thanks to Isabelle Schuster for providing me clear explanations about the PhD application, Jerôme Planes for the annual and very lively discussions we had about the PhD, Laurent Miquet for explaining me the security related to my working environment, Brigitte Foyot, Carmelo Castagna, Cecile Blanc, Sandra Pisa and Sarah Mauduit for their great help with administrative procedures. I also acknowledge the Bachelor and Master students I had the pleasure to supervise during the past three years, Irène Ventrillard, Elodie Bidal and Guillermo Martin for their useful advice concerning the students supervisions and the Editors of the Journal of Applied Physics for trusting me as one of their reviewers.

I am very grateful to Thierry Deutsch for helping me to implement the FDTD MEEP program on a multiprocessors cluster by setting the Message Passing Interface version of the software and for giving me access to an eight cores Intel Xeon computer named Girofle.

Thank you to my friends, interns, PhD and Post-doctoral mates: Adrien Delga, Emmanuel Peinke, Thomas Auzelle, Xin Zhang, Mark Beeler, Manos Trichas, Elodie Boursier, Elodie Jordan, Pamela Rueda Fonseca, Lionel Gérard, Damien Salomon, Damien Massy, Giovanni Altamura, Agnès Messanvi, Anna Mukhtarova, Sirona Valdueza-Felip, Rafael Bortolin-Pinheiro, Laurent Fauquier, Zhihua Fang, Juhi Pandey, Bobin Varghese, Albert Fan, Valentina Zannier, Woojin Lee, Hammouda Benallali, Marta Orrù, Alberto Artioli, Mathieu Jeannin, Tobias Sattler, Petr Stepanov, Giovanni Altamura, Matthias Belloeil, Siewli Tan, Himwas Chalermachai, Gaston Hornecker, Luca Redaelli, Fabien Rortais, Jérémie Rousseau, Kévin Guilloy, Olivier Marconot, Mustapha Boukhari, Maxime Morinière, Dilyara Timerkaeva, Fabio Agnese, Bastien Bonef, Khalid El Hjraoui, Benedikt Hass, Samuel Tardif (congratulations for your position at CEA!), Karim Vindas, Daria Beznasiuk, Caroline Lim, Akhil Ajay, Mister Browne, Amine Elkacimi, Martin Vallo, Marion Gruart, Alexandra-Madalena

Siladie, Kévin Tekaya, Tristan Agaesse, Bruno Salque, Anna Senegas, Pierre Dorion, Maxime Godfroy, Lucia Mattera, Louis Vaure, Damien Tristant, Armelle Poux, Romain Bontems, Manon Gilles, Gaëlle Panisset for the good times we had together. A special thank to Adrien Delga and David Browne for sharing my office over the past three years! It has been a great pleasure to laugh with you guys and share stimulating daily discussions ;-).

Finally, I deeply thank my whole family for their strong support: Serge Dalbion, Pierre, Marie, Jean, Monique, Isabelle Mendez, la famille Coche, Charles et Marie-Madeleine Josserond, Didier Legeais, Alain et Christine Caël, Jean-Claude Buffet, Delphine et Emmeline Gautheron, Charles et Martin Blondel and Nelly Salomon.

With the bottom of my heart, I thank my parents Florence and Hervé, my bro' Théo, my grand-parents Manuela and Emile, along with Yvette and JoJo, and *Ista Owanca* Flora.

# Contents

# Résumé en Français

## Introduction

Les **boîtes quantiques** ont fait l'objet d'un grand intérêt ces dernières années auprès de la communauté scientifique: elles sont composées d'une inclusion semiconductrice de taille nanométrique dans laquelle les électrons et les trous subissent un confinement tridimensionnel. Du fait de cette limitation spatiale, les niveaux électroniques d'une boîte quantique sont discrets comme pour un atome: c'est pour cette raison que les boîtes quantiques sont parfois appelées "atomes artificiels".

Les premières boîtes quantiques ont été créées dans du verre avec des inclusions semiconductrices (nanocristaux) de diamètre inférieur aux longueurs d'onde visibles (typiquement inférieur à cent nanomètres). Elles ont été utilisées pour teinter les vitraux des Eglises et leur confinement quantique a été mis en évidence plus tard. Néanmoins, leur incorporation dans une matrice de verre entrave leur utilisation dans des composants d'opto- ou de microélectronique.

Dans les années soixante, le développement de l'épitaxie par jet moléculaire a permis de créer des empilements de couches semiconductrices; les puits quantiques ont été les premiers systèmes de dimensionnalités réduite. Ils consistent en une couche semiconductrice ultra fine (quelques plans atomiques) insérée entre deux matériaux semiconducteurs de plus grands gap, appelés barrières. Les électrons confinés dans ce puits ont des niveaux d'énergie discrets selon l'axe de croissance, et ont toujours deux degrés de liberté dans le plan de la couche.

Grâce au développement des techniques de lithographie dans les années 80, des puits quantiques ont été gravés pour former des boîtes quantiques insérées dans des nanopilliers de quelques dizaines de nanomètres de diamètre. Néanmoins, les défauts cristallins induits par la gravure dégradaient sérieusement les propriétés optiques des boîtes quantiques. Il a aussi été observé que sous certaines conditions (généralement grâce à la contrainte mécanique), des plans semiconducteurs ultra fins (destinés initialement à devenir des puits quantiques) formaient spontanément de petites boîtes quantiques au-delà d'une certaine épaisseur critique. Les boîtes quantiques ainsi formées sont de type Stranski-Krastanov, en honneur à Ivan Stranski et Lyobomir Krastanov qui en découvrirent le mode de croissance.

La croissance de nano-objets unidimensionnels - appelés **nanofils** - a été largement étudiée depuis que Wagner et Ellis présentèrent leur fameuse croissance catalysée de nanofils de silicium grâce à des gouttelettes d'or en 1964 [1]. Ces nanostructures assurent une relaxation efficace des contraintes mécaniques, ce qui offre la possibilité de faire croître des nanofils de différents matériaux sur des substrats, même si la différence de paramètre de maille nanofil-substrat est importante [2]. De plus, la relaxation des contraintes sur les flancs des nanofils permet de faire croître des hétérostructures axiales de matériaux désaccordés en paramètre de maille, sans dislocations aux interfaces [3]. Il est ainsi possible d'insérer une petite inclusion semiconductrice ou boîte quantique à l'intérieur d'un nanofil de plus grand gap.

Les nanofils et boîtes quantiques sont utilisés comme sources de lumière dans les LEDs (Light-Emitting Diodes) ou encore les **sources de photons uniques**. Ces dernières émettent - comme leur nom l'indique - des photons uniques - qui interagissent faiblement avec leur environnement (peu de décohérence), ce qui leur permet d'être utilisés pour transmettre des informations sur de larges distances. De façon plus générale, l'intérêt de la communauté scientifique pour ces sources est relié au développement récent de la théorie de l'information quantique [4, 5]. En effet, ces sources peuvent être utilisées pour le calcul quantique optique [6] ou la cryptographie quantique pour améliorer les performances de distribution des clés et éviter les écoutes ou tentatives de hacking [7]. Les sources de photons uniques peuvent aussi être utilisées dans le traitement quantique de l'information et la métrologie [8]. Par conséquence, il est nécessaire de disposer de sources fiables [9] et pour des applications réalistes, le défi est d'obtenir des sources de photons uniques qui fonctionnent jusqu'à température ambiante. En effet, lorsque la température augmente, l'excitation thermique induit des recombinaisons non-radiatives qui diminuent l'efficacité des sources utilisées.

# Objectifs et motivations de la thèse

Notre groupe à récemment démontré qu'en insérant une boîte quantique de CdSe dans un nanofil de ZnSe, l'émission de photon unique pouvait être obtenue jusqu'à température ambiante [10]. Néanmoins, ces nanofils avaient un rendement quantique faible et n'étaient pas orientés verticalement à la surface des échantillons du fait de leur croissance suivant l'orientation cristallographique (001). Ces nanofils verticaux ont pour intérêt de pouvoir être aisément couplés à des structures photoniques pour augmenter la collection des photons, comme nous le verrons dans ce manuscrit. La croissance de nanofils verticaux est favorisée avec des substrats orientés suivant l'orientation cristallographique (111). Pour ces raisons, le but de ce travail de doctorat est de développer la croissance de boîtes quantiques de CdSe dans des nanofils de ZnSe verticaux afin d'en améliorer les propriétés optiques.

**Plus spécifiquement, le but de ce travail de doctorat est de développer la croissance de nanofils verticaux suivant l'orientation cristallographique (111) par épitaxie par jet moléculaire et d'en étudier les propriétés optiques jusqu'à température ambiante, pour des applications potentielles en tant que sources de photons uniques.**

Dans ce contexte, nous avons travaillé sur les propriétés fondamentales de:

1. *nanofils de ZnSe* (chapitre 2 qui suit un premier chapitre introductif)
2. *boîtes quantiques de CdSe* insérées dans des nanofils de ZnSe (chapitre 3)
3. le *couplage* de boîtes quantiques de CdSe insérées dans des nanofils de ZnSe *à des structures photoniques* pour augmenter la collection de photons (chapitre 4).

Le contenu de ces chapitres est décrit ci-après.

## Chapitre 1 - Boîtes quantiques semiconductrices II-VI pour l'émission de photons uniques

Ce premier chapitre passe en revue l'état de l'art des sources de photons uniques et répond à la question: *"pourquoi utilisons-nous des nanofils de ZnSe avec boîtes quantiques de CdSe pour l'émission de photons uniques?"*. Il donne ensuite une vue d'ensemble des propriétés électroniques et structurales de semiconducteurs II-VI à base de sélénium, ainsi que les outils expérimentaux utilisés. La machine de croissance en épitaxie par jet moléculaire et les outils de caractérisation structurale sont introduits ainsi que les bancs optiques utilisés pour les études de photoluminescence et de cathodoluminescence. Ce chapitre a pour but d'introduire les fondements nécessaires à la compréhension des résultats de ce manuscrit.

## Chapitre 2 - Croissance et caractérisation de nanofils de ZnSe

Ce second chapitre est dédié à la croissance et la caractérisation de nanofils de ZnSe. ***Premièrement, des nanofils de ZnSe développés sur des substrats de GaAs (111)B*** (surface terminée As) sont étudiés conjointement par une étude structurale et optique. Ces nanofils - composés principalement de la phase wurtzite - montrent une excellente émission de bord de bande, avec l'identification de l'exciton de la phase wurtzite du ZnSe (rarement observé). Ces nanofils émettent une lumière polarisée perpendiculairement à l'axe du nanofil, en accord avec les règles de sélection de la phase wurtzite. Des observations par microscopie électronique à transmission confirment que la majorité des nanofils sont en phase wurtzite, avec parfois des alternances de phases wurtzite et blende de zinc. Par des mesures de photoluminescence résolues en temps, un alignement de type II a été révélé entre ces deux phases cristallines et nous en déduisons les premières valeurs expérimentales des décalages de bande de conduction et de valence. Nous verrons que, de par leurs conditions de croissance, ces nanofils sont coniques et que cette géométrie est défavorable pour l'insertion de boîtes quantiques uniques dans les nanofils. Un moyen de contourner ce problème est de faire croître les nanofils ZnSe sur un buffer de ZnSe.

Pour cette raison, la croissance de ***nanofils de ZnSe a été développée sur des buffers de ZnSe(111)***. La croissance de ces nanofils suivant l'orientation cristalline (111)A (surface terminée Zn) n'étant pas favorable, l'étude des meilleures conditions de croissance suivant l'orientation (111)B (surface terminée Se) nous permet de conclure que des nanofils verticaux peuvent être obtenus à 400°C sous excès de sélénium. En recouvrant ensuite ces nanofils d'une coquille semiconductrice de ZnMgSe de gap supérieur, les nanofils peuvent être efficacement passivés. En effet, l'intensité de la luminescence de nanofils uniques est augmentée de plus de deux ordres de grandeur.

## Chapitre 3 - Boîtes quantiques de CdSe insérées dans des nanofils de ZnSe: croissance et caractérisation

Dans ce troisième chapitre, nous montrons la possibilité d'insérer des boîtes quantiques de CdSe dans des nanofils de ZnSe développés suivant l'orientation cristallographique (111)B. Dans ce chapitre, deux échantillons sont caractérisés: ils sont respectivement composés d'une et de deux boîtes quantiques insérées suivant deux conditions de croissance différentes. Le but est d'analyser l'effet de ces conditions de croissance sur le rapport d'aspect des boîtes quantiques. En effet, ce rapport d'aspect permet de modifier l'orientation du dipole (paire électron- trou) de la boîte quantique, ce qui est utile pour coupler la boîte à des structures photoniques (comme nous le verrons au chapitre quatre).

***Tout d'abord***, la caractérisation *structurale* (phase cristalline et paramètre de maille) de ces nano-objets par microscopie électronique en transmission montre que les boîtes de CdSe et les fils de ZnSe sont composés des phases blende de zinc et wurtzite respectivement. Cette distribution de phases cristallines est opposée à ce qui est observé dans des structures massives (le CdSe est en phase wurtzite et le ZnSe en phase blende de zinc). Ce phénomène pourrait s'expliquer par le diamètre nanométrique des nanofils qui changerait de structure cristalline pour minimiser leur énergie de surface [11] ou résulter d'effets complexes pendant la croissance [12].

De plus, la *composition* d'une boîte quantique unique de CdSe a pu être observée par une analyse dispersive en énergie qui révèle la présence d'un gradient de Cd au sein de cette boîte. Une autre technique sensible à la composition, appelée sonde atomique tomographique, est calibrée sur des boîtes de CdSe Stranski-Krastanov insérées dans une matrice de ZnSe, ce qui nous permettra prochainement de caractériser de nanofils uniques, déjà isolés sur des pointes par nanomanipulation.

***Dans une seconde partie***, les propriétés optiques de ces nanofils sont étudiées. Des mesures de polarisation montrent différentes orientations de dipôles induites par les rapports d'aspect des boîtes quantiques. Des mesures en fonction de la température montrent que ces nanofils émettent jusqu'à température ambiante. De plus, l'étude du temps de déclin de nanofils uniques révèle que ces fils sont robustes et insensibles aux canaux de recombinaison non-radiatifs jusqu'à 200 K.

## Chapitre 4 - L'augmentation de la collection de photons

Le **quatrième chapitre** aborde l'augmentation de la collection de photons. ***Premièrement***, en combinant des mesures de photoluminescence et de cathodoluminescence, nous observons une modification du temps de déclin en comparant des boîtes quantiques dans le *vide* et *insérées dans une matrice de ZnMgSe*. Cette modification résulte de la différence d'environnement des boîtes quantiques et peut être quantifiée en utilisant la règle d'or de Fermi. Cette règle indique que le temps de déclin des boîtes est inversement proportionnel à l'indice de réfraction de son environnement. Nous montrerons que la modification attendue théoriquement est en bon accord avec notre valeur expérimentale et que le taux d'émission des boîtes peut être augmenté, augmentant de la même façon l'émission et la collection de photons.

***Dans une seconde partie***, nous montrons la possibilité de créer des fils photoniques à partir des boîtes quantiques insérées dans des nanofils, en recouvrant ces fils d'une épaisse coquille diélectrique. Nous montrerons la possibilité de déposer divers matériaux comme du $ZrO_2$, $TiO_2$, $HfO_2$ et $Al_2O_3$; ce dernier matériau sera choisi pour la qualité de son dépôt conforme. A la lumière d'expériences de microphotoluminescence et de simulations, nous discutons l'intérêt de l'orientation du dipôle (aligné ou perpendiculaire à l'axe de croissance du nanofil) dans ces structures et montrons que dans notre cas, ces fils photoniques augmentent efficacement la collection de photons de près d'un ordre de grandeur.

## Annexe A

Dans cette **première annexe**, nous discutons l'intérêt de deux méthodes pour collecter les photons émis dans le substrat. Elles consistent à (1) faire croître les nanofils à travers des miroirs pour réfléchir et collecter la lumière initialement émise vers le substrat et (2) déposer les nanofils sur des substrats transparents à indice de réfraction élevé. Dans ce cas, la majorité de la lumière est émise vers le substrat pour ensuite être collectée sous ce substrat. Des simulations montrent que la collection de photons de nos nanostructures peut être augmentée de un à deux ordres de grandeurs, ce qui représente une marge de progression encourageante pour ces sources de photons uniques prometteuses.

## Annexe B

**Cette seconde Annexe** présente des résultats préliminaires et détaille la procédure à suivre pour faire croître des nanofils localisés de ZnSe à travers un miroir d'aluminium. En plus de l'augmentation de la collection de photons attendue par la réflexion du miroir, cette croissance localisée permettrait de parfaitement contrôler la position du nanofils à la surface de l'échantillon.

# List of Acronyms

| | |
|---|---|
| **ALD** | Atomic Layer Deposition |
| **ALE** | Atomic Layer Epitaxy |
| **APD** | Avalanche PhotoDiode |
| **APT** | Atom Probe Tomography |
| **BEP** | Beam Equivalent Pressure |
| **CCD** | Charge-Coupled Device |
| **CL** | CathodoLuminescence |
| **CW** | Continuous Wave |
| **CX** | Charged exciton |
| **DAP** | Donor-Acceptor Pair |
| **DBR** | Distributed Bragg Reflector |
| **DOS** | Density Of States |
| **EDX** | Energy-Dispersive X-ray spectroscopy |
| **FDTD** | Finite Difference Time Domain |
| **FFT** | Fast-Fourier Transform |
| **FIB** | Focused Ion Beam |
| **FWHM** | Full Width at Half Maximum |
| **GPA** | Geometrical Phase Analysis |
| **HH** | Heavy Hole |
| **IBE** | Ion Beam Etching |
| **LH** | Light Hole |
| **MBE** | Molecular Beam Epitaxy |
| **MEE** | Migrated Enhanced Epitaxy |
| **MEEP** | MIT Electromagnetic Equation Propagation |
| **ML** | MonoLayer |
| **NA** | Numerical Aperture |
| **NBE** | Near-Band-edge |
| **NV** | Nitrogen-Vacancy |
| **NW** | NanoWire |
| **PID** | Proportional-Integral-Derivative |
| **PL** | PhotoLuminescence |

| | |
|---|---|
| **QD** | Quantum Dot |
| **RBS** | Rutherford BackScattering |
| **RHEED** | Reflection High Energy Electron Diffraction |
| **RIE** | Reactive Ion Etching |
| **SEM** | Scanning Electron Microscopy |
| **SK** | Stranski-Krastanov |
| **SPS** | Single-Photon Source |
| **SR** | Surface Reconstruction |
| **TEM** | Transmission Electron Microscopy |
| **TE** | Transverse Electric |
| **TM** | Transverse Magnetic |
| **TR** | Time-Resolved |
| **UHV** | Ultra High Vacuum |
| **VLS** | Vapor-Liquid-Solid |
| **VSS** | Vapor-Solid-Solid |
| **WZ** | Wurtzite |
| **X** | Exciton |
| **XX** | Biexciton |
| **ZB** | Zinc Blende |
| **$\mu$PL** | microPhotoLuminescence |

# Introduction

The recent development of the quantum information theory focuses the interest of the scientific community on single-photon sources (SPS) [4, 5]. These SPS emit single photons which have a low interaction with their environment (low decoherence), allowing one to use them for transmission of quantum information over large distances. For instance, these sources can be used for optical quantum computing [6, 13] or quantum cryptography to improve the quantum key distribution performances and avoid eavesdropping [7]. They can also be used in quantum information processing and metrology [8].

In the past few years, several types of SPS have been developed like single atoms [14], single ions [15], single molecules [16] and atomic ensembles [17]. However, these systems are very complex to handle. More accessible SPS systems employ the use of non-linear optics [18], intrinsic defects [19], colored centers [20] and semiconductor Quantum Dots (QDs) [21–23]. The interest of the research community for epitaxial semiconductor QDs can be explained by their numerous advantages: they can be implemented in compact devices, scaled to large quantum networks and embedded in high-quality nanostructure cavities and waveguides to generate bright sources of single and entangled photons. Moreover, they can be excited both optically and electrically for single-photon applications.

The demonstration of single-photon emission is usually carried out at cryogenic temperature. However, for realistic SPS applications, reliable SPS are necessary [9] and the challenge is to get a SPS operating up to room temperature. Indeed when the temperature is increased, the thermal excitation leads to non-radiative recombinations and decreases the SPS efficiency.

Our group recently demonstrated that a QD of CdSe in a NanoWire (NW) of ZnSe can emit single-photons up to room temperature [10]. Still, these NWs had a low quantum yield and were not vertically oriented on their samples since they were grown along the (001) crystallographic orientation. The interest of vertically oriented NWs is to be easily coupled to photonic structures to increase their photon collection, as we will see in this manuscript. The growth of such vertically oriented NWs is favored on (111)-oriented substrates.

**In this context, the aim of this PhD work is to develop the growth of vertically oriented ZnSe-CdSe NW-QDs along the (111) crystallographic orientation by molecular beam epitaxy, to study their luminescence up to room temperature for SPS applications, and to couple these nano-objects to photonic structures to increase the photon collection.**

The manuscript is organized as follows:

1. The **first chapter** aims at introducing the fundamentals necessary to understand the results of this manuscript. We review the SPS state-of-the-art and answer the question: *"why are ZnSe-CdSe NW-QDs promising candidates as SPS?"*. Then we provide an overview of the II-VI Se-based semiconductors electronic and structural properties, along with the experimental tools used in this work. The molecular beam epitaxy growth machine and the structural characterization tools are introduced, followed by the optical benches used for photo- and cathodoluminescence studies.

2. The **second chapter** is devoted to the growth and characterization of ZnSe NWs. The growth of these ZnSe NWs is compared on GaAs(111)B (As-terminated) substrates and on ZnSe(111) (Zn and Se-termined) buffer layers. We determine the best conditions to grow high quality and vertically oriented NWs. Then, we develop the passivation of these NWs with a higher bandgap material (ZnMgSe) to enhance the NWs luminescence.

3. In the **third chapter**, we demonstrate for the first time the possibility to insert CdSe QDs in ZnSe NWs grown on (111)B-oriented surfaces. The CdSe QDs are inserted using two different growth conditions. The impact of these growth conditions is analyzed by structural and composition investigations, along with (time-resolved) photoluminescence studies.

4. The **fourth chapter** deals with the photons enhancement from these NW-QDs. First, we modify the NW-QDs dielectric environment to see if it has an effect on the NW-QDs decay-rate. Then, we study the possibility to create photonic wires from the NW-QDs by covering them with a thick dielectric shell. The aim is to guide the photons along the wire axis to enhance the photon collection.

5. Finally, after the **global conclusion** and **perspectives**, the **Appendix** presents some possibilities to further increase the collection of photons by gathering the photons emitted in the substrate.

## Collaborations

This PhD work is the result of several fruitful collaborations, with colleagues from the *NanoPhysics and SemiConductors* (NSPC) group and external collaborators. The list of the collaborators is given hereafter:

- The **tapered ZnSe NWs** were grown by Valentina Zannier from Trieste in Italy (IOM-CNR laboratorio) and the corresponding cathodoluminescence characterization was performed along with Alberto Artioli and David Ferrand (NPSC).

- The **decay-time measurements** on the ZnSe-CdSe NW-QDs were performed on Mathieu Jeannin and Gilles Nogues photoluminescence setup. The measurements were performed with Mathieu and Woojin Lee, a Korean PhD student from Pusan National University who came in our laboratory during 4 months. We also used the time-resolved optical setup of Joël Bleuse for the characterization of ZnSe NWs.

- Catherine Bougerol and Martien Den Hertog carried out the **high-resolution transmission electron microscopy** shown in this manuscript.

- The **nanomanipulation** of the NW-QDs was handled by Nicolas Mollard (LEMMA from CEA-Grenoble) and the **energy-dispersive X-ray spectroscopy** was performed by Eric Robin (LEMMA).

- The **atom probe tomography** of self-assembled CdSe QDs was achieved by Hammouda Benallali, Khalid Hoummada and Dominique Mangelinck from the IM2NP-CNRS in Marseille.

- The **time-resolved cathodoluminescence** measurements were realized with Fabrice Donatini.

- The **theoretical decay-time calculations** were accomplished by Niels Gregersen and Teppo Häyrynen from DTU Photonik.

- The **simulation** results presented on **NW-QDs deposited on high refractive index and transparent substrates** were obtained by Flora Gautheron during her optional L3 internship, under the supervision of Gilles Nogues.

Chapter 1

# II-VI semiconductor quantum dots for single-photon emission

## Contents

This chapter aims at introducing the fundamentals necessary to understand the results of this manuscript. First, we review the Single-Photon Sources (SPS) state-of-the-art and answer the question: *"why are ZnSe-CdSe NW-QDs promising SPS?"*. In a second part, an overview of the II-VI semiconductor properties will be provided and the experimental tools used in this work will be presented in a third part.

## 1.1 II-VI nanowire quantum dots for single photon emission

### 1.1.1 Semiconductor QDs single-photon sources

To explain the QDs optical properties and more precisely how they can emit single-photons, let us take a general example of a QD with its discrete energy levels: the fundamental $s$ states and excited $p$ states. When the QD is excited with a laser, electron-hole pairs (usually called exciton in the context of semiconductor QDs) are created and fill the QDs energy levels, as shown in Figure 1.1a. The QD energy levels are populated according to the laser excitation power, as illustrated in Figure 1.1b which shows a CdTe QD emission intensity as a function of the Continuous Wave (CW) laser power. The low-excitation spectrum is dominated by the recombination of single-excitons in the ground state ($X \rightarrow 0$) and by increasing the laser excitation power, the biexciton ($XX$), three-exciton ($X_3$) and four-exciton ($X_4$) complexes are progressively visible. The combination of spatial confinement and Coulomb interaction leads to *spectrally different emission energies for each excitonic complex* (for instance, $\mathrm{E_X} \neq \mathrm{E_{XX}}$), which is the key to get a single-photon emission as we will see.

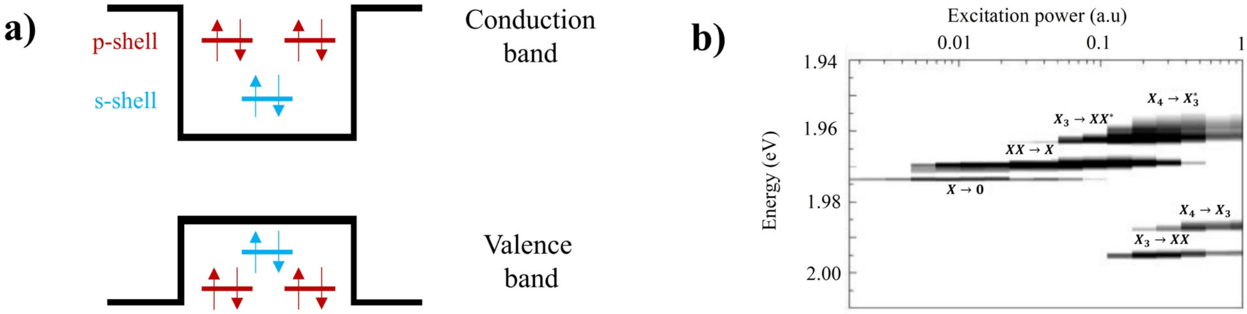

Figure 1.1: a) QD fundamental $s$ states and excited $p$ states filled with excitons. b) Figure extracted from Ref.[24]. Contour plot of the variation of the emission intensity of a CdTe QD *vs.* excitation power *vs.* emission energy. Dark regions indicate strong emission intensities and bright regions low intensities. The multi-exciton excited state is labeled with a *.

When the QD is excited with a pulsed laser of sufficiently high power, the QD states are filled and the exciton complexes progressively recombine. This process is called a *radiative cascade* (illustrated in Figure 1.2): a multiexciton $X_n$ (composed of $n$ excitons) recombines, emits a photon $h\nu_n$ and becomes the $X_{n-1}$ state. This process continues until the two final excitonic states $XX$ and $X$ are reached (with their respective $h\nu_{XX}$ and $h\nu_X$ photon emissions) and then the QD is empty. Since each of these recombinations emits a single-photon at a different energy, by spectrally filtering a certain excitonic emission, a SPS can be created. Usually, the $XX$ and $X$ emissions are used for single-photon emissions.

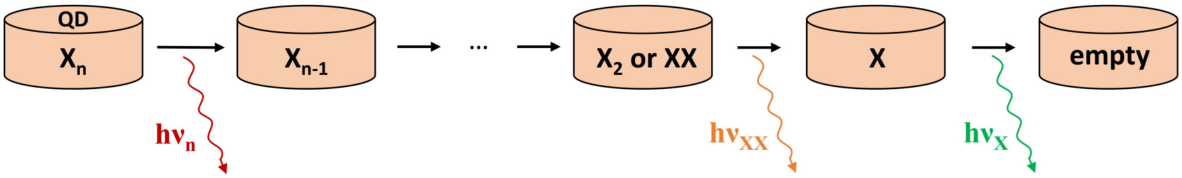

Figure 1.2: Illustration of a radiative cascade in a QD where $X_n$ recombines, emitting a photon $h\nu_n$ , followed by $XX$ and $X$ emissions.

Recently, different types of semiconductor QDs were used for SPS, such as InAs [25, 26], GaN [27–29], InGaAs [30, 31], CdTe [32], and CdSe [23, 33]. At this time, the best result at cryogenic temperature has been reported in Ref.[34] on an InAs/GaAs self-assembled QD embedded inside a micropillar cavity composed of distributed Bragg reflectors (a complex system compared to our ZnSe-CdSe NW-QDs). It simultaneously announces a deterministic generation of single-photons with an extraction efficiency of 66%, single-photon purity of 99.1% and a photon indistinguishability of 98.5%.

Indeed, to be useful, a SPS should meet some criteria. First, it should be able to emit only single-photons, a quality evaluated by the value of $g^2(\tau = 0)$ given by a photon correlation measurement. Secondly, the SPS repetition rate given by $\Gamma = 1/\tau_{rad}$ should be high (with a low decay-time in the ns scale) to maximize the SPS bandwidth. Another important criterion is a high emitted photons indistinguishably which imposes a long photons coherence length. Such a criterion is necessary for quantum calculation using linear optics [35]. Finally, the SPS should also have a high quantum yield, a single mode spatial emission, a well defined polarization and emit at high temperature (up to room temperature).

Most of the results obtained on SPS are measured at cryogenic temperature, which is too low for industrial applications. At this temperature, the excitonic lines are sharp (below 1 meV) and well separated. A problem arises when the temperature increases (more relevant for realistic applications). In this case, the carriers can escape from the QD due to a coupling to phonons, which leads to non-radiative recombinations. In addition, the *QD emission lines broaden due to a coupling to phonons* [36]. At room temperature the X-XX lines separation should be higher than the lines broadening $\Delta h\nu_X$ and $\Delta h\nu_{XX}$ to clearly separate X from XX and remain in the single-photon regime. This phenomenon is illustrated in Figure 1.3.

Such a X-XX separation is not sufficient for InAs/GaAs QDs where X and XX merge usually below 100 K. For III-V semiconductors, a sufficient X-XX separation can be obtained at room temperature for AlGaN QDs inserted in GaN NWs [28, 29]. These QDs showed a constant $g^2(\tau = 0)$ value around 0.34 ± 0.12 up to 350 K but their main drawback is to emit in the deep ultraviolet (4.0-4.6 eV or 310-270 nm). At this wavelength, the photons are absorbed by the atmosphere [37] and also in optical fibers. The impossibility to transfer these photons over long distances is unfavorable for realistic applications.

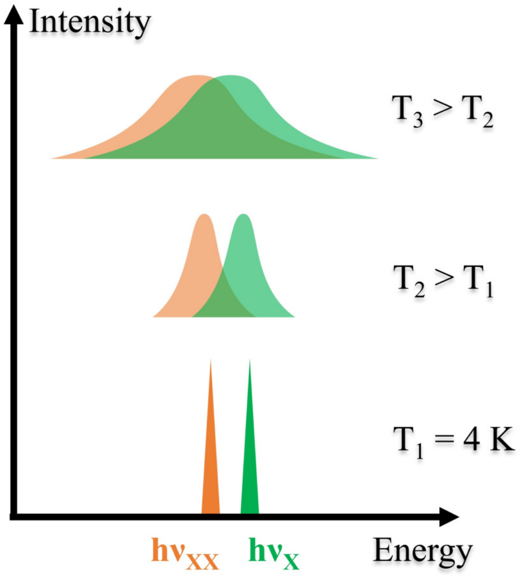

Figure 1.3: Illustration of the X and XX lines broadening occurring during an increase of temperature. At $T_1 = 4$ K, the X and XX lines are sharp and well separated. At $T_2 > T_1$, the lines broaden but are still separable. At $T_3 > T_2$, the lines broadening is too high to spectrally separate both X and XX lines.

Another system based on II-VI semiconductors permits to obtain single-photon emission up to room temperature: a CdSe QD inserted in a ZnSe NW [10], which is the system we will use in this work. These nano-objects emit in the visible range (typically from 500 to 600 nm): their wavelengths are well transmitted through the atmosphere [37] and could be used for practical applications. Indeed, we can easily imagine the implementation of SPS-based quantum cryptography protocols between adjacent buildings that would be operated through the air. Such implementation is ideal in the visible range since it can be operated through the air. For the emission of InAs QDs embedded in GaAs, emitting in the near-infrared, the photons are absorbed by the atmosphere but can be transmitted through optical fibers. However, it requires a more complex and expensive implementation than the use of visible photons since optical fiber networks need to be built.

### Room temperature SPS emitting in the visible

At room temperature, only a few candidates emitting in the visible remain with some promising systems such as Nitrogen-Vacancy (NV) centers [38], CdSe nanocrystals [39] and our ZnSe-CdSe NW-QD system [10]. Figure 1.4 presents the emission of these three systems at room temperature and Table 1.1 summarize the properties of these three systems. We can first notice the large Full Width at Half Maximum (FWHM) of the NV centers ($\sim$ 100 nm), compared to the CdSe nanocrystals ($\sim$ 55 nm) and the ZnSe-CdSe NW-QDs ($\sim$ 3.5 nm). Moreover, the number of counts/s is higher for the NV centers and the CdSe nanocrystals ($\sim$ 5 $10^4$) compared to the ZnSe-CdSe NW-QDs. However, when the number of counts/s is normalized to the FHWM, the ZnSe-CdSe NW-QDs shows the highest number of counts/s/nm.

In addition, the highest repetition rate (~ 3.5 GHz) is given by the ZnSe-CdSe NW-QDs. It is much faster than the two other systems (0.08 and ~$10^{-3}$ GHz for the NV centers and the CdSe nanocrystals respectively), positioning these nano-objects as a very promising SPS for realistic room-temperature applications.

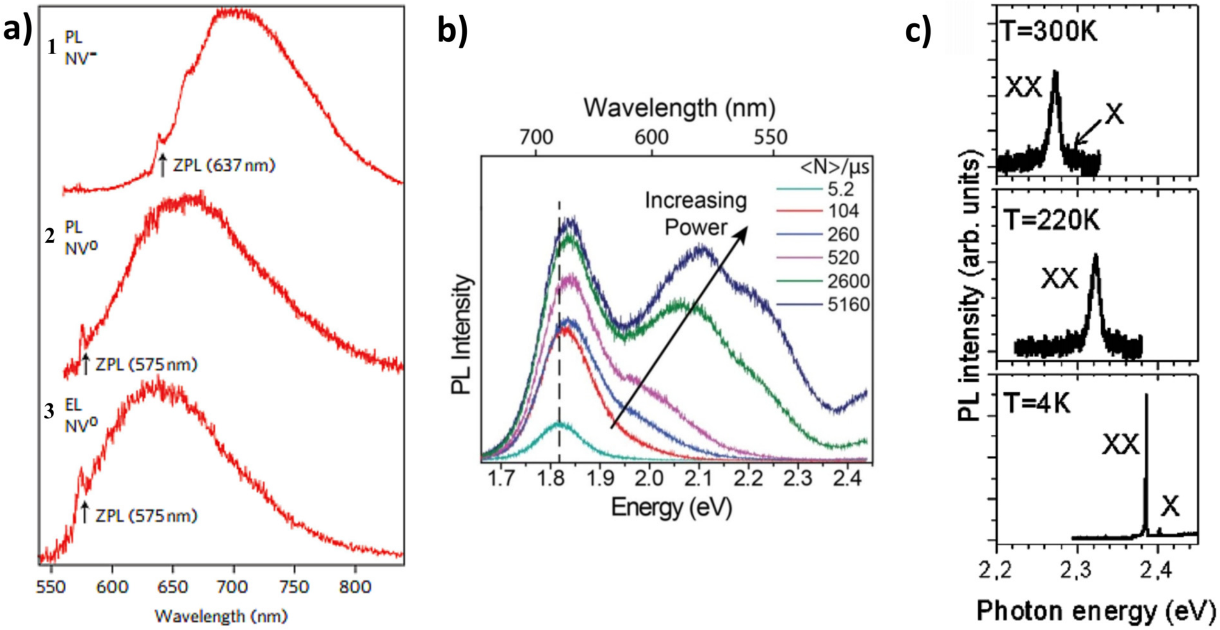

Figure 1.4: a) Extracted from Ref.[38]: photoluminescence (PL) spectra of (1) a NV⁻ center, (2) a $NV^0$ center and (3) electroluminescence spectrum of a single $NV^0$ center. The zero-phonon line is accompanied by intense photon side-bands giving a PL Full-Width at Half Maximum (FWHM) around 100 nm. b) Extracted from Ref. [38]: PL spectrum of a single CdSe nanocrystal at increasing excitation powers. The second excitation power (red) is taken as a reference for single-photon emission (exciton without multiexcitonic pollution) with a FWHM around 55 nm. c) Extracted from [10]: PL spectra of a ZnSe-CdSe NW-QD. The biexciton XX remains up to room temperature with a FWHM around 3.5 nm at 300 K.

| | NV centers [38] | CdSe nanocrystals [39] | ZnSe-CdSe NW-QDs [10] |
|---|---|---|---|
| FWHM (nm) | 100 | 55 | 3.5 |
| Counts/s | $\sim 5\ 10^4$ | $\sim 5\ 10^4$ | $\sim 10^4$ |
| Counts/s/nm | 500 | 1000 | 2900 |
| Repetition rate (GHz) | 0.08 | $2.5 \times 10^{-4}$ to $6.7 \times 10^{-3}$ | 3.3 |

Table 1.1: Comparison between the room temperature luminescence properties (FWHM, counts/s, counts/s/nm and repetition rate) of promising room temperature SPS: NV centers, CdSe nanocrystals and ZnSe-CdSe NW-QDs.

For these reasons, this work focuses on ZnSe-CdSe NW-QDs. This system has been previously studied in our laboratory and we review in the next part the main results obtained so far.

#### Previous studies in our laboratory on CdSe QDs inserted in ZnSe(001)-oriented NWs

In the past few years, investigations on CdSe QDs has been performed. First, the growth of ZnSe-CdSe NW-QDs has been performed by Aichele et *al.* [40] on the oxide layer of Si(001) substrates. The (001) surface orientation was chosen since the group had a strong 2D growth experience on this surface. At this time, it was the very beginning of the NW development in our group. Because these NW-QDs were grown on an oxide layer, they had no epitaxial relation with the substrate and the NW growth orientation was uncontrolled. More recently, Elouneg-Jamroz et *al.* *[41]* developed the growth of ZnSe NWs on ZnSe(001) buffer layers, grown on top of a GaAs(001) substrate with the aim to be in epitaxial relation with the substrate, control the NW diameter and start NW growth on a clean ZnSe buffer layer. The main advantages of this ZnSe buffer layer is to avoid the incorporation of Ga or As in the NWs, improve the surface quality and the epitaxial relation between the NWs and the substrate. Using these NW-QDs, Bounouar et *al.* obtained antibunching measurements up to room temperature [10]. During these previous photoluminescence investigations, NW-QDs were mechanically deposited on top of a patterned substrate (see Part 1.3.4) and the laser was blindly moved at its surface until a clear excitonic signature was recorded. In this PhD work, we insured the observation of NW-QDs by imaging them with a scanning electron microscope before their characterizations (see Part 1.3.4).

In spite of the numerous results obtained by our group on these (001)-oriented NW-QDs, the creation of (111)-oriented ZnSe-CdSe NW-QDs is not documented in the literature and we develop it in this manuscript. Such **(111) surface orientation** permits to grow **vertically oriented NW-QDs** which can easily be coupled to photonic structures to increase their photon collection, as we will see in Part 4.2. They also permit to get a more uniform size of the QDs within the sample since all the NW-QDs are similar (vertically oriented), to the contrary of the NW-QDs grown on the (001) surface orientation, which grow along different orientations, resulting in several NW-QDs morphologies.

### 1.1.2 Advantages of the NW geometry compared to self-assembled QDs

In addition to the NW-QDs, room temperature single-photon emission can be reached using **self-assembled QDs** [22] (epitaxial self-assembled QDs are usually strained-induced and called Stranski-Krastanov (SK) QDs). However, these structures present several limitations:

- Their shape and density are strongly dependent on the lattice mismatch between the substrate and the QD material, and cannot be adjusted independently. The capping layer also influences their final shape.

- Their size dispersion results in a relatively broad spectral distribution (inhomogeneous broadening) of their emission wavelength.
- Before the QD formation, a wetting layer covers the whole substrate surface uniformly. This wetting layer, which subsists even after the QD capping, is a pathway for carriers to escape more easily from the QD when the temperature increases, drastically degrading the QD properties at room temperature [42].
- Their exact location is not predetermined due to the self-forming nature which makes their spatial distribution unavoidable. There were several attempts to localize SK QDs by mean of substrate patterning or substrate masking (selective growth). However, the QDs must be formed directly on these processed surfaces where residual contamination may play a role in degrading the optical properties of the QDs. A recent time-demanding alternative is to localize single SK-QDs by photoluminescence [43] or cathodoluminescence [44] and etch the semiconductor to isolate them.

These limitations certainly hinder the use of SK-QDs for realistic applications. On the other hand, the interest of the scientific community for the **NW** geometry can be explained by its advantages:

- NWs can be grown on a foreign substrate with no stringent lattice-matching condition. Indeed, the strain applied by the substrate on the NW can be efficiently relaxed on the NW sidewalls [2].
- In catalyst-assisted growth, the NW density is fixed by the density of the catalyst particles which can be relatively independent of their size.
- A NW containing a single QD is an object which can be conveniently manipulated: it can be easily removed from its original substrate, transferred on a host substrate, isolated from the others by dispersion or nanomanipulation (as we will see in Part 3.3.2).
- Metallic contacts can be deposited at both ends of a single NW, allowing the electrical injection of carriers in a single QD.
- Organized arrays of NWs can be realized. The exact locations where the NWs will grow and their densities can be pre-determined by positioning the catalyst particles.

Moreover, for **NW-QDs**, great improvements of the qualities of the QDs are expected from the flexibility of the NW system:

- The heterostructure forming the QD can be grown far enough from the substrate interface to minimize the effect of contaminants related to the substrate preparation.
- The size and the shape of QDs formed in NWs are independent of the strain involved in the heterostructure. Consequently, there is more flexibility to control the geometry of the QDs as compared to the SK QD case. For instance, the aspect ratio of the QD

inserted in the NW can be changed to control the dipole[1] orientation (see Part 1.2.4) inside the QD [45, 46] to the contrary of SK-QDs which have a fixed low aspect ratio (thickness/diameter).

For all these reasons, this PhD work focuses on vertically oriented ZnSe-CdSe NW-QDs grown along the (111) crystalline orientation. To get a deeper understanding of these structures, the next parts review the fundamental properties of II-VI Se-based semiconductors.

## 1.2 II-VI Se-based semiconductors

II-VI semiconductors are alloys composed of one or several atoms from the II column of the periodic table (for instance Zn, Cd and Mg) and atoms from the VI column (for instance Se, Te, S and O). The group II atoms have two valence electrons on their external s-shell while the group VI atoms have six valence electrons, two on their s-shell and four on their p-shell. By sharing their valence electrons, II and VI atoms create covalent bonds. This project focuses on Se-based NW-QDs and for this reason, this section mainly describes the properties of Se-based semiconductors.

### 1.2.1 Crystal structures

The stable crystalline structure of bulk ZnSe and ZnMgSe is the ZB crystal structure. The zinc blende (ZB) structure consists in two face-centered cubic lattices - one of the group II and one of the group VI - shifted from each other by 1/4 of the distance along the [111] direction. Nevertheless, we show in this work that in the form of NWs, ZnSe can also be in the hexagonal wurtzite (WZ) structure. Interestingly, the WZ phase corresponds to the stable bulk structure of CdSe and our CdSe QDs are composed of the ZB phase, as we will see in Part 3.2.2. Both ZB and WZ structures are illustrated[2] in Figure 1.5. The existence of these two phases (polytypism) within NWs has been reported [47, 48]. Many researchers try to understand and control this NW polytypism since the crystal phases rules the electronic band structures.

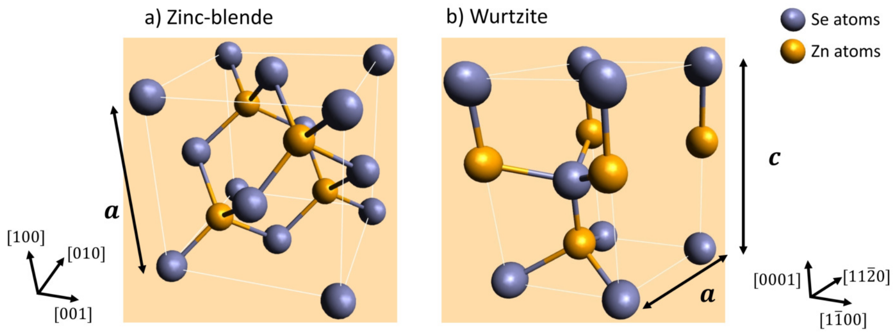

Figure 1.5: Zinc blende and wurtzite crystal structure of ZnSe.

---

[1] The exciton can be seen as an oscillating dipole.

[2] The atomic illustrations are created with the Sofware *Avogadro*.

The stacking sequences of the ZB along the [111] direction and the WZ along the [0001] direction are shown in Figure 1.6. While the ZB atomic layers sequence is ABCABC (with the C atomic plane rotated by 60° compared to A atomic plane), the WZ atomic sequence is ABAB. For ZB, the [111] and $[\bar{1}\bar{1}\bar{1}]$ directions are on the same axis (with opposite directions) but are not equivalent due to their different polar surfaces, as illustrated in Figure 1.7. This phenomenon is the same for WZ along the [0001] (c-axis) and $[000\bar{1}]$ directions.

By convention, the surface with the last atomic layer composed of:

- **II** (III) atoms - **Zn** (Ga) - is called (111)**A**,
- **VI** (V) atom - **Se** (As) - is called (111)**B**.

We will see in the next Chapter that the two surfaces induce different growth mechanisms and we will prefer the (111)B surface orientation for the growth of straight and vertically oriented ZnSe NWs.

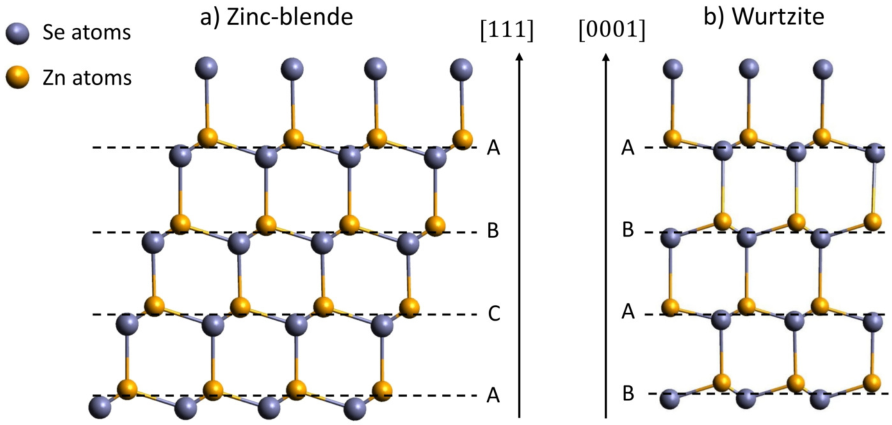

Figure 1.6: ZB and WZ stackings along the [111] and [0001] directions respectively.

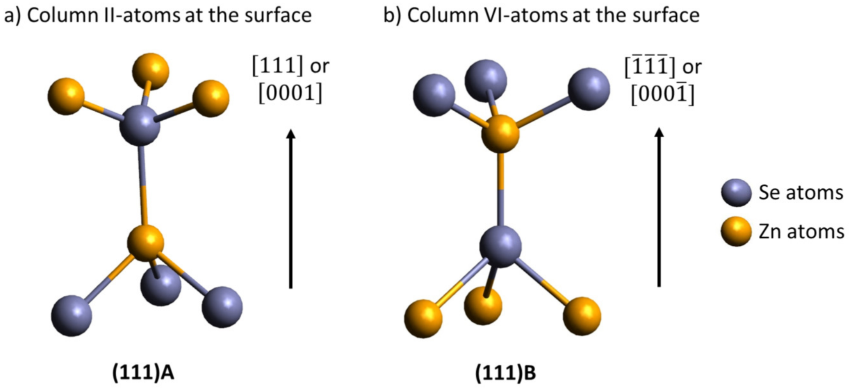

Figure 1.7: Illustrations of a (111)A (last atomic layer composed of Zn atoms) and a (111)B (idem with Se atoms) atomic stacking.

### 1.2.2 Band structure

To understand the electronic properties of a crystal - which can be seen as a giant molecule - let us first consider the case of a Cd atom with a Se atom, which have two and six valence electrons respectively. When these electrons are shared (creating covalent bonds), they lift the energies of the *s* and *p* bonding and antibonding orbitals. This principle is illustrated in Figure 1.8.

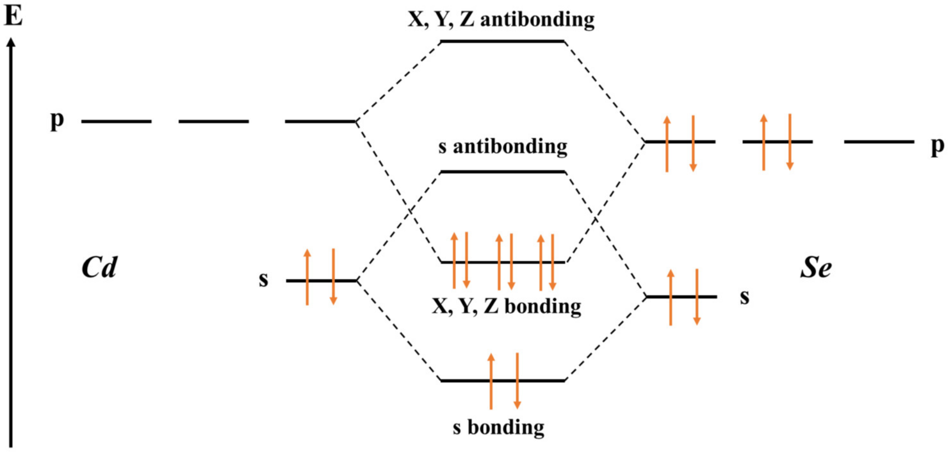

Figure 1.8: Lift of the degeneracy and electronic filling between a Cd and a Se atom.

The relevant energy levels correspond to the last saturated level: the bonding $\mathrm{p}_{\mathrm{X,Y,Z}}$ orbitals and the first empty level: the *s* antibonding orbital. These two levels are energetically separated (presence of an energy gap). When a coupling of all the atoms of a crystal is considered, energy bands are created with a broadening of the previous levels. The bonding orbitals form the so-called *valence band* and the antibonding orbitals the *conduction band*. The energy separation between these two bands corresponds to the bandgap. By taking into account the spin, at the center of the Brillouin zone the conduction band is twice degenerated with a $\Gamma_6$ symmetry and the valence band has $\Gamma_7$ and a $\Gamma_8$ symmetries and is respectively twice and four times degenerated[3]. By taking into account the spin-orbit coupling, the $\Gamma_7$ and a $\Gamma_8$ bands are separated by the energy $\Delta_{SO}$.

Therefore, the $\Gamma_6$ and a $\Gamma_8$ bands enclose the bandgap. Close to the center of the Brillouin zone (k =0), the conduction band $\Gamma_6$ (projection of the total angular momentum $j_z = \pm 1/2$) can be approximated by a parabola:

$$E(\overrightarrow{k}) = \frac{\hbar^2 |\overrightarrow{k}|^2}{2m_e^*} \tag{1.2.1}$$

---

[3] The total angular momentum $J$ of a particle of spin $S$ and orbital momentum $L$ is $J = L + S$. It is conservative and the eigenstates of $J^2$ are $j(j+1)$ with $|l-s| \leq j \leq |l+s|$. For the electrons (conduction band) $l = 0$ and $j = \frac{1}{2}$ ($\Gamma_6$ symmetry) and for the holes (valence bands) $l = 1$, so $j = \frac{1}{2} \rightarrow j_z = -\frac{1}{2},\frac{1}{2}$ ($\Gamma_7$ symmetry) and $j = \frac{3}{2} \rightarrow j_z = -\frac{3}{2},-\frac{1}{2},\frac{1}{2},\frac{3}{2}$ ($\Gamma_8$ symmetry).

with $\hbar$ the reduced Planck constant ($h/2\pi$), and $m_e^*$ the electron effective mass in the conduction band (around 10% of the free electron mass in ZnSe and CdSe).

The $\Gamma_8$ valence band is composed of two bands with a different curvature, which induces two effective masses: a heavy (projection of the total angular momentum $j_z = \pm 3/2$) and a light mass ($j_z = \pm 1/2$). As the band curvature is negative, the concept of hole is introduced. It corresponds to a positively charged quasi-particle which is an electronic vacancy moving inside the valence band. The band with the highest curvature corresponds to the Light Holes (LHs) and the other band to the Heavy Holes (HHs).

The same band structure development can be followed for the WZ band structure. In this case, the conduction band has a $\Gamma_8$ symmetry and the valence bands are denoted A ($\Gamma_9$), B ($\Gamma_7$) and C ($\Gamma_7$). Both ZB and WZ band structures are illustrated in Figure 1.9 and tight-binding calculated band structures of ZB ZnSe and CdSe are presented in Figure 1.10.

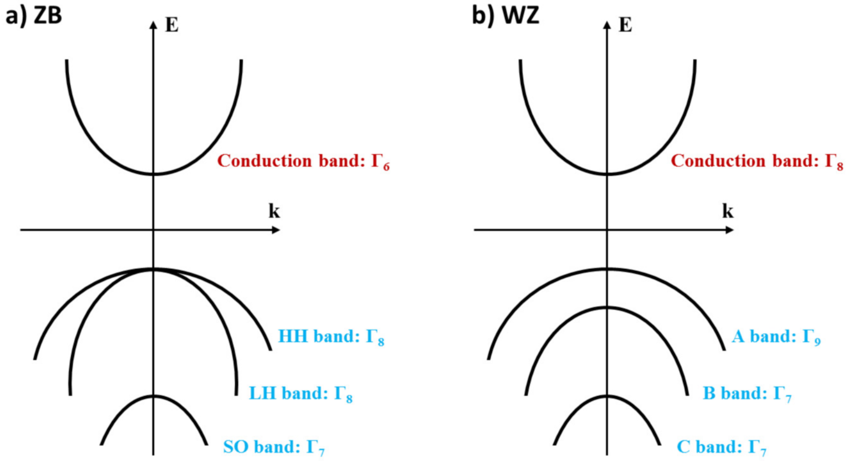

Figure 1.9: Schemes of the a) ZB and b) WZ band structures.

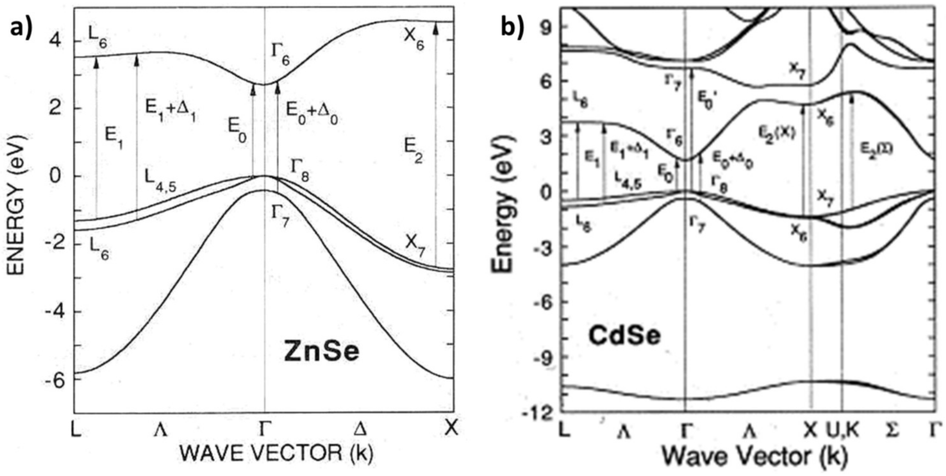

Figure 1.10: Tight-binding calculated band structures and a) ZB ZnSe b) ZB CdSe.

### 1.2.3 Electronic properties and bandgaps

The lattice parameters and bandgap values of the Se-based semiconductors used in this work are presented in Table 1.2 [49].

| | ZnSe (ZB) | ZnSe (WZ) | CdSe (ZB) | CdSe (WZ) | MgSe (ZB) | MgSe (WZ) |
|---|---|---|---|---|---|---|
| $a\,(\mathring{A})$ | 0.566 | 0.398 | 0.604 | 0.430 | 0.589 | 0.414 |
| $c\,(\mathring{A})$ | | 0.653 | | 0.701 | | 0.672 |
| $E_G$(eV) | 2.800 | 2.851 | 1.77 | 1.82 | 2.47 to 5.6 | 2.44 to 3.6 |

Table 1.2: Lattice parameters and bandgap energies at 5 K of the Se-based semiconductor materials used in this work. Notice that the bandgap of MgSe varies a lot in the literature.

For ternary alloys like $Cd_xZn_{1-x}Se$, the lattice parameter $a$ depends on its composition $x$ and can be calculated by a linear interpolation of the two binary alloys ZnSe and MgSe:

$$a_{(Cd_xZn_{1-x}Se)} = x\,a_{CdSe} + (1-x)\,a_{ZnSe} \tag{1.2.2}$$

It is called the Vegard's law [50]. On the other hand, the bandgap of a ternary alloy like $Cd_xZn_{1-x}Se$ presents a nonlinear behavior with the composition $x$ and can be calculated with the quadratic formula [51]:

$$E_G^{Cd_xZn_{1-x}Se}(x) = x\,E_G^{CdSe} + (1-x)E_G^{ZnSe} - b_{Cd_xZn_{1-x}Se}\;x\;(1-x) \tag{1.2.3}$$

with $b_{Cd_xZn_{1-x}Se}$ the bowing parameter. Figure 1.11 displays the variation of the bandgap with the lattice parameter for some semiconductor materials.

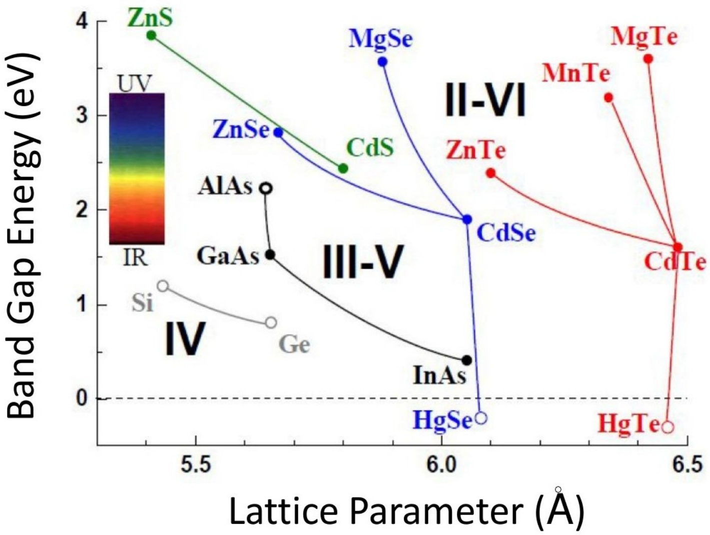

Figure 1.11: Bandgap energy at 4 K as a function of the lattice parameter for different semiconductors. Filled and empty symbols correspond to the semiconductors with direct and indirect bandgaps, respectively. Figure taken from Ref.[52].

As can be seen in Figure 1.11, the lattice parameters of ZnSe and GaAs are very similar (0.567 and 0.565 nm respectively at 300 K). Moreover, (111)-oriented ZnSe substrates are not commercially available. A possibility is to grow the ZnSe NWs directly on commercially available (111)-oriented GaAs substrates (see Part 2.1) or to first grow a ZnSe buffer layer on top of a (111)-oriented GaAs substrate prior to growing the ZnSe NWs (see Part 2.2).

### 1.2.4 Optical polarization properties

By using the previously mentioned symmetries of the conduction and valence bands, it is possible to determine the polarization selection rules of a given crystal structure. The symmetry of the initial and final states have to be known, along with the Hamiltonian symmetry. For instance in a WZ crystal, the dipolar Hamiltonian $H_{em}$ ($em$ stands for electromagnetic) describing the coupling to the electromagnetic field has the symmetry $\Gamma_1$ for an electromagnetic field parallel to the c-axis ($E||c$) and $\Gamma_5$ for an electromagnetic field perpendicular to the c-axis ($E \perp c$) [53]. A transition is allowed if the matrix element:

$$\langle u_h | H_{em} | u_{el} \rangle \tag{1.2.4}$$

is not vanishing, with $u_h$ and $u_{el}$ the hole and electron wavefunctions respectively.

In the language of group theory, this is equivalent to:

$$\Gamma_1 \subset (\Gamma_h \otimes \Gamma_{em} \otimes \Gamma_{el}) \quad (= \Gamma_{exciton} \otimes \Gamma_{em})$$

Since an electron and a hole form in our case an exciton, $\Gamma_h \otimes \Gamma_e = \Gamma_{exciton}$. Starting from the exciton symmetry, it is possible to deduce the polarization selection rules in both WZ [54] and ZB [55] crystals, as illustrated in Table 1.3.

| Exciton in a WZ crystal | $E \perp c$ | $E\|\|c$ |
|---|---|---|
| A | ✓ | × |
| B and C | ✓ | ✓ |

| Exciton a ZB crystal | $E \perp z$ | $E\|\|z$ |
|---|---|---|
| HH-electron transition | ✓ | × |
| LH-electron transition | ✓ | ✓ |

Table 1.3: Polarization selection rules for electronic transitions in the dipolar approximation for excitons in (left) a WZ and (right) a ZB crystal. In this case, $z$ corresponds to the (001) orientation in the ZB crystal.

In a WZ crystal, a recombination from an electron and a hole from the A-band is polarized perpendicularly to the c-axis, a result that we will experimentally evidence (see for instance Part 2.1.3).

**Effect of the QD aspect ratio on the QD polarization** In the case of a ZB QD, the HH- or LH-electron transition, which rules the QD polarization depends on the QD aspect ratio, as reported in Ref.[45, 46]. Figure 1.12 (extracted from Ref.[46]) shows the calculated evolution of the hole character (linear combination of HH and LH) of the ground hole state in an InAs/InP NW-QD with a base diameter of 9.6 nm as a function of the QD height. We can see that for a flat QD (height from 0 to $\sim 7$ nm), the ground hole state is mainly governed by the HH with a contribution above 60 %, while it is governed by the LH above this height. The HH-LH crossing corresponds approximately to an aspect ratio of 1 (thickness/diameter) and the small deviation observed on Figure 1.12 originates from the strain, Coulomb and quantum confinement effects.

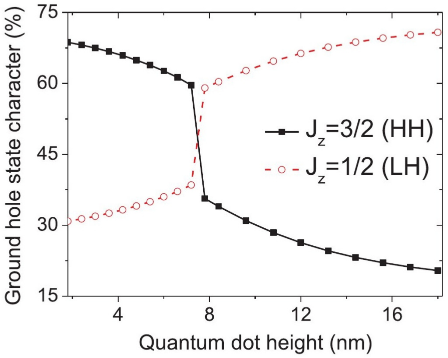

Figure 1.12: Evolution of the hole character of the ground hole state (mainly HH or LH) in an InAs/InP NW-QD with a base diameter of 9.6 nm as a function of the QD height. Figure extracted from Ref.[46].

### Effect of the dielectric screening on the NW polarization

In the previous part, we treated the ZB and WZ polarization selection rules and these rules apply to bulk semiconductors. For a NW, an additional effect plays a role on the polarization property: the *dielectric screening*. It consists in the damping of the electric field perpendicular to the NW axis caused by the presence of mobile charge carriers in the NW. Figure 1.13 permits to visualize this effect. When the NW is excited with an incident electric field *perpendicular to the NW axis* ($\overrightarrow{E}_{ext}$), the electric field inside the NW is attenuated due to the creation of a counter internal electric field ($\overrightarrow{E}_{induced}$). Indeed, $\overrightarrow{E}_{ext}$ moves charges inside the NW ($\overrightarrow{F} = q\overrightarrow{E}$) and these charges induce $\overrightarrow{E}_{induced}$ ($\overrightarrow{E} = -\overrightarrow{grad}V$ ).

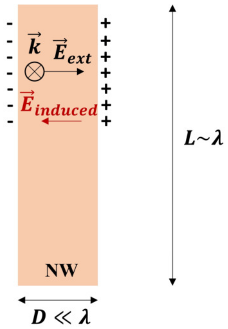

Figure 1.13: Dielectric screening effect in a NW. When the NW is excited with an external electric field perpendicular to the NW axis ($\overrightarrow{E}_{ext}$), the electric field inside the NW is attenuated due to the creation of a counter internal electric field ($\overrightarrow{E}_{induced}$).

In the electrostatic limit ($d_{NW} << \lambda$), the screening effect of a NW (refractive index $n_{NW}$) embedded in a medium of refractive index $n_{medium}$ can be estimated. We have to use the ratio of the NW decay time $\tau_{NW}$ compared to $\tau_{bulk}$ (emitter in a bulk of refractive index $n_{NW}$), using the following formula derived from Ref.[56]:

$$\frac{\tau_{NW}}{\tau_{bulk}} = \frac{1}{4}\frac{n_{NW}}{n_{medium}}[(\frac{n_{NW}}{n_{medium}})^2 + 1]^2 \tag{1.2.5}$$

This ratio corresponds to the modification of the NW decay-time compared to the bulk reference: for $n_{NW}/n_{medium} > 1$, the NW decay-time $\tau_{NW}$ is longer than the bulk reference.

For an electric field *parallel to the NW axis*, the electric field inside the NW is not attenuated and behaves like in the bulk case. The dielectric screening permits to better understand why most of the time, a NW polarization in emission is aligned with the NW axis. Indeed, since a light polarized perpendicularly to the NW axis is damped by the dielectric screening, an absence of (or a very small) polarization component along the NW axis is needed to observe such perpendicularly polarized light. This is the case in WZ NWs grown along the c-axis due to the selection rules.

### NW polarization measurements in excitation and in emission

During photoluminescence measurements of NWs deposited on patterned substrates (later discussed in Part 1.3.4) and it is possible to probe the NW polarization: in *excitation* and in *emission*. In *excitation*, a linear polarizer is placed on the laser beam, followed by a $\lambda/2$ plate as illustrated in Figure 1.14. By rotating this $\lambda/2$ plate, the polarization angle of the exciting beam changes and the NW emission is recorded as a function of the excitation polarization angle. In this case, a maximum intensity from the NW is recorded when the NW axis is aligned with incident light polarization. This result can be understood from the previous discussion on the dielectric screening. Indeed, an electric field parallel to the NW axis is totally absorbed, resulting in the creation of a lot of excitons. On the other hand, an electric field perpendicular to the NW axis is attenuated inside the NW, resulting in the creation of less excitons and therefore, a smaller emission. This technique permits to precisely determine the NW angle with respect to the main axis of the linear polarizer (see Figure 1.14 ).

In *emission*, the NW emission is rotated by the $\lambda/2$ plate and passes through a linear polarizer prior to be recorded in a monochromator (later discussed in Figure 1.14). This useful characterization technique is used in this work to probe the NW polarization resulting from the selection rules and the dielectric screening.

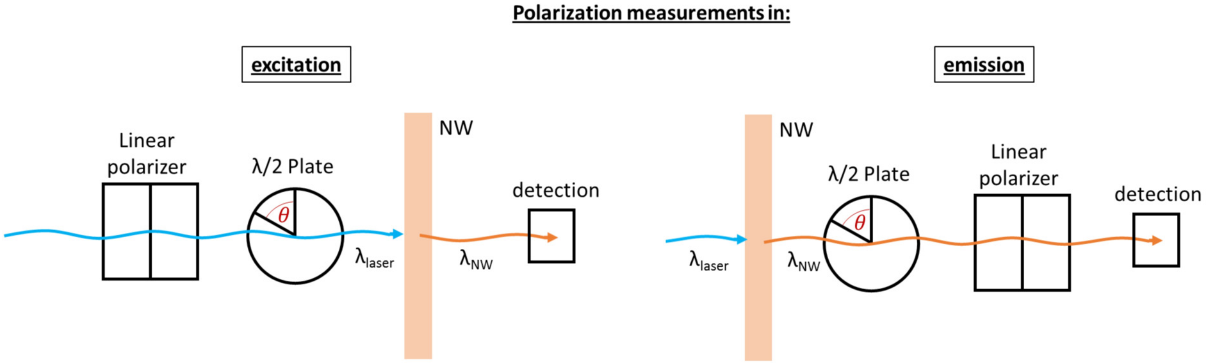

Figure 1.14: Illustration of polarization measurements in excitation (left) and in emission (right). In excitation, the laser beam is linearly polarized by a linear polarizer, followed by a $\lambda/2$ plate. By rotating this $\lambda/2$ plate, the polarization angle of the exciting beam changes and the NW emission is recorded as a function of the excitation polarization angle. In emission, the NW emission is rotated by the $\lambda/2$ plate and passes through a linear polarizer prior to be recorded in the monochromator.

## 1.3 Experimental tools

After reviewing the SPSs state-of-the-art and summarizing the II-VI semiconductor properties, it is now time to describe the main experimental tools used in this work. First, the growth by molecular beam epitaxy will be described, followed by the description of structural and optical characterization devices.

### 1.3.1 Molecular beam epitaxy setup

**Molecular Beam Epitaxy (MBE)**

As previously mentioned, the crystalline SPS developed in this work are composed of a CdSe QD inserted in a ZnSe NW. To obtain bright SPS, it is essential to have a high crystalline quality and control the growth process at the monolayer (ML) level. To do so, we used Molecular Beam Epitaxy (MBE). This appropriate growth method consists in sending several atomic (Zn, Cd or Mg) or molecular ($Se_2$) fluxes toward a heated crystalline substrate under Ultra High Vacuum (UHV) to generate an epitaxial growth. A picture of the MBE used during the work is shown in Figure 1.15: the samples are inserted in the introduction chamber and can then be heated (usually one hour at 340°C) in the preparation chamber to remove surface impurities. Then, the growth takes place in the II-VI and III-V semiconductor chambers. Eventually, metallic depositions can be performed in a dedicated chamber. These chambers are all connected by UHV.

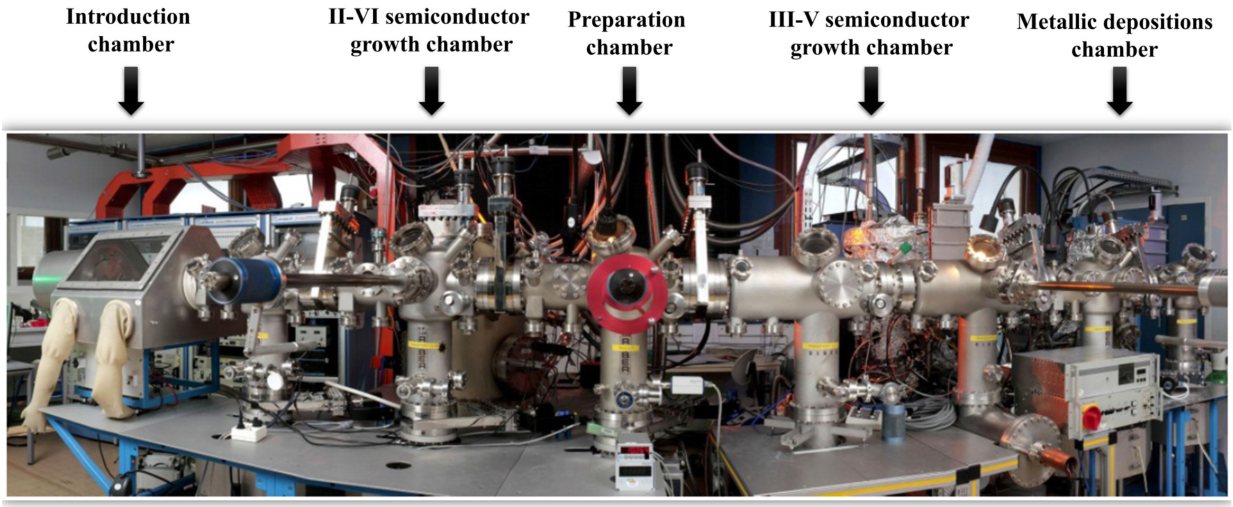

Figure 1.15: Image of the MBE used during this PhD with its corresponding chambers.

The molecular fluxes are generated by evaporation or sublimation of materials placed in crucibles called Knudsen effusion cells. These crucibles are composed of boron nitride, a thermally stable and ultra-pure material. The crucible temperatures are controlled via thermocouples and regulated toward their target values via Proportional–Integral–Derivative (PID) controllers. Thanks to the UHV, the atomic and molecular fluxes are in the ballistic regime, meaning that their mean free path[4] is longer than the crucible-substrate distance. In front of each crucible, metallic shutters permit to control the fluxes sent onto the substrate. Another big shutter permits to stop all the fluxes at once.

Figure 1.16 shows a sketch of the II-VI MBE chamber used in this work with a) a top-view and b) a side-view. This chamber is cooled down by cryopanels down to liquid nitrogen temperature ($\sim$ 77 K) during the growth to capture remaining impurities and further cryopump the chamber (in addition to the II-VI chamber pumping system, composed of a permanent cryopump operating around 10 K, an ionic pump and a tungsten sublimation pump, not shown here). These impurities are monitored with a mass spectrometer. A sample manipulator permits to rotate the sample during the NW growth and the MBE fluxes can be measured using a beam flux sensor. Different materials can be sent onto the sample: Cd, Se, ZnTe, Mn, Mg, CdTe, Zn and Te. For instance, the growth of ZnSe (CdSe) is carried out by sending a flux of Zn (Cd) and a flux of Se. These materials are radially (Figure 1.16a) and vertically (Figure 1.16b) distributed around the chamber.

During a 2D MBE growth, different kinetic processes occur as displayed in Figure 1.17. First, when the adatoms reach the substrate surface, they physisorb; they are adsorbed by Van der Waals interactions (weak forces which do not implicate the electronic structure). These adatoms can diffuse at the surface or be thermally expulsed (desorption). Secondly, the adatoms - which did not desorb - chemisorb, meaning that they create chemical bonds

---

[4] The mean free path $\lambda$ can be calculated with the formula $\lambda = \frac{1}{\sqrt{2}\pi\sigma^2 n}$ with $\sigma$ is the distance at which the molecules are in collision and $n$ is the atoms density (atoms/m$^3$).

with the substrate atoms, changing the interface chemical nature. These adatoms can be absorbed in surface vacancies and lead to the formation of aggregates (nucleation), or they can be absorbed in ledge vacancy sites and lead to a step-flow growth mode. Note that the substrate growth temperature plays a key role in the diffusion of the adatoms onto the surface.

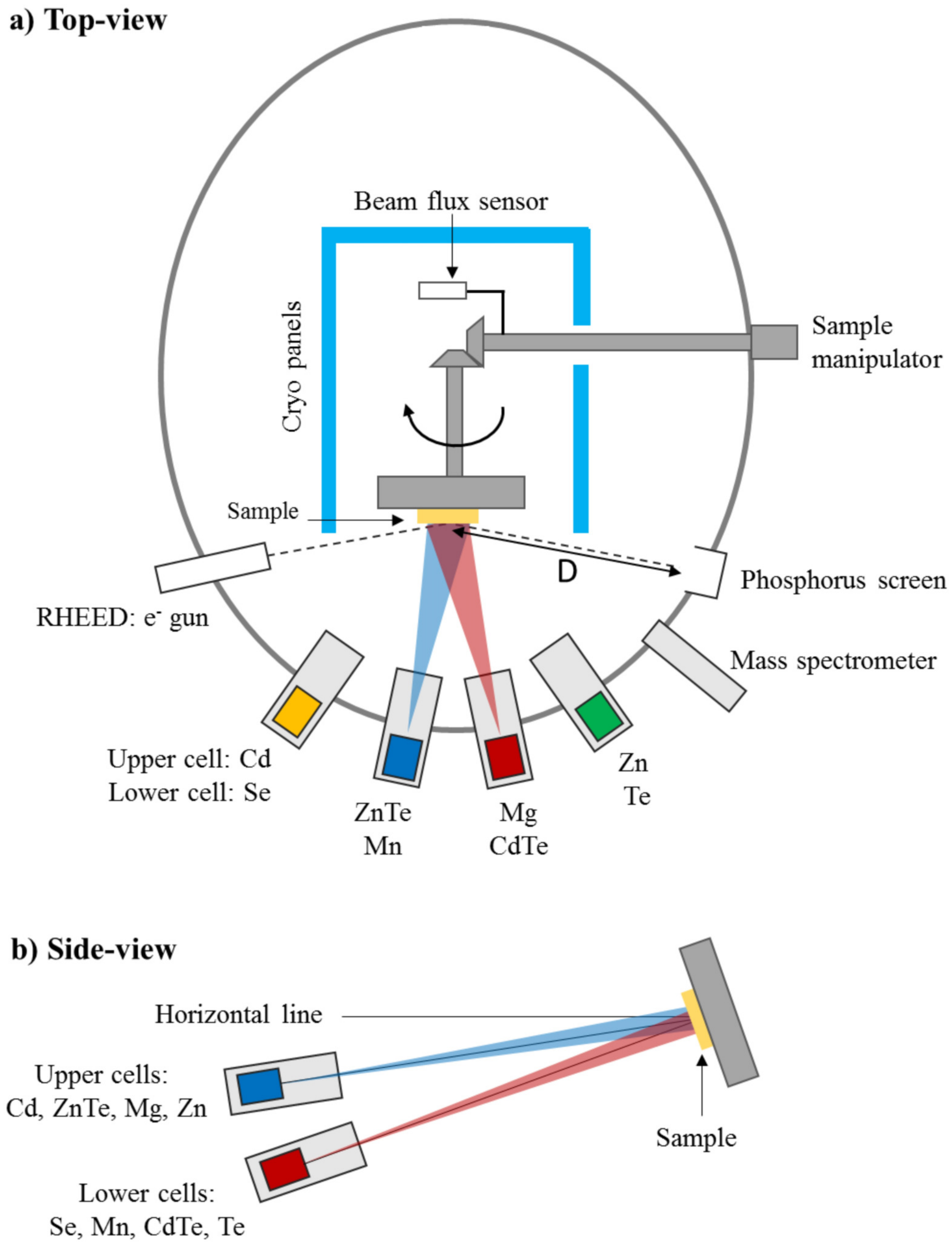

Figure 1.16: Scheme of the II-VI MBE set up used in this work with its a) top-view and b) side-view.

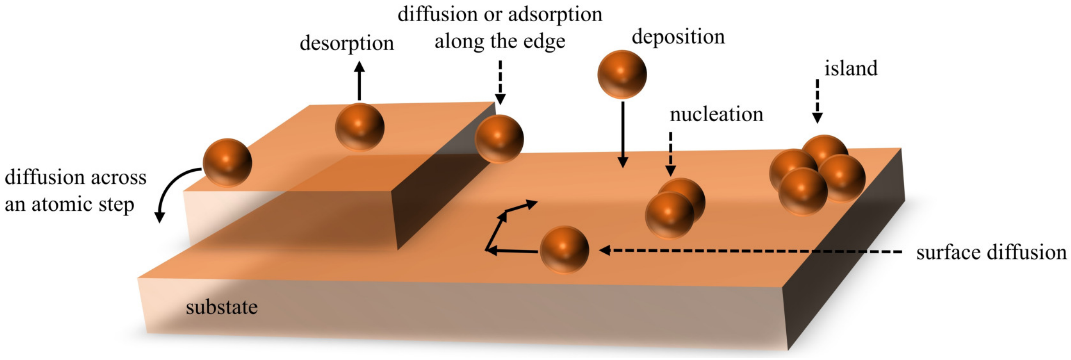

Figure 1.17: Sketch of the kinetic processes taking place during a 2D MBE growth.

The MBE permits to grow samples of excellent crystalline quality and very high purity. Its advantages compared to other growth methods are:

- a low 2D growth speed: below a ML per second, which permits to finely tune the thickness of the deposited layers.
- a relatively low growth temperature: up to 400°C for our ZnSe-CdSe NW-QDs.
- the UHV environment which allows one to use in-situ characterization techniques such as Reflection High Energy Electron Diffraction (RHEED).

**The control of the growth by RHEED oscillations** The RHEED permits to determine the crystalline structure at the substrate surface and to control in-situ the surface evolution during growth. It consists in an electron gun facing a phosphor screen inside the MBE chamber. Its working principle is illustrated in Figure 1.16. The electrons are accelerated at 30 kV, collimated and sent onto the substrate with a grazing incidence (around 2-3°). The electron beam scatters within a few atomic MLs onto the sample surface (the electron beam has a low penetration due to the grazing incident angle and its low wavelength[5], around 0.0698 $\mathring{A}$). It results in a diffraction pattern visible on a phosphor screen, which is recorded with a Charge-Coupled Device (CCD) camera. Schematically, it corresponds to the reciprocal lattice of the substrate surface but actually, the complete picture is very complex and should be treated with the dynamical theory of electron diffraction[57]. A certain surface morphology gives rise to a certain diffraction pattern, for instance:

- A perfectly two dimensional crystal surface will induce a streaky diffraction pattern with the streaks oriented perpendicularly to the surface.
- A polycrystalline surface (a powder or an array of NWs oriented in different directions) will show series of circles. Indeed, the random atomic planes orientations will diffract in all directions.

---

[5] $\lambda_{electron} = \frac{h}{\sqrt{2m_0eV(1+\frac{eV}{2m_0c^2})}}$ with $h$ the Planck constant, $m_0$ the electron rest mass, $e$ its charge, $V$ the accelerating voltage (30 kV) and $c$ the speed of light in vacuum.

- A surface with nano-objets on top (for instance vertical NWs or SK-QDs) will display a spotty diffraction pattern.

Figure 1.18 illustrates some common RHEED diffraction patterns encountered during MBE growths.

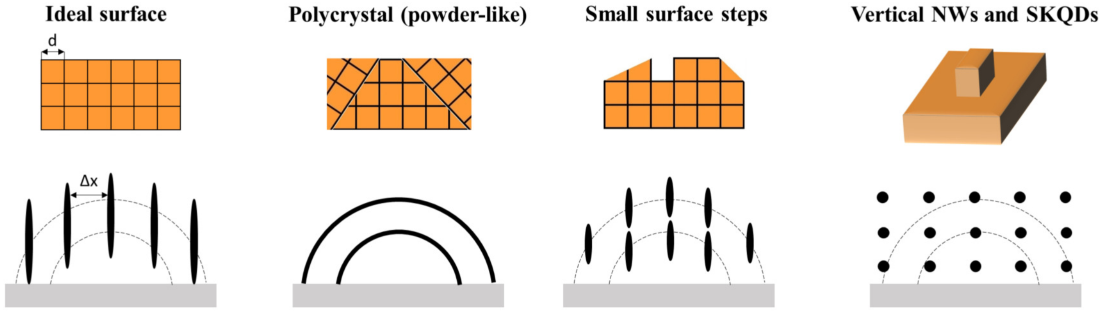

Figure 1.18: (Upper part) Illustration of surface morphologies that can be encountered during MBE growths and (lower part) the corresponding RHEED patterns. $d$ is the in-plane distance at the sample's surface and $\Delta x$ is the vertical streaks horizontal separation on the RHEED pattern.

The diffraction patterns can be numerically studied during the growth thanks to a home-made RHEED software[6]. It permits for instance to follow in real time surface modifications and to precisely calibrate the growth speed. For the surface modifications, in-plane lattice parameter modifications can be followed. Indeed, the in-plane distance $d$ is inversely proportional to the horizontal separation $\Delta x$ between streaks or spots (see Figure 1.18): $\Delta x \sim \frac{\lambda D}{d}$ with $D$ the sample-screen distance (see Figure 1.16) and $\lambda$ the electron wavelength. Furthermore, the specular RHEED spot intensity (reflected spot) depends on the coverage of the surface ML. It will oscillate in time during the growth: it is maximal for a smooth surface (integer coverage rate $\Theta$ in Figure 1.19) and minimal for a rough surface (half-integer $\Theta$). Its period is therefore equal to the deposition time of exactly one ML. By measuring these RHEED oscillations (displayed in Figure 1.19), the growth rate can be measured, usually in MLs per second.

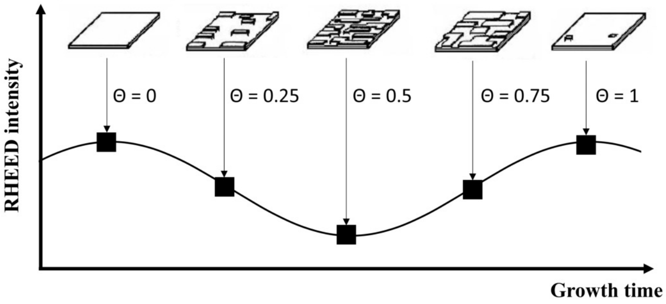

Figure 1.19: Scheme of the RHEED oscillations principle. $\Theta$ is the fractional layer coverage.

---

[6] The sofware is called *AnaRheed* and has been developed by Yoann Curé from our research group.

### Surface reconstructions (SRs)

When atoms at the surface of a crystal show a different structure than the bulk structure, surface reconstructions (SRs) occur. In Wood's notations, a $A \times B$ SR means that the two unit vectors of the bulk Bravais net are amplified by a factor A and B respectively. For instance, the $1 \times 1$ SR corresponds to the bulk termination. Note that in this case, the surface can be different from the bulk but the average periodicity is the same. Examples of SRs are provided in Figure 1.20 which shows a $\sqrt{3} \times \sqrt{3}$ R30° (rotated by 30°), $\sqrt{2} \times \sqrt{2}$R45°, $2 \times 2$ and $2 \times 1$ SRs.

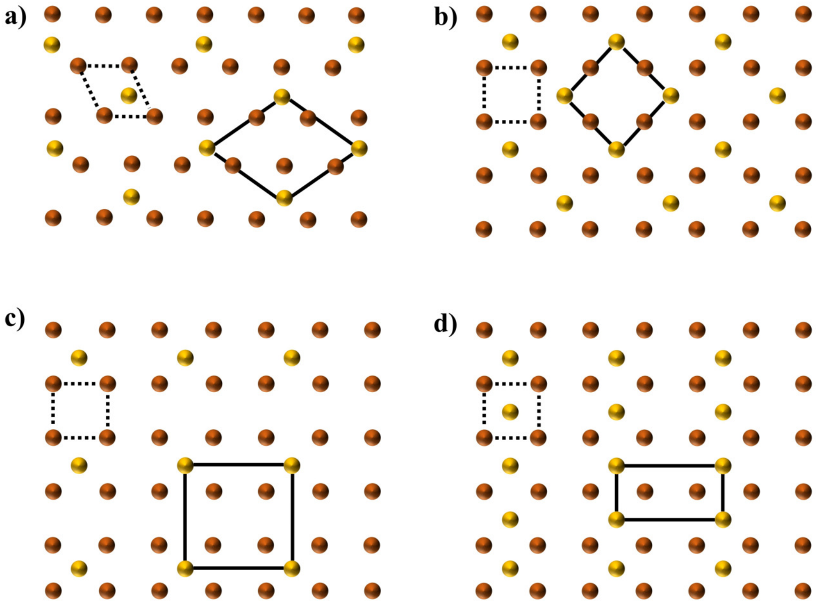

Figure 1.20: Examples of overlayer structures: the brown and yellow circles represent respectively the substrate and the surface periodicity. The substrate and surface Bravais nets are shown with dashed and full lines respectively. a) $\sqrt{3} \times \sqrt{3}$ R30° (rotated by 30°), b) $\sqrt{2} \times \sqrt{2}$R45°, c) $2 \times 2$ and d) $2 \times 1$ SRs.

For instance, SRs are visible when a GaAs(111)B 2D layer is covered by less than one ML of gold. In this case, a $\sqrt{3} \times \sqrt{3}$ SR (usually the angle is omitted) can be observed [58, 59], as displayed in Figure 1.20a. A review of solved SRs can be found in Ref.[60]. During the growth of 2D layers, SRs are visible in the RHEED patterns in the form of vertical streaks (see Part 2.2).

### NW growth model: Vapor-Liquid-Solid (VLS) and Vapor-Solid-Solid (VSS)

In the 1960s, Wagner and Ellis first proposed the Vapor-Liquid-Solid (VLS) growth mechanism to explain the growth of silicon wires catalyzed by gold particles [1]. The NW growth results from the minimization of the chemical potential ($\mu$) as mass migrates from one phase to another. The chemical potentials of these phases are equal at thermodynamic equilibrium, resulting in no transfer of mass. To favor the growth of NWs, a non-equilibrium state needs to be reached with mass transfers induced by a difference in the phases chemical potentials. Harmand et *al.* remarked that such a state is possible if the following inequality is satisfied [61]:

$$\mu_{vapor} > \mu_{adatoms} > \mu_{liquid} > \mu_{NW} \tag{1.3.1}$$

with $\mu_{vapor}$, $\mu_{adatoms}$, $\mu_{liquid}$ and $\mu_{NW}$ the chemical potentials of respectively the adatoms in the vapor state, the physisorbed adatoms (onto the NW sidewalls and substrate surface), the liquid catalyst and the NW (see Figure 1.21). These chemical potentials depend on the materials (not known for ZnSe and CdSe), the temperature and the pressure. Moreover, to model the NW growth, five parameters are generally used (in blue in Figure 1.21): the adatoms 1) adsorption, 2) desorption, 3) their nucleation at the catalyst-NW interface, 4) their diffusion on the NW sidewalls and the substrate surface, and 5) the 2D growth occurring during the NW growth. Note that to permit an homogeneous deposition of the adatoms onto the substrate surface and the NWs sidewalls, we rotate our samples around their normal direction (or vertical NW axis) during the growth.

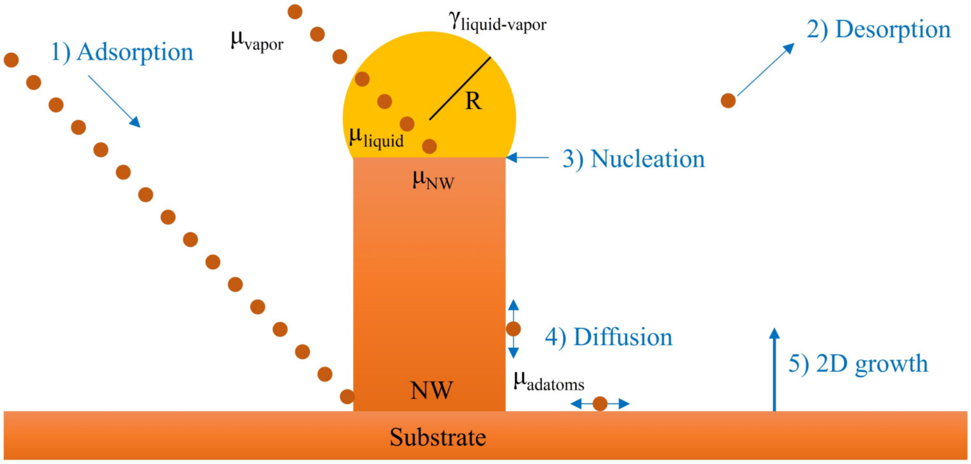

Figure 1.21: Illustration of the VLS NW growth: $\mu_{vapor}$, $\mu_{adatoms}$, $\mu_{liquid}$ and $\mu_{NW}$ are the chemical potentials of respectively the adatoms in the vapor state, the physisorbed adatoms (onto the NW sidewalls and substrate surface), the liquid catalyst and the NW. In addition, five mechanisms generally used to model the NW growth are presented in blue: 1) adsorption, 2) desorption, 3) nucleation at the catalyst-NW interface, 4) diffusion on the NW sidewalls and the substrate surface, and 5) 2D growth occurring during the NW growth.

When the catalyst is exposed to the vapor phase, its concentration shifts from its thermodynamic equilibrium value $C_{eq}$ due to the mass transfer described by the inequality 1.3.1. Therefore, the liquid catalyst reaches a supersaturated state defined by $s = C - C_{eq}$ with $C$ the non-equilibrium local concentration in the liquid. Due to the mass transfer at the phase interfaces, the liquid catalyst has a continuous gradient of C (and consequently $\mu_{liquid}$). Such a gradient moves the mass flow from the liquid-vapor surface to the liquid-NW interface according to Fick's law of mass transfer $\overrightarrow{J} = -D\overrightarrow{\nabla}n$ with $n$ the concentration of field and $D$ the species diffusion coefficient.

Moreover, the surface tension of the curved gold catalyst (of finite curvature R, see Figure 1.21) locally modifies the pressure inside the liquid catalyst. This effect is known as the Gibbs-Thompson effect:

$$\Delta P = 2\frac{\gamma_{liquid-vapor}}{R} \tag{1.3.2}$$

with $\gamma_{liquid-vapor}$ the surface tension of the liquid at the vapor interface. This effect increases the chemical potential by $\delta\mu_{liquid} = 2\frac{\phi\gamma_{liquid-vapor}}{R}$ with $\phi$ the liquid atomic volume. The chemical potentials then yields $\mu_{liquid} = \mu_{liquid}^{\infty}(T, P) + 2\frac{\phi\gamma_{liquid-vapor}}{R}$ with $\mu_{liquid}^{\infty}$ the chemical potential when the radius curvature is infinite. From Equation 1.3.2, we can see that the Gibbs-Thompson effect increases as the gold droplet radius $R$ decreases.

The melting point of pure gold is at 1064°C and when mixed with another material, a gold particle induces a low melting temperature eutectic, for instance around 360°C with Si or Ge. The eutectic temperature can be even smaller when the gold particle size is nanometric [62] due to the Gibbs-Thompson effect. This effect can partially explain why the VLS growth mechanism can sometimes happen below the catalyst eutectic temperature.

When the NW growth involves only one atom type (Si or Ge), the growth process can be clearly attributed to the precipitation of this type of atoms at the liquid-solid interface. When the NW is a binary compound, the growth mechanism is less obvious. For instance, in gold-catalyzed GaAs, Ga forms a AuGa eutectic with Au with 34% of Ga at 339.4°C [63] while the solubility of As in Au is known to be very low [64]. The VLS growth of GaAs NWs has been modeled by Glas et *al.* [12].

**Au-Zn and Au-Se eutectics** For the growth of ZnSe NWs, the eutectic will occur between ZnSe and Au. The lowest temperature eutectic of AuZn (Au-rich) and AuSe occur respectively at 684°C with 34.5 % of Zn and 760°C with 52 % of Se [65], as shown in Figure 1.22. These two eutectic temperatures are well above the ZnSe NW growth temperature used in this work (400°C, as we will see). One could argue that according to the Gibbs-Thompson effect (Equation 1.3.2), the melting point of gold catalysts can be lowered when their size decreases. However, Buffat et *al.* [62] determined that the melting point of 5 nm-diameter gold particles can be lowered by almost 200°C. If a similar temperature lowering takes place with AuZn or AuSe eutectics, the modified eutectic temperatures would still lie above the NW growth temperature and the Au catalyst would remain *solid* during the NW growth: this growth mode is called Vapor-Solid-Solid (VSS). The main advantage of the VSS growth compared to the VLS growth is:

- to *prevent the incorporation of the catalyst atoms into the NW*, which leads to deep-level impurities and degrades the NW optical properties.
- to *achieve more abrupt interfaces*: during the growth, the atoms in the catalyst progressively deplete from the droplet which acts as a reservoir. During a CdSe insertion in a ZnSe NW, the Zn flux will be replaced by a Cd flux. At this moment, both Zn

and Cd are present in the catalyst until all the Zn atoms are consumed and only Cd atoms remain. The length of this transition (the CdSe QD and ZnSe NW interface) depends on the solubility of the growth atoms in the catalyst droplet. The solubility of the atoms in the catalyst is lower in the VSS growth, which reduces the growth rate [66] and consequently, the interfaces can be more abrupt [67].

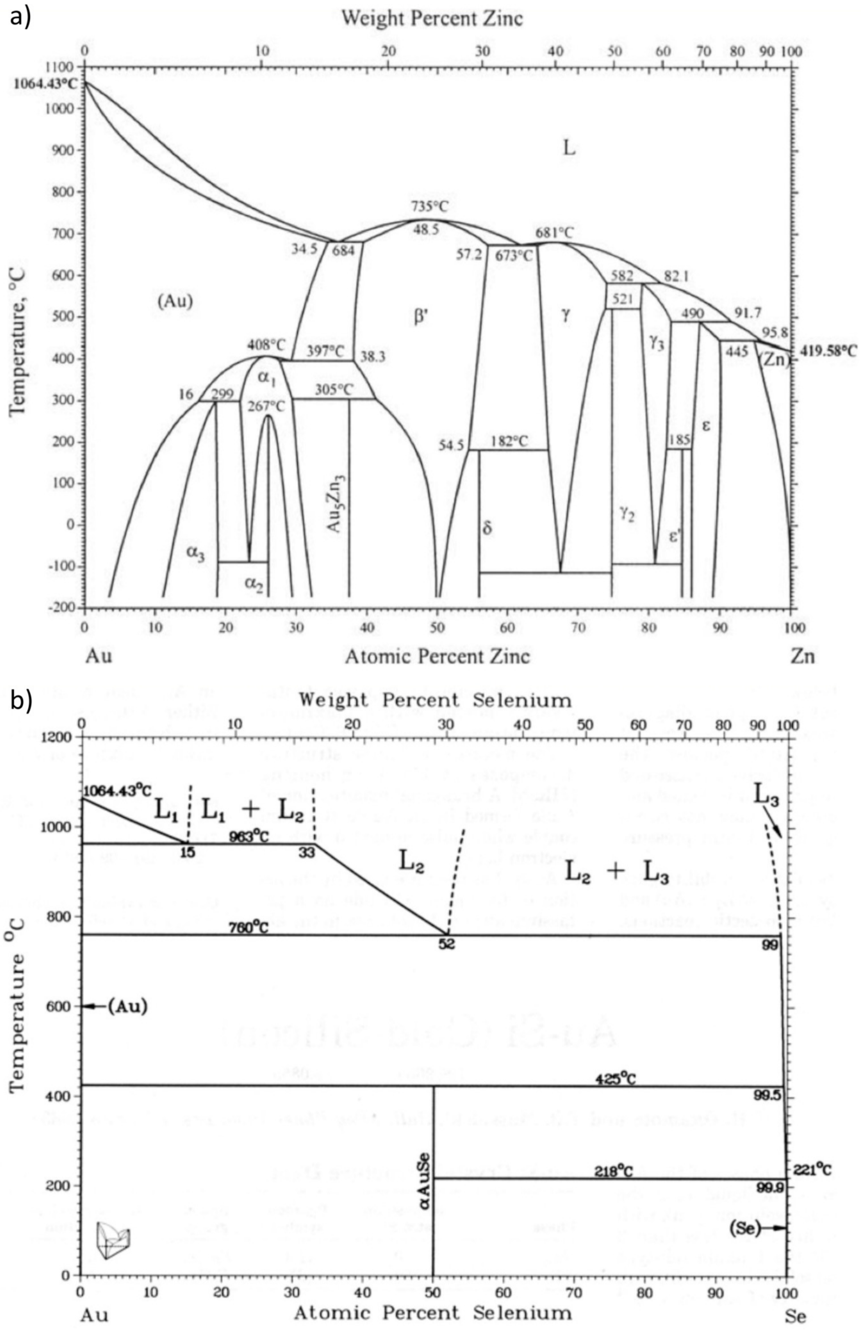

Figure 1.22: Phase diagram of a) AuZn and b) AuSe, extracted from Ref. [65].

### 1.3.2 Structural and composition analysis setups

To get a deep physical understanding of single NWs, we need to access their structure (for instance: size, crystalline structure, lattice parameters, defects) and composition. For this reason, we use different characterization techniques detailed hereafter.

#### Structural analysis setups: electron microscopy

**Scanning Electron Microscopy (SEM)** In a Scanning Electron Microscope (SEM), incoming electrons penetrate a certain volume of the observed sample with a pear-like shape. The volume of this pear depends on the mean atomic number of the sample and on the incident electrons energy. In this volume, the electrons will loose their energy due to multiple collisions with the sample atoms, generating several secondary emissions. These main secondary emissions are displayed in Figure 1.23.

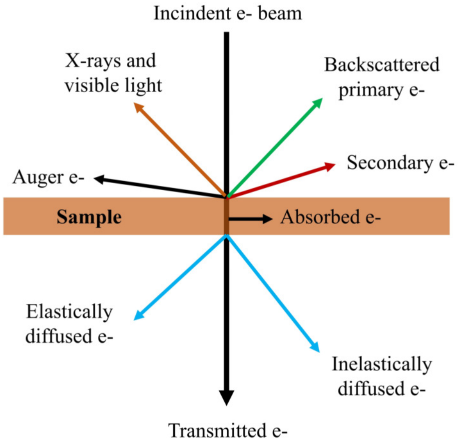

Figure 1.23: Scheme of the different mechanisms involved during a SEM observation (e- stands for electron).

In principle, a SEM has three detectors for secondary electrons, backscattered electrons and X-rays. Part of the energy of the primary beam is dissipated in the form of heat on the SEM chamber walls or are electrically grounded. In this study, the secondary electrons were collected. Due to their low energy, only those generated close to the surface (below 10 nm) can escape the sample and be collected. The quantity of secondary electrons detected is very sensitive to the sample topography. *Since we are interested by the topography of our NW-QDs, all the SEM images of this study were recorded using the secondary electrons detector*[7].

**Transmission Electron Microscopy (TEM)** Transmission Electron Microscopy (TEM) is a microscopy technique based on the transmission of an incident electron beam through a very thin sample (10 to 100 nm-thick). The sample can then be imaged with an ultra high

---

[7] In-lens detector in our ZEISS SEM.

resolution (below 1 $\AA$) and its diffraction pattern can be visualized. This powerful technique allows one to determine for instance the crystal structure of NWs, their crystallographic growth direction and their dimensions with a sub-nanometric precision.

### Composition analysis setups

**Energy-dispersive X-ray spectroscopy (EDX)** Energy-dispersive X-ray spectroscopy (EDX) has a similar working principle compared to the SEM, except that it will focus on the collection of the emitted X-rays. The X-ray emission is caused by an atom - ionized by the incident electron beam - which comes back to its fundamental level. Indeed, when a core electron is ejected from an atom, another electron from the external electronic shell will fill in the vacancy. The energy difference between these two layers will induce an Auger or a X-ray emission. These X-rays have a certain energy characteristic of the element from which they have been emitted. They are collected and ordered as a function of their energy to characterize the elements present in the studied sample.

The X-ray detector is composed of a lithium-doped silicon diode which acts as an energy detector. Every X-ray photon reaching the detector creates a tension proportional to the photon energy. The resulting spectrum is an histogram of the number of collected photons as a function of their energy. An example of such a spectrum is visible in Figure 3.20.

**Atom Probe Tomography (APT)** The working principle of the Atom Probe Tomography (APT) is illustrated in Figure 1.24 and consists in the evaporation by field effect of the surface of a sample. This technique is part of the field emission microscopy field, which consists in evaporating and ionizing the atoms at the surface of a sample with a very high electric field and a 532 nm pulsed-laser excitation (for semiconductors). The sample is therefore evaporated atomic layer by atomic layer. The evaporated atoms are collected by ions detectors which permit to determine the nature of each atom by time-of-flight mass spectrometry and to determine their initial position in the sample. The atoms distribution is then obtained in 3D within a typical 50 x 50 x 200 nm$^3$ volume and an atomic resolution around 0.1 nm in depth and 0.5 to 1 nm laterally. More information about APT can be found in Ref.[68].

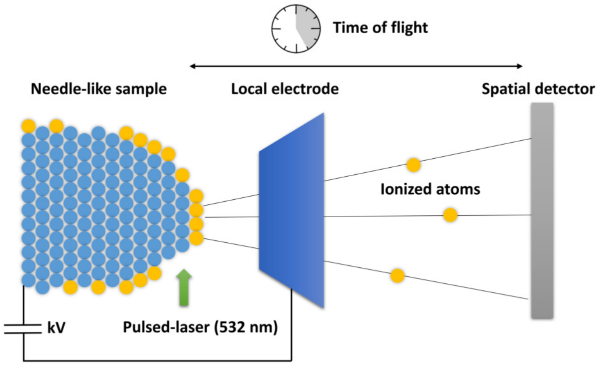

Figure 1.24: Scheme of the APT working principle.

### 1.3.3 Cathodo and photoluminescence spectroscopy

Collecting the luminescence of single NWs is an efficient way to probe the NWs fundamental properties. It also permits to correlate the NWs structural properties to their luminescence. For these reasons, different setups are used in this work to excite and collect the NWs luminescence. We first present a cathodoluminescence (CL) setup, followed by different photoluminescence (PL) setups. The main optical setup used in this work is a standard microphotoluminescence (µPL) setup and to access the dynamic of the excitons recombinations as a function of time, we could also use a time-resolved photoluminescence (TRPL) setup.

#### Cathodoluminescence setup

As illustrated in Figure 1.25, the CL setup is composed of an electron beam sent onto a sample. This sample gets excited by the electron beam and emits light which is collected by a parabolic mirror. This light goes through a collective lens, is focused on a Jobin Yvon HR460 spectrometer and is detected by an APD. Thanks to this electron beam, the sample can also be visualized as in a SEM with a high spatial resolution of 10 nm. We used a FEI Quanta 200 SEM (30 kV; 5mA) and a Gatan stage cooled down to 5 K by liquid helium [69].

Moreover, this setup can be used to probe the dynamics of our samples as a function of time, using time-resolved CL (see Part 4.1.3). In this case, the electron beam is periodically deflected by a beam deflector (10 MHz). This fantastic technique permits to clearly visualize single NWs, collect their luminescence and measure their decay-time.

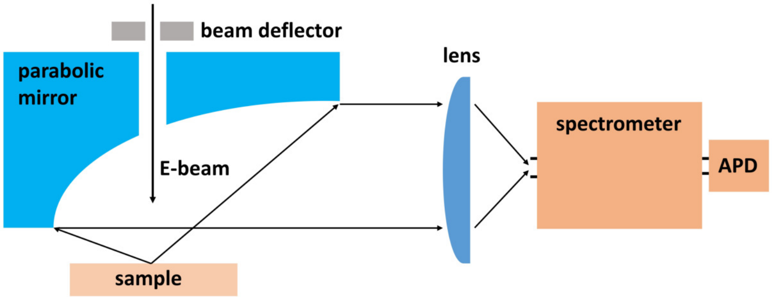

Figure 1.25: Scheme of the TRCL setup. A sample is excited with an electron beam periodically deflected at a 10 MHz rate. The sample luminescence is collected with a parabolic mirror, focused at the entrance slit of a spectrometer and recorded by an APD.

#### Standard microphotoluminescence setup

To the contrary of CL experiments which use electrons, PL measurements use light to excite the studied sample. The main PL setup used in this work is illustrated in Figure 1.26.

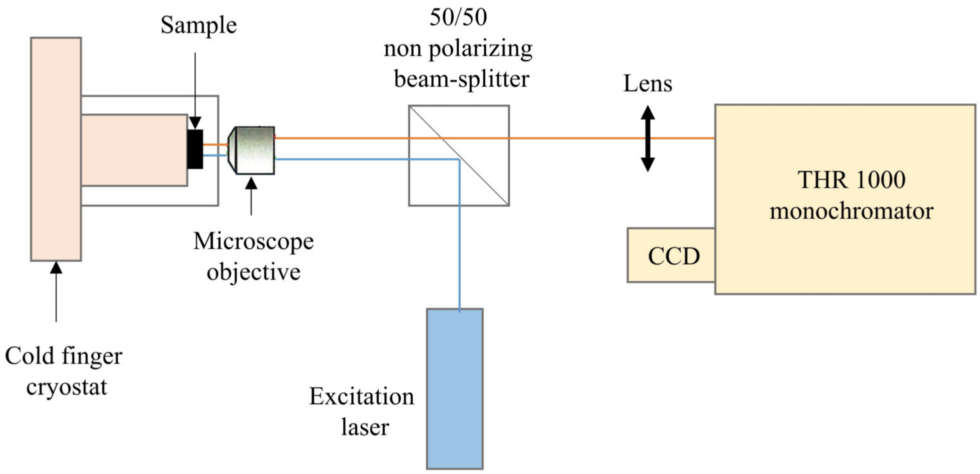

Figure 1.26: Scheme of the µPL setup used in this study.

The main structure of the setup can be decomposed in three parts. The first part is destined to the sample optical excitation. Three lasers are available:

- a CW 405 nm (3.06 eV) Thorlabs laser diode,
- a CW high performance 488 nm (2.54 eV) Oxxius laser diode,
- a pulsed Fianium WhiteLase Supercontinuum fiber laser [8] tunable from 450 to 800 nm (2.76 to 1.55 eV).

The bulk ZnSe and CdSe QD emit respectively at 440 nm (2.82 eV, bandgap) and 500-600 nm (2.48 to 2.07 eV). Consequently, the CdSe QD can be excited (for the CW lasers):

- with the 405 nm (3.06 eV) laser. In this case, carriers are created in the ZnSe NW, relax into the CdSe QD and recombine.
- with the 488 nm (2.54 eV) laser. In this case, a 0D-1D transition is induced: it excites carriers from the QD (0D) into the ZnSe NW (1D) or vice-versa (see Figure 1.27). For this reason, the 488 nm CW laser is well adapted since it only excites the CdSe QDs.

These laser beams are focused down to a 1 µm-diameter spot onto the sample with a microscope objective of Numerical Aperture (NA) 0.6. This microscope objective is mounted on a piezoelectric stage for nanometric adjustements of the laser spot at the sample's surface.

The second part of the setup deals with the studied sample. This sample is placed inside a helium-cooled cold finger cryostat which permits to reach cryogenic (helium) temperature down to 4 K. The helium flow is provided by a 100 l helium bottle connected to the cryostat through a transfer tube. Besides, the cryostat is mounted on an aluminum block which can be moved in three dimensions with micrometric screws.

---

[8] repetition rate 76 MHz - bandwidth 10 nm - tunable from 400 to 800 nm with a SuperChrome filter

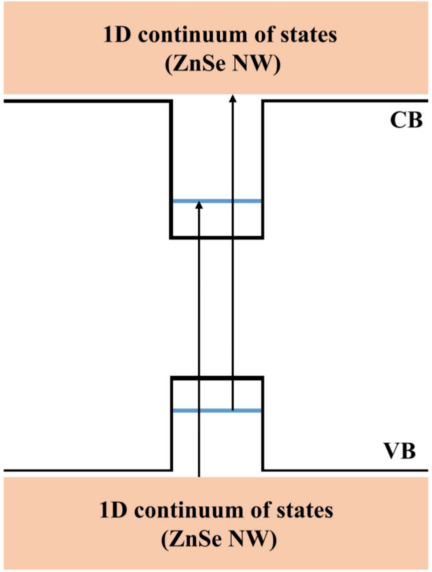

Figure 1.27: Scheme of possible 0D-1D transitions in a CdSe QD inserted in a ZnSe NW. An electron can jump from the ZnSe NW 1D Density Of States (DOS) to the CdSe QD conduction band (the remaining hole will diffuse toward the QD valence band), or an electron from the QD valence band can jump in the ZnSe NW 1D DOS (relaxing afterwards toward the QD conduction band). CB and VB respectively stand for conduction band and valence band.

Finally, the last part of the setup is dedicated to the collection and analysis of the photons emitted by the NWs. These photons are collected by a THR 1000 Jobin Yvon spectrometer and sent on a CCD cooled down with liquid nitrogen.

A half-wave plate ($\lambda/2$) and a fixed linear polarizer can be added to the setup for polarization measurements (see Figure 1.14). Notice in Figure 1.26 that a 50/50 beam-splitter is used to both reflect the laser beam onto the sample and collect its PL. Since this setup only allows us to carry out µPL measurements, we also used another type of setup to carry out TRPL measurements and more precisely decay-time measurements.

### Decay-time measurement setup

A decay-time measurement consists in measuring the PL of a sample as function of time and to fill an histogram. An example of the resulting spectrum can be seen in Figure 3.41.

To perform these measurements, we used the previously mentioned tunable pulsed Supercontinuum laser and a tunable Ti:Sapphire laser (76 MHz repetition rate) for the excitation. The detection part was composed of an Avalanche PhotoDiode (APD) or a streak camera. The streak camera working principle, displayed in Figure 1.28, is the following: the light emitted by the sample enters the adjustable streak camera entrance slit before being focused by two lenses on a photocathode. This photocathode emits electrons (proportionally to the incident PL intensity) which are accelerated in the direction of a microchannel plate. They are therefore multiplied (up to $10^4$) to be detected on a fluorescent screen. Finally, the time-resolved detection is formed by applying a vertical voltage ramp which deflects the electrons differently according to their arrival time. The result consists in a bidimensional intensity distribution. The horizontal (x-axis in Figure 1.28) and vertical (y-axis in Figure 1.28) axis correspond respectively to spectral and temporal distributions. Notice that the voltage ramp needs to be synchronized with the laser pulses: this is done by sending a part of the laser beam on a triggered diode.

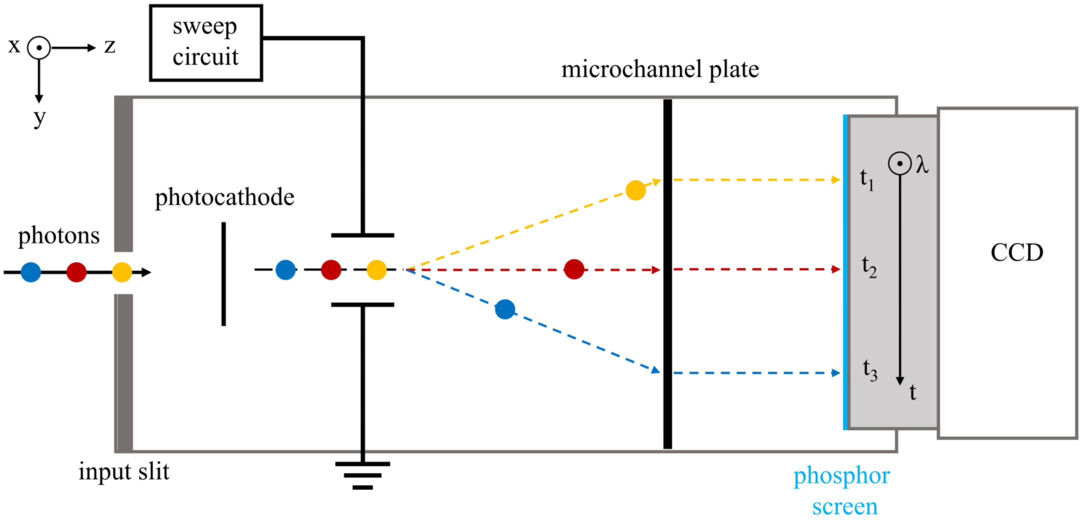

Figure 1.28: Side-view model of a streak-camera. On the final 2D intensity distribution, the horizontal (x-axis) and vertical (y-axis) axis correspond respectively to spectral and temporal distributions.

### 1.3.4 Patterned substrates

For PL investigations, NWs could have been directly deposited on a Si wafer but due to its higher refractive index in comparison to air, the NW emission will preferentially be directed toward the Si substrate. The NWs could also have been deposited on an Al mirror but the $\pi$-phase-shift induced by the Al metallic reflection would create *destructive interferences.*

A way to enhance the collected luminescence from the NWs is to deposit them on specially prepared patterned substrate. These substrates are composed of a silicon wafer on which a 100 nm-thick Al layer is deposited by Joule evaporation, followed by a 200 nm-thick $Al_2O_3$ atomic layer deposition (see Figure 1.29a). The goal of the $Al_2O_3$ layer is to induce *constructive interferences* to increase the photon collection. The calculation of the optimal $Al_2O_3$ thickness to maximize the constructive interferences has been carried out using the *theory of the radiation of dipoles placed within a multilayer system* (Ref.[70]) and is visible in Figure 1.29b. According to this calculation carried out for a 550 nm-wavelength emitter, the first two optimal thicknesses are 50 and 200 nm. To avoid any plasmonic contribution from the Al mirror at the 50 nm-thickness (which would reduce the number of reflected photons), the 200 nm-thickness was preferred.

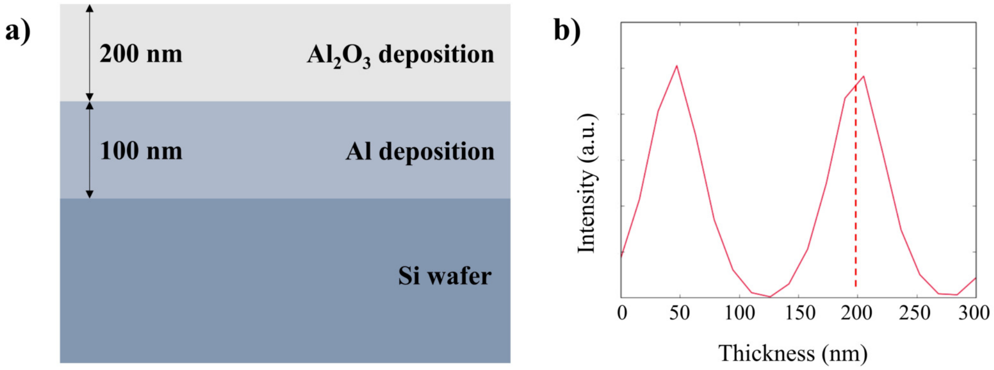

Figure 1.29: a) Side-view scheme of a patterned substrate with its $Al_2O_3$/Al mirror. b) Corresponding $Al_2O_3$/Al mirror efficiency as a function of the $Al_2O_3$ deposited thickness.

In addition to this intensity increase, the aim of the patterned substrates is to study single well-isolated NWs. For this reason, the substrates are patterned using photolithography by etching the Si. These marks are still visible after the $Al_2O_3$ deposition and allow us to map the surface of the sample, as displayed in Figure 1.30. After a careful mechanical deposition of the NWs at the surface of a patterned substrate, this sample is observed by SEM until single well-isolated NWs are found. These NWs can then be studied by µPL, by precisely focusing the laser spot (∼ 1 µm in diameter) onto the corresponding substrate surface.

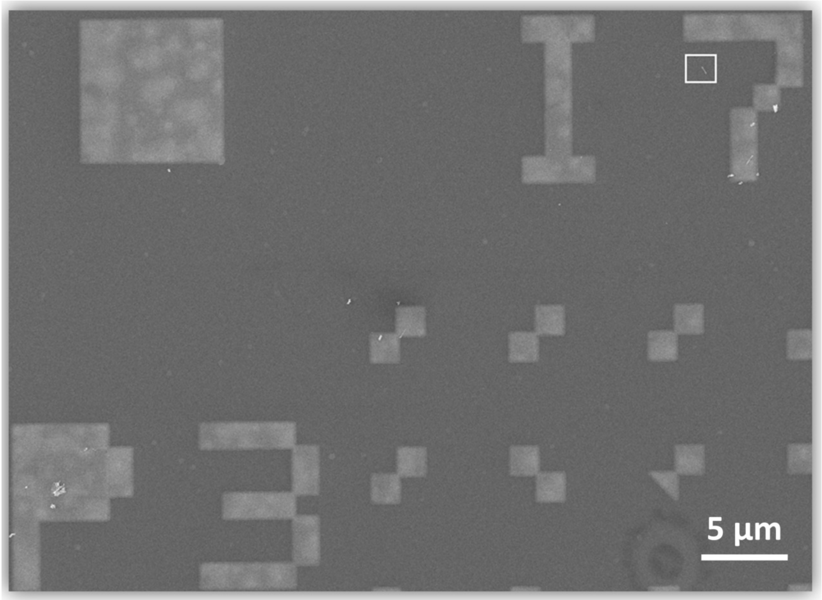

Figure 1.30: SEM image of a patterned substrate after the mechanical deposition of NWs. A single NW is visible in the white framed rectangle on the top right corner of the image.

**In the rest of the manuscript, all the samples defined as patterned substrates will correspond to the type of substrate described in this Part.**

# Chapter 2

# Growth and characterization of ZnSe nanowires

## Contents

Semiconductor NWs have been increasingly studied in the past few years, both for fundamental research and applications in optoelectronics [71]. Among the many attractive properties they offer, they present a high surface/volume ratio which has a profound effect on the crystal growth and can result in crystal structures not observed in the bulk. This effect has been observed for group IV [72], III-V [73] and II-VI [74] semiconductor NWs.

One dimensional structures of ZnSe, such as NWs, nanorods and nanoribbons, have been fabricated using a wide variety of growth techniques such as MOCVD [75–80], thermal evaporation [81, 82], vapor-phase [83, 84], solution-based growth [85] and pulsed-laser deposition [86]. For Au-assisted MBE, studies have been carried out on several substrates like Si [87–91], GaAs [92–98], GaP [99, 100] and even molybdene TEM grids [101]. Among these different materials, several surface orientations have been investigated such as [001], [110] and [111] in order to control the NW growth orientation. In addition, their potential applications in photodetectors [102], sensors [103] and lasers [104] have already been demonstrated.

The stable crystal structure of ZnSe is ZB, but it also occurs in the WZ structure, metastable at room temperature and which is difficult to obtain. Unlike the bulk case, ZnSe NWs show sometimes the WZ crystal structure, although the number of reports on ZB ZnSe NWs [93, 100, 105, 106] exceeds those of WZ ones [78, 106]. Periodically twinned ZnSe NWs with enhanced conductance have also been reported [107]. However, the PL of such twinned NWs was dominated by a broad deep-level emission between 500 and 650 nm, with a very weak (if not absent) Near-Band-Edge (NBE) emission [107, 108], suggesting that twins and stacking faults have detrimental effects on the optical properties of ZnSe NWs. Thus, defect-free NWs are desirable to achieve good optical responses [40, 109].

To obtain good quality (single crystal) ZnSe NWs, the VLS mechanism has usually been exploited [110]. Indeed, it is well known that the VLS mechanism offers a good control over the NW morphology, orientation and crystal quality. Uniform arrays of long, straight and well-oriented ZnSe NWs have been obtained using liquid catalyst particles to assist the growth [75, 111]. However, it has been reported that some atoms of the liquid catalyst droplet can be incorporated as impurities along the wire's body, creating point defects that strongly affect their optical quality [75, 112]. If solid particles are used instead of liquid droplets in the so-called VSS mechanism (see Part 1.3.1), the probability of impurity atoms incorporation may be reduced and the optical properties of the NWs should be improved [10, 95, 113].

This chapter deals with the growth and luminescence properties of ZnSe NWs; the control of their growth is a mandatory step prior to insert CdSe QDs. In a first part, we fully characterize **ZnSe NWs grown on a GaAs(111)B substrate** (section §2.1) *by the group of Silvia Rubini from the IOM-CNR Laboratory* (Trieste in Italy) and especially developed by the PhD student Valentina Zannier. In spite of their bright NBE luminescence, we will show that these NWs are not adapted for single CdSe insertions. For this reason, we developed **ZnSe NWs grown on ZnSe(111)B buffer layers** to later insert single CdSe QDs. These efficient QDs insertions and emissions will be detailed in Chapter 3.

## 2.1 ZnSe NWs grown on a GaAs substrate: heteroepitaxy

In recent papers [95, 111, 114], the group of Rubini et *al.* reported the growth of vertically oriented ZnSe NWs by Au-assisted VSS growth on GaAs(111)B using MBE. This study evidenced that NWs exhibit an enhanced NBE luminescence when they are grown directly onto a *GaAs(111)B surface (heteroepitaxy)* at 300°C. This temperature is below the AuGa eutectic (339.4°C, see Part 1.3.1) to avoid the incorporation of Ga atoms in the ZnSe NWs.

The group of Rubini grew these NWs and could characterize ensembles of NWs by macroPL. However, this technique also probes the 2D layer underneath the NWs. The optical characterization of single NWs is a powerful tool to access the NWs fundamental and structural properties, but Rubini et *al.* did not have access to such characterization tools. Since a detailed optical characterization of those NWs is needed to relate their luminescence properties to their crystal structure, **we characterized these NWs provided by Professor Silvia Rubini.** In this part, we present a low-temperature µPL and CL study of individual ZnSe NWs epitaxially grown on GaAs(111)B at 300°C by MBE assisted by solid Au nanoparticles and we correlate the optical response of the NWs with their crystal structure. This study resulted in a publication in the Journal of Applied Physics (JAP Ref.[48]).

### 2.1.1 Experimental details

The ZnSe NWs were grown by MBE: the GaAs(111)B substrates were first deoxidized at 600°C in the III-V chamber and then a 0.2 nm-thick Au layer was deposited at room temperature in the metallization chamber. The substrates were finally transferred into the II-VI chamber where a 10 minutes annealing at 300°C was followed by ZnSe deposition at the same temperature for 1 hour. The Zn and Se fluxes were calibrated on a reference sample, with a corresponding 2D ZnSe growth rate of 0.6 µm/h at 280°C (calibrated on GaAs(100)) and a Zn/Se Beam Equivalent Pressure (BEP) ratio of 0.4 [95]. TEM was performed using a JEOL 2200 microscope operated at 200 keV with a Scherzer resolution of 0.19 nm and 0.14 nm respectively for TEM and scanning TEM. The NWs were excited with a 405 nm laser and CL images of the same NWs deposited on a patterned substrate were recorded at 5 keV. The TRPL was performed on the as-grown sample using a Ti:sapphire laser exciting at 390 nm and a Hamamatsu C10910 streak camera. The laser-pulse width and the repetition rate were 200 fs and 76 MHz respectively.

### 2.1.2 Structural characterization

In Figure 2.1a, we show a representative SEM image of the as-grown GaAs(111)B substrate with ZnSe NWs obtained after 60 minutes of deposition at 300°C. Straight and vertically oriented NWs (with the growth axis along the (111)B substrate direction) grew together with 3D non-catalyzed islands. The NWs have an average length of 1.8 µm and are strongly tapered, with a thick base (140 – 160 nm) and a thin tip (10 – 15 nm), roughly of the same size of the gold particle. Their pyramidal shape is a consequence of the low growth temperature which results in a low adatoms mobility, i.e. in a substantial lateral growth, at the same time that the axial growth occurs.

Even though the NWs have a quite homogeneous shape and morphology, TEM analyses (Figure 2.1b) reveal the presence of different types of NWs: some of them have an almost defect-free WZ structure with the c-axis parallel to the growth direction (Figure 2.1c) while others exhibit an alternation of WZ and ZB segments all along their body (Figure 2.1d), with a variable thickness and periodicity.

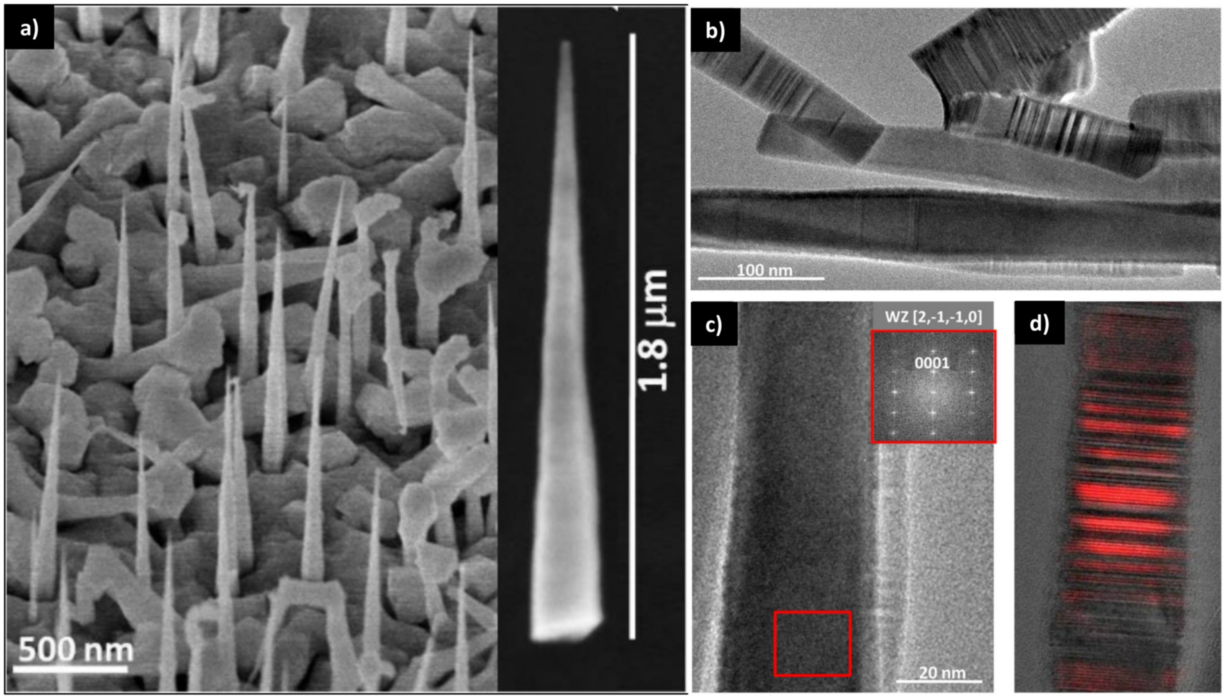

Figure 2.1: a) Tilted-view SEM image (45°) of ZnSe NWs grown at 300°C on GaAs(111)B. The inset on the right is a magnified image of a representative NW, mechanically transferred onto a patterned substrate. b), c) and d): TEM images of ZnSe NWs transferred on a TEM grid from the same as-grown sample as displayed on the left. b) Ensemble of NWs. c) Representative image of a defect-free WZ NW. Inset: Fourier transform of the red rectangle on c) highlighting the WZ structure of the NW (zone axis WZ [2,-1,-1,0]). d) False-color high resolution TEM image of a NW with alternating WZ (red) and ZB crystal phases of various thickness.

### 2.1.3 Catho and microphotoluminescence on single NWs

Low temperature polychromatic CL images of the transferred NWs were recorded to assess the homogeneity of their optical properties. A CL emission was systematically detected from all the analyzed NWs, as shown in Figure 2.2.

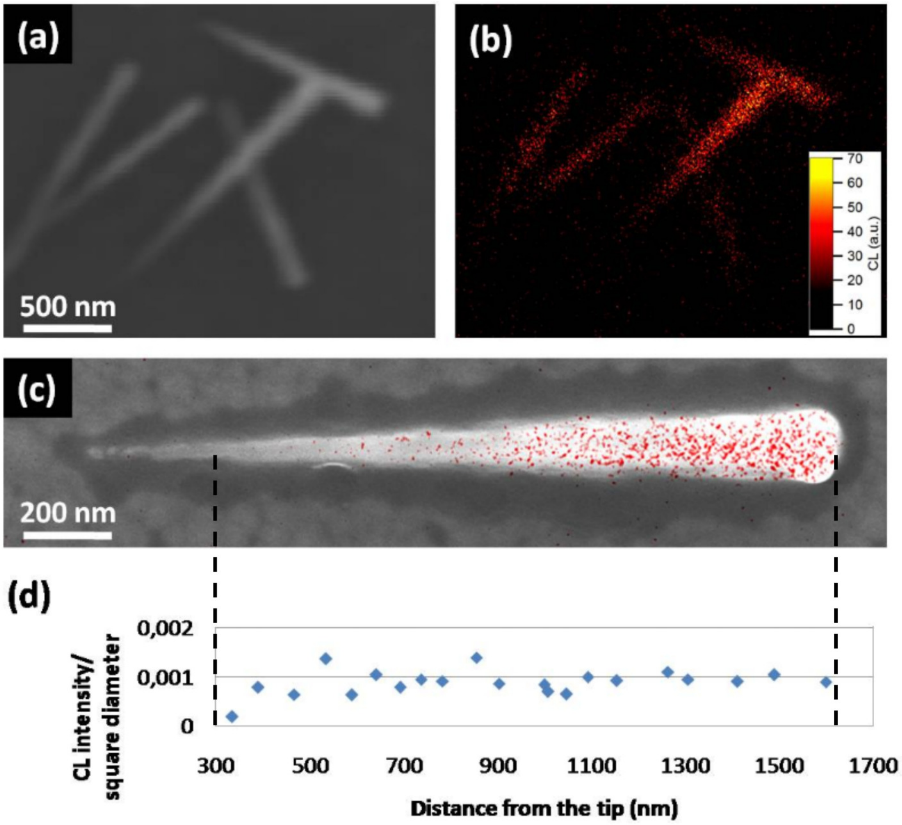

Figure 2.2: a) Top-view SEM image of a bundle of ZnSe NWs mechanically transferred from the as-grown sample onto a patterned substrate. b) CL image of the NWs shown in a) recorded at 5 K. c) Superimposition of the SEM image and the CL map (red pixels) of a ZnSe NW (NW1). d) Plot of the CL intensity integrated across the NW diameter and divided by the NW square diameter, as a function of the position along the growth axis (distance from the tip) of NW1 depicted in panel c).

When an ensemble of NWs was imaged, the polychromatic map depicted the SEM image (Figure 2.2a and b), indicating that all the NWs are emitting light. Moreover, light is emitted all along the NW body and the CL intensity increases from the tip to the base, as highlighted in Figure 2.2c which is a superimposition of the SEM image and the CL map of a single NW, called NW1. In Figure 2.2d we report the plot of the CL intensity integrated across the NW diameter at different positions along its axis, divided by the square of the diameter, as a function of the distance from the tip. This ratio is a constant, as already observed in similarly tapered ZnTe NWs [115]. This indicates that the radiative efficiency remains constant along the NW body and the CL intensity is determined by the excitation density, proportional to the square diameter.

For small objects such as these NWs, the CL excitation efficiency is much lower than the PL one [115]. Indeed an incident electron has a very small probability to be scattered inelastically and create an electron-hole pair in the NW. As a result, this low excitation density prevents any spectral analysis of the CL signal of the NWs studied in this work. For this reason, we carried out low temperature PL measurements to analyze the NWs spectral response. Figure 2.3a shows that the NWs PL spectrum of the as-grown sample is dominated by a very intense NBE emission, within a range between 2.70 and 2.85 eV. No emission is found below 2.70 eV, which indicates the absence of deep levels and donor-acceptor pair (DAP) recombination related to either impurity atoms [116–118] or extended structural defects known to occur in ZnSe crystals of both cubic [119] and hexagonal [120] structures. The presence of such deep level and DAP emission has been found also in the PL of ZnSe NWs grown by MBE at higher temperature [109] and with other deposition techniques [121–124]. Our results indicate that low temperature VSS-grown ZnSe NWs obtained by Au-assisted MBE provide less DAP and more NBE emissions. Indeed, we believe that the low growth temperature together with the solid state of the Au nanoparticle catalyst reduces the incorporation of impurities and the formation of thermally-activated defects along the NWs, improving their NBE emission.

The as-grown sample shows a broad band centered at 2.802 eV - ascribed to the ZB ZnSe free exciton recombination expected at 2.800 eV and labeled $FX_{ZB}$ in Figure 2.3a [125] - with a FWHM of 35 meV (red curve in Figure 2.3a). Single-NW spectra of two distinct ZnSe NWs are also reported in Figure 2.3a. Some differences in peak shapes are found from wire to wire and explain the broadening of the as-grown-sample PL where an array of NWs is measured. Some NWs, such as NW1 in Figure 2.2c, exhibit few narrow lines (see Figure 2.3) above the bandgap of ZB ZnSe (2.820 at 6 K). Saxena et *al.* [125] reported on the PL of pure WZ ZnSe NWs showing a spectrum characterized by the presence of a broad DAP peak at 2.747 eV and two narrow lines at 2.841 and 2.833 eV respectively. Those peaks were attributed to the exciton bound to neutral acceptors involving Zn-vacancies and Zn-vacancies complexes, with a calculated dissociation energy (defined as the energy difference between the free and the bound exciton emission) of 11 and 19 meV respectively. In our case, NW1 shows three well defined peaks above the ZB bandgap: a narrow line at 2.848 eV, a most intense line centered at 2.837 eV and a weak line at 2.829 eV. We speculate that the line at 2.848 eV, which is close to the highest energy peak reported by Liang and Yoffe at 2.851 eV [120], is the free A exciton emission in the WZ phase, thus labeled $FX_{WZ}$ in Figure 2.3a. The other two lines at lower energy can be attributed to recombinations of excitons bound to neutral acceptors of the same nature of what is reported in [125]; the most intense one is labeled $BX_{WZ}$. Even though this interpretation is not straightforward, the presence of Zn-vacancies in the NWs is probable due to the Se-rich growth conditions used during the growth.

Figure 2.3b displays the intensity variation of the NW1 $FX_{WZ}$ line when rotating the linear polarization of the detection with respect to the NW axis. The maximum of the emission intensity is reached when the polarization is perpendicular to the NW axis ($\theta = 90°$). The polarization ratio of the lines $BX_{WZ}$ and $FX_{WZ}$ is 78 ± 3% and this behavior has been observed on other NWs. This uncommon result can be understood taking into account the prevalent WZ crystal structure of these NWs: indeed, as mentioned in the introduction Part 1.2.4, a polarization perpendicular to c-axis (NW growth axis here) is expected from the WZ polarization selection rules.

As also found for WZ NWs of other materials [126–128], the degree of polarization is lower in WZ (polarization perpendicular to the NW axis) compared to ZB NWs (polarization parallel to the NW axis). A quantitative explanation of this polarization reduction in a WZ NW requires a more complicated calculation. Ruda et *al.* [129] calculate that the NW polarization in emission depends on the NW diameter. According to their calculation, an isotropic (unpolarized) internal emission in a NW of diameter 100 nm (diameter of our NW base from which the light is mainly emitted) has an external polarization ratio of 23% along its axis. This could explain why we did not observe a fully polarized emission but a 78% polarization perpendicular to the NW axis.

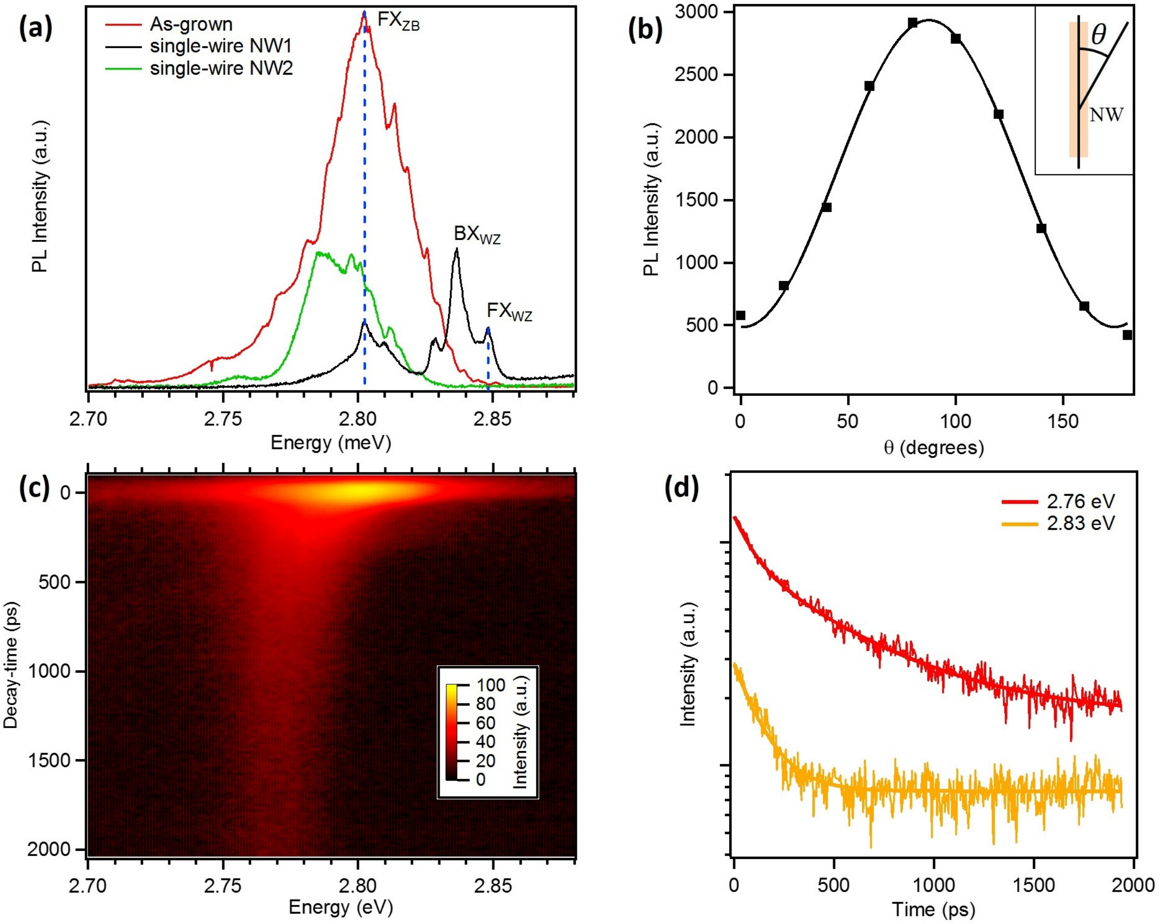

Figure 2.3: a) PL spectra of the as-grown sample and single NWs labeled NW1 and NW2 acquired at 5 K with a 405 nm laser excitation of 30, 300 and 300 µW respectively. b) Dependence of the intensity of the PL line $FX_{WZ}$ on the angle $\theta$, between the NW1 axis and the direction of the linear polarization of the emitted light (sketched in the top-right inset). Continuous line: Malus law fitting of the NW polarization and squares: experimental data. c) As-grown sample decay-time map recorded with the streak camera. d) Decay-time spectra of the PL lines at 2.76 (red) and 2.83 eV (black) measured on the as-grown sample.

### 2.1.4 WZ and ZB ZnSe type II heterostructure

NW1 and NW2 also show a peak at the $FX_{ZB}$ energy of 2.800 eV and most of the analyzed NWs show only a rather broad emission between 2.788 and 2.816 eV (see NW2 in Figure 2.3a). This band includes the excitonic lines of ZB ZnSe known to appear between 2.780 and 2.800 eV [106], but also interband transitions occurring at the WZ/ZB interfaces. Indeed it has been shown by TEM (Figure 2.1) that many of these NWs present an alternation of WZ and ZB portions all along their body. ZB ZnSe has a smaller bandgap and large negative band offset respect to WZ ZnSe [130]. Hence, the WZ/ZB interface gives a type II alignment, with the conduction and the valence bands of the ZB segments lower than those of the WZ portion. At the interface, electrons are confined in the ZB region and holes in the WZ region of the NW; their recombination will result in emission lines at a lower energy than the ZB bandgap (see the schematic diagram in Figure 2.5). Moreover, a short ZB section into a WZ crystal defines a quantum well. In a NW, such a structure forms a crystal phase QD [47, 131]. The ZB segment length sets the confined electron energy levels; therefore when ZB insertions of different thickness are present in the same WZ matrix, as for these NWs, the PL spectrum will be composed of a broad band instead of a few narrow lines. If WZ sections are also short, confined energy levels will be found also for holes in the WZ phase increasing the range of the spectral emission.

Spatially-indirect e-h recombinations are expected to be characterized by longer lifetimes, due to the reduced overlap of the electron and hole wave functions [47]. Figure 2.3c is a decay-time map of ZnSe NWs (the as-grown sample) recorded with the streak camera, which shows the time evolution of the PL after excitation by the Ti:Sapphire pulsed laser. The low-energy peaks (from 2.75 ± 0.01 eV to 2.79 ± 0.01 eV) present a longer tail signal than the high-energy peaks (from 2.80 to 2.86 eV). Indeed, as shown in Figure 2.3d, the lifetime of the high energy PL line at 2.83 eV is 140 ± 10 ps (fitted with a monoexponential plus a constant for the background). Besides, the low energy peak at 2.76 eV has a non-monoexponential behavior with a lifetime longer than 1.7 ± 0.2 ns (fitted with a biexponential) presented in Figure 2.3d. For this low energy peak, the detection of photons after 2000 ps highlights a slow electron-hole pairs recombinations dynamic. This measurement reinforces our hypothesis that the lower energy peaks are due to spatially indirect recombinations in type II heterostructures.

Moreover, we can notice in Figure 2.3c that at time t=0, the type-II emission lines are blue-shifted. This blue-shift is explained as follows: during the NW excitation, electrons and holes are spatially separated across the type-II heterojunctions. Such space charges induce an electric field and a band bending, modifying the electron and hole energy levels via the Stark effect, leading to the PL blue-shift [132]. Then a PL red-shift as a function of time is observed due to the reduction of the Stark effect while the electron-hole pairs progressively recombine. This is why the type II recombinations in Figure 2.3c have the shape of an inverted comma.

While the TEM analysis has shown that the prevalent NWs structure is WZ, the PL spectrum of the as-grown sample shows only a slight emission at the energy of WZ ZnSe free exciton (2.848 eV). This result can be explained by the low excitation power of 30 µW used to excite the as-grown sample. Indeed, when the excitons are created in the mainly but not completely WZ NWs, they diffuse within the NW and encounter a ZB NW segment.

According to Figure 2.5, the electrons will be trapped within the ZB segment while the holes will remain in the WZ part and a type II recombination will occur. In order to observe the luminescence from the WZ part - as for NW1 excited with a laser power of 300 µW - we first need to saturate the ZB segments. This phenomenon is shown in Figure 2.4. Indeed, at a high enough laser power, the WZ ZnSe free exciton is visible.

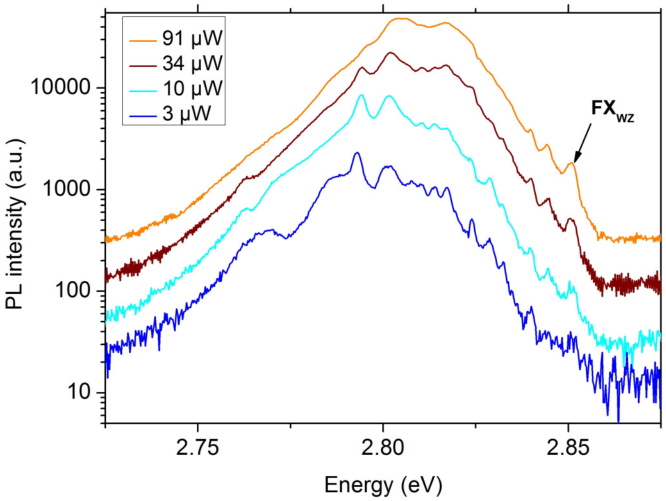

Figure 2.4: Log-scale PL spectra of the as-grown sample as a function of the laser (CW 405 nm) power recorded at 5 K (acquisition time 0.75 s).

To conclude this part, we observe a long decay-time within the energy range from 2.75 ± 0.01 eV to 2.79 ± 0.01 eV and we assume that these transitions correspond to type II recombinations.

### 2.1.5 Estimation of the conduction and valence band-offsets

To go further with the analysis of the ZnSe WZ/ZB alternations, we can estimate values for their conduction and valence band offsets. We expect the recombination energy for the type II transition (see orange arrow in Figure 2.5) to be given by:

$$E_{type\,II} = E_{FX_{ZB}} + (E_{b_{ZB}} - E_{b_{ind}}) + e_1 + h_1 - \Delta E_V \tag{2.1.1}$$

with $E_{FX_{ZB}}$the ZB ZnSe free exciton energy of 2.800 eV, $E_{b_{ZB}}$ and $E_{b_{ind}}$ are the exciton binding energy for ZB (21 meV [124]) and the type II indirect recombination respectively, $e_1$ and $h_1$ are the electron and hole confinement energy and $\Delta E_V$ is the valence band offset. We neglect the binding energy difference $(E_{b_{ZB}} - E_{b_{ind}})$ due to their small and expected similar values, as well as piezoelectric effects induced by the ZB/WZ lattice mismatch, since this mismatch is negligible.

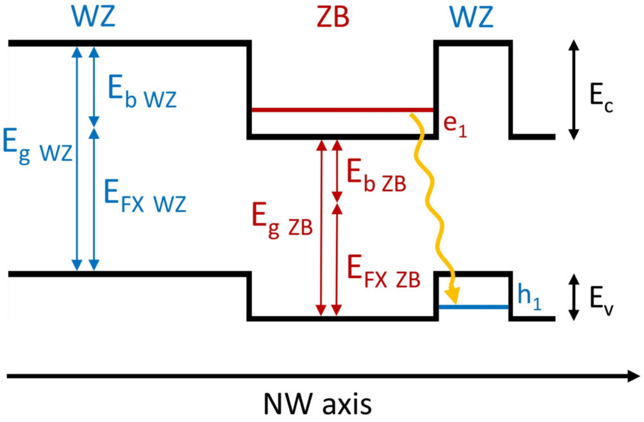

Figure 2.5: Illustration of the band profile and transitions in the ZnSe WZ and ZB heterostructure.

If the experimentally observed transitions are due to type II recombinations in ZB/WZ crystal phase heterostructures, the lowest emission energy should correspond to interface recombinations without confinement effects. The conduction and valence band-offsets at the interface are $\Delta E_C = E_{FX_{WZ}} - E_{type\,II}$ and $\Delta E_V = E_{FX_{ZB}} - E_{type\,II}$ respectively ($E_{FX_{WZ}}$= 2.848 eV). According to the decay-time measurements and as discussed above, the lowest type II recombination energy is at 2.75 ± 0.01 eV. Therefore we estimate an upper limit for the conduction and the valence band-offsets to be 98 ± 10 meV and 50 ± 10 meV respectively.

On the other extreme, the shortest period of a ZB/WZ alternation should give the highest recombination energy, due to the presence of confined states for holes in ZB and for electrons in WZ. According to Caroff and *al.* [133], the smallest possible ZB and WZ portions within a NW are composed of three and four bilayers along the ZB (111) or WZ c-axis. Therefore along this growth direction, the smallest ZB and WZ portions have a length of 1.96 and 2.62 nm respectively. Assuming the ZB ZnSe electron and hole masses along (111) to be 0.16 and 1.09 $m_0$ [49] we calculate the confined states and determine the higher energy limit of the type II recombinations to be 2.84 ± 0.01 eV, quite close to the highest energy transition (2.80 eV) attributed to type II recombinations in Figure 2.3c. The calculated energy overestimation is probably due to the use of the ZB (111) hole mass for the calculation because the WZ structure value is unknown. Another possible reason is the formation of minibands caused by the electron and hole wave functions overlap that reduce the confinement energy when there is a high density of short ZB and WZ portions [131].

To summarize this part, we experimentally estimate for the first time the conduction and valence band-offsets between ZB and WZ ZnSe to be 98 ± 10 meV and 50 ± 10 meV respectively.

## 2.1.6 CdSe QD insertions in tapered ZnSe NWs

The growth of high quality ZnSe NWs described in the previous section is a necessary step prior to inserting a CdSe QD. Such a QD should be very bright with a clear excitonic signature (exciton and biexciton) for single-photon applications. In this section, we will briefly review our first trials at inserting CdSe QDs within tapered ZnSe NWs. We will see with µPL that these tapered NWs are inconvenient at reaching this aim and our effort at growing efficient and bright QD insertions will then be described in details in Chapter 3.

### CdSe insertion of 30 s

In order to insert a CdSe QD within the tapered ZnSe NWs, the same method described in section 2.1.1 (Zn:Se BEP of 0.4) has been followed. The difference resides in the NW growth which consisted of 30 min of ZnSe followed by a 30 s insertion of CdSe and 5 minutes of ZnSe afterwards. The growth temperature was kept at 300°C directly on a GaAs(111)B substrate.

Figure 2.6a shows a SEM image of the as-grown GaAs(111)B substrate with the NW-QDs. They are mainly vertically oriented and their density is similar to the ZnSe NWs displayed in Figure 2.1. Figure 2.6b displays a macroPL spectrum of these NW-QDs recorded at 5 K with a laser excitation of 2 mW (emission too small at a lower power excitation). The laser beam was defocused via a beam-expander prior to the microscope objective (NA = 0.6) to an approximately 3 µm spot in diameter. Thanks to this 488 nm laser (2.54 with a 2.52 eV filter) we could obtain the Gaussian distribution of the QDs energies ranging from 2.10 to 2.52 eV approximately.

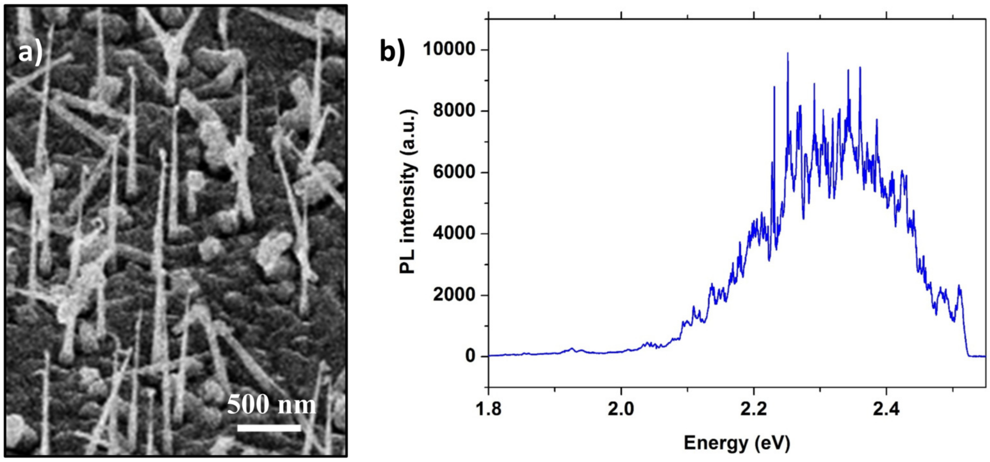

Figure 2.6: a) Tilted view SEM image (45°) of ZnSe NWs grown at 300°C (Zn:Se BEP of 0.4) directly on a (111)B GaAs substrate with a 30 s CdSe insertion. b) PL spectrum of this as-grown sample recorded at 5 K with a 488 nm laser excitation of 2 mW.

The NW-QDs were then softly dispersed on a patterned substrate, localized with a SEM and single NW-QDs were probed by µPL.

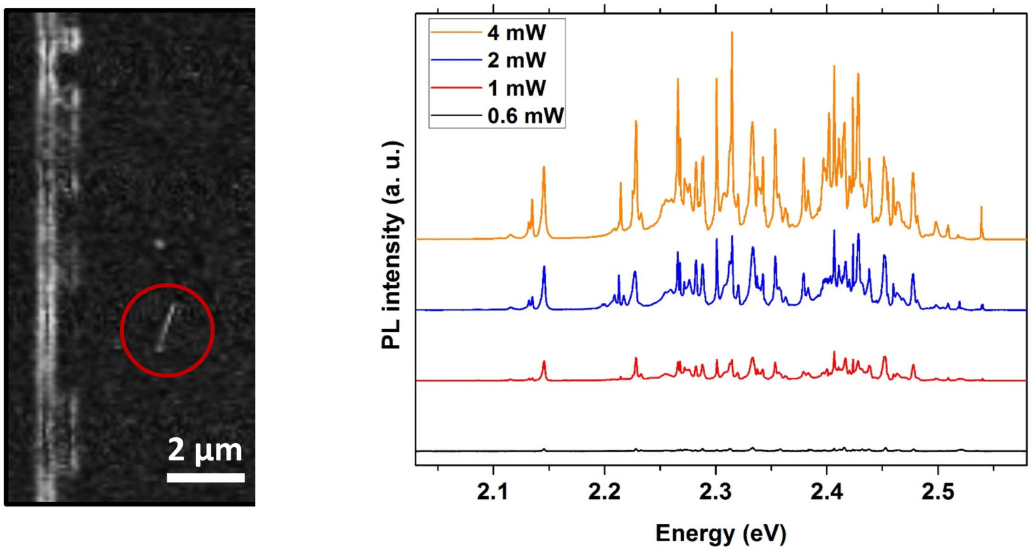

Figure 2.7: Left: Top-view SEM image of a single NW-QD measured by µPL (30 s CdSe insertion) and deposited on a patterned substrate. Right: PL spectra of this single NW-QD recorded at 5 K as a function of the 488 nm laser power.

Figure 2.7 presents a single NW-QD spectrum from this sample. The tremendous amount of sharp lines makes it challenging to isolate an exciton/biexciton couple. For this reason, we lowered the laser excitation power to isolate such an excitonic couple, but even in this condition, the number of lines was too high.

To better understand the origin of these lines, we carried out CL on the as-grown sample, as displayed in Figure 2.8. We first collected light at a low energy of 2.14 eV (left part of the Gaussian distribution in Figure 2.6) and observed a localized emission near the NW tip, where the QD is supposed to be localized. We then collected light at an energy of 2.38 eV (maximum of the Gaussian distribution in Figure 2.6) and observed emissions coming from the main NW body.

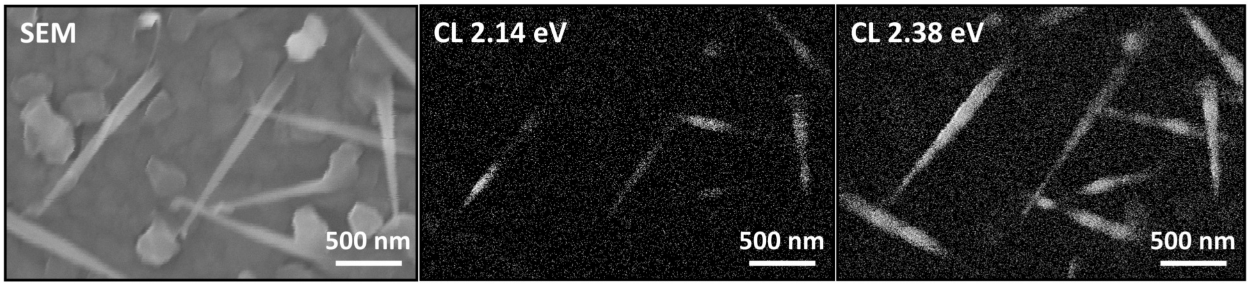

Figure 2.8: Left: Top-view SEM image of a bundle of ZnSe-CdSe NW-QDs on the as-grown sample. Middle: CL image of the NW-QDs recorded at an energy of 2.14 eV and (right) 2.38 eV.

### Hypothesis of CdSe clusters on the NW sidewalls

The high number of lines in the PL spectra and the CL observations can be explained by the adatoms diffusion during the NW-QDs growth. Indeed, tapered NWs are formed at a low growth temperature which reduces the adatom mobility on the NWs sidewalls and explains their conical shape. During the insertion of the CdSe QD, CdSe regrowth also occurs on the NWs sidewalls. We hypothesize that this regrowth is not homogeneous and gives rise to CdSe clusters. In this case, a main QD is created at the NW tip, along with other smaller CdSe clusters forming localization centers on the sidewalls (covered afterward by ZnSe, see Figure 2.9a), emitting at a higher energy due to a higher quantum confinement. These clusters contribute to the µPL spectra and explain the high number of excitonic lines.

This phenomenon has been reported for ZnTe-CdTe NW-QDs [134]. In this case, the presence of a thin layer containing Cd has been observed on the sidewalls of a ZnTe NW as displayed in Figure 2.9b.

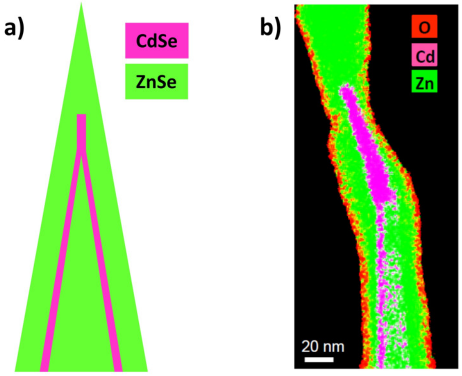

Figure 2.9: a) Illustration of the CdSe distribution on the NW sidewall during its insertion within a ZnSe NW. b) Extracted from Ref.[134]: EDX hypermap of a ZnTe NW with a CdTe QD insertion. The distribution of Zn, Cd and O is presented.

For this reason, we grew another NW-QDs sample by reducing the insertion time of CdSe from 30 s to 10 s. The aim is to reduce the lateral growth and therefore the number of CdSe clusters on the NWs sidewalls to obtain clearer sheared off PL spectra.

### CdSe insertion of 10 s

Figure 2.10 shows SEM images of the NW-QDs with a 10 s CdSe insertion. Figure 2.10a provides an overview of the sample and Figure 2.10b displays a single NW-QD.

A typical macroPL spectrum of the sample is presented in Figure 2.10c. The sample has been probed in the same conditions as in Part 2.1.6. The spectral filter we have used to cut the laser emission above 2.52 eV allows us to estimate the distribution of the QDs energies ranging from 2.3 to slightly above 2.52 eV. This energy distribution is blue-shifted compared to the 30 s CdSe insertions distribution, which is consistent with smaller QDs and a higher quantum confinement.

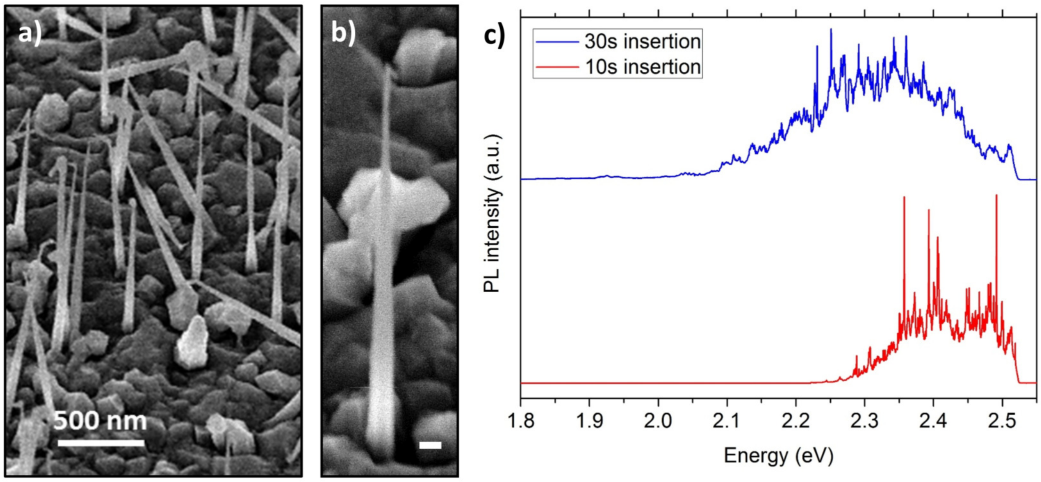

Figure 2.10: Tilted view SEM images (45°) of ZnSe NWs grown at 300°C directly on a (111)B GaAs substrate with a 10 s CdSe insertion: a) as-grown sample and b) single NW (scale bar: 100 nm). c) PL spectra of the as-grown sample with CdSe insertions of 10 and 30 s recorded at 5 K with a 488 nm laser excitation of 2 mW.

The µPL spectrum of a single NW-QD of this sample is shown in Figure 2.11 as a function of the laser power. The peaks distribution between 2.45 and 2.55 eV seems to correspond to three QDs emissions. However, the NW-QDs still show a high number of lines and a low luminescence of the QDs; below 1000 counts/s with a laser excitation of 2 mW. The high number of lines is not well suited for room temperature single-photon emission since when the temperature is increased, the lines broaden and can overlap. With the overlap of the QDs emission lines, it is then impossible to filter a single-photon emission. Besides, a QD emission below 1000 counts/s at 5 K is not viable for room temperature SPS applications. Several NW-QDs have been observed on this sample and present similar emissions.

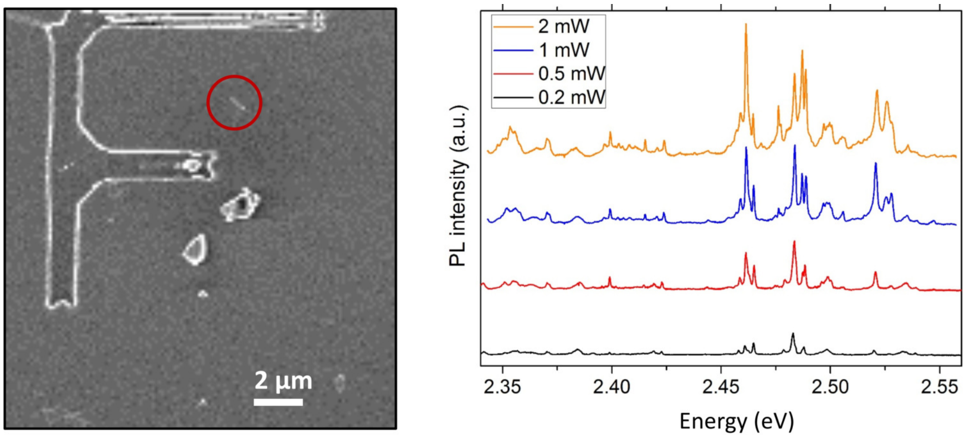

Figure 2.11: Left: Top-view SEM image of the single NW-QD measured by µPL and deposited on a patterned substrate. Right: PL spectra of this single NW-QD recorded at 5 K with the 488 nm laser.

### 2.1.7 Summary of ZnSe NWs grown on GaAs(111) substrates

To summarize, we presented a combined structural and optical characterization of ZnSe NWs grown at 300°C by MBE *on GaAs(111)B substrates*. TEM analysis reveal the presence of NWs with pure WZ structure together with NWs with alternations of WZ and ZB phase. The NWs show an excellent optical quality, with a dominant NBE emission where the ZnSe WZ free exciton line can be identified. The polarization of the emitted light is found perpendicular to the NW axis, in agreement with what is expected considering the dominant WZ structure. Moreover, single-NW CL images show a homogeneous radiative efficiency along the NW body despite the presence of mixed phase regions. Using TRPL, we revealed a type II band alignment between ZB and WZ ZnSe (electrons and holes in the ZB and WZ phases) and deduced the conduction and valence band offsets to be respectively 98 ± 10 meV and 50 ± 10 meV.

These NWs are grown at 300°C (below the AuGa eutectic temperature of 339°C to avoid a Ga incorporation in the Au droplet). This low growth temperature reduces the adatoms mobility on the NWs sidewalls and explains their tapered shape. Indeed, during the insertion of the CdSe QD, CdSe regrowth also occurs on the NWs sidewalls and gives rise to small CdSe clusters emitting at a higher energy due to a higher quantum confinement. These QDs contribute to the µPL spectra and induce a high number of excitonic lines which are not beneficial for single-photon emission up to room temperature.

A way to go from a tapered to a cylindrical NW shape is to increase the adatoms mobility on the NWs sidewalls by increasing the growth temperature. However, on a GaAs substrate, increasing the ZnSe NW growth temperature modifies the Au catalyst which becomes liquid: the growth is in the VLS mode. Such a VLS growth will incorporate Ga atoms in the ZnSe NWs and will lead to poor optical properties [75, 112].

For these reasons, we used another approach to increase the growth temperature and induce cylinder shaped NWs while remaining in the VSS growth mode: the growth of *ZnSe NWs on a ZnSe buffer layer*.

## 2.2 ZnSe NWs grown on a ZnSe buffer layer: homoepitaxy

To control the insertion of single CdSe QDs in the ZnSe NWs, we have developed the growth of **ZnSe NWs on a ZnSe buffer layer** (homoepitaxy) deposited on top of a GaAs substrate. The main advantages of this growth method is that we can avoid the incorporation of Ga or As in the NWs, improve the surface quality and the epitaxial relation between the NWs and the substrate, and increase the NW growth temperature while remaining in the VSS growth mode. This later advantage will be used to increase the growth temperature from 300°C (previously used to grow the NWs on GaAs(111)B) to 400°C. This temperature increase enhances the adatoms mobility on the NWs sidewalls and permits to grow *cylinder-shaped NWs*, to later insert a single CdSe QD for SPS applications.

Therefore, this section describes the MBE growth and optical properties of homoepitaxial ZnSe NWs developed in our laboratory on the (111) surface orientation. As previously mentioned, the goal of this surface orientation is to provide vertical NWs of high crystallinity. First, we describe the procedure developed to grow ZnSe buffer layers on top of GaAs(111) substrates, followed by the gold deposition and dewetting of gold particles to catalyze the NW growth. We will then show the striking difference between the NW growth on (111)A (Zn-terminated) and (111)B (Se-terminated) and determine the optimal conditions to grow high quality and vertically oriented NWs. Finally, we will study the passivation of these NWs with a higher bandgap material and show a remarkable improvement of the NW luminescence.

### 2.2.1 Deoxidization and growth of a thin GaAs buffer layer

The surface of commercial GaAs substrates is protected by a thin oxide layer which needs to be removed before any growth process. For this reason, we deoxidized GaAs(111)A and B substrates at 680°C under a strong As flux of $1.10^{-5}$ Torr in the III-V MBE chamber. This annealing is monitored by RHEED. Thanks to this technique, we can determine when the substrate is well deoxidized. When we first insert the sample at room temperature in the MBE III-V chamber, the oxide layer covering the substrate surface hinders the diffraction patterns which is imperceptible. The sample temperature is increased and when it reaches 400°C, a strong As flux is sent onto the surface up to 680°C. After approximately 15 minutes at this temperature, the RHEED diffraction is bright and very distinct.

To flatten the surface and prepare a clean GaAs surface for the ZnSe buffer layer, we followed a usual procedure to deposit GaAs on a (111) surface. It consists in reducing the temperature to 630°C and depositing GaAs at a speed of 2 $\mathring{A}/s$ with an As beam flux of $9 \times 10^{-6}$ Torr. The Ga beam flux should be 10 to 12 times lower than the As flux [135, 136] to be under stoichiometric growth conditions. After 2 minutes of deposition (24 nm), the fluxes were stopped during 30 s before sending back the As flux only. Indeed, it has been noticed that the surface is smoothed during this procedure.

We are therefore able to see the typical $2 \times 2$ GaAs(111)A [137–140] along with the $\sqrt{19} \times \sqrt{19}$ (observed only during the temperature cooling) and the $2 \times 2$ GaAs(111)B [138, 140]

SRs visible in the form of vertical streaks, labeled in yellow in Figure 2.12.

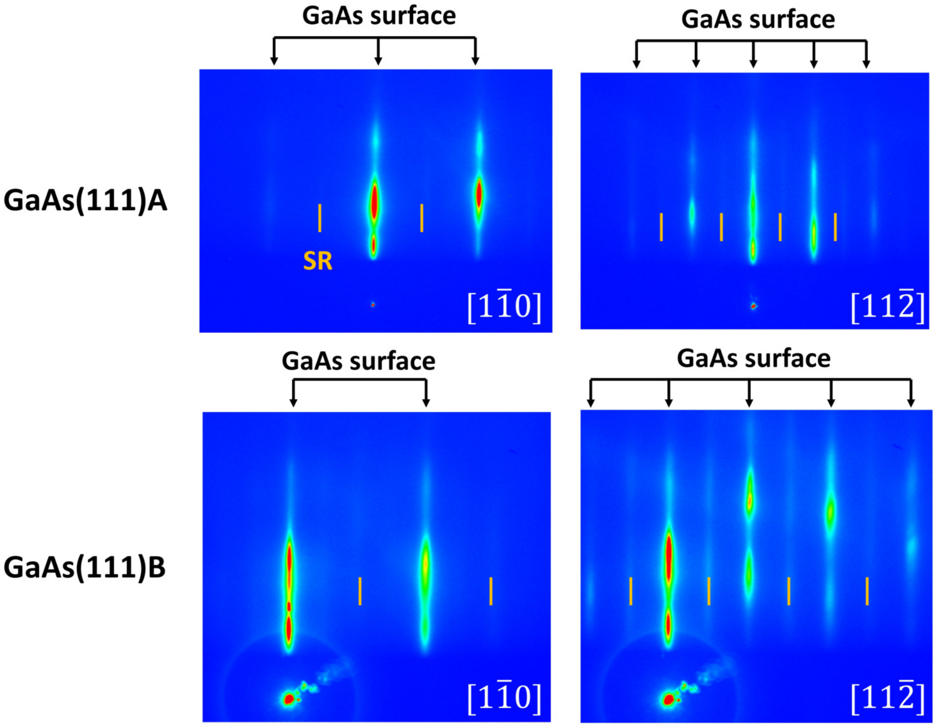

Figure 2.12: RHEED diffraction pattern of GaAs(111)A (top) and (111)B (bottom) surfaces along the [1$\bar{1}$0] (left) and [11$\bar{2}$](right) azimuths recorded at room temperature. The streaks corresponding to the SRs are indicated in yellow.

### 2.2.2 ZnSe(111)A and B surface preparation

#### ZnSe RHEED oscillations

After the deoxidation of the GaAs substrate, the sample is cooled down and transferred to the II-VI chamber. The ZnSe buffer layer (about 35 nm) is deposited at 280°C and smoothed at 380°C under a Zn flux during 10 min. The growth of a smooth ZnSe(111) surface is relatively straightforward on the (111)A surface [141] but very challenging on the (111)B surface. Indeed, Gard et *al.* [142] characterized the smoothness of ZnSe(111)B surfaces according to the substrate temperature and the Se:Zn flux ratio. Their conclusion is that whatever the growth conditions, the ZnSe (111)B surface always remains rough. However, our effort to obtain smooth ZnSe(111)B surfaces was rewarded by numerous and clear RHEED oscillations visible in Figure figure 2.13. With these RHEED oscillations[1], we measured a ZnSe growth speed of 0.25 MonoLayer (ML) per second and calculated the ZnSe layer thickness (around 35 nm). These ZnSe buffer layers were very thin because thicker layers gave rise to rougher

---

[1] In this example, the Zn and Se growth speed were calibrated at 0.28 and 0.33 ML per second on a reference ZnTe(001) sample 280°C.

surfaces (characterized by thicker vertical streaks on the RHEED pattern).

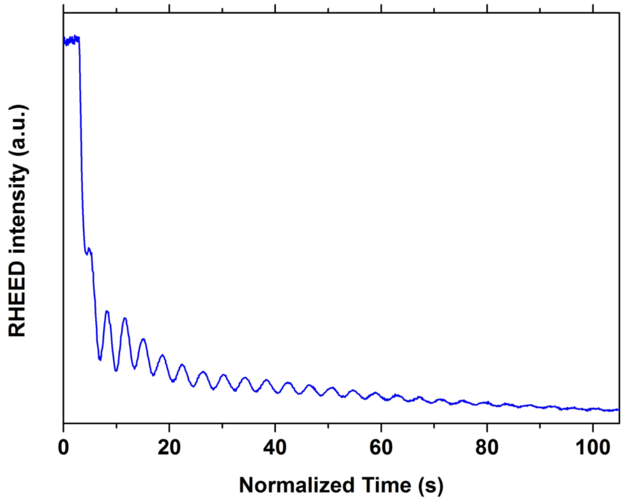

Figure 2.13: RHEED oscillations mesured during the deposition of a ZnSe layer on a GaAs(111)B surface at 280°C. The measured growth speed is 0.25 ML/s.

### ZnSe growth speed calibration

The ZnSe growth was carried out with individual Zn and Se effusion cells. To be reproducible, we always calibrated the Zn and Se growth speeds with RHEED oscillations at 340°C. This temperature is an intermediate value between the optimal buffer and the NWs temperature (280°C and 400°C respectively) that we will present later on. It also corresponds to the optimal temperature to deposit materials on the reference sample - a ZnTe(001) sample - to keep an atomically flat surface and clearly observe the RHEED oscillations. The calibration of the Zn growth speed was performed by sending an additional flux of Te in excess, leading to a ZnTe deposition. Such a ZnTe deposition is homoepitaxial onto the ZnTe(001) reference sample. Then, the Se growth speed calibration was performed by sending an additional flux of Cd, leading to a CdSe deposition. Such a CdSe deposition is possible without surface relaxations due to the small lattice mismatch of 0.3% with ZnTe.

Interestingly, we observed that a stoichiometric Zn:Se growth speed corresponds to a Zn:Se BEP flux ratio of at least 1:3. It means that the Se flux should be at least 3 times higher than the Zn flux to be under stoichiometric conditions. This discovery is in contrast with the previous work of Elouneg-Jamroz [41] who only considered BEP flux ratios. For this reason, we did not rely on the BEP flux ratio but on the RHEED oscillations to calibrate the growth speed of our samples. **In the rest of the manuscript, the growth speed will not be indicated as the usually mentioned BEP flux ratio, but as the calibrated growth speed ratio on reference [001]-oriented samples.**

### Best growth conditions for the ZnSe buffer layer

For the ZnSe buffer layers, the best growth conditions were found with a growth temperature of 280°C using Se-rich (Zn:Se nominal growth speed ratio of 1:2) conditions for both (111)A and B surfaces. We used individual Se and Zn effusion cells with fluxes in the 1.0 to 9.0 Torr range and a Zn:Se nominal growth speed of 1:2. These conditions were found by comparing the RHEED diffraction patterns between different conditions according to:

- the Zn or Se exposure prior to the growth,
- the choice of the MBE or ALE growth,
- the Se:Zn nominal growth speed ratio,
- the growth temperature (according to the induced roughness measured by AFM),
- the smoothing of the surface after the growth under Zn or Se and the temperature used for this smoothing.

Figure 2.14 is an overview of RHEED diffraction patterns during the growth of ZnSe(111)B layers. The best conditions - sharpest vertical streaks and brightest RHEED intensity - are displayed on the right part of the Figure. First, we determined that Se-rich conditions gave better 2D surfaces compared to Zn-rich growth (Figure 2.14a), as reported by Gard et *al.* [141–143]. In a second step, we compared MBE growth with Atomic Layer Epitaxy (ALE) (Figure 2.14b). This growth technique can be followed by RHEED, as displayed in Figure 2.15, and consists in depositing alternating MLs, in our case of Zn (green arrows) and Se (orange arrows). These atoms are sent onto the surface as alternating pulses with dead times in between to flush the excess materials. During the deposition of Zn (Se) atoms, the RHEED intensity increases (decreases) and reaches a saturation regime when the Zn (Se) atoms saturate the surface of the sample.

ALE has been successfully used to grow smooth ZnSe(001) layers [144] but we found no reports of this growth process for ZnSe(111) layers. Therefore, ZnSe(111) surfaces were grown using different atomic and dead time pulses to determine the best growth conditions but every time, the surface turned 3D very fast: consequently, we chose to grow the samples by MBE. In addition, the RHEED diffraction patterns indicated that a smoothing of the sample surface at 380°C was better induced by a Zn flux compared to a Se-flux (Figure 2.14b).

Finally, we tried different growth temperatures. Figure 2.14d corresponds to AFM profiles estimating the samples average roughness over a surface of 1 µm × 1 µm which is 0.89 and 0.72 nm for samples grown at 320 and 280°C respectively. As we are interested by the flattest surface, we grew the samples at 280°C. Interestingly, half-spheres are visible (on average 50 nm in diameter and 15 nm in height) which might be due to Se droplets on the ZnSe surfaces due to the Se-rich conditions used to grow these buffer layers. Indeed, the observation of Se droplets has been reported by other groups [145–148].

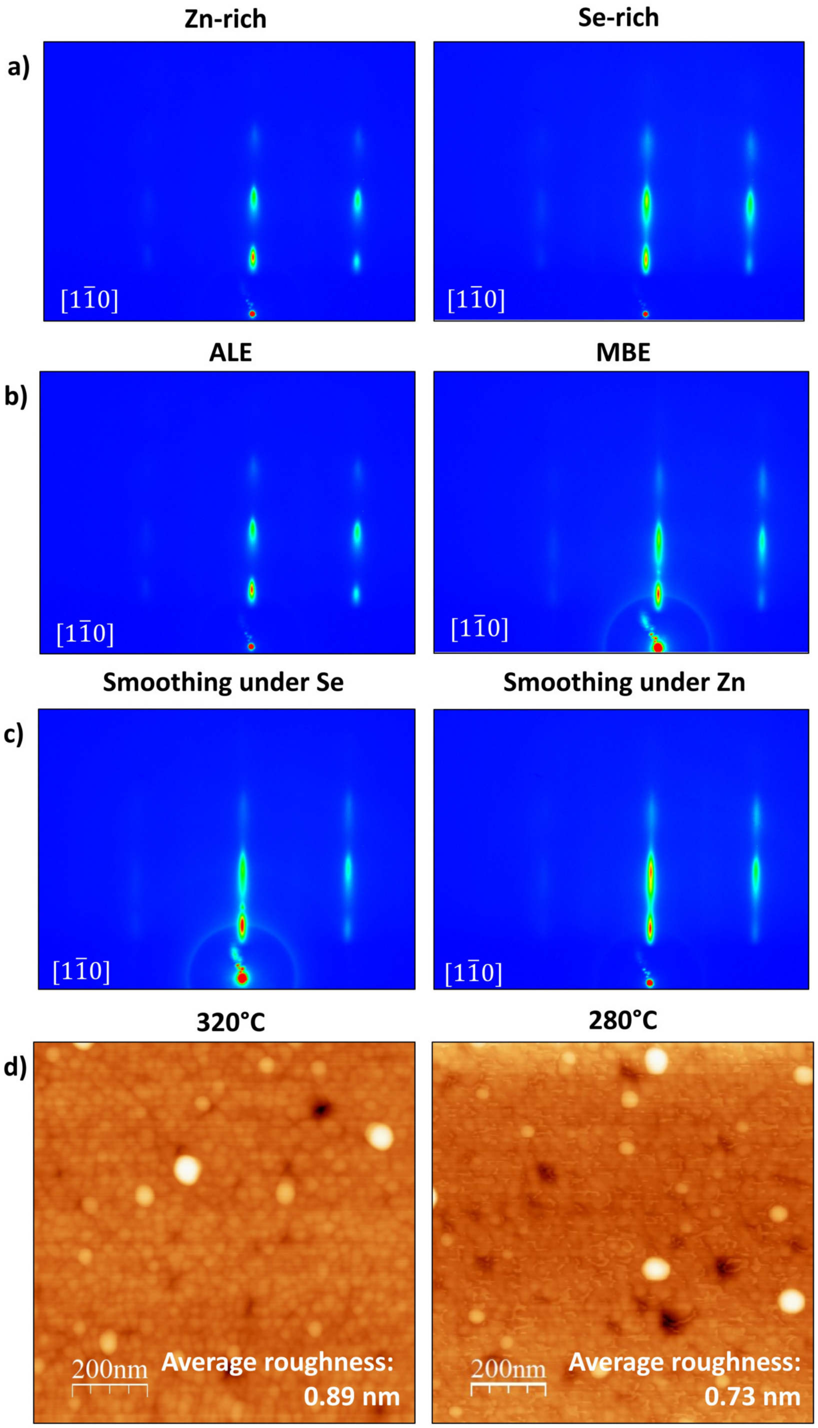

Figure 2.14: Overview of RHEED diffraction patterns during the growth of ZnSe(111)B layers under different conditions: a) Zn or Se-rich growth conditions, b) ALE or MBE growth techniques and c) smoothing under Se or Zn flux. d) The last line corresponds to 1 µm x 1 µm AFM profiles of samples grown at 320°C and 280°C with a sample roughness of 0.89 and 0.72 nm respectively, used to determine the best growth temperature. For each comparison, the best conditions are displayed on the right part of the Figure.

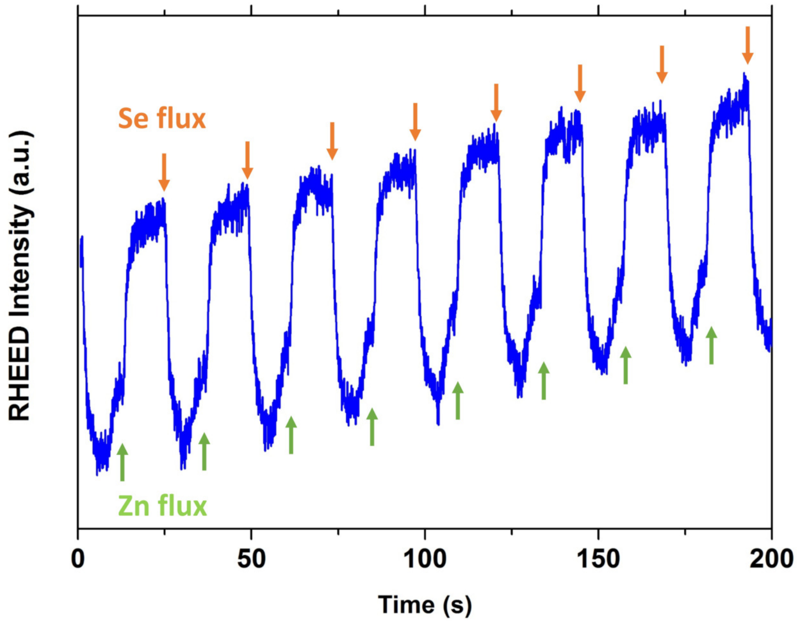

Figure 2.15: Example of an ALE growth of a ZnSe(111)B layers. In this example, the growth consists in alternating the elemental flux beams of Zn (green arrows) and Se (orange arrows) during 5 s, with dead times under vacuum of 7 s between the exposures.

Table 2.1 summarizes the best growth conditions for both (111)A and B surfaces.

| | (111)A | (111)B |
|---|---|---|
| Pre-exposure | No pre-exposure | 30 s of Zn |
| Growth by MBE or ALE? | MBE during 6 min | MBE during 6 min |
| Zn:Se nominal growth speed and temperature | 1:2 (Se-rich) at 280°C | 1:2 (Se-rich) at 280°C |
| Smoothing | Flash at 380°C under **Se** | Flash at 380°C under **Zn** |

Table 2.1: Overview of the best growth conditions for a ZnSe(111)A and B buffer layer

Besides, it is possible to observe rotational twins on the $[11\overline{2}]$ azimuth of the ZnSe(111)B RHEED diffraction pattern, as shown in Figure 2.16a). The rotational twins are characterized by slightly inclined brighter segments along the ZnSe surface vertical streaks. They correspond to a 180° rotation of the ZnSe surface along the [111] direction. Such rotational twins are common and have been reported for GaAs(111)B [149] and other materials like Ag nano-islands on Si(111) [150].

SRs are visible on the $[11\overline{2}]$ and $[1\overline{1}0]$ azimuths of the ZnSe(111)A and B surfaces respectively, as shown in Figure 2.16b. These SRs might originate from the $2 \times 2$ ZnSe(111)A and the $1 \times 1$ ZnSe(111)B SRs reported by Gard et *al.* [141].

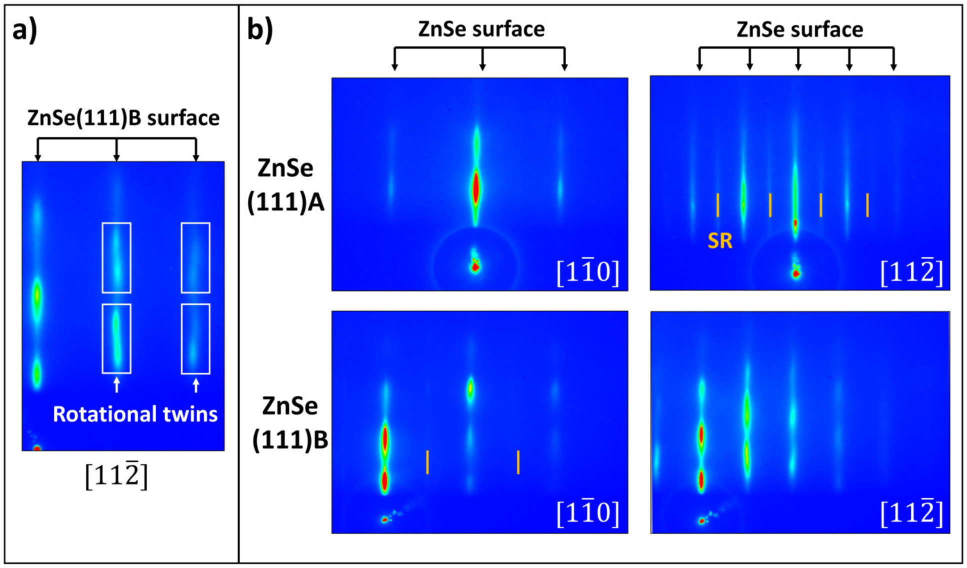

Figure 2.16: Typical RHEED diffraction patterns. a) Highlight of rotational twins along the [11$\bar{2}$] azimuth characterized by slightly inclined brighter segments along the ZnSe surface vertical streaks. b) Overview of ZnSe(111)A and B layers. Both [1$\bar{1}$0] and [11$\bar{2}$] azimuths are displayed. The vertical lines corresponds to the ZnSe(111) surface diffraction (black arrows) and the ZnSe SRs (yellow segments).

### 2.2.3 Gold deposition

In catalyzed NW growth on semiconductor substrates, the catalyst seed determines the size and location of the NW. In this project, we used Au catalyst particles by dewetting a gold thin film on a ZnSe surface. More precisely, a fraction of a ML of gold is deposited at room temperature in the III-V chamber under UHV on top of a ZnSe buffer layer. To assure an excellent gold deposition under UHV, we leave the III-V chamber during one day to pump the residual As prior to the gold deposition. Then, when heating the sample, Au droplets are formed. This process is illustrated in Figure 2.17.

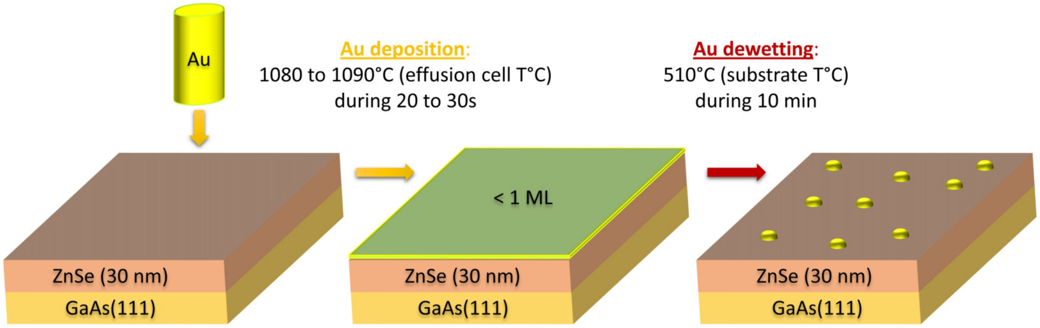

Figure 2.17: Scheme of the Au deposition and dewetting process.

### Effect of the dewetting temperature on the gold particles diameter

The Au dewetting process on ZnSe has already been studied by a previous PhD student from our group, Miryam Elouneg-Jamroz. She studied the influence of the dewetting temperature on the diameter of the Au particles when a gold layer is annealed for 10 min. This annealing has been studied at six temperatures ranging from 425 to 530°C and each temperature induces a distribution of the particle diameters. The mean particle diameter increases monotonically with the annealing temperature from 4.1 to 11.6 nm with a standard deviation in the diameter distribution between 1.0 and 3.0 nm [41] which is very narrow as displayed by the histograms of Figure 2.18.

Interestingly, the dewetting temperature fixes the Au particles size distribution independently of the thickness of the deposited Au layer (below 1 ML), which rules the particles density.

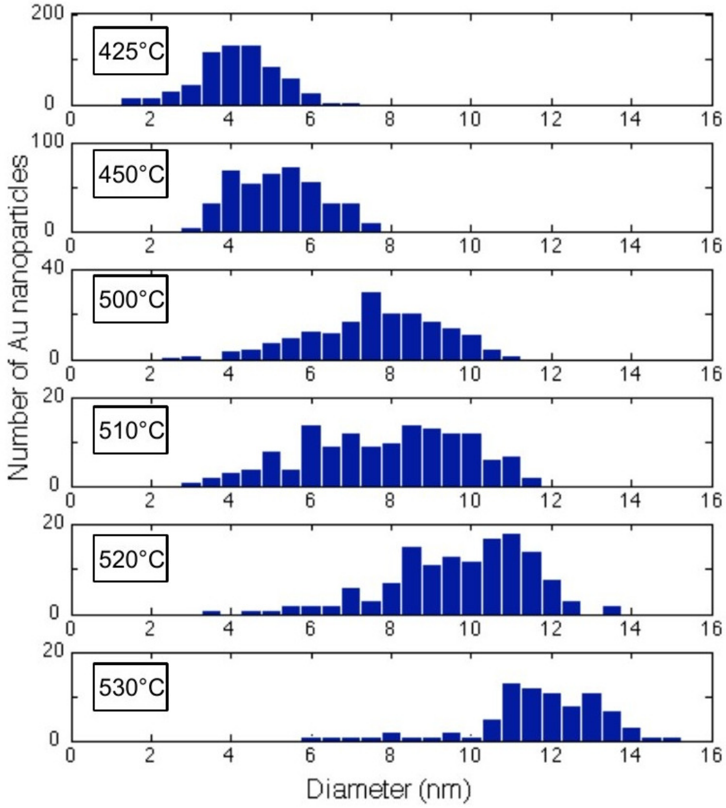

Figure 2.18: Size of Au catalyst nanoparticles observed as a function of the annealing temperature for an initial amount of Au=0.5 MLs and an annealing time of 10 min. This Figure has been taken from Ref.[41].

### Effect of the amount of gold deposited on the gold particles density

The amount of Au deposited in our chamber has been calibrated by a previous PhD student Pamela Rueda-Fonseca [134] on ZnTe(111)B samples dewetted during 5 min at 350°C with a fixed Au cell temperature (1090°C) to determine the Au particles density. This Au particles density can be calculated using the formula:

$$D_{Au} = P_{Au} \times t \times C \tag{2.2.1}$$

with $P_{Au}$ the Au vapor pressure[2], $t$ the time of gold deposition (s) and $C$ a constant equal to 4.52, determined with Rutherford BackScattering (RBS) measurements (more details in Ref.[134]).

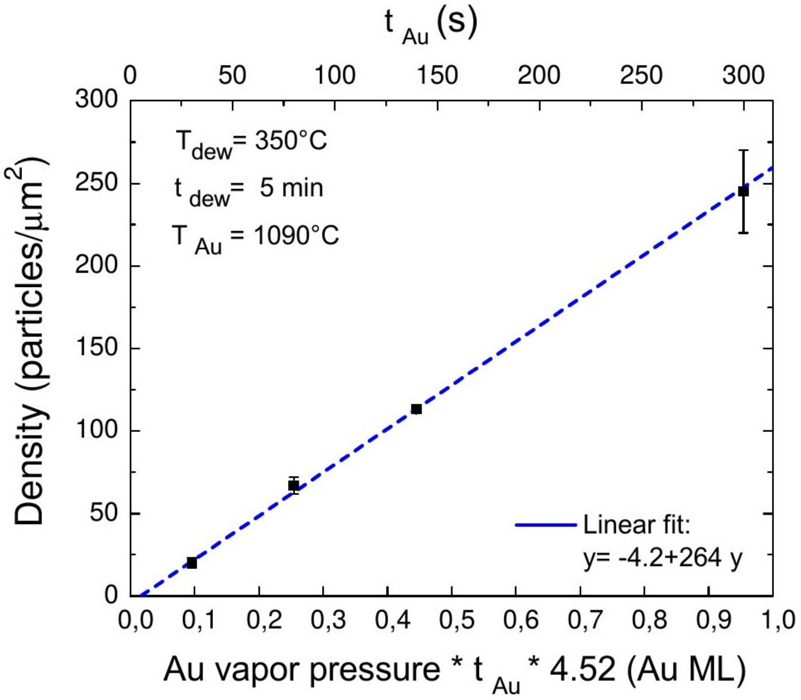

Figure 2.19: Gold droplets surface density as a function of the total amount of gold sent to the surface. This quantity is calculated as the Au cell vapor pressure times the exposure time times 4.52 (RBS calibrating constant). The exposure time ($t_{Au}$) is the only parameter changed in this set. For all samples: $T_{Au}$= 1090°C, $T_{dew}$=350°C and $t_{dew}$=5 min. The blue line is a linear fit of the data. This Figure is extracted from Ref.[134].

### Chosen NWs density and dewetting temperature

At the surface of the ZnSe samples, we want to grow NWs with a density ranging from 10 to 20 NWs per µm$^2$, getting a large amount of NWs to later mechanically deposit onto pattern

---

[2] The Au vapor pressure is linked to the Au cell temperature by the following equation [151]: log(P) = 14.158 - 19343/T - 0.7479 log(T); with the units in Pascal and Kelvin.

substrates for PL characterizations. To obtain such a NW density, we deposited gold during 30 s with a Au cell temperature of 1090°C (see Figure 2.19).

Next, to ensure a strong quantum confinement of the exciton in our CdSe QD (CdSe exciton Bohr diameter of 11 nm) and have large enough NWs to observe them using a standard SEM (few nanometers resolution), we decided to grow our nanostructures with a 10 nm-diameter. Since the gold catalyst size fixes the NW-QD diameter, we chose[3] a gold dewetting temperature of 510°C carried out during 10 min (see Figure 2.18) detailed in the next Part.

### 2.2.4 Gold dewetting

The nucleation of the Au particles could be followed by looking at the RHEED pattern of the samples during the annealing of the thin gold film deposited at the surface of the ZnSe buffer layer. From room temperature to 300°C, only the RHEED pattern of the ZnSe(111) surfaces is visible. Additional diffraction spots appear between 300 and 400°C and correspond to gold diffraction spots. These spots are large and diffuse with a low intensity, and become smaller and brighter during the temperature increase, up to the annealing temperature at 510°C. This reduction of the gold diffraction spots size indicates that the real size of the gold droplets increase, as the diffraction spots are in the reciprocal space. This observation is consistent with Figure 2.18 which shows an increase of the dewetting temperature with the gold particles diameter.

Figure 2.20 presents a typical RHEED diffraction pattern for ZnSe(111)A and B samples annealed at 510°C during 10 min for both $[1\bar{1}0]$ and $[11\bar{2}]$ azimuths. The spots highlighted by orange arrows indicate the presence of solid Au particles on the surface. The vertical streaks corresponds to both the ZnSe(111) surface diffraction (black arrows) and Au SRs (yellow). Due to its roughness, the ZnSe(111)B surface only displays a faint SR along the $[1\bar{1}0]$ azimuth. On the other hand, because the ZnSe(111)A surface is very flat, it can show clearer Au SRs as displayed in Figure 2.20. Au SRs have already been observed on other surfaces like Si(111) [152] and GaAs(111)B [58, 59] and to the best of our knowledge, this is the first report of Au SRs on ZnSe(111).

---

[3] We should notice that the study of Miryam Elouneg-Jamroz has been carried out on ZnSe(001) substrates so one could expect a difference during the dewetting on a ZnSe(111)A or B surface. However, as will be seen in the section 2.2.6, we still observed NW with a diameter around 10 nm.

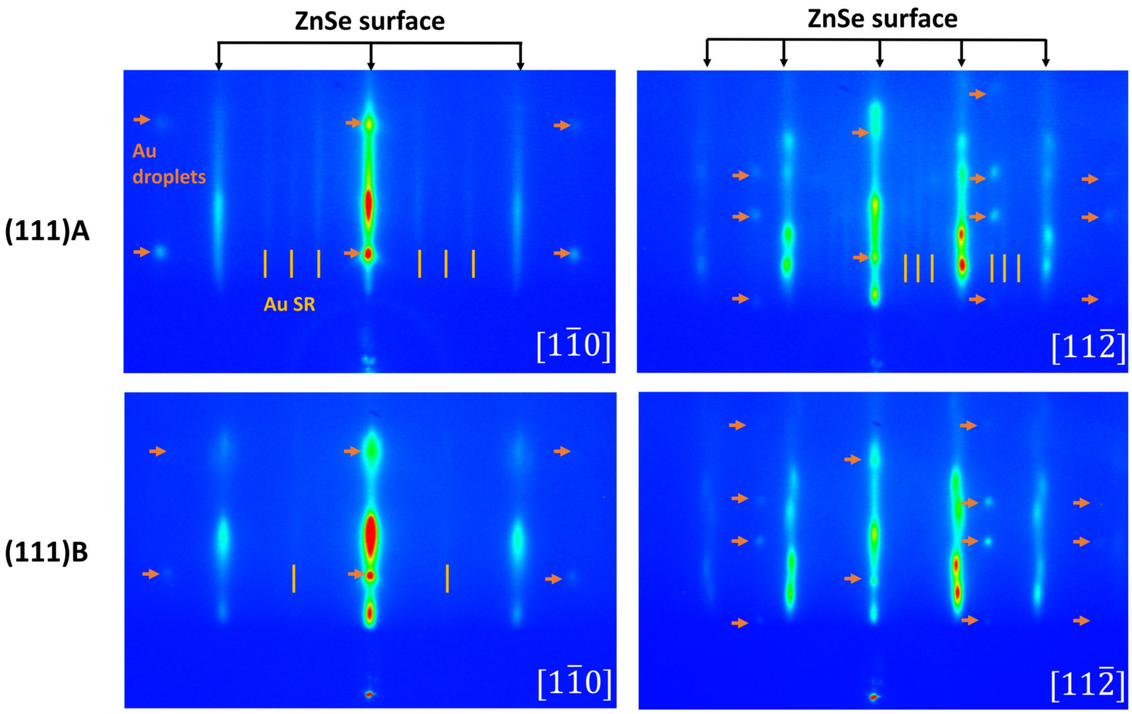

Figure 2.20: Typical RHEED diffraction pattern of ZnSe(111)A and B layers covered with Au particles dewetted at 510°C during 10 min. Both [1$\bar{1}$0] and [11$\bar{2}$] azimuths are displayed. The spots indicated with orange arrows highlight the presence of solid Au particles on the surface. The vertical lines corresponds to the ZnSe(111) surface diffraction (black arrows) and Au SRs (yellow lines).

In the next parts, ZnSe NWs will be grown on both (111)A and B surfaces to determine which one is more beneficial for the growth of vertically oriented and highly crystalline NWs.

### 2.2.5 NWs grown on a (111)A surface

After the successful dewetting of the gold particles, we can use them to catalyze the growth of our NWs. Figure 2.21 shows SEM images of NWs samples and its inset displays single NWs. These samples were grown at 400°C on a (111)A surface. This growth temperature is a good compromise for the growth of ZnSe(111)B NWs as we will later see, this is why we chose this temperature for (111)A ZnSe NWs. We used different Se:Zn nominal growth speed ratios to be under (a) Zn-rich (Zn:Se of 3:2) and (b) Se-rich (Zn:Se of 1:2) conditions. Under both conditions, the NWs are mainly bent during the growth with worm or saw-like shapes, which suggests that they are composed of a lot of defects.

For these reasons, we conclude that the (111)A surface is not the right surface orientation to start with to obtain straight and vertically oriented NWs.

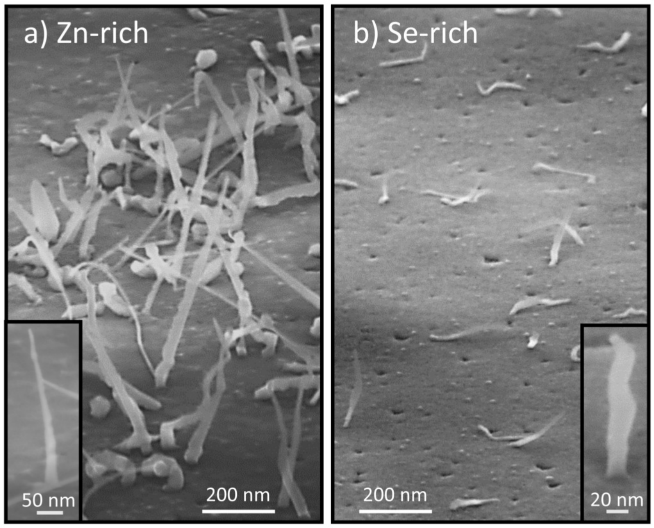

Figure 2.21: Tilted view SEM images (65°) of ZnSe NWs grown on a (111)A substrate at 400°C under a) Zn-rich conditions (Zn:Se of 3:1) and b) Se-rich conditions (Zn:Se of 1:2).

### 2.2.6 NWs grown on a (111)B surface

Figure 2.22 shows SEM images of NWs samples grown under different Zn:Se nominal speed ratios along (111)B. They were carefully grown during the same day at 400°C for 20 min with a constant Se flux of $5.10^{-7}$ Torr. The nominal speed ratios are the following: (a) Zn-rich conditions (Zn:Se of 3:2), (b) stoichiometric (Zn:Se of 1:1) and (c) Se-rich (Zn:Se of 1:2).

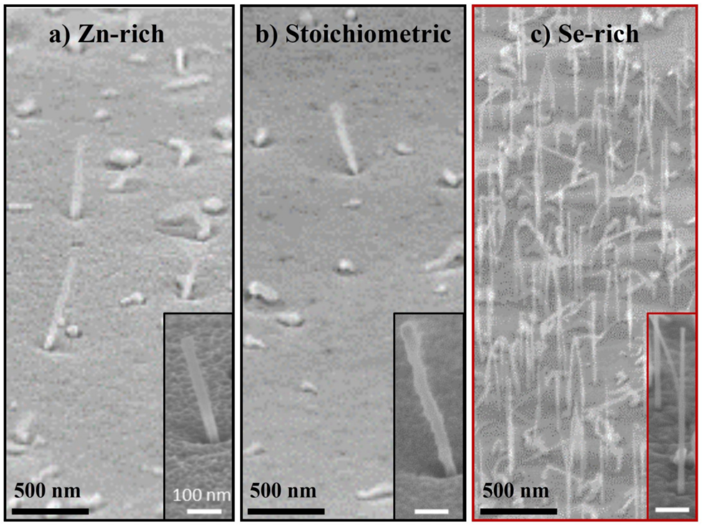

Figure 2.22: Tilted view SEM images (65°) of ZnSe NWs grown on a (111)B substrate at 400°C under a) Zn-rich (Zn:Se nominal growth speed ratio of 3:2), b) stoichiometric (Zn:Se of 1:1) and c) Se-rich conditions (Zn:Se of 1:2). All the white scale bars of the insets represent 100 nm.

Under a Zn excess and stoichiometric conditions (Figures 2.22a and b), the NW growth is hindered. The longest NWs are tilted and display a rough lateral surface (inserts of Figures 2.22a and b). However, under Se-rich conditions (Figure 2.22c), the NWs are mainly vertical (with the growth axis along the (111)B substrate direction) and their growth is greatly improved. For this reason, we decided to grow our NWs on the (111)B surface under Se-rich conditions.

In Figure 2.23, we show the effect of the temperature on the NW growth under Se-rich conditions. At 350°C (Figure 2.23a), the NWs are cone-shaped with a base and tip diameter of respectively 20 ± 2 nm and 11 ± 1 nm. The later corresponds to the gold droplet diameter. The NWs cone-shape is a result of the low growth temperature which leads to a low adatoms mobility and a sizable lateral growth, as discussed in Part 2.1. At 400°C, the NWs are cylindrical with a uniform diameter of 12 ± 2 nm. For those two temperature conditions, the NWs are mainly vertical and uniform in length and diameter. At 450°C, the NW growth is greatly inhibited. The very few vertical NWs are 415 ± 75 nm long with a diameter of 12 ± 2 nm. Table 2.2 summarizes the NWs height and diameter.

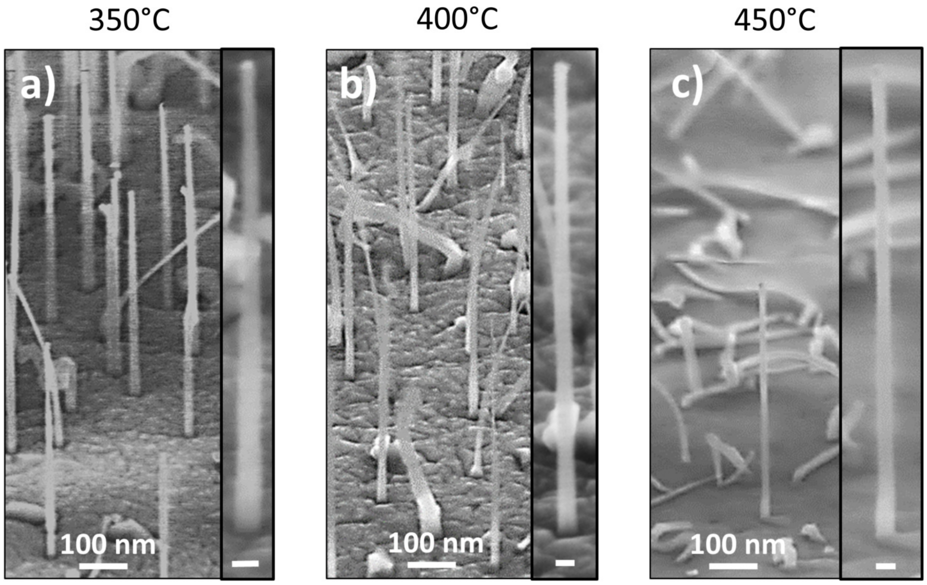

Figure 2.23: Tilted view SEM images (65°) of ZnSe NWs grown on a (111)B substrate under Se-rich (Zn:Se of 1:2) conditions at a) 350°C b) 400°C and c) 450°C. Insets highlight individual NWs with a scale bar of 20 nm.

| | 350°C (Figure 2.23a) | 400°C (Figure 2.23b) | 450°C (Figure 2.23c) |
|---|---|---|---|
| Height (nm) | 405 ± 65 nm | 490 ± 25 nm | 415 ± 75 nm |
| Base diameter (nm) | 20 ± 2 nm | 12 ± 2 nm | 12 ± 2 nm |
| Tip diameter (nm) | 11 ± 1 nm | 12 ± 2 nm | 12 ± 2 nm |

Table 2.2: Statistics on the height and diameter of the NWs displayed in Figure 2.23.

The ZnSe NW growth temperature of 400°C is well-suited to create cylindrical and vertically oriented NWs. For this reason, *we chose to grow in the rest of the manuscript all the NWs at this temperature (400°C), under Se-rich conditions on (111)B surface orientations.*

### 2.2.7 ZnMgSe shell deposition and structural characterization

Because the ZnSe NWs have a small diameter and therefore a large surface-to-volume ratio, their surface passivation is essential to ensure good optical properties. For this reason, we worked on the passivation of the ZnSe NWs by covering them with a higher bandgap semiconductor of ZnMgSe.

For this deposition, the sample surface was tilted by 7° (toward the horizontal line in Figure 1.16 to expose more the NWs sidewalls to the Mg flux, still with a rotation of the sample) and the temperature was reduced from 400 to 220-250°C to ease the shell deposition on the NWs sidewalls. Such a drop of temperature is mandatory to ensure the ZnMgSe radial deposition, otherwise no deposition is observed on the ZnSe NWs sidewalls. Moreover, as we will later see with the NWs RHEED and TEM analysis, these NWs are essentially composed of the WZ phase. Since it is a very unstable phase, the 2D growth (usual calibration used for MBE shell depositions) of this WZ ZnSe phase is not reported in the literature and we could not rely on previous knowledge to investigate the ZnMgSe shell deposition. To the best of our knowledge, the group of Kahen et *al.* has been the only one to report the passivation of ZnSe NWs [80, 110]. They grew by MOCVD ZnSe NWs and studied their passivation with ZnSSe, ZnMgSSe and ZnMgSe alloys. Similarly to our case, their NW growth temperature of 550°C was reduced down to 320°C to ease the shells depositions.

To deposit the $Zn_{1-x}Mg_xSe$ shell, we used the Mg effusion cell (in addition the the Zn and Se cells). The growth speed calibration was carried out on a CdTe(001) substrate at 280°C which is the optimal temperature to deposit Mg under a Te excess (MgTe). We can already notice that such a temperature is close to 220°C, the temperature we will use later on to deposit the ZnMgSe shell. In order to favor the radial shell deposition on the NWs sidewalls, we chose to deposit a $Zn_{0.80}Mg_{0.20}Se$ shell. We aimed 20 % of Mg to get a reasonable lattice mismatch (estimated ∼0.7%) between the ZnSe core and the ZnMgSe shell and a sufficient bandgap barrier passivation of the shell (around 3 eV compared to 2.85 eV for the $FX_{WZ}$ ZnSe). During the calibration, we measured a very stable 17% of Mg and chose to keep this Mg concentration for the ZnMgSe shell deposition.

In order to verify our nominal growth speed calibrations, we performed PL on the as-grown sample with a 405 nm (3.06 eV) laser. The aim is to excite and collect luminescence directly from the ZnMgSe shell. As its bandgap is higher than the ZnSe bandgap, we looked at the highest energy part of the spectrum displayed in Figure 2.24: the ZnMgSe luminescence is visible around 2.965 eV (418 nm).

The bandgap of MgSe varies a lot in the literature with many values [153–156] ranging from 2.47 eV [157] (below the bandgap of ZnSe) to 5.6 eV [158, 159]. We used the value of 3.6 eV reported in Ref.[153, 156]. Due to the uncertainty of the MgSe bandgap, we do not consider the bowing of the ZnMgSe alloy but estimate its bandgap with a linear relation between ZnSe (2.800 eV [106]) and MgSe (3.6 eV). This estimation yields 20% of Mg within the ZnMgSe alloy, which is in good agreement with the 17% calibrated.

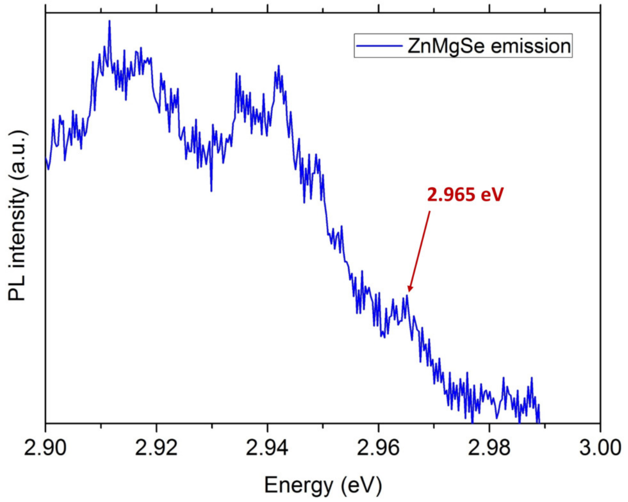

Figure 2.24: Zoom on the high energy part (above the ZnSe emission) of a PL spectra measured on an as-grown sample composed of ZnSe NWs passivated with a nominal $Zn_{0.83}Mg_{0.17}Se$ shell. The measurement was performed at 10 K with a 1 mW 405 nm (3.06 eV) laser diode excitation. The highest peak at 2.965 eV (418 nm, attributed to the ZnMgSe NBE emission) is used to estimate the Mg concentration within the $Zn_{1-x}Mg_xSe$ shell. The estimation yields 20% of Mg, close to the nominal 17% calibrated during the growth.

The shell passivation effect was studied on three samples. They were carefully grown the same day to keep the same Mg concentration (nominal $Zn_{0.83}Mg_{0.17}Se$ shell) under the following conditions:

1. at 250°C during 10 min.
2. at 220°C during 5 min
3. at 220°C during 10 min.

Table 2.3 summarizes the mean diameter of these shelled NWs compared to the unshelled NWs.

|  | *Unshelled* | and *shelled* ZnSe NWs |  |  |
|---|---|---|---|---|
|  |  | Condition 1:<br>**250°C / 10 min** | Condition 2:<br>**220°C / 5 min** | Condition 3:<br>**220°C / 10 min** |
| Mean diameter | 12 ± 2 nm | 17 ± 2 nm | 16 ± 2 nm | 21 ± 3 nm |
| Shell radius | 0 nm | 2.5 ± 1 nm | 2.0 ± 1 nm | 4.5 ± 1.5 nm |

Table 2.3: Statistics on the diameter and shell radius of ZnSe NWs without and with a nominal $Zn_{0.83}Mg_{0.17}Se$ shell. The three conditions correspond to the previously listed shell deposition conditions 1, 2 and 3.

The mean NW diameter of the unshelled and shelled (conditions 1, 2 and 3) are respectively 12 ± 2 nm, 17 ± 2 nm, 16 ± 2 nm and 21 ± 3 nm. By comparing conditions 1 and 3, we notice that the temperature lowering from 250°C to 220°C permits to deposit a thicker shell on the NWs sidewalls. The increase of the deposition time from 5 to 10 min (between conditions 2 and 3) shows that the shell thickness also increases, as expected. Note that the ZnMgSe deposition on the NWs sidewalls is very slow ($\sim$ 0.5 nm/min) compared to the 2D growth ($\sim$ 8 nm/min) in between the NWs. Therefore, the deposition time cannot be arbitrarily increased or the NWs will be buried in a ZnMgSe matrix (an effect we will later use in Chapter 4). The ZnMgSe shell deposition results from a compromise between depositing a thick enough shell for the NWs passivation, while keeping the NWs out of the burying 2D layers.

To know more about the NWs structure, we performed a SEM analysis. Figure 2.25a displays a single NW before the shell deposition. The NW is straight, vertically oriented with a uniform 12 nm-diameter. Figures 2.25b, c and d show single NWs after the deposition of the ZnMgSe shell under the previously listed conditions 1, 2 and 3 respectively. Their mean diameters are listed in Table 2.3. Note that these shelled NWs display some modulations and localized swellings as large as 40 nm. Moreover, Figure 2.25e shows a zoom at the tip of a ZnSe NW after the deposition of a ZnMgSe shell. This tip has a *flag-like shape* only visible after ZnMgSe depositions: it seems that during the ZnMgSe deposition, the gold droplet continues to catalyze a tiny (dozens of nm) ZnMgSe NW growth in a worm-like shape.

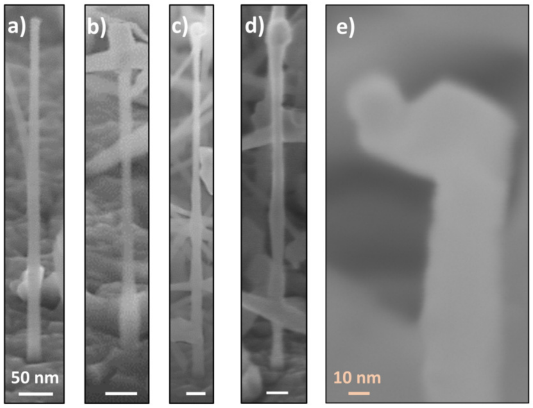

Figure 2.25: Tilted view SEM images (65°) of single ZnSe NWs grown at 400°C under Se-rich conditions a) before and after the deposition of the ZnMgSe shell during b) 10 min at 250°C, c) 5 min at 220°C and d) 10 min at 220°C. e) Zoom at the tip of a ZnSe NW after a ZnMgSe shell deposition. This NW tip has a clearly visible flag-like shape, suggesting that during the ZnMgSe deposition, the gold droplet continues to catalyze a tiny (dozens of nm) ZnMgSe NW growth in a worm-like shape

After the SEM structure analysis of these NWs, a first indication of the NWs crystallinity can be given by the RHEED diffraction patterns recorded during the NW growth, as displayed in Figure 2.26. At the beginning of the growth (after 1 min 30 s - Figure 2.26a), both ZB and WZ phases are visible. During the growth, the intensity of the WZ phase becomes progressively stronger while it decreases for the ZB phase (Figure 2.26b). After the ZnMgSe shell deposition, the WZ phase is clearly visible while the ZB phase diffraction spot almost vanishes (Figure 2.26c). The TEM NWs analysis carried out in the next Chapter will further confirm that the ZnSe NWs are indeed composed of the WZ phase.

Moreover, the diffraction pattern of the gold droplets is still visible during the NW growth, as shown in Figure 2.26a. This indicates that the gold particles remain solid during the NW growth. The NWs are therefore grown in the VSS growth mode which is of high interest for CdSe insertions due to its sharper interfaces compared to the VLS growth [66, 160].

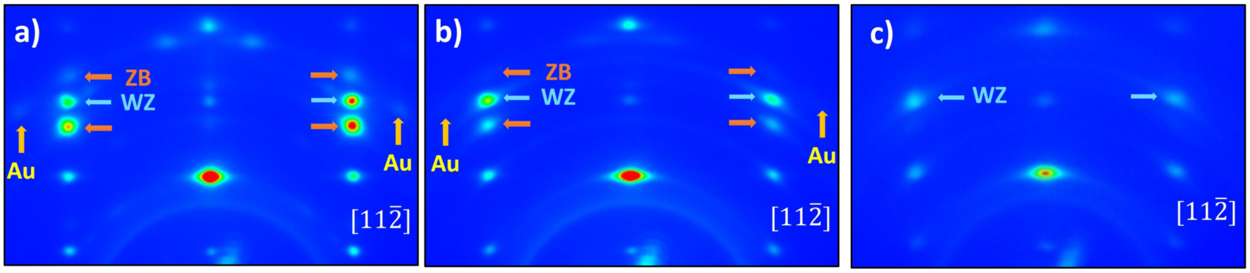

Figure 2.26: a) RHEED capture along the [11$\bar{2}$] plan revealing the presence of the ZB/WZ polytypism with the ZnSe NWs at the very beginning of the growth (after 1m 30 s) at 400°C, b) after the growth of the ZnSe NWs at 400°C and c) after the ZnMgSe shell deposition at 220°C. The light blue and orange arrows highlight the WZ and ZB ZnSe NWs diffraction spots respectively, and the yellow arrows the presence of the gold droplets.

## 2.2.8 Photoluminescence of unshelled and shelled ZnSe NWs

### Unshelled NWs as-grown luminescence

In this part, we compare the as-grown samples luminescence of the *unshelled* NWs grown at 350, 400 and 450°C. Figure 2.27 shows that the unshelled samples emissions are dominated by an intense broad band emission from 1.8 to 2.5 eV. This emission is not observed for single NWs and is therefore attributed to the 2D buffer layer emission. Moreover, the origin of this deep-level emission is unclear and could be due to the diffusion of Zn and Ga atoms at the ZnSe/GaAs interface [118, 161] and/or to donor acceptor pair recombinations due to a doping of ZnSe by Au [162].

The ZB ZnSe free exciton emission is expected at 2.800 eV [106]. Its emission from these unshelled samples is very weak and visible in the inset of Figure 2.27 with the label $\mathrm{FX_{ZB}}$. From this measurement, we can clearly conclude that the as-grown emission of the unshelled samples is dominated by the deep-level emissions and that the NBE NWs emission is very weak.

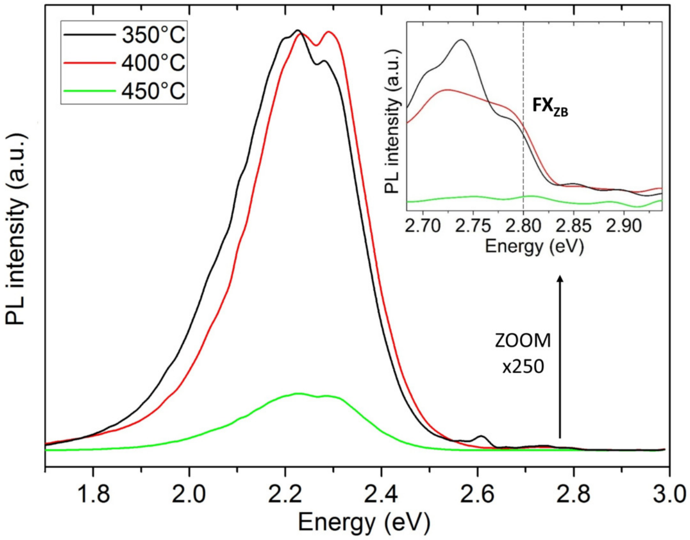

Figure 2.27: MacroPL spectra of the unshelled NWs as-grown samples grown at 350 (black), 400 (red) and 450°C (green). The measurements were performed at 10 K with a 1 mW 405 nm laser diode excitation. The inset is a zoom on the NBE PL emission.

### Shelled NWs as-grown luminescence

In a second time, we compare the as-grown samples luminescence of the *shelled* NWs grown following the 3 conditions summarized in Table 2.3. Since these shelled NWs were grown at 400°C, their luminescence is compared to the emission of unshelled NWs also grown at 400°C (same as in Figure 2.27), as shown in Figure 2.28. The three shelled NWs samples present a NBE emission which is $\sim$ 1000 times more intense than the unshelled NW sample grown at 400°C and without deep-level emissions below 2.6 eV. Since a negligible deep-level emission is observed from the shelled NWs as-grown sample, we hypothesize that the ZnMgSe buffer layer deposited on top of the ZnSe buffer layer hinders the ZnSe deep-level emission.

The as-grown sample grown under condition 3 provides the strongest NBE signal compared to the other shell depositions (conditions 1 and 2) with a FWHM of 26 meV. This result is consistent with the previous SEM observations of the NWs, Figure 2.25. Indeed, the NWs with the best passivation (condition 3) have the largest shell radius 4.5 $\pm$ 1.5 nm (Table 2.3) compared to the NWs of conditions 1 and 2, which have shell radii of 2.5 and 2.0 $\pm$ 1 respectively. It seems that an effective passivation of the NWs occurs with a shell radius in the 2.5-4.5 nm range. This result highlights that very thin shell radii ($<$ 10 nm) can efficiently passivate the NWs. This results also agrees with a recently published study from our group [163] which concludes that a thin 7 nm AlGaAs shell deposited on GaAs NWs is sufficient to efficiently passivate the NWs.

The maximum NBE emission of the NWs grown under condition 3 is at 2.838 eV with a left shoulder around 2.806 eV. These lines cannot be easily labeled due the expected red-shift induced by the ZnMgSe shell strain on the ZnSe NW core (calculated in the next section).

However, we can notice that the NBE emission is above the $FX_{ZB}$ (2.800 eV [106]) which indicates that the main contribution of the PL originates from the ZnSe WZ phase ($FX_{WZ}$ expected at 2.851 eV [120]).

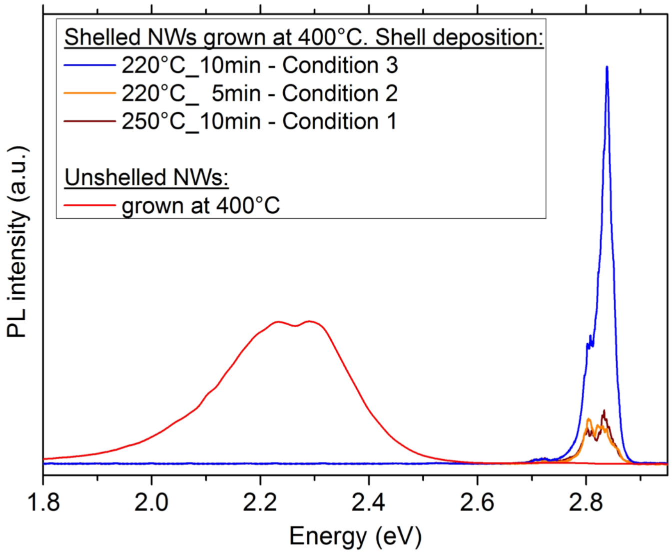

Figure 2.28: PL spectra of as-grown samples composed of ZnSe NWs grown at 400°C under Se-rich conditions and passivated with nominal $Zn_{0.83}Mg_{0.17}Se$ shells deposited the same day. These shells were deposited following the 3 conditions summarized in Table 2.3. The measurements were performed at 10 K with the same 405 nm laser excitation of 1 mW. These spectra are compared to the emission spectrum of unshelled NWs grown at 400°C.

These PL measurements on as-grown samples are practical ways to probe the samples luminescence but they also probe the ZnSe and ZnMgSe 2D layers growing in between the NWs which can bias the results. To get a more quantitative estimation of the shell passivation on the NWs luminescence, we carried out µPL measurements on single NWs.

### PL on single shelled and unshelled NWs

Since we are interested in a quantitative optical study of the NWs, they were gently deposited on patterned substrates and precisely located by SEM to carry out µPL on single NWs:

1. without a ZnMgSe shell (red curve magnified 100 times in Figure 2.29)
2. with a ZnMgSe shell (blue curve in Figure 2.29).

The unshelled NW emission intensity is very low and the peak is centered around 2.85 eV. An emission above the $FX_{WZ}$ is observed, up to approximately 2.875 eV. It can be attributed to a Burstein-Moss effect[4] [164] due to the high 880 µW laser excitation focused on the NWs

---

[4] During the Burstein-Moss effect, the energy of a semiconductor NBE increases when all states close to the conduction band are populated. The measured bandgap $E_{g-measured}$ is shifted from the bandgap $E_g$ according to: $E_{g-measured} = E_g + \Delta E$ with $\Delta E$ the Moss-Bustein shift.

(laser beam of 1 µm in diameter). Interestingly, the $FX_{ZB}$ emission is not visible; this suggests that the unshelled NW could be completely composed of the WZ phase.

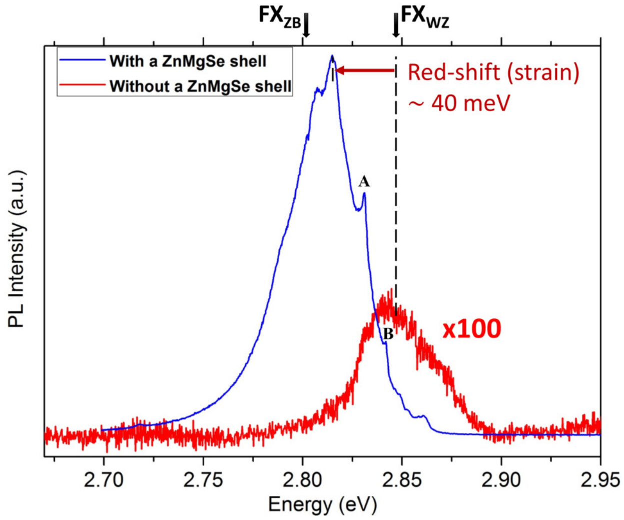

Figure 2.29: PL spectra of single ZnSe NWs grown at 400°C under Se-rich conditions with (red curve) and without (blue curve zoomed x100) a ZnMgSe passivating shell. The measurements were performed at 10 K with a 880 µW 405 nm laser diode excitation. The laser beam is focused down to 1 µm in diameter. The A and B labels show pics visible on the high energy part of the spectrum at 2.831 and 2.842 eV respectively).

Moreover, the shelled NW emission intensity is very strong. Indeed, we measure more than **two orders of magnitude of intensity enhancement thanks to the passivating shell**. The passivation is therefore very effective, even with a thin shell of 5 nm. This shelled NW emission shows a maximum at 2.815 eV. While the low energy side shows a smooth shape, several sharp peaks are observed at higher energies (for instance at 2.831 and 2.842 eV labeled A and B in Figure 2.29) and the highest energy peak is at 2.861 eV. These high energy sharp lines are very similar to the sharp lines observed on ZnSe doped with Te atoms, as displayed in Figure 2.30 taken from Ref.[165]. However, the sharp lines reported in this paper are below the expected ZB ZnSe free exciton energy of 2.800 eV. In our case, the highest energy peak at 2.861 eV is higher than the highest energy WZ ZnSe line at 2.851 eV reported by Liang and Yoffe [120] and hypothesized to be the free A exciton emission in the WZ phase.

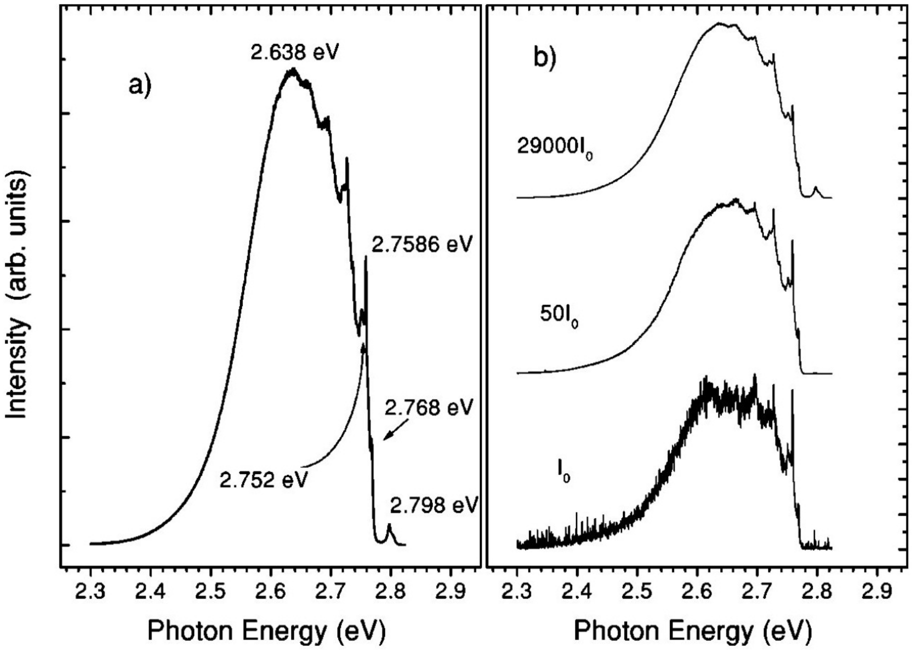

Figure 2.30: a) Low-temperature (10 K) PL from a $\delta$-ZnSe:Te sample; b) the same spectrum recorded at different excitation intensities (spectra arbitrarily shifted in vertical direction for convenience). Image taken from Ref.[165].

We can also note that the emission of the shelled NW is red-shifted compared to the unshelled NW by approximately 40 meV (by comparing the position of their maximum). Since ZnMgSe has a larger lattice constant than ZnSe (see Table 2.4), it induces a tensile strain in the NW core which is expected to shift the emission to longer wavelengths. David Ferrand and Joël Cibert from our group recently published an analytical procedure to calculate the shift of the exciton due to the strain in a core-shell NW [166]. The calculations are performed for the WZ and ZB crystal phases. As the strain coefficients of WZ ZnSe are not reported in the literature, we approximate our WZ ZnSe NWs grown along the [0001] c-axis by ZB ZnSe NWs grown along the [111] direction. For NWs grown along this direction, the exciton energy shift can be calculated according to the following formula [166]:

$$\Delta E_X = (a' + a)\frac{(c_{11} - c_{12} + 6c_{44})}{c_{11} + c_{12} + 2c_{44}}(\eta - 1)f \; - \; \frac{d}{\sqrt{3}}\frac{(c_{11} + 2c_{12})}{c_{11} + c_{12} + 2c_{44}}(1 - \eta)f \qquad (2.2.2)$$

with $c_{ij}$ the components of the stiffness tensor, $f$ the lattice mismatch between the core and the shell, $\eta$ the ratio of the core to NW cross-section areas (for a NW with a circular cross-section, $\eta = r_c^2/r_s^2$), $a'$ describing the coupling of the conduction electrons to strain and $a$, $b$, $d$ the coupling of holes (Bir-Pikus Hamiltonian [167]). From the Landolt and Bornstein database [49], we collected the following values summarized in Table 2.4.

| | $a'(eV)$ | $a(eV)$ | $b$ | $d$ | $c_{11}$ | $c_{12}$ | $c_{44}$ | $R_{c,s}$ | a (nm) |
|---|---|---|---|---|---|---|---|---|---|
| ZnSe | 5.93 | 1.97 | -1.2 | -3.81 | 82.6 | 49.8 | 40.8 | 6, 10 nm | 0.566 |
| MgSe | | | | | | | | | 0.589 |

Table 2.4: Summary of the strain shift coefficients used to calculate $\Delta E_X$.

Using our nominal Mg concentration of 17%, we obtain an energy red-shift around 50 meV. Despite the uncertainty on the values reported in Table 2.4 which varies from one report to another, this calculation is in good agreement with the observed red-shift of 40 meV.

### NW polarization in emission

Figure 2.31 displays the PL polarization in emission of three single ZnSe NWs with a ZnMgSe shell deposited at 220°C during 10 min (condition 3). In this figure, the x-axis origin at 0° corresponds to the polarizer axis parallel to NW axis. The figure shows that the NWs emission is maximum when the polarizer axis is perpendicular to the NW axis ($\theta = 90°$) - with NW polarization ratio ranging from 45 to 76% - as previously observed with tapered ZnSe NWs in section 2.1.3 and explained by the selection rules induced by the WZ phase. Therefore, this polarization behavior further confirms the presence of the WZ crystal phase within our NWs.

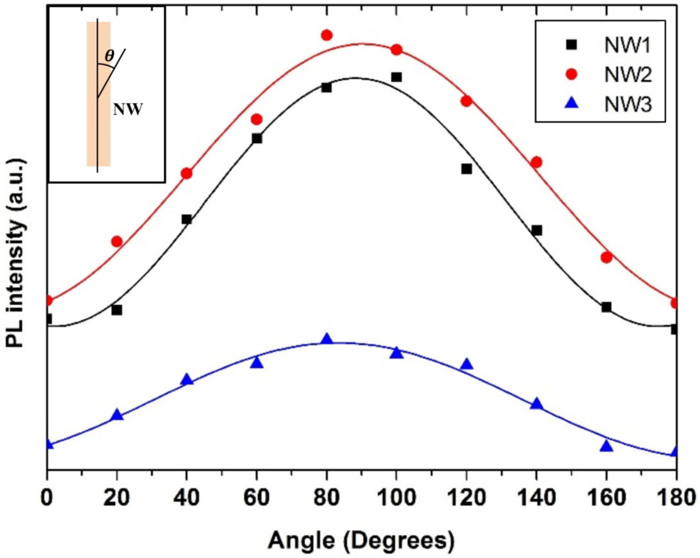

Figure 2.31: Dependence of the PL intensity of three ZnSe NWs on the angle $\theta$, between the NW axis and the direction of the linear polarization of the emitted light (sketched in the top-left inset). The x-axis origin at 0° corresponds to the NWs axis. Circles: experimental points. Continuous line: Malus law fitting of the NW polarization.

**To summarize** the PL measurements on ZnSe NWs grown on a ZnSe buffer layer, we observed that a thin ZnMgSe shell (5 nm in radius) can very efficiently passivate a ZnSe NW and increase its luminescence by more than two orders of magnitude. This enhancement of the luminescence has also been measured on an ensemble of ZnSe NWs. First, it greatly improved the NBE to deep-level PL intensity ratio. In addition, the NBE emission from the passivated NWs can be more than 1000 times higher than the unshelled NWs. In addition, the NW polarization is perpendicular to the NWs axis - due to the selection rules induced by the WZ phase - and further confirms the presence of the WZ crystal phase within our NWs.

## 2.3 Conclusion of the chapter

To summarize this chapter, we first presented a combined structural and optical characterization of *ZnSe NWs grown on a GaAs(111)B substrate* at 300°C by MBE. TEM analyses reveal the presence of NWs with a pure WZ structure together with NWs presenting alternations of WZ and ZB phases. The NWs show an excellent optical quality, with a dominant NBE emission where the rarely reported ZnSe WZ free exciton line can be identified. The polarization of the emitted light is found perpendicular to the NW axis, in agreement with what is expected considering the dominant WZ structure. Moreover, single-NW CL images show a homogeneous radiative efficiency along the NW body despite the presence of mixed phase regions. Using TRPL, we revealed a type II band alignment between ZB and WZ ZnSe and deduced the conduction and valence band offsets to be 98 and 50 meV respectively. Then, we showed that tapered NWs are not well suited for single CdSe insertions and therefore room temperature single-photon emission.

In a second step, we worked on the growth of *ZnSe NWs on ZnSe buffer layers* prior to insert a single CdSe QD within the NWs (which will be presented in Chapter 3). While the ZnSe(111)A surface orientation was unfavorable to grow straight and vertical NWs, we determined the most favorable growth conditions with a temperature and a nominal-growth-speed-ratio study on the ZnSe(111)B surface: a growth at 400°C under Se-rich conditions. Then, by covering these NWs with a higher bandgap semiconductor material ZnMgSe, we increased the luminescence of single-NWs by more than two orders of magnitude. The measured polarization perpendicular to the NWs axis further confirms that these ZnSe NWs are composed of a highly crystalline WZ phase, as explained by the selection rules.

The growth of vertically oriented ZnSe NWs presented in this Chapter is a determinant basis prior to inserting single and bright CdSe insertions. The study of such CdSe insertions is the subject of the next Chapter.

## Chapter 3

# CdSe quantum dots inserted in ZnSe nanowires: growth and characterization

## Contents

This chapter deals with the growth, the structural/chemical characterization and optical investigations of CdSe QDs inserted in ZnSe NWs. **We show for the first time the possibility to insert CdSe NW-QDs in ZnSe NWs grown on the (111)B surface orientation.** The growth mechanism of the three NW-QDs samples that yielded most of the results of this manuscript is described. Due to the very thin dimensions of the NW-QDs, each characterization represents a challenge in itself and needs to be pushed to its limits. In this Chapter, we present a complementary structural and composition study carried out by TEM and EDX on single NW-QDs. Another composition analysis, called atom probe tomography is introduced, along with corresponding preliminary results on CdSe SK-QDs to prepare the observation of single NW-QDs. Finally, we probe the excitons dynamics in the QDs by studying the decay-time of single NW-QDs up to room temperature.

## 3.1 Growth of the ZnSe-CdSe NW-QDs

### 3.1.1 Issues related to the QD insertions

In Part 1.3.1, the NW growth process has been described. To grow a ZnSe NW, individual fluxes of Zn and Se are sent onto the sample's surface and a priori, it seems that by just changing the Zn flux by a Cd flux, a CdSe QD can be grown. However, the growth process is not that simple and several questions arises, for instance:

- Will a CdSe QD grow in the ZnSe NW?
- How much time is needed to initiate the grow of the CdSe QD (incubation time [168])?
- Is the QD growth time linear and the same as the NW?
- Will the NW/QD interface be very diffuse or abrupt?
- Will the QD growth continue along the NW growth axis or in another growth direction, creating a kinked NW [169]?

In this Chapter, we show for the first time the possibility to insert CdSe NW-QDs in ZnSe NWs grown on the (111)B surface orientation. To do so, two different growth procedures were followed for the CdSe insertions. After the growth of the ZnSe NW:

1. Both Zn and Se fluxes were interrupted for 30 s to consume the Zn atoms present in the gold catalyst before the CdSe insertion. The aim is to reduce the amount of Zn atoms in the gold catalyst during the CdSe insertion to sharpen the NW/QD interface. After this growth interruption, the Cd and Se fluxes were sent for 10 or 20 s to grow the CdSe QD, followed by the interruption of the Cd and Se fluxes for 20 s. The aim of this second growth interruption is also to consume the Cd present in the gold catalyst before the regrowth of the ZnSe NW, to sharpen the QD-NW interface. *Since no fluxes are sent before and after the CdSe insertion, the samples using this QD growth procedure will be said to be grown* ***under vacuum****.*

2. Instead of interrupting the Zn and Se fluxes, only the Zn flux was interrupted with a remaining Se flux. The aim is to better consume the Zn atoms present in the gold catalyst to get a sharper interface and to remain closer from the catalyst supersaturation. Therefore, when the Cd flux is sent for 10 s, the CdSe QD is expected to grow faster compared to the previous QD growth condition 1. Then, only the Cd flux is interrupted (with a remaining Se flux). The goal is also to better consume the Cd atoms present in the gold catalyst to sharpen the QD-NW interface. This technique of sending a constant flux (Se) and to alternate the other flux (Zn and Cd) is called Migrated Enhanced Epitaxy (MEE) [170]. *Since a Se flux is sent before and after the CdSe insertion, the sample using this QD growth procedure will be said to be grown* ***under Se****.*

Prior to the CdSe insertion, the NW growth was performed like the ZnSe NWs grown on ZnSe buffer layers presented in Part 2.2: on GaAs(111)B with a ZnSe buffer layer, a thin 0.1 ML gold deposition and dewetting at 510°C. The NW growth was performed at 400°C under Se-rich conditions. As mentioned in the previous Chapter, to be reproducible the effusion cells were always calibrated by RHEED oscillations: the Zn and Se effusion cells were calibrated on a ZnTe(001) at 340°C (described in Part 2.2.2), while we used a CdTe(001) substrate at 280°C to calibrate the Mg (described in Part 2.2.7) and Cd cells. The calibration of the Cd growth speed was carried out by sending an additional flux of Te in excess, leading to a CdTe deposition - homoepitaxial and strain-free onto the CdTe(001) reference sample. For all the CdSe QDs, the Se:Cd nominal growth speed ratio was 2:1. The growth procedure of the three NW-QDs samples that yielded most of the results of this manuscript is described in the following.

### 3.1.2 Low density NW-QDs with a single QD: $S_{1QD}^{vacuum}$

The first sample is composed of a ZnSe NW with one CdSe QD inserted using the QD growth procedure 1 (under vacuum) and covered by a ZnMgSe shell. This sample is therefore labeled $\mathbf{S_{1QD}^{vacuum}}$. More precisely, simultaneous fluxes of Zn and Se were first sent for 15 minutes. Next, the fluxes were interrupted for 30 s. The Cd and Se fluxes were then sent during 20 s and suppressed for 20 s. The Zn and Se fluxes were sent back for an additional 5 minutes of ZnSe wire growth to cap the heterostructure. The temperature was later reduced from 400 to 220°C to deposit a $Zn_{0.83}Mg_{0.17}Se$ shell during 5 min. These NW-QDs have mean lengths and diameters of 550 nm and 20 nm respectively, and are visible in Figure 3.1. Note that the flag-like shape induced by the deposition of the ZnMgSe shell (see Part 2.2.7) is visible at the NWs apex. Figure 3.2 summarizes the $S_{1QD}^{vacuum}$ growth conditions.

The gold deposition of 30 s with an effusion cell temperature of 1090°C calibrated in Part 2.2.3 yields a NW density of 10 to 20 NWs per µm². This density is too high to probe individual NW-QDs directly at the surface of the as-grown sample. To reduce the NWs density, the gold deposition was reduced to 20 s using a gold effusion cell of 1080°C, corresponding to a reduction of the deposited quantity of Au from 0.1 to 0.06 ML (see Part 2.2.3) and less than 4 NWs per µm². This NW density is sufficiently low to probe individual

NW-QDs on the as-grown sample, which will later be studied in Chapter 4, Part 4.2.2 to create photonic wires.

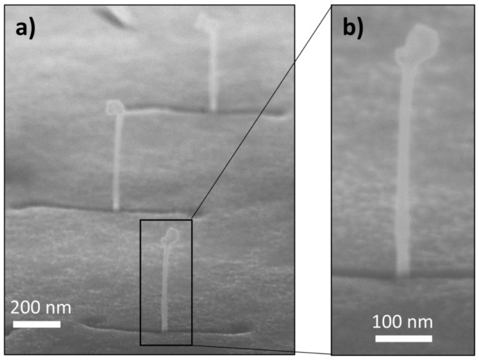

Figure 3.1: Tilted-view SEM images (65°) of $S_{1QD}^{vacuum}$: a) ensemble and b) zoom on a single ZnSe NW with one CdSe QD insertion (20 s) grown at 400°C under Se-rich conditions, a nominal $Zn_{0.83}Mg_{0.17}Se$ shell deposited during 5 min at 220°C (gold deposition of 20 s at 1080°C). The reduction of the NW-QDs density can be clearly observed compared to the previously studied as-grown samples.

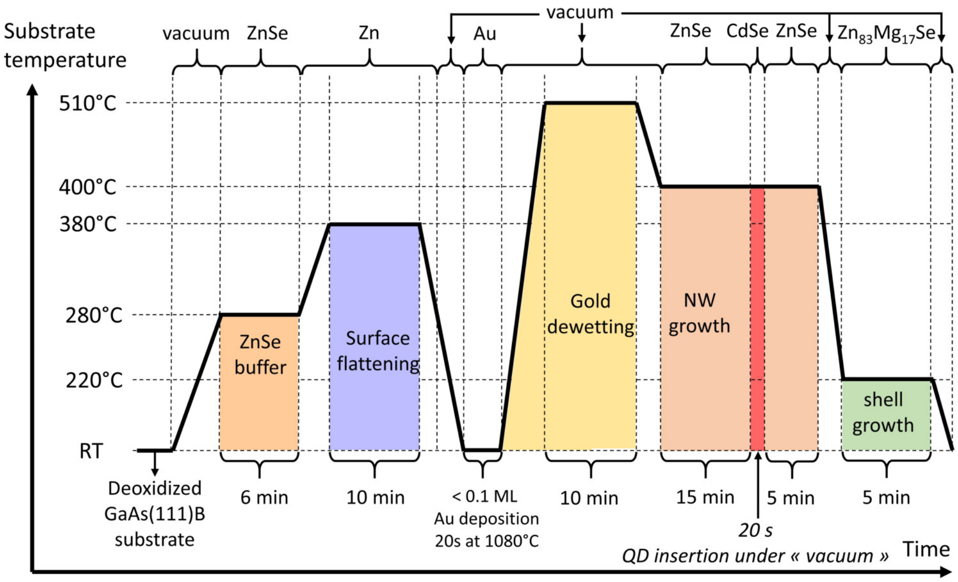

Figure 3.2: Illustration of the growth process of $S_{1QD}^{vacuum}$: ZnSe NWs with one CdSe QD insertion (20 s under vacuum) grown at 400°C under Se-rich conditions and a nominal $Zn_{0.83}Mg_{0.17}Se$ shell deposited during 5 min at 220°C. The gold deposition was reduced from 30 s at 1090°C to 20 s at 1080°C to reduce the NW-QDs density and probe individually single NW-QDs by µPL.

Due to a restricted access to TEM characterizations, this sample $S_{1QD}^{vacuum}$ will not be studied by TEM, to the contrary of the next two samples.

### 3.1.3 Two CdSe QDs in the same ZnSe NW: $S_{2QDs}^{vacuum}$

In a second time, we wanted to test the possibility to insert two QDs of different size in the same NW. The aim is to study the possibility to modify the QD aspect ratio, useful to modify the QD dipole orientation and couple the NW-QDs to photonic structures (see Chapter 4). Two CdSe insertions were grown during 10 and 20 s under vacuum (QD growth condition 1) and the sample is therefore labeled $S_{2QDs}^{vacuum}$. After 13 minutes of ZnSe growth, the first QD was inserted using the shortest time of 10 s to minimize the time spent for the insertion and reduce the probability of the QD to kink [169]. Then we grew approximately 60 nm of ZnSe NW (during 1 min 40 s) prior to the insertion of the second QD during 20 s. Then, we sent the Zn and Se fluxes for an additional 6 minutes to cap the second CdSe QD. The aim is to keep the same total time of ZnSe NW growth for $S_{2QDs}^{vacuum}$ and the sample presented in the next Part called $S_{1QD}^{Se}$. Next, a nominal $Zn_{0.90}Mg_{0.10}Se$ shell was deposited during 10 minutes at 220°C.

In comparison to the previously studied cylindrical ZnSe NWs and the sample $S_{1QD}^{vacuum}$ (nominal Mg content of 17%), the shell was composed of 10% of Mg to reduce the lattice mismatch between the ZnSe core and the ZnMgSe shell and therefore reduce the potential appearance of crystalline defects. To verify this nominal percentage of Mg, we carried out PL on the as-grown sample with a 405 nm (3.06 eV) laser and observed a clear emission at 2.91 eV (426 nm) attributed to the ZnMgSe NBE emission, as displayed in Figure 3.3.

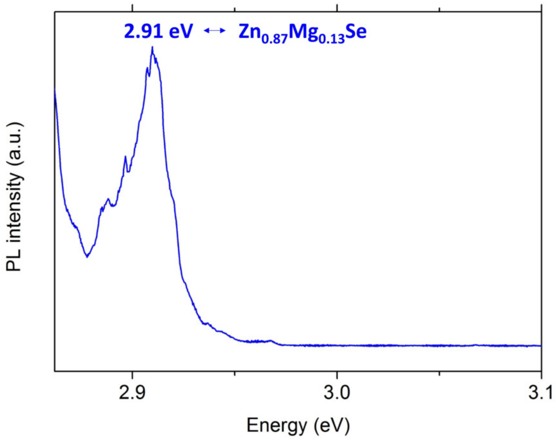

Figure 3.3: MacroPL spectra of the as-grown sample composed of ZnSe NWs passivated with a nominal $Zn_{0.90}Mg_{0.10}Se$ shell. The measurements were performed at 10 K with a 120 µW 405 nm laser diode excitation. The highest peak at 2.91 eV is attributed to the ZnMgSe NBE emission and is used to estimate the Mg concentration within the $Zn_{1-x}Mg_xSe$ shell. The estimation yields 13% of Mg, close to the nominal 10% calibrated during the growth.

Using the same bandgap calculation than in Part 2.2.7 (previous Chapter), our estimation yields 13% of Mg with the ZnMgSe alloy, which is in good agreement with the 10% calibrated and consistent with the 3% Mg uncertainty calculated in the Previous Chapter. Figure 3.4 details the whole growth process of $S_{2QDs}^{vacuum}$.

Figure 3.5 provides an overview and a zoom on a single NW-QD. The vertically oriented NW-QDs are straight despite the two CdSe QDs which could have induced kinks. Two types of straight NW-QDs can be observed: vertically oriented and tilted, with in between NW-QDs with a hindered growth. The tilted NW-QDs display thicker shell thicknesses (50 to 70 nm); their lateral surfaces are more exposed to the MBE fluxes compared to the vertically oriented NW-QDs (mean diameter of 30 nm with some modulations). In addition, due to their different crystalline orientation (they grow in a different direction compared to the vertically oriented NW-QDs) and possibly their different crystalline phase, their sidewalls surface energy might be lower, easing the adatoms radial deposition. This diameter difference is a way to distinguish both NW-QDs orientations. During structural (TEM) or optical (µPL) characterization techniques, the NW-QDs will be mechanically deposited onto patterned substrates. Since we are interested in the vertically oriented NWs, we will analyze 30 nm-diameter NW-QDs.

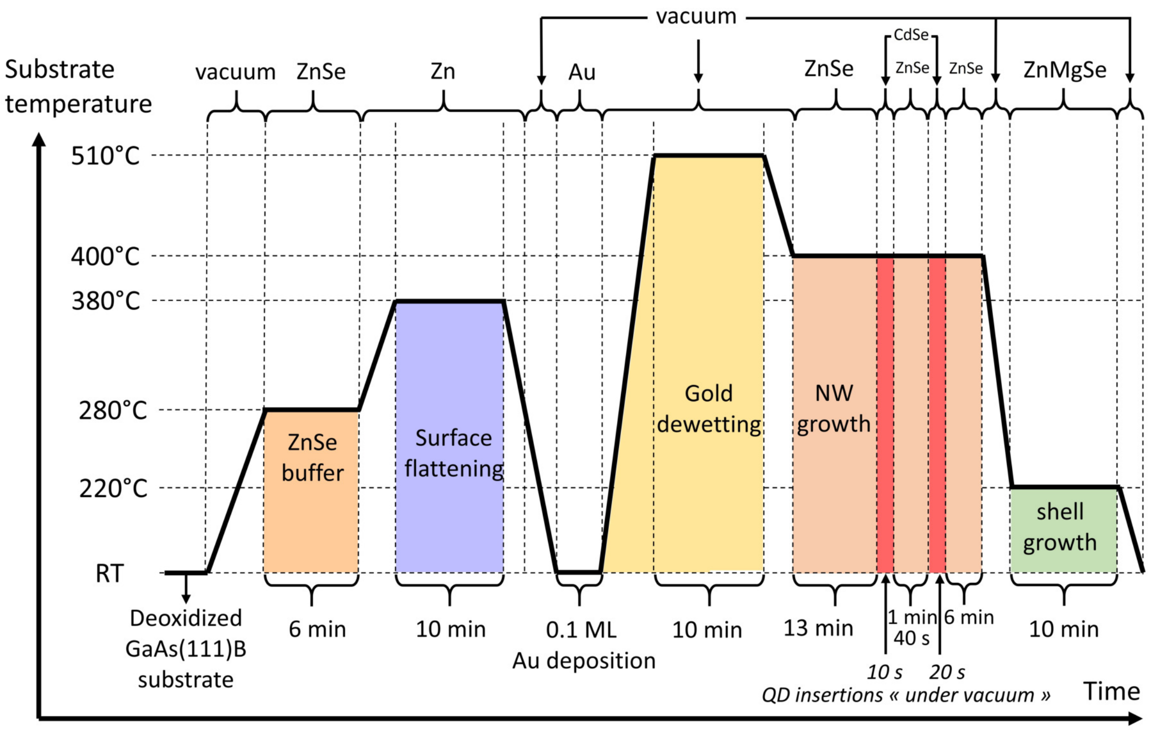

Figure 3.4: Illustration of the growth process of $S_{2QDs}^{vacuum}$: ZnSe NWs with two CdSe QD insertions of 10 and 20 s grown at 400°C under Se-rich conditions and a nominal $Zn_{0.90}Mg_{0.10}Se$ shell deposited during 10 min at 220°C.

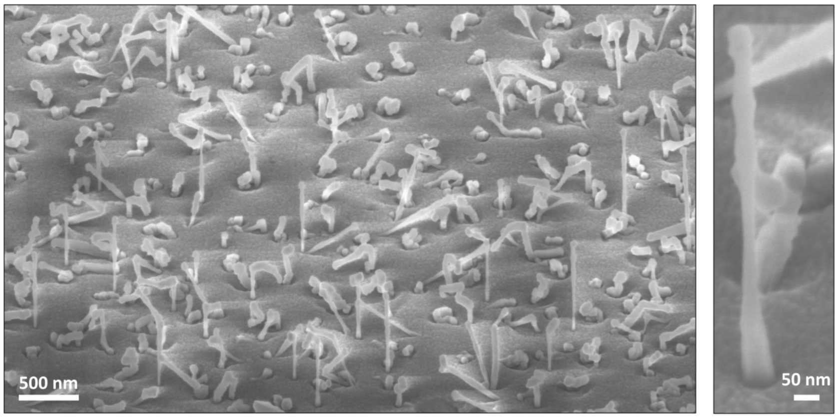

Figure 3.5: Tilted-view SEM images (65°) of $S_{2QDs}^{vacuum}$: ZnSe NWs with two CdSe QD insertions (10 and 20 s) grown at 400°C under Se-rich conditions and a nominal $Zn_{0.90}Mg_{0.10}Se$ shell deposited during 10 min at 220°C. Left: ensemble, and right: zoom on a single NW-QD.

### 3.1.4 Single CdSe QD in a ZnSe NW with Se flux: $S_{1QD}^{Se}$

Finally, the last sample we present is composed of one CdSe QD inserted during 10 s under Se (QD growth condition 2) and is called $\mathbf{S_{1QD}^{Se}}$. The aim of this sample is to study the effect of the remaining Se flux during the QD insertion on the QD aspect ratio. The first ZnSe NW part was grown during 15 and 5 min before and after the CdSe QD respectively. Then, the temperature was decreased to 220°C to deposit a $Zn_{0.90}Mg_{0.10}Se$ shell during 10 minutes. The whole growth process of $S_{1QD}^{Se}$ is summarized in Figure 3.6.

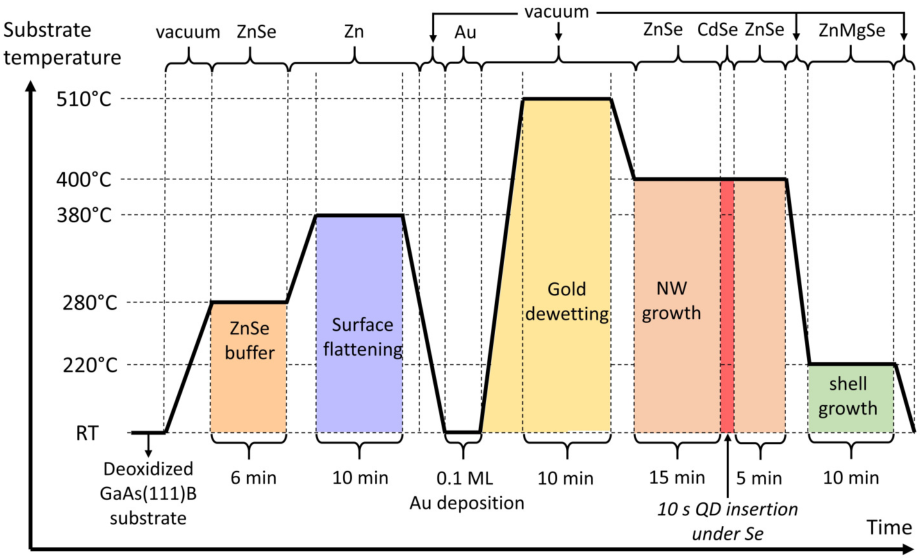

Figure 3.6: Illustration of the growth process of $S_{1QD}^{Se}$: ZnSe NWs with one CdSe QD insertion (10 s) grown at 400°C under Se-rich conditions and a nominal $Zn_{0.90}Mg_{0.10}Se$ shell deposited during 10 min at 220°C.

Figure 3.7 shows an overview and a zoom on single (vertically oriented and tilted) NW-QD from $S_{1QD}^{Se}$. Despite the presence of the QD, the vertically oriented NW-QDs also remained straight during their growth. The same remarks mentioned for $S_{2QDs}^{vacuum}$ concerning the tilted and vertically oriented NW-QDs hold for this sample: we will characterize the vertically oriented 30 nm-diameter NW-QDs. The height and diameter of vertically oriented NW-QDs for both $S_{2QDs}^{vacuum}$ and $S_{1QD}^{Se}$ are summarized in Table 3.1. Notice that they are very similar due to their similar growth conditions for the ZnSe growth time and the ZnMgSe shell deposition.

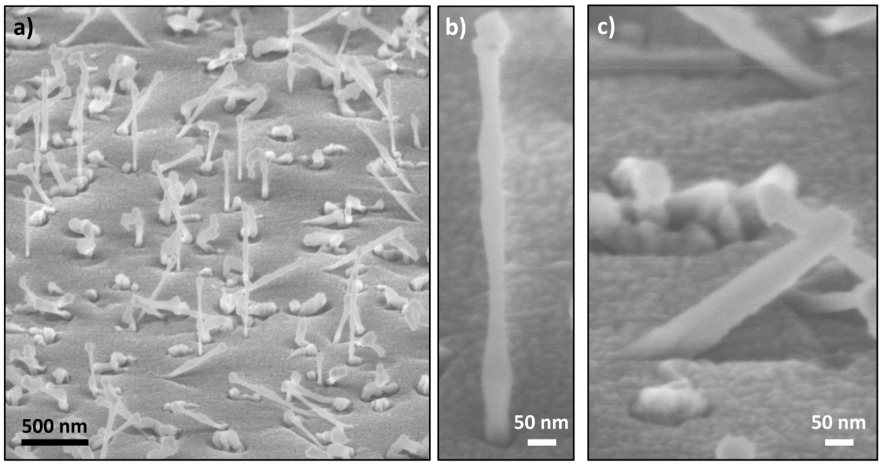

Figure 3.7: Tilted-view SEM images (65°) of $S_{1QD}^{Se}$: ZnSe NWs with one CdSe QD insertion (10 s) grown at 400°C under Se-rich conditions and a nominal $Zn_{0.90}Mg_{0.10}Se$ shell deposited during 10 min at 220°C. a) Ensemble, b) vertically oriented and c) tilted NW-QDs.

| | $S_{2QDs}^{vacuum}$ | $S_{1QD}^{Se}$ |
|---|---|---|
| Height (nm) | $700 \pm 60$ nm | $710 \pm 50$ nm |
| mean diameter (nm) | $31 \pm 3$ nm | $32 \pm 3$ nm |

Table 3.1: Statistics on the height and diameter of the vertically oriented NWs from $S_{2QDs}^{vacuum}$ and $S_{1QD}^{Se}$.

## 3.2 Structural characterizations

To access the crystallinity of $S_{2QDs}^{vacuum}$ and $S_{1QD}^{Se}$ and study the effect of the two QD growth conditions (under vacuum and Se), TEM characterizations have been carried out with a FEI Tecnai operated at 200 kV. Prior to the TEM characterization, the NW-QDs have been carefully deposited on TEM grids and these TEM measurements have been performed by Catherine Bougerol from the NPSC group.

### 3.2.1 Structural characterization of NWs from $S_{2QDs}^{vacuum}$

#### QD identification

Figure 3.8 displays the TEM image of a single NW-QDs from $S_{2QDs}^{vacuum}$. Along the NW-QD axis, two darker zones are visible, separated by 60 nm. These two zones could be attributed to crystal phase insertions (for instance, ZB insertions in a WZ NW) or to the CdSe QDs.

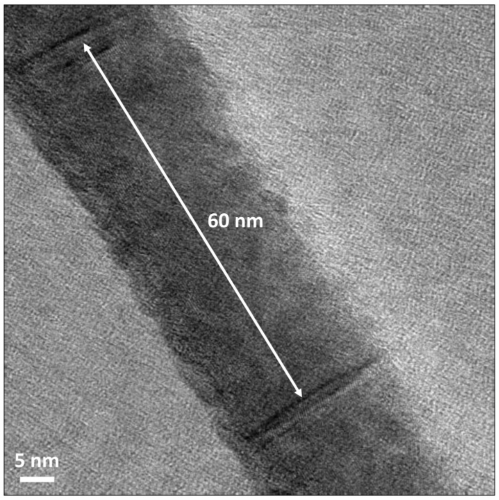

Figure 3.8: TEM image of a single ZnSe NW from $S_{2QDs}^{vacuum}$ with two darker zones attributed to two CdSe insertions. These insertions are very thin (2 to 3 nm along the NW axis while the NW-QD is 29 nm large) and separated by 60 nm.

To clarify this issue, Figure 3.9a presents a zoom on one darker zone of the NW-QD presented in Figure 3.8. The inset shows the corresponding Fast-Fourier Transform (FFT) which displays WZ diffraction spots (the WZ ZnSe NWs), confirming that these ZnSe NWs are composed of the WZ phase, as already seen with the RHEED patterns in Part 2.2.7. Then, a Geometrical Phase Analysis (GPA) was carried out: from high resolution images, this analysis carried out in the Fourier space enables to get the variation of a given interreticular distance $d_{hkil}$ (corresponding to a selected diffraction spot in FFT) over the image with respect to a chosen reference region (central part of the NW in our case).

Figure 3.9b shows the $d_{0002}$ (along the NW axis) map associated to Figure 3.9a. While the lattice parameter is quite constant along the NW axis (green area), the darker insertion displays a higher lattice parameter highlighted in red. To better visualize this change of lattice parameter, a profile along the growth axis has been extracted (see Figure 3.9c), integrated over the white rectangle visible in Figure 3.9b. In this Figure, we can clearly see an increase of the lattice parameter at the position of the insertion. This result permits to dismiss the possibility that this insertion corresponds to ZB ZnSe, since in this case no difference of lattice parameters would have been measured (equivalent ZB(111) and WZ(0002) interatomic distances). Moreover, since the lattice parameter of CdSe is higher than ZnSe, this observed insertion is attributed to the CdSe QDs.

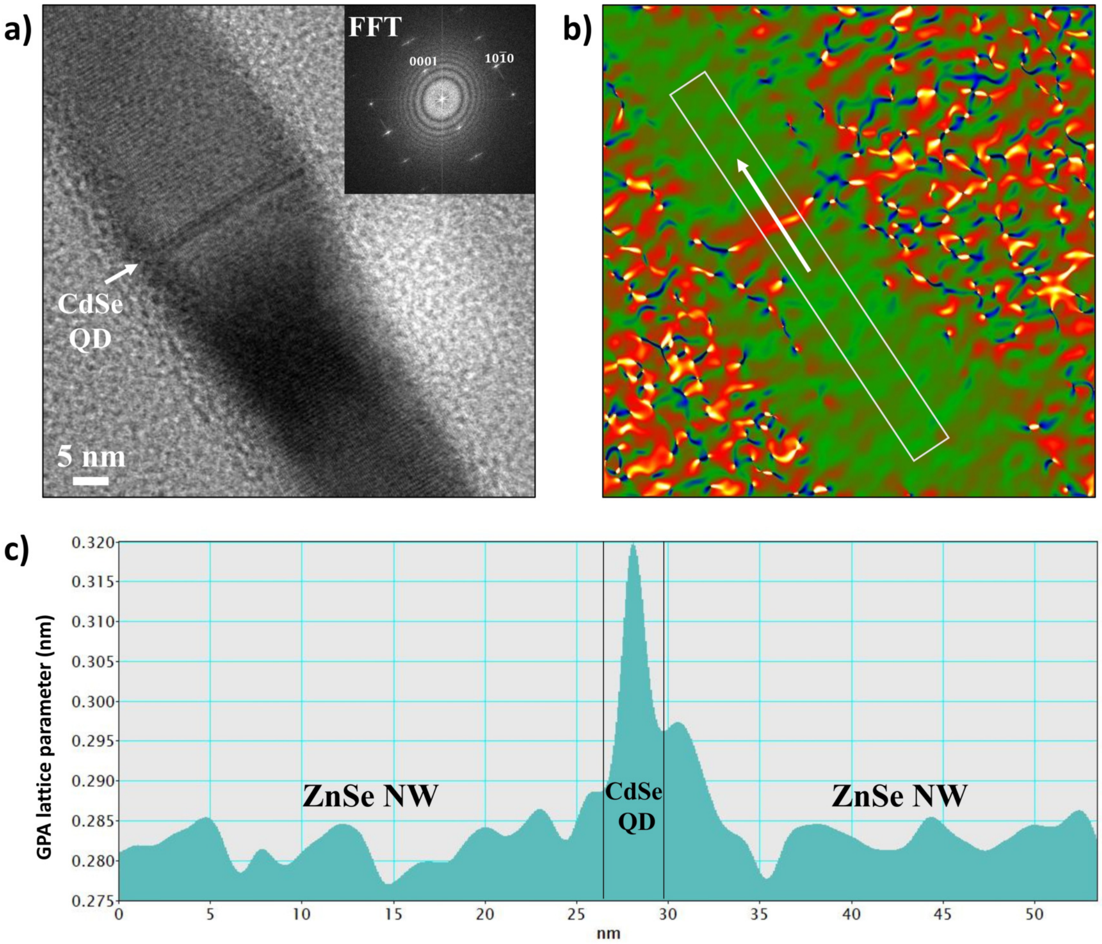

Figure 3.9: a) TEM image: zoom on the CdSe QD of a WZ ZnSe NW from $S_{2QDs}^{vacuum}$. The corresponding FFT is displayed in the inset. b) GPA analysis along the NW growth direction of the same TEM image. The NW central part has been taken as a reference. A lattice parameter profile (integrated over the white rectangle) along the growth axis has been extracted and is visible in c). In this latter figure, a section with a higher lattice parameter is visible and is attributed to a CdSe insertion.

In this sample, the separation between the two CdSe QDs is expected[1] to be around 57 nm, which is in good agreement with what is observed on Figure 3.8. Unexpectedly, the two CdSe QDs are very thin with similar thicknesses from 2 to 3 nm, even though a significant difference would have been expected since one QD has been grown during 10 s and the other one during 20 s. Moreover, these two CdSe QDs can be used as markers to calculate the ZnSe NW growth speed of 0.6 nm/s. If the CdSe QDs growth speed was similar, QD sizes of 6 and 12 nm would have been expected, larger than the observed 2-3 nm.

---

[1] Total growth of 1246 s for a 700 nm long NW-QD and 101 s of ZnSe insertion in between the CdSe insertions.

### Shell identification

From the same TEM image (Figure 3.9a), a lattice mismatch (defined as $\frac{d-d_{NW\,core}}{d_{NW\,core}}$) map is extracted, visible in Figure 3.10b. On this map, the NW core has been taken as a reference (from the image) and a small color difference is visible between the NW core and its shell. To further analyze the radial NW profile, the variation of the mismatch across the NW (along the $[10\bar{1}0]$ direction) is shown in Figure 3.10c (integrated over the white rectangle visible in Figure 3.10b). It reveals a core-shell type structure composed of a 10 nm core surrounded by an approximately 9 nm shell. This result agrees with the mean diameter of the NW-QDs from $\mathrm{S}_{\mathrm{2QDs}}^{\mathrm{vacuum}}$ observed by SEM, 31 ± 3 nm as displayed in Table 3.1 on page 90.

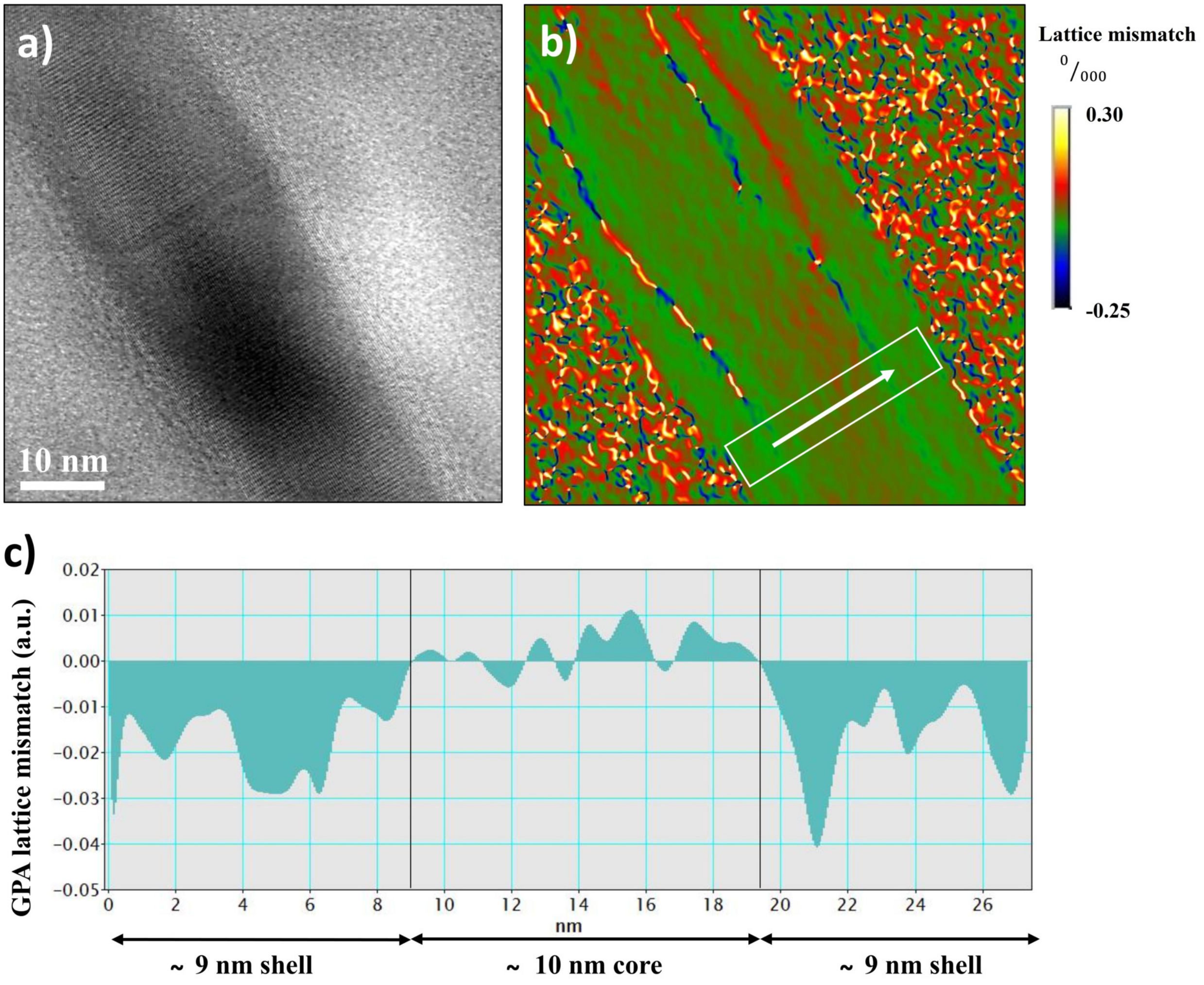

Figure 3.10: a) TEM image: zoom on the NW-QD displayed in Figure 3.9. b) Corresponding lattice mismatch map. The core of the NW has been taken as a reference. A GPA radial profile across the NW (along the $[10\bar{1}0]$ direction and integrated over the white rectangle) has been extracted and is visible on c). A 10 nm core surrounded by an approximately 9 nm shell is visible.

We can also notice in Figure 3.10c the negative mismatch at the shell position. This result is in disagreement with the literature since the lattice parameter of WZ MgSe [171] (a = 0.4145 nm and c = 0.6723 nm) is expected to be higher than WZ ZnSe (a = 0.3996 nm et c = 0.6626 nm). This result should be cautiously analyzed since the WZ phase is a metastable MgSe and ZnSe phase and very few reports of their WZ lattice parameters are available. This negative lattice mismatch could result from an oxidation of the ZnMgSe shell during the TEM measurements, leading to a ZnMgSe/ZnO alloy of reduced lattice parameter[2]. Moreover, a significant change in the ionic polarization (observed for instance during a Mg incorporation in WZ ZnO crystals [172]) between the WZ ZnSe core and the ZnMgSe shell could play a role on this negative lattice mismatch. Further investigations need to be carried out to clarify if this observation is induced by the TEM observation or is representative of the real ZnSe/ZnMgSe lattice mismatch.

### Gold droplet identification

During this TEM investigation, the gold droplet used to catalyze the NW-QD growth has been observed, as displayed in Figure 3.11. Figure 3.11a shows the top part of a NW-QD which has a *flag-like* shape (as already shown in Figure 2.25) and is clearly visible on the top part of the NW-QDs, for instance in Figures 3.5 and 3.7. This flag-like shape is only visible after the ZnMgSe shell deposition and the gold droplet is located at its end. Consequently, we conjecture that during the ZnMgSe deposition, the gold droplet continues to catalyze a ZnMgSe NW growth in a worm-like shape. Figure 3.11b is a zoom on the gold droplet. Its facets can be clearly observed and it has a 10 nm-diameter, in agreement with the 10 nm-diameter ZnSe core of NW-QDs (since the ZnSe NW diameter is fixed by the gold droplet diameter).

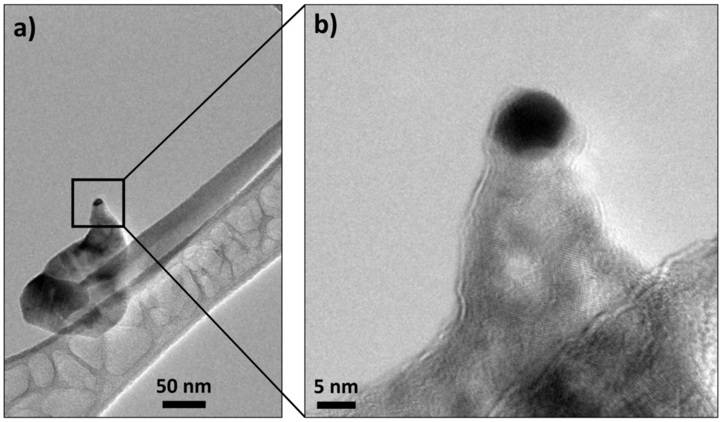

Figure 3.11: TEM image of a) the top part of a NW-QD which has a typical *flag-like* shape and a distinctly visible gold droplet at its end. b) Zoom on the gold droplet. It shows clear facets and a 10 nm-diameter which is in agreement with the 10 nm-diameter ZnSe core of the NW-QDs, since the gold droplet fixes the ZnSe NW diameter.

---

[2] WZ ZnO: a = 0.325 nm et c = 0.52 nm, smaller than the WZ ZnSe lattice parameters

### Tilted-NW identification

A thicker 70 nm-diameter NW was also studied, as shown in Figure 3.12a. Figure 3.12b provides a zoom on this NW-QD and Figure 3.12c shows the corresponding FFT. This FFT indicates that the NW is composed of WZ ZnSe and is oriented along the $[01\bar{1}1]$ axis, to the contrary of vertically oriented NW-QDs, oriented along the c-[0001] axis (62° difference). This result indicates that this thicker NW was tilted on the as-grown sample and that our diameter-based method to discriminate the tilted from the vertically oriented NWs is relevant.

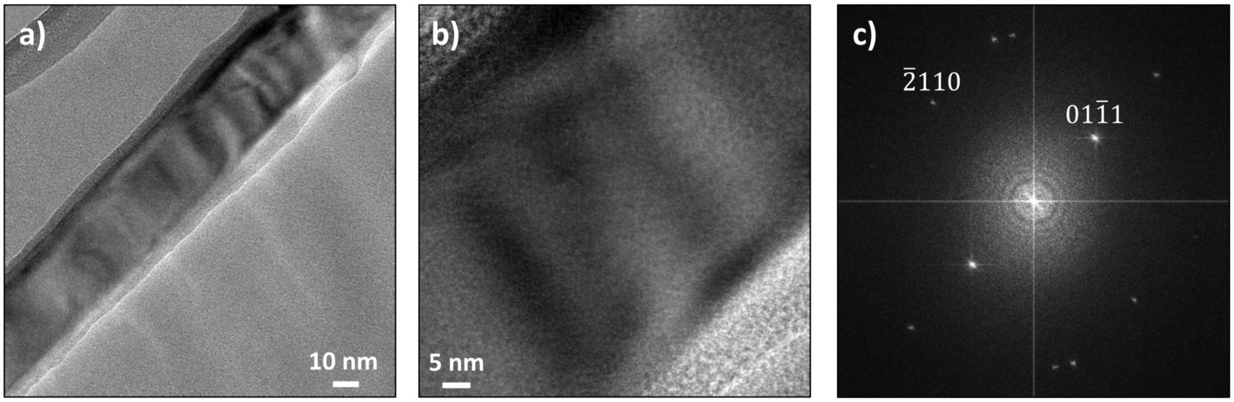

Figure 3.12: a) TEM image of a single NW-QD tilted on the as-grown sample and recognizable by its 70 nm-diameter (30 nm-mean-diameter for vertically oriented NW-QDs). b) Zoom on the same NW-QD and c) corresponding FFT. The FFT indicates that the NW is composed of the WZ phase grown along the $[01\bar{1}1]$ axis direction, to the contrary of vertically oriented NW-QDs which are oriented along the c-[0001] axis.

## 3.2.2 Structural characterization of NWs from $S_{1QD}^{Se}$: effect of the Se flux

### QD size

The structure of NWs from $S_{1QD}^{Se}$ (CdSe insertion grown under a Se flux) has also been characterized by TEM. Figure 3.13a shows a NW-QD with a darker zone along the NW axis. This darker zone is 9 nm-thick (along the NW axis) and at its position, the NW diameter is 50 nm. The tip of this NW-QD (shown in Figure 3.13b) is 30 nm in diameter, confirming that this NW was vertically oriented on the as-grown sample. The corresponding FFTs of both Figures 3.13a and b are visible in Figures 3.13c and d respectively. When the FFT is carried out on both the ZnSe NW and the darker zone (Figure 3.13a), WZ and ZB diffraction spots are clearly visible (Figure 3.13c). On the other hand, when the FFT is only carried out on the ZnSe NW (Figure 3.13b), only the WZ phase diffraction spots are visible (Figure 3.13d).

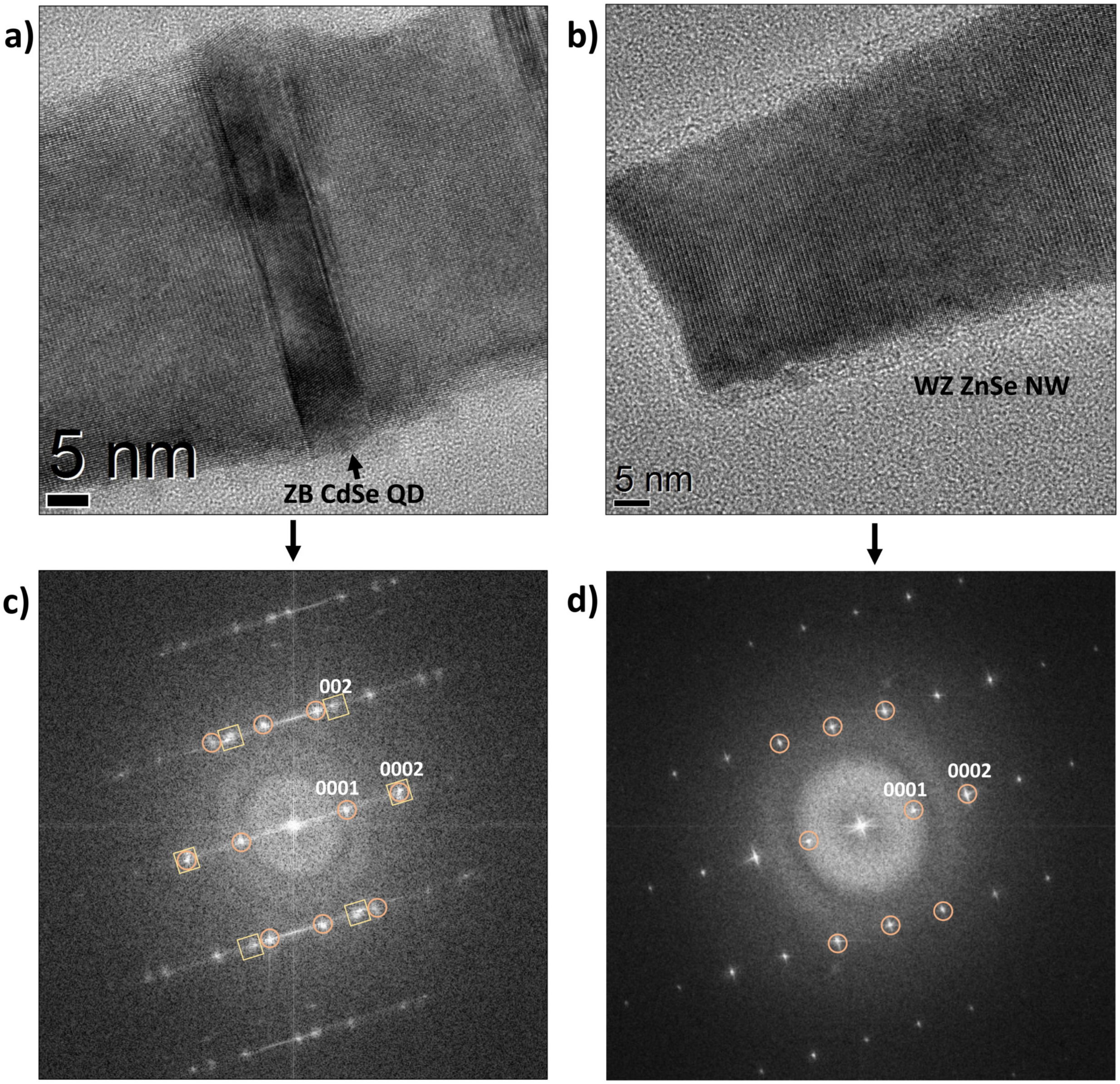

Figure 3.13: a) TEM image of a ZB CdSe QD in a WZ ZnSe NW. b) TEM image of the same NW-QD taken at the apex. c) Fast-Fourier Transforms (FFTs) of the NW-QD displayed in a). The main WZ and ZB diffraction spots are highlighted by orange circles and yellow squares respectively. d) FFT of Figure b), showing only WZ diffraction spots.

On this image, a GPA analysis could not be performed due to the presence of defects at the bottom and top of the darker zone. To further analyze this darker zone, we compared the interatomic distances of ZB(111) and WZ(0002). As previously mentioned, in a WZ ZnSe NW with ZB ZnSe insertions, the ZB(111) and WZ(0002) interatomic distances are equivalent (see the indexation in Figure 3.13c) and no difference between them should be noticed. However, if this observed ZB(111) part has a larger lattice parameter, it could correspond to a CdSe insertion, which can be verified quantitatively. For this comparison, we applied a mask to only reveal the spots of interest in Figure 3.13c, carried out an inverse Fourier transform and measured the corresponding interatomic distance over 20 periods to maximize the measure accuracy. The experimentally measured ZB(111)/WZ(0002) ratio is 1.044 for a 1.053 ratio[3] expected between a WZ ZnSe NW and a ZB CdSe QD[4]. With a relative difference of 0.82%, these results are in fairly good agreement and we attribute this darker zone to a CdSe QD. This measurement has been carried out in the core part of the NW-QD to minimize the ZnMgSe shell contribution.

In this sample $\mathrm{S}_{\mathrm{1QD}}^{\mathrm{Se}}$, the QD insertion is thicker (9 nm) than the QDs observed for $\mathrm{S}_{\mathrm{2QDs}}^{\mathrm{vacuum}}$ (2-3 nm). This difference can be explained by the two distinct QD growth processes:

- for $\mathrm{S}_{\mathrm{2QDs}}^{\mathrm{vacuum}}$, the Zn and Se fluxes were interrupted before the CdSe insertion. During this interruption, the Au catalyst will consume its atomic elements (Zn and Se atoms) and go off the supersaturation needed for the growth. When the Cd and Se fluxes are sent, a delay time (incubation time) is required for the Au catalyst to reach again the supersaturation and catalyze the CdSe QD growth, resulting in **flat QDs along the NW axis**. Notice that such a flat QD shape is favorable to induce a *radial dipole orientation* (see Part 1.2.4).

- for $\mathrm{S}_{\mathrm{1QD}}^{\mathrm{Se}}$, the Se flux remains before the CdSe insertion. Our results suggest that this remaining flux permits to keep the Au catalyst in (or close to) the supersaturation regime. In this case, when the Cd flux is sent, the QD growth can directly start without delay time, resulting in a **longer QD along the NW axis**. Notice that this longer QD shape is favorable to induce a *longitudinal dipole orientation* if the QD height is large enough to be close to or exceed a QD aspect ratio of 1.

Note that for the TEM measurements, the QD size along the NW axis is very accurate, but its radial size is more difficult to quantify due to the presence of the shell. A more accurate radial measurement of the QD diameter will be later presented from the EDX analysis in Part 3.3.1. In addition, notice the crystalline relation between the ZnSe NW core and the ZnMgSe shell in Figure 3.13a and b. This is an indication that the shell is in epitaxial relation with the NW, which is expected and has been reported for instance in the case of Si-Ge heterostructures [173].

### QD crystal structure

Interestingly, these results obtained from Figure 3.13 indicate that the CdSe QD is composed of the ZB phase. These results contrast with the stable crystal phases of ZnSe and CdSe which are ZB and WZ respectively. Such a change of crystal structure could be explained by the nanometric size of the NW-QD. In a theoretical paper, Akiyama et *al.* [11] demonstrated that

---

[3] $a_{\mathrm{ZnSe\_WZ}}$: 3.996 $\mathring{A}$, $c_{\mathrm{ZnSe\_WZ}}$: 6.626 $\mathring{A}$ -> $d_{\mathrm{ZnSe\_WZ\_(0002)}}$: 3.313 $\mathring{A}$. In addition, $a_{\mathrm{CdSe\_ZB}}$: 6.04 $\mathring{A}$ -> $d_{\mathrm{CdSe\_ZB\_(111)}}$: 3.487 $\mathring{A}$. Finally, $\frac{d_{CdSe\,ZB\,(111)}}{d_{ZnSe\,WZ\,(0002)}} = 1.053$

[4] Note that if the ZB insertion would have correspond to a ZnSe ZB rotational twin, no difference of lattice parameter would have been observed.

when the diameter of a ZB ZnSe NW is reduced below 10 nm, the number of dangling bonds at the surface increases and the ZB phase becomes metastable. At this scale, the WZ phase becomes more favorable since it reduces the number of dangling bonds and two-coordinated atoms (see Figure 3.14a) compared to the ZB phase (Figure 3.14b). Since the NW-QDs growth involves a lot a parameters (see Part 1.3.1), such a change of crystal structure could also originate from the complex dynamic taking place during the MBE growth [174].

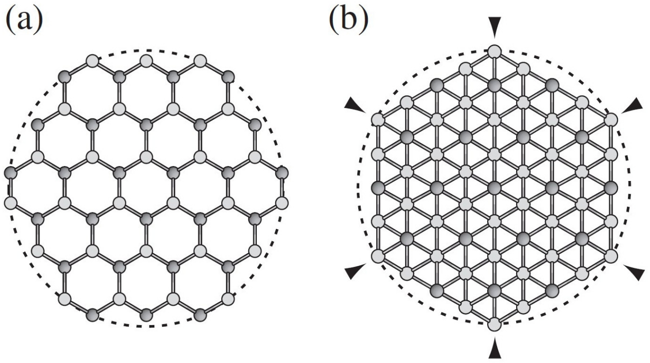

Figure 3.14: Cross-sectional view of hexagonal NWs with a) WZ and b) ZB structures. Light (dark) circles denote cation (anion) atoms. The NW diameter is defined with a dashed circle to precisely enclose an hexagonal wire. The arrowheads show two-coordinated atoms located at the boundaries of the NW facets. This Figure is extracted from Ref.[175].

Other WZ ZnSe NWs have been observed by TEM (not shown) and always display a larger diameter at the position of the ZB insertions. These results suggest that it may be easier for the shell to be deposited on a ZB rather than on a WZ structure. Moreover, the NW from $S^{Se}_{1QD}$ observed in Figure 3.13 shows a diameter of 50 nm at the position of the QD, which is bigger than what has been observed on $S^{vacuum}_{2QDs}$ (29 nm). This could be explained as follows: since the ZB QD insertions on $S^{Se}_{1QD}$ are longer (9 nm along the NW axis) compared to the QDs of $S^{vacuum}_{2QDs}$ (2-3 nm), the $S^{Se}_{1QD}$ QDs have a larger lateral surface exposed to the ZnMgSe flux, which can result in a better shell deposition and a larger diameter.

### Shell identification

Figure 3.15a presents the apex of another NW-QD from this sample. The FFT in the inset indicates that this part of the NW is purely composed of the WZ phase. Figure 3.15b shows the corresponding lattice mismatch map of the NW. A radial profile (along the $[10\bar{1}0]$ direction), visible in Figure 3.15c, has been extracted by integrating over the white rectangle in Figure 3.15b and by taking the NW central part of a reference. It reveals a core-shell type structure composed of a 12 nm core surrounded by a $\sim$ 5 nm shell, which is consistent with the analysis of the ZnSe NWs diameters presented in Chapter 2 even if a slightly larger diameter ($\sim$ 30 nm) would have been expected. Similarly to $S^{vacuum}_{2QDs}$, a negative mismatch at the shell position is visible on Figure 3.15c (see Part 3.2.1 for the discussion relative to this effect).

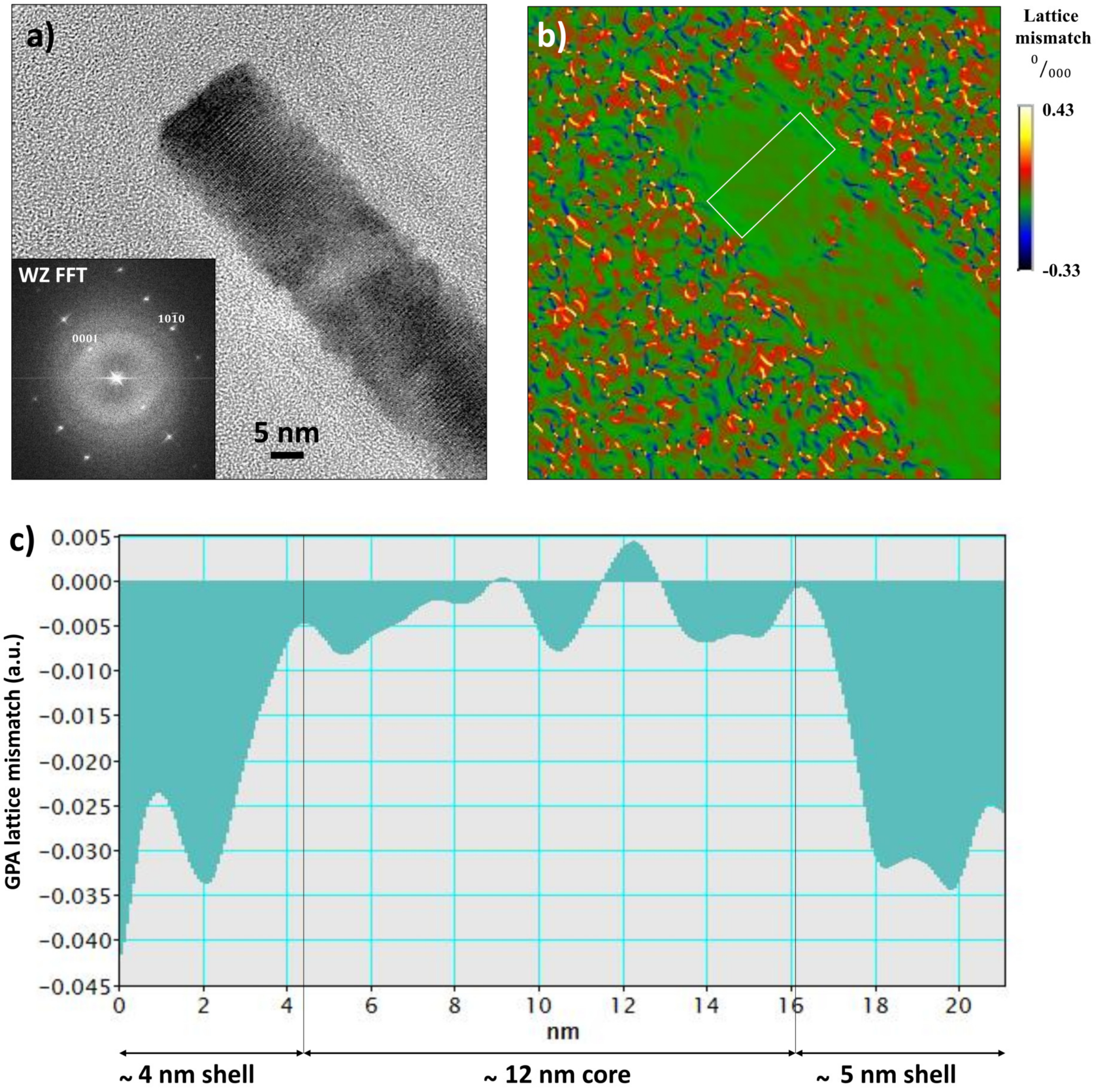

Figure 3.15: a) TEM image of a NW-QD apex. The inset shows the FFT of this ZnSe NW and confirms its WZ structure. b) Corresponding lattice mismatch map. The NW central part has been taken as a reference. A profile along the [10$\bar{1}$0] direction and integrated over the white rectangle has been extracted and is visible in c). A 12 nm core with a shell of $\sim 5$ nm on each side are visible.

All these TEM results were very difficult to obtain due to the very rapid destruction of the NW-QDs and the setup was pushed to its limits. Figure 3.16a, b and c display single NW-QDs after less than one minute of TEM observation. The observed damages clearly show that the NW-QDs are very prone to TEM electron beam damages.

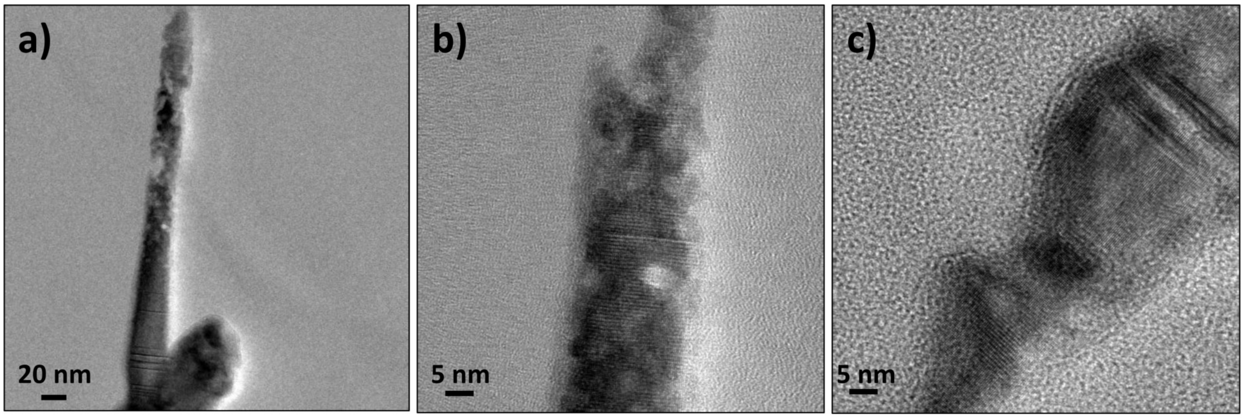

Figure 3.16: TEM images of single NW-QDs from $S_{2QDs}^{vacuum}$ after less than one minute of TEM observation. On the three Figures a, b and c, clear deteriorations can be observed, indicating that the NW-QDs are very prone to TEM electron beam damages.

### Summary of these structural characterizations

To summarize these structural characterizations, CdSe insertions from $S_{2QDs}^{vacuum}$ and $S_{1QD}^{Se}$ NW-QDs could be observed with thicknesses of 2-3 and 9 nm respectively. Such a difference of thickness could be explained by the growth procedure of the insertion.

- for $S_{2QDs}^{vacuum}$, the *Zn and Se fluxes were interrupted before the CdSe insertion.* During this interruption, the Au catalyst will consume its atomic elements and go off the supersaturation needed for the growth. When the Cd and Se fluxes are sent back, a delay time is required for the Au catalyst to reach again the supersaturation and catalyze the CdSe QD growth. Since this growth condition results in **flat QDs** (along the NW axis), it is favorable to induce a **radial dipole orientation**.
- for $S_{1QD}^{Se}$, the *Se flux remains before the CdSe insertion.* Our results suggest that this remaining flux permits to keep the Au catalyst in (or close to) the supersaturation regime. In this case, when the Cd and Se fluxes are sent, the QD growth can start directly without delay time, resulting in a longer QD size along the NW axis. Since this growth condition results in **longer QDs** (along the NW axis), it is favorable to induce a **longitudinal dipole orientation** (if the QD height is large enough to exceed a QD aspect ratio of 1).

Interestingly, the CdSe QD and ZnSe NW are composed of the ZB and WZ phases respectively. These results contrast with the stable crystal phases of ZnSe and CdSe which are ZB and WZ respectively. Such a change of crystal structure could be explained by the nanometric size of the NW-QD [11] which reduces its surface energy or result from the complex dynamic taking place during the MBE growth [174].

The 10 nm-diameter gold droplet used to catalyze the NW-QDs growth was observed, in agreement with the 10 nm ZnSe core diameter observed in the previous Chapter. A GPA radial profile permitted to confirm that the NWs are composed of a 10 nm ZnSe core, surrounded by a 5 to 10 nm shell. A negative lattice mismatch is measured between the core reference and the shell, which contrasts with the positive lattice mismatch expected from the literature. This result could originate from an oxidation of the ZnMgSe shell during the TEM measurements, leading to a ZnMgSe/ZnO alloy of reduced lattice parameter. Moreover, a significant change in the ionic polarization (observed for instance during a Mg incorporation in WZ ZnO crystals [172]) between the WZ ZnSe core and the ZnMgSe shell could play a role on this negative lattice mismatch. Further investigations need to be carried out to clarify if this observation is induced by the TEM observation or is representative of the real ZnSe/ZnMgSe lattice mismatch.

Moreover, by distinguishing NW-QDs vertical and tilted on the as-grown sample, we observed that their growth axis are oriented along the c-[0001] and the $[01\bar{1}1]$ axes respectively. This result suggests that the difference of diameter between both NW-QDs orientations is due to: (1) a difference of surface energy on the NW-QDs sidewalls and (2) a difference of NW surface exposure to the MBE cells fluxes (the tilted NWs are more exposed compared to the vertical ones).

Note that the TEM measurement of the QD size along the NW axis is very accurate. However, it remains challenging to estimate its radial dimensions due to the ZnMgSe shell. To overcome this issue, we carried out a complementary NW characterization called Energy-Dispersive X-ray spectroscopy or EDX (working principle explained in the Introduction Chapter, Part 1.3.2).

## 3.3 Composition analysis

### 3.3.1 EDX characterization of $S^{Se}_{1QD}$

This section explains the EDX measurements[5] carried out on a NW-QD from $S^{Se}_{1QD}$ and describes the model used to quantify the elements concentration in this NW-QD geometry. This EDX measurement has been carried out by Eric Robin from CEA-Grenoble/INAC/MEM/LEMMA and **it is the first time it is carried out on such a small diameter NW-QD** (∼30 nm).

#### EDX model

This EDX NW setup has been recently developed for the characterization of ZnTe-CdTe NW-QDs [176] (diameter from ∼40 to 80 nm). The challenging NW characterization consists in recording hypermaps: for each pixel, a full EDX spectrum is recorded (see Figure 3.20a) where the emission of elementary atoms can be distinguished at different energies. In this analysis, Se, Zn Cd and Mg were mainly detected. To acquire more information about the 3D spatial and chemical composition of the NW-QD, several hypermaps of the same NW-QD

---

[5] A FEI TITAN Themis S/TEM equipped with four silicon 157 drift detector and operating at 200 kV was used.

were recorded. Indeed, at least two hypermaps recorded at two different tilt angles (rotation around the NW axis) are needed to reconstruct the whole structure in 3D.

The *absolute* quantification of each element concentration is reached by calibrating the EDX signal in [counts/s]. Without taking into account absorption effects (for the moment), a NW-QD EDX signal is equal to:

$$I_i = I_0\, N_0\, \sigma_i \int x_i(y)\, dy \tag{3.3.1}$$

with $i$ is an element (Se, Zn, Cd or Mg), $I_0$ the excitation current [electrons/s], $\sigma_i$ the scattering cross section [cm$^2$], $N_0$ the density of available sites for atoms $i$ [cm$^{-3}$] and $x_i$ the proportion of an element $i$ (local composition, from 0 to 1). Figure 3.17 shows the axis orientation used in this work: the NW-QD axis corresponds to the Z-axis, the electron-beam to the Y-axis and the X-axis goes through the NW-QD. The elements distributions maps correspond to the composition projection in the X-Z plane.

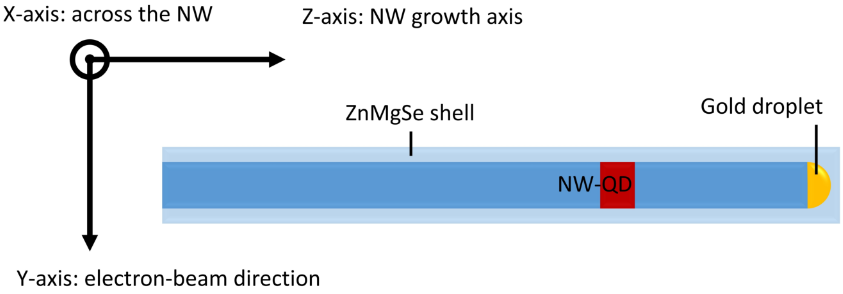

Figure 3.17: Scheme of the axis orientation used in this work.

The determination of the NW-QD thickness $\int dy = t(x)$ is calculated using the $\zeta$-factors calibration method [177]. These $\zeta$-factors are measured using standard samples of each element with a well known thickness and composition, under the same experimental condition as the EDX measurement. Once these factors are known for each elements, the thickness crossed by the electron beam at each scanned position t(x) is:

$$t_i(x) = \frac{I_i^{generated}\zeta_i}{C_i} \times \frac{1}{\rho I_0} \;\; with \;\; t(x) = \sum_i t_i(x) \;\; and \;\; \sum_i C_i = 1 \tag{3.3.2}$$

with $I_i^{generated}$ the intensity of the EDX signal, $\rho$ the mass density and $C_i$ the mass concentration of the element $i$. Moreover, the absorption of the X-ray going through the sample thickness permits to convert the measured EDX intensity to the generated EDX intensity according to:

$$I^{generated} = I^{measured} \times A(\rho, t, C) \tag{3.3.3}$$

with $A(\rho, t, C)$ the absorption which needs to be calculated for each element and depends on the sample density $\rho$, the thickness $t$, the concentration $C$. More information can be found in Ref. [176].

In the case of a cylinder-shaped CdSe QD of radius $r_1$ inserted in a ZnSe NW of radius $r_2$ and a ZnMgSe shell of radius $r_3$, we expect for the elementary atoms the following profile displayed in Figure 3.18. Note that in this example, the radius of the Cd profile visible in red is smaller compared to the Zn profile radius (in blue). This is only true if the CdSe insertion diameter is smaller than the ZnSe diameter, but in reality, the CdSe and the ZnSe diameters are expected to be equivalent and fixed by the gold droplet which catalyzes the growth. This example is provided for visualization purpose.

The NW projection is observed with the horizontal axis corresponding to the cylinder radius and the vertical axis to the NW thickness. The observed circular shapes are the result of the in-plane NW projection. In this ideal case where Cd+Zn=Se, we see that from 0 to $r_1$ the Cd profile is subtracted to the Zn profile. The ZnSe cylindrical core of radius $r_2$ surrounded by a cylindrical ZnMgSe shell of radius $r_3$ should have the same circular profile for Zn and Mg on the exterior part ($x > |r_2|$). For $|r_1| < x < |r_2|$), the Mg content decreases and the Zn profile increases even more (than the continuation of the circular profile at $x > |r_1|$) due to the addition of Zn from the ZnMgSe shell.

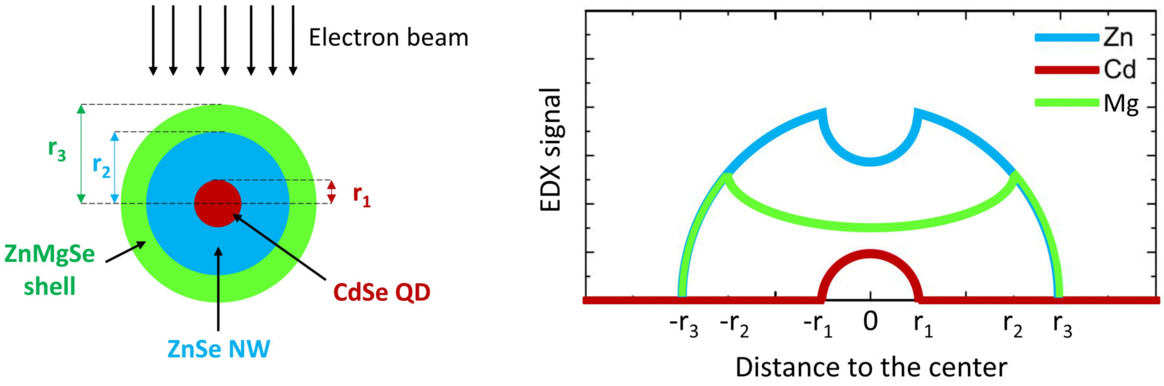

Figure 3.18: Left: scheme of a cylinder-shaped CdSe QD of radius $r_1$ inserted in a ZnSe NW of radius $r_2$ and a ZnMgSe shell of radius $r_3$. Right: EDX profile expected for such a nano-object.

For the sake of simplicity and visualization purpose, we used in the previous example cylindrical NW-QD profiles. For a real NW analysis, a more complex structure can be used. In our case, a set of hexagons[6] placed one inside another have been used to reconstruct the whole nanostructure[7]. An homogeneous concentration of elements is attributed to each hexagon. Besides, each hexagon can be adjusted using five parameters: the axes length *a* and *b*, the tilt angle $\theta$ and the position of the center ($X_0$,$Y_0$), as displayed in Figure 3.19.

---

[6] Easier models using circles or ellipses could have been used. However, hexagons provide the best fit.

[7] The reconstruction software has been developed by E. Robin from CEA-Grenoble/LEMMA.

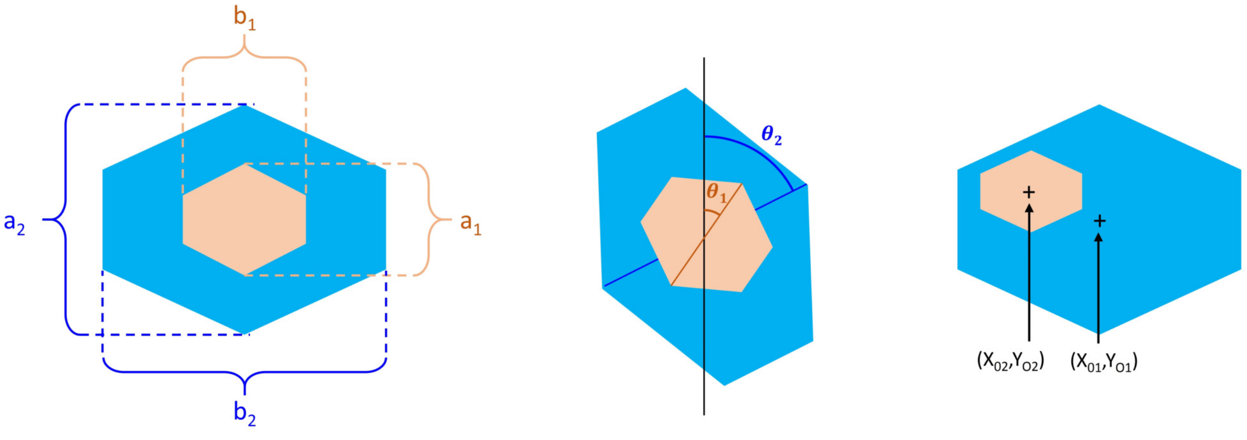

Figure 3.19: The hexagons have five parameters that can be tailored: their axes length *a* and *b*, their tilt-angle and the position of the center ($X_0$,$Y_0$).

After the acquisition of the hypermaps, quantitative information can be extracted by processing the raw data. First, each emission line of the spectrum needs to be labeled with an element[8], the backgrounds needs to be subtracted and each peak is deconvoluted. A relative quantification of how much of an element is more detected in one pixel than another can be accessed with the ESPRIT-QUANTAX software from Braker. Figure 3.20a presents one spectrum recorded for the ZnSe-CdSe NW-QD we analyzed. Figure 3.20a and b show the same spectrum before and after the background deconvolution.

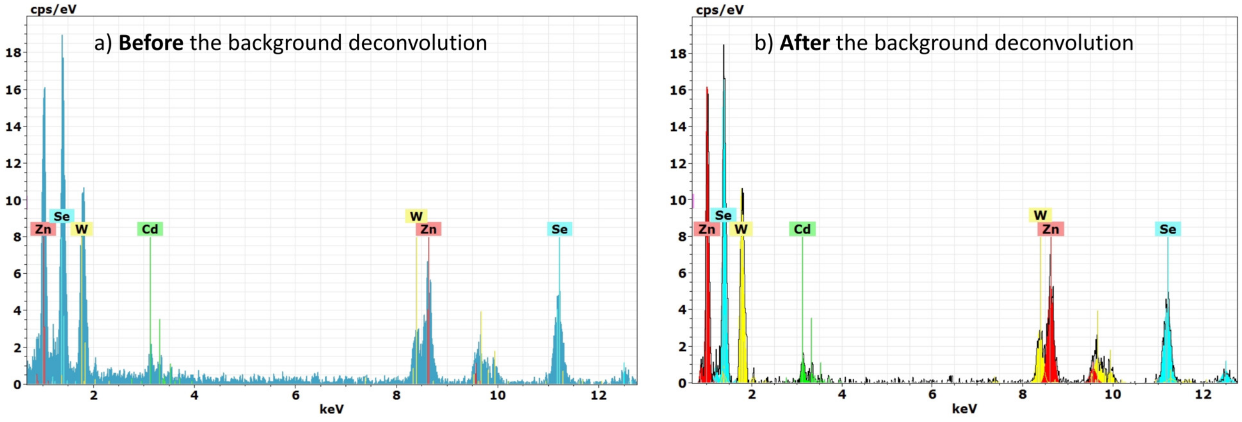

Figure 3.20: EDX spectrum from the analyzed ZnSe-CdSe NW-QD from $S_{1QD}^{Se}$ a) before and b) after the background deconvolution. Only the colored peaks are used to quantify the concentration of each element.

---

[8] The Se and Cd L-lines, and the Zn K-line have been used for the analysis.

### Results on a NW-QD from $\mathbf{S^{Se}_{1QD}}$

EDX measurements have been carried out on a single vertically oriented NW-QD from $S^{Se}_{1QD}$. This NW-QD has been extracted by nanomanipulation and fixed on top of a TEM tip (visible in Figure 3.32). The nanomanipulation technique will be later explained in Part 3.3.2 of this Chapter, we focus here on the EDX results.

During this EDX measurements, a first hypermap[9] has been recorded at a 0° tilt-angle. A part of this hypermap has been superimposed on top of the studied NW-QD SEM image in Figure 3.21. On this hypermap, despite the ZnMgSe shell, the presence of a localized Cd region is visible in a $5 \times 5$ nm$^2$ zone (in orange) within the 30 nm-diameter NW and can be attributed to the CdSe QD.

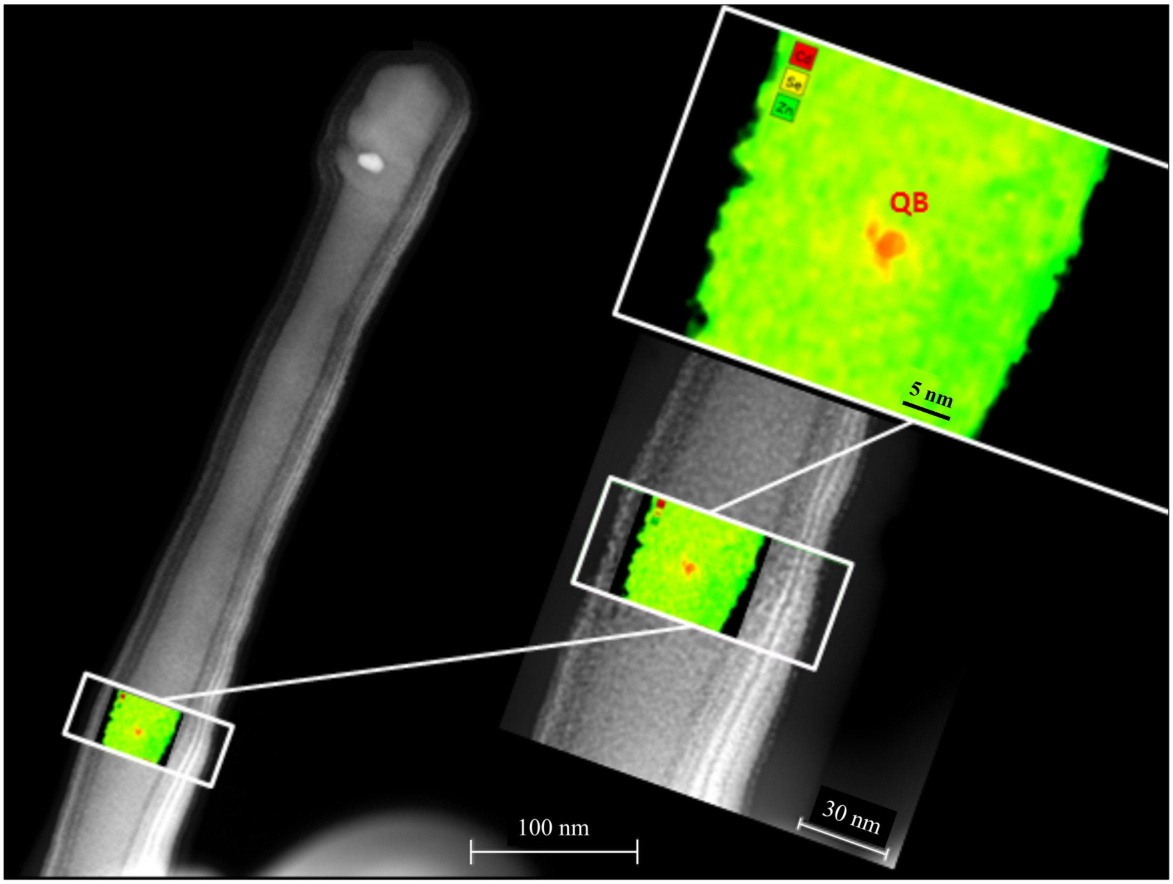

Figure 3.21: Superimposition of a TEM image and the corresponding EDX elements maps of Cd, Se and Zn (recorded at a 0°-tilt angle) of a ZnSe-CdSe NW-QD, with (left to right) a progressive zoom on the CdSe QD. The white layers stacking visible on the NW sidewalls consist in tungsten layers, used to fix the NW on top of a TEM tip. This procedure will be later explained in Part 3.3.2.

---

[9] Hypermap 0°: image 317 x 133 pixels (85 nm x 36 nm; 0.27 nm of resolution); 57 µs/pixel, acquisition along ~ 15 nm and 392 passages.

In this EDX characterization, the Mg content can not easily be fitted due to an overlap of the Mg and Se pics in the EDX spectra (not shown in Figure 3.20). The modest quantity of Mg in the $Zn_{0.90}Mg_{0.10}Se$ shell is drowned in the Se pic which is abundant in our ZnSe-CdSe NW-QD. Consequently, the $Zn_{0.90}Mg_{0.10}Se$ shell is seen as a pure ZnSe shell in this EDX characterization.

For the 3D reconstruction of the CdSe QD, a second hypermap[10] has been recorded at a +45° tilt-angle. The corresponding elements maps of Cd and Zn for the 2 tilt angles are visible in Figure 3.22a and b. The central red part corresponds to the CdSe insertion and the yellow part to the ZnSe and ZnMgSe part. Figure 3.22c shows the Cd profile integrated over the whole regions of the Figures 3.22a and b. The localized Cd concentration highlights the presence of the CdSe QD. By considering that the Cd atomic concentration below 1% corresponds to the background, the QD shows a FWHM of ∼6 nm and a longitudinal size of ∼10 nm. This result is consistent with the 9 nm thick QD measured from the same sample $S^{Se}_{1QD}$ by TEM in Part 3.2.2.

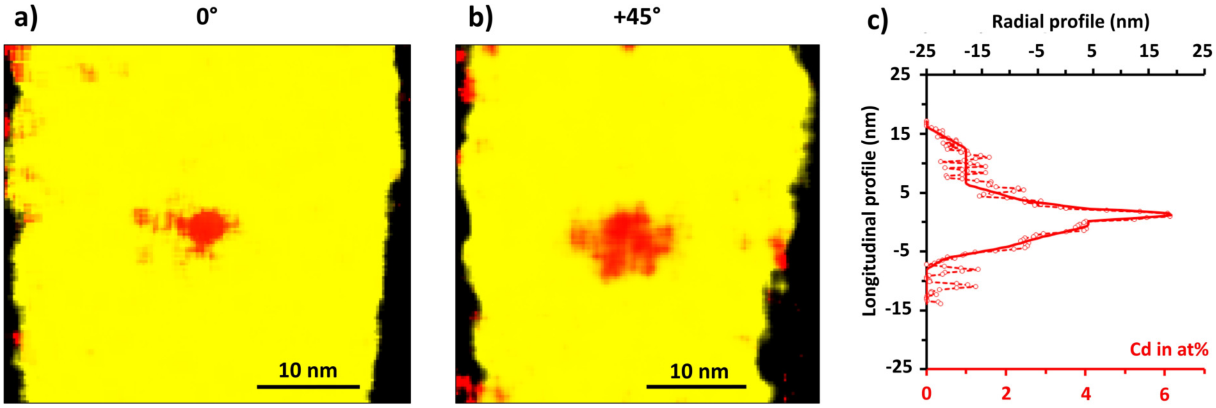

Figure 3.22: Cd (red) and Zn (yellow) elements maps recorded at a) 0° and b) +45° tilt-angles of the same NW-QD shown in Figure 3.21. The 3D NW-QD reconstruction was carried out in the whole displayed regions. c) Longitudinal Cd profile highlighting the presence of the CdSe QD.

These NWs are composed of the WZ structure: they are expected to be faceted with an hexagonal shape. To verify this assumption, Figure 3.23a shows the NW total thickness projected on a plane (open dots: experimental data; solid black curve: model) and the reconstructed NW section from the hexagonal model (dashed lines). This projection is well fitted by an hexagonal shape and therefore, the 3D reconstruction at the position of the QD has been carried out with a set of 5 imbricated hexagons, as displayed in Figure 3.23b.

---

[10] Hypermap +45°: image 317 x 133 pixels (85 nm x 36 nm; 0.27 nm of resolution); 57 µs/pixel, acquisition along ∼ 9 nm and 214 passages.

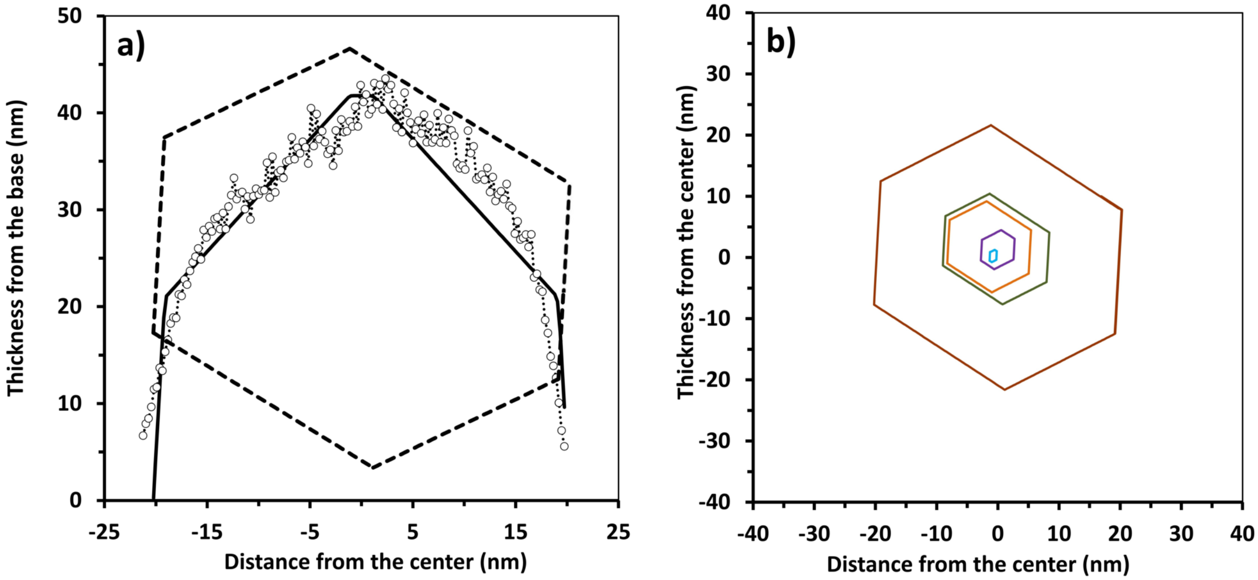

Figure 3.23: a) NW thickness projected on a plane (experimental data: open dots; model: solid black curve) and the reconstructed NW section from the hexagonal model (dashed lines). b) Model used for the 3D reconstruction of the NW-QD measured by EDX. The hexagonal cross-section is simulated with 5 imbricated hexagons of homogeneous composition.

The detailed procedure of the reconstruction is provided in the supplementary information of Ref.[176]. To give an overview of this reconstruction procedure, all the elements profiles (integrated over the whole regions displayed in Figure 3.22a and b) have to be fitted altogether for the two hypermaps (made at different tilts) using the hexagonal cross-section. Examples of such fits are provided in Figure 3.24a, b and c for the Cd, Zn and Se elements respectively for the 0° tilt-angle hypermap. The Table shown in Figure 3.24d details the parameters that provide the best fit. According to this fit, the NW structure across the CdSe QD is composed of the following imbricated hexagons:

- a pure CdSe center of 1-2 nm in diameter (hexagon 1)
- a 5-6 nm-thick $Cd_xZn_{1-x}Se$ zone with 36% of Cd and 64% of Zn[11] (hexagon 2)
- a 10-14 nm-thick $Cd_xZn_{1-x}Se$ zone with 18% of Cd and 82% of Zn (hexagon 3)
- a 14-23 nm-thick $Cd_xZn_{1-x}Se$ zone of 6% of Cd and 94% of Zn (hexagon 4)
- a 35-41 nm-thick ZnSe zone (hexagon 5).

---

[11] Using the traditional notation for semiconductor alloys - $Cd_xZn_{1-x}Se$ - which only considers one sub-lattice used throughout this manuscript. On the other hand, EDX characterizations usually uses concentrations in atomic percentage (at. %, with the total percentage of all elements equal to 100%), like in Figure 3.24. A factor 2 needs to be applied on Cd and Zn to convert one notation from the other. For instance: $Cd_{36}Zn_{64}Se$ corresponds to a Cd and Zn atomic percentage of respectively 36/2 = 18 and 64/2 = 32 (example extracted from Figure 3.24).

We can first note that most of the Cd is concentrated within a 10-14 nm-thick zone (first three hexagons) and is surrounded by an almost pure 10 nm-thick ZnSe zone (hexagons 4 and 5). The diameter of the main CdZnSe part (hexagons 1 to 3) corresponds to the Au droplet size observed by SEM and TEM, around 10 to 14 nm (TEM image provided in Figure 3.11). It is coherent with our previous observations of an approximately 10 nm-large ZnSe-CdSe NW-QD surrounded by a ZnMgSe shell. Note also that the NW is not perfectly symmetric; hexagon 5 indicates that its hexagonal structure is 35 nm x 41 nm. This result suggests that the ZnMgSe shell is not homogeneously deposited on the NW-QD sidewalls, as already observed by SEM (diameter modulations in Part 2.2.7).

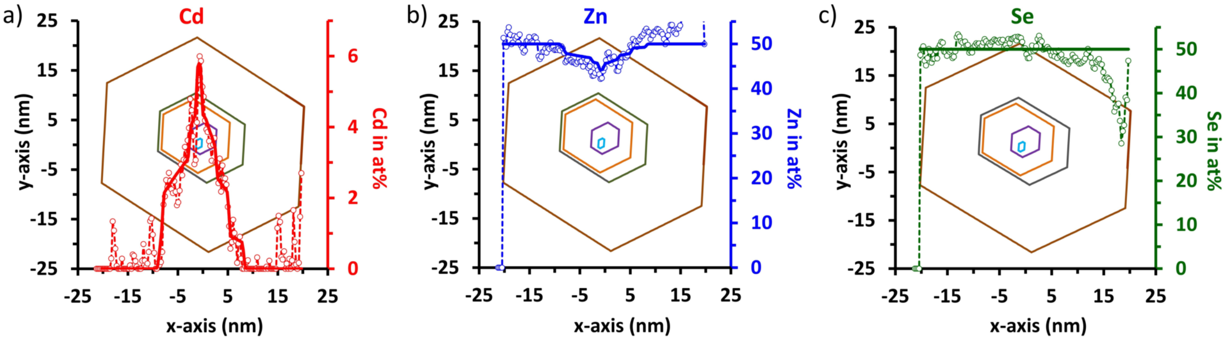

| d) | Local concentration $Cd_xZn_{1-x}Se$ (%) | | Size (nm) | | | Position (nm) | | Orientation |
|---|---|---|---|---|---|---|---|---|
| Ellipse | Cd (x) | Zn (1-x) | a (x-axis) | b (y-axis) | c (z-axis) | $X_0$ | $Y_0$ | θ (deg) |
| 1 | 100 | 0 | 2.0 | 1.0 | 1.0 | -0.8 | 0.0 | -15.0 |
| 2 | 36 | 64 | 6.0 | 5.0 | 5.0 | -0.8 | 1.0 | 5.0 |
| 3 | 18 | 82 | 12.0 | 14.0 | 10.0 | -2.2 | 0.5 | 5.0 |
| 4 | 6 | 94 | 14.0 | 23.0 | 18.0 | -1.0 | 1.0 | 0.0 |
| 5 | 0 | 100 | 35.0 | 41.0 | | 0.0 | 0.0 | 0.1 |

Figure 3.24: a) Cd, b) Zn and c) Se relative composition (atomic % of content averaged over the local thickness) along the line scan across the QD insertion at a 0° tilt-angle (see rectangle in Figure 3.22). Experimental data: open dots; calculated values using the 5 imbricated hexagons.: solid black curve). d) Table summarizing the set of parameters used to fit our data. For each hexagon, the parameters are the Cd, Zn and Se concentrations, the size of the hexagon (along the x, y and z axis), its center position ($X_0$,$Y_0$) and orientation ($\theta$). The colors used for each imbricated hexagons are reported in the Table for visualization purpose.

During this EDX measurement, a third hypermap[12] has been recorded at a tilt angle of -45°, as seen in Figure 3.25, with the aim to ease the NW-QD 3D reconstruction. However, during this hypermap acquisition, the CdSe QD has been damaged (NW-QDs proned to beam damages, as already shown in Figure 3.16). The diffusion of the Cd is visible in Figure

---

[12] Hypermap -45°: image 297 x 127 pixels (80 nm x 34 nm; 0.27 nm of resolution); 57 µs/pixel, acquisition along ∼ 19 nm and 533 passages.

3.25 (in red) within the ZnSe NW (yellow). This hypermap could not properly be fitted with the other hypermaps (at 0° and +45°) and we decided to omit it for the data analysis.

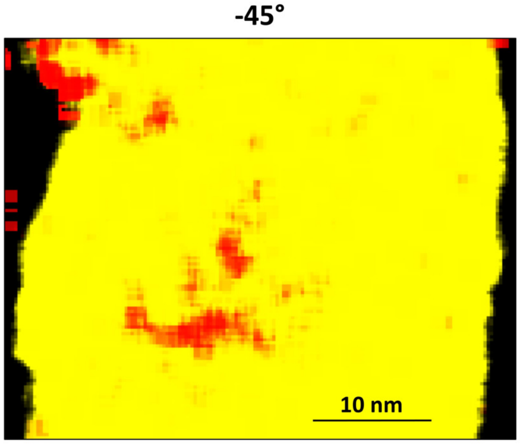

Figure 3.25: Cd (red) and Zn (yellow) elements maps recorded at a -45° tilt-angle of the same NW-QD shown in Figure 3.21.

Several factors indicate that the CdSe QD has not been damaged during the first two hypermaps acquisitions, since:

1. a correct fit could be obtained by using simultaneously the first two hypermaps,
2. the CdZnSe QD diameter (first three hexagons) corresponds to the gold droplet diameter.

### Summary of the EDX measurements

In summary, a vertically oriented ZnSe-CdSe NW-QD from $S^{Se}_{1QD}$ has been extracted from its as-grown substrate by nanomanipulation and fixed on top of a tip for EDX measurements. These measurements indicate that the QD size along the NW axis is ~10 nm, a result consistent with the 9 nm previously measured by TEM. The CdSe QD is composed of a pure CdSe zone of 1-2 nm in diameter, embedded in a 10-14 nm-diameter CdZnSe alloy with decreasing Cd content from 36 to 18% (x in $Cd_xZn_{1-x}Se$). This radial QD size is coherent with the gold droplet diameters around 10 nm in diameter observed by SEM and TEM. Moreover, the QD is surrounded by a 10 nm-thick ZnSe structure which corresponds to the $Zn_{0.90}Mg_{0.10}Se$ shell (Mg not visible in the EDX spectrum). These results, first obtained on such a thin diameter NW-QD, permitted to push the limits of this EDX setup.

## 3.3.2 Preparatory atom probe tomography study

This part introduces a complementary composition sensitive technique called Atom Probe Tomography (APT). This powerful technique introduced in Part 1.3.2 offers both 3D imaging and chemical composition measurements at the atomic scale.

### Challenge to observe single II-VI semiconductor QDs

At the origin, APT was mainly used for the characterization of metals [178] by using a high DC voltage. The use of pulsed-lasers allowed the characterization of poor-electrically-conducting materials [179], column IV [180] and III-V semiconductors [181]. They are very few reports on semiconductor QDs APT characterizations [182–184] due to the experimental difficulties. Moreover, the characterization of II-VI semiconductors by APT is relatively recent and at the time of this investigation in 2013, there were no reports of CdSe and ZnSe APT characterizations.

With the idea to develop this recent characterization technique and to determine the best experimental conditions (evaporation field, laser power and post data analysis) to observe CdSe and ZnSe semiconductor materials, we collaborated with the IM2NP group from Marseille. The PhD student Hammouda Benallali made a major effort to characterize the properties of II-VI semiconductors [51, 185] provided by our group [68]. The study of a single 30 nm-diameter NW-QD by APT represents a huge ongoing challenge and we will not show results on such nanostructure in this manuscript. The first step of a NW APT characterization, which consists in isolating a single 30 nm-diameter NW-QD at the apex of a tip, is presented at the end of this section.

In this part, we present the composition analysis of self-assembled CdSe QDs embedded in a ZnSe matrix. The APT measurements and analysis were carried out by Hammouda Benallali. The QDs composition and size strongly affect the QDs optical proprieties. To fully characterize these QDs, we performed PL measurements and set up a model to correlate both APT and PL measurements. This work has been the result of a publication in Applied Physics Letters (Ref.[185]).

### APT study of CdSe QDs capped in a ZnSe matrix

**Studied sample** The sample presented in this study is composed of a single CdSe QD plane inserted between ZnSe barriers grown by MBE. First, 60 nm-thick ZnSe buffer layer was grown at 280°C on a (100) GaAs substrate. Then 3 MLs of CdSe were deposited on the ZnSe layer by ALE (at 280°C). To induce the 2D–3D transition of the strained CdSe layer, amorphous selenium was first deposited at low temperature (10°C) and then desorbed by heating up to 240°C where spotty 3D RHEED patterns appear and indicate the typical QDs formation [144]. Finally, the CdSe QDs layer was capped with a 40 nm ZnSe layer (grown in two steps: 2 min at 240°C then 5 min at 280°C). Details of the growth method can be found in Ref.[144]. In contrast to III-V materials like InAs/GaAs, the formation of these CdSe QDs differs significantly from the Stransky-Krastanov growth mode [186] so that interdiffusion and/or segregation phenomena based on Cd-Zn exchanges [187, 188] may take place in the QD formation mechanism.

**APT tip preparation and APT experimental details** The APT analysis is carried out in three steps: (1) the sample is shaped with a tip geometry, (2) the APT measurement is carried out and (3) the data analysis is performed to correctly reconstruct the studied volume in 3D with the correct stoichiometry.

First, the sample is shaped[13] using a Ga Focused Ion Beam (FIB) with a 50 nm apex tip geometry to ease the evaporation of the atoms by field effect. To protect the remaining semiconductor tip from a Ga doping from the FIB, a 100 nm-thick Ni protection layer is deposited by physical vapor deposition on top of the ZnSe capping layer before the etching process.

The measurements and analysis conditions were carefully determined to optimize the APT studies. In particular, a major effort was made[14] to obtain the expected stoichiometry of the semiconductor compounds - minimizing for instance the formation of molecular ions - by reducing the laser energy, increasing the evaporation rate and/or the tip shape.

**APT results** Figure 3.26a shows the 90 x 90 x 100 nm$^3$ volume obtained by the reconstruction of the APT data, in which the layers of ZnSe and CdSe are clearly visible on the GaAs substrate. From the atoms distribution in this 3D-volume, a 15 nm-diameter cylinder perpendicular to the ZnSe/CdSe interface was used to extract a one dimensional (1D) mean concentration along the axis of the reconstructed volume, visible in Figure 3.26b. This 1D composition profile shows that the average composition of ZnSe corresponds to the expected 50:50 stoichiometry, validating the analysis method. The mean composition of Cd measured in $Cd_xZn_{1-x}Se$ layer is 37 %, and the layer thickness is about 3–4 nm. Moreover, the Se concentration is constant throughout the II-VI layer.

From the APT measurements, two dimensional (2D) mapping has also been extracted to show Cd atoms lateral distribution in the $Cd_xZn_{1-x}Se$ layer. Figure 3.27 shows the 2D maps of the Cd concentration obtained by integrating over 3 nm **a) in parallel** and **b) perpendicularly to the growth direction.**

These 2D-mapping clearly show variations of the Cd concentration within the $Cd_xZn_{1-x}Se$ layer: small Cd-rich regions - attributed to the $Cd_xZn_{1-x}Se$ QDs - are surrounded by Cd-poor regions attributed to the wetting layer. The lateral QDs surface in the (x, y) plane varies between 16 and 35 nm$^2$.

---

[13] The tips were shaped along the (001) growth direction using the lift-out technique and the annular milling method. The sample preparation was performed in a FEI Helios dualbeam–focused ion beam and the APT measurements in a LEAP 3000X HR microscope. This microscope is equipped with a pulsed-laser source ($\lambda = 532$ nm, pulse duration ∼10 ps, spot size $< 5$ µm).

[14] APT measurements were carried out at 23 K under a pressure below $5\times10^{-11}$ Torr and using a picosecond laser pulse with an energy of 0.004 nJ and a 100 kHz repetition rate. During the analysis, an evaporation rate of 0.002 ions per pulse was kept constant. The 3D reconstruction was carried out by using the shank-based algorithm [189–191] in the IVAS commercial software, a field factor of 3.3 and an evaporation field of 23 V/nm to provide a flat interface and layers thicknesses close to the values measured by TEM.

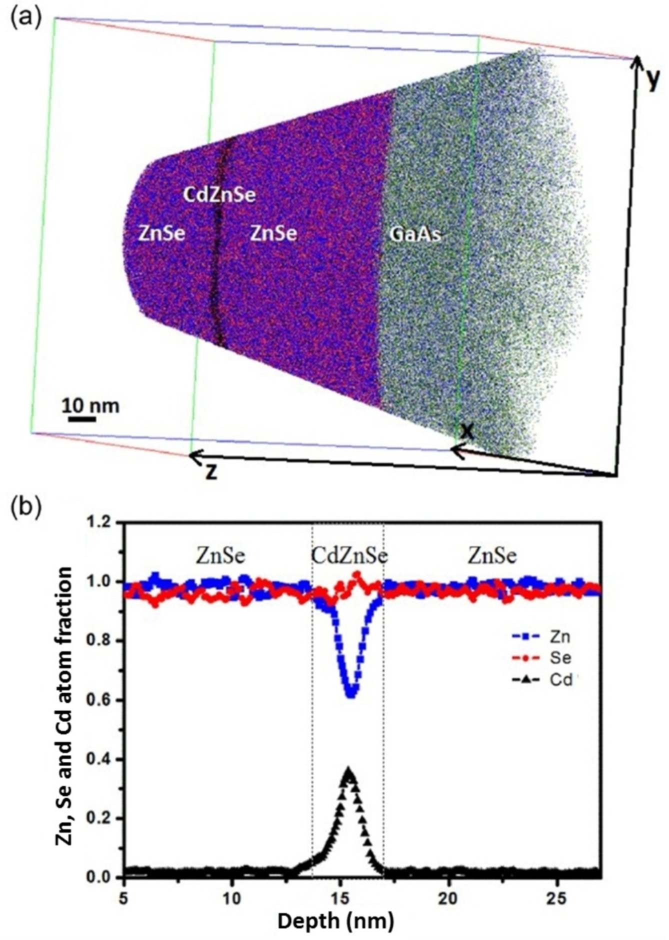

Figure 3.26: a) Reconstructed volume 90 x 90 x 100 nm$^3$, showing the ZnSe/ CdSe/ZnSe layers on top of the GaAs substrate. The 3D atom map shows the abrupt interface between layers. b) Concentration profile along the growth direction z measured inside a cylinder of 15 nm-diameter in the reconstructed volume; the average concentration of Cd is about 37 % in the $Cd_xZn_{1-x}Se$ layer.

The 2D Cd concentration maps in Figure 3.27 only give an average concentration of the $Cd_xZn_{1-x}Se$ QDs (integration over the thickness of a slice). To get a more accurate QDs concentration, 1D profiles across the QDs were extracted. Figure 3.28 shows two examples of 1D profiles generated along the z-axis using 3 nm-diameter cylinders: cylinders 6 and 7 of Figure 3.27a. The cylinder 6 intersects the *Cd richest QD* with a maximum Cd content of 65 ± 4 %. On the other hand, cylinder 7 intersects a thinner and Cd-poor region with a typical Cd content of 26 ± 4 % which is attributed to the *wetting layer*. Altogether, six QDs were identified in the volume of Figure 3.26 (see Figure 3.27a) and their characteristics are listed in Table 3.2 with varying Cd concentration ranging from 39 to 65 %. The QDs sizes correspond to the FWHM of the concentration profiles: the QD length (along the x and y-axis) are bigger than their height (along the z growth axis), indicating that these in-plane QDs are flat, as expected.

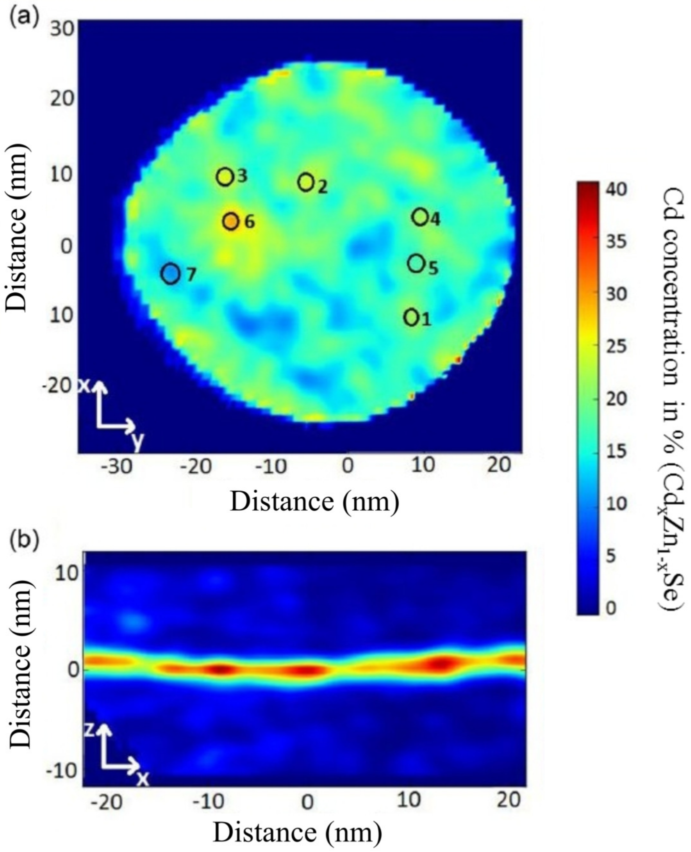

Figure 3.27: a) 2D map concentration of the CdZnSe layer through a 3 nm slice a) parallel and b) perpendicular to the growth direction. The color range goes from blue (poor Cd concentration) to red (high Cd concentration).

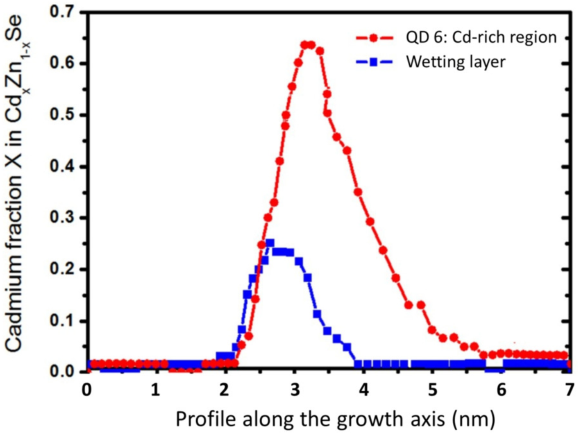

Figure 3.28: 1D Cd composition profiles from two different regions in the CdZnSe layer using a 3 nm-diameter cylinder parallel to the growth direction. Profile through the QD6 (red) and the wetting layer (blue) labeled regions 6 and 7 respectively in Figure 3.27a.

|  | Cd concentration (%) | Height (nm) | Length along the: |  |
|---|---|---|---|---|
|  |  |  | x-axis (nm) | y-axis (nm) |
| QD1 | 39 | 2.1 | 3 | 7 |
| QD2 | 55 | 1.4 | 5 | 7 |
| QD3 | 58 | 1.3 | 3 | 8 |
| QD4 | 40 | 1.7 | 4 | 4 |
| QD5 | 45 | 1.6 | 3 | 7 |
| QD6 | 65 | 1.4 | 4 | 5 |
| Wetting layer | 26 | ∼3 | Sample size |  |

Table 3.2: Characteristics of the QDs found in the 3D volume in Figure 3.26a): The concentration and the height were deduced from 1D profiles using 3 nm cylinder and the width and lengths from 2D maps. These sizes correspond to the FWHM of the concentration profiles.

To summarize this part, the APT measurements show the presence of a CdZnSe in-plane layer inserted in a ZnSe matrix. By revealing the spatial and chemical 3D distribution of the $Cd_xZn_{1-x}Se$ QDs with atomic scale measurements, the size and composition of individual QDs has been determined: their height is always smaller than their in-plane diameter and their Cd composition ranges from 39% to 65% in QDs (Cd-rich regions) and 26% in the so called wetting layer (Cd-poor region).

### Correlation between the APT and PL results

The QDs composition and size strongly affect the QDs optical proprieties since the $Cd_xZn_{1-x}Se$ composition determines the bandgap and the QDs sizes define the confinement energies and Coulomb interactions. In this part, we correlate the QDs characteristics measured by APT to their PL properties. The inset of Figure 3.29 shows the PL spectrum of an ensemble of QDs at 10 K, excited by a CW 488 nm laser with an incident power of 200 µW focused with a microscope objective (NA of 0.4 and 1 µm spot diameter). The PL signal is distributed over a range of energy from 2.28 to 2.48 eV. In order to check the consistency of the APT analysis with the PL measurements, we first calculate the confinement energy of an electron and a hole assuming a lateral cylindrical shape for the QD using the effective mass model (with finite barrier and Ben Daniel-Duke boundary conditions [192, 193] for the wave functions). A quadratic bandgap variation is applied as a function of the Cd alloy composition:

$$E_g(x) = x\, E_{g_{CdSe}} + (1-x)\, E_{g_{ZnSe}} - b\, x\, (1-x) \tag{3.3.4}$$

The following experimental values are used: bowing parameter b = 0.35 eV, energy gaps $E_{g_{CdSe}} = 1.765$ eV and $E_{g_{ZnSe}} = 2.82$ eV, taken from Refs. [194–196], effective masses along [100] $m_e{}^* = 0.12$ and $m_{hh}{}^* = 0.9$ for CdSe [197], $m_e{}^* = 0.145$ and $m_{hh}{}^* = 1.04$ for ZnSe [198]. A linear interpolation from the binary materials values was used to determine the alloy effective masses. The main confinement energy is given by the QD thickness (size along the growth axis z). The lateral confinement [199] of the QDs has been calculated for two diameters of 5 and 10 nm to cover the QDs lateral size distribution, yielding values of respectively 160 and 54 meV. Figure 3.29 shows the QDs emission energy as a function of their thickness. The dashed lines display the calculated transition energies as a function of the QD thickness, taking into account the alloy concentration and the lateral confinement. This calculation does not take into account the exciton effect and gives, as expected, transition energies higher than the experimental PL energy distribution illustrated by a shaded area in Figure 3.29.

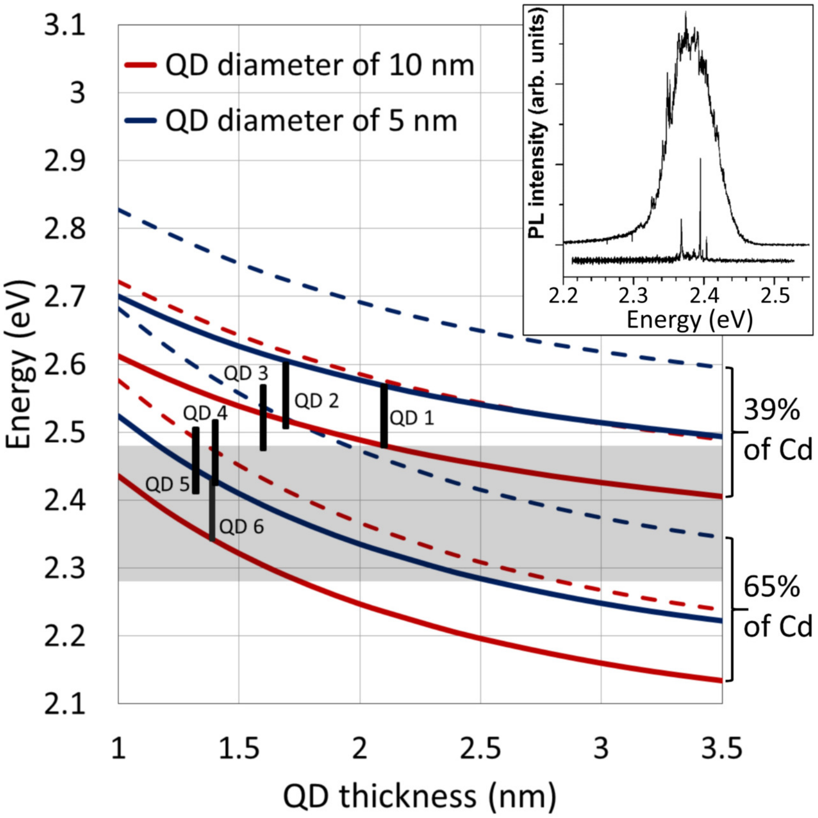

Figure 3.29: PL transition energies as a function of the QD thickness. Two sets of four curves are displayed; the higher set corresponds to a Cd concentration of 39% and the lower set to 65% of Cd. Solid (dashed) curves are the transition energies with (without) excitonic and strain effects. Blue (red) curve is the transition energies for QD diameter of 5 nm (10 nm). Within the 5–10 nm-diameter, the expected transition energies are represented by vertical black lines for each QD reported in Table 3.2. The inset shows the PL spectra of an ensemble (upper part) and few (lower part) QDs measured on a mesa (100 nm lateral size). The corresponding PL energy distribution is reported by the shaded area in the figure.

To better calculate the QD emission energies, the *exciton* and the *strain* effects (induced by the lattice mismatch between ZnSe and the $Cd_xZn_{1-x}Se$ QD) have been calculated using the software Nextnano [200]. The exciton binding energy depends on the QD diameter. Thus, for QDs diameter of 5 and 10 nm, we computed values of -87 and -69 meV by calculating in both cases the average exciton binding energy over the QDs thickness measured by APT. Besides, the strain depends on the Cd concentration and we computed values of -4 and -25 meV for the extrema Cd concentrations of 39% (QD1) and 65% (QD6), respectively. In Figure 3.29, solid lines correspond to transition energies taking into account the exciton and strain effects. Similar calculations have been performed for the other QDs (QD2–QD5) according to their thickness and Cd concentration. The vertical black lines correspond to each QD transition energy and show the energy dispersion as a function of the QD diameter from 5 to 10 nm. Within the 5–10 nm lateral size confinement, the calculated transition energies of the QDs are in good agreement with the PL energy distribution.

In summary, APT provides a powerful 3D characterization of $Cd_xZn_{1-x}Se$ QDs at the atomic scale. This study reveals the variability of QDs size and shape, the complexity of their chemistry, and a strong intermixing between the Cd and the Zn within the QDs. The comparison between the PL emission energy and the calculation of the transition energies including excitonic and strain effects shows that the PL measurements and the APT study are quantitatively consistent.

**Challenge to characterize single ZnSe-CdSe NW-QDs by APT** The APT analysis permitted to successfully determine the best experimental conditions for the study of CdSe and ZnSe materials by APT. The characterization of this 2D QDs distribution represented a challenge and the characterization of a single NW is even more challenging: at this time, they are no reports of APT measurements on NWs as small as 30 nm in diameter [201]. Indeed, the measured NWs had a base diameters above 100 nm and were carried out on metallic [202], column IV [203, 204], and III-V [205, 206] semiconductor NWs. To ensure the successful NW evaporation, they have been vertically oriented with their tip facing the high voltage apex. These NWs had base diameters above 100 nm, bigger than our 30 nm-diameter NW-QDs.

Therefore, the APT characterization of our NW-QDs faces two challenges:

- **the nanomanipulation of such small diameter NW-QDs,**
- **the determination of the NW-QDs optimal evaporation conditions**. For this part, we can rely on the preparatory work presented in the previous section on the 2D plane distribution of $Cd_xZn_{1-x}Se$ QDs in ZnSe.

### Nanomanipulation of our 30 nm-diameter NW-QDs

In the next paragraphs, we present the first step necessary to carry out a NW APT analysis: the nanomanipulation of such small diameter NW-QDs, performed with the great help of Nicolas Mollard from CEA-Grenoble/INAC/MEM/LEMMA.

To favor the manipulation of our NW-QDs, a STRATA 400 FIB-Dual Beam[15] was used to visualize and prepare the sample. Usually, to access the 3 spatial dimensions, both the SEM and FIB are used to visualize the sample with a different point of view of 52°. However,

---

[15] This system is equipped with an AutoProbe 200 micromanipulator, a 3D-motor (100 nm steps minimum), a 2 µm tungsten tip (at the apex) and a gas injector system.

we decided not to use the FIB visualization tool since it uses Ga atoms. These Ga atoms could be implanted in our NW-QDs and potentially dope, damage or even destroy the NWs. By choosing to keep the NW-QDs safe from this Ga pollution, we could not see the NW-QDs in 3D: we only accessed the 2D SEM imaging and were missing the depth on the images, making this manipulation more challenging.

The nanomanipulation was carried out in three main steps: (1) create a *fishing rod-like* system to (2) catch a full single-NW without destroying it and (3) detach the NW from the fishing rod and strongly fix it at the apex of a TEM tip.

**Creation of the fishing rod-like system** To create the fishing rod-like system, the tip of the micromanipulator was first etched down to a 500 nm-apex with the FIB. Then, a 200 nm-diameter Ge NW was welded at the apex of the tip, as displayed in Figure 3.30a). The weld of the Ge NW was performed by zooming with the SEM and sending a tungsten precursor onto the sample with a pipe visible in Figure 3.30b). This weld technique is carried out with the gas injector system. This latter permits to inject a gas in a defined zone close to the sample surface. This gas is composed of metal-organic molecules which can be dissociated by interaction with the SEM electron beam. The metal is then deposited at the sample surface in the zone swept by the electron beam and the organic part is expelled by the pumping system. Here a tungsten precursor has been used to carry out tungsten welds.

Then, we used this whole system - the micromanipulator tip plus the Ge NW - as the *fishing rod* to grab the NW-QDs, as shown in Figure 3.30c.

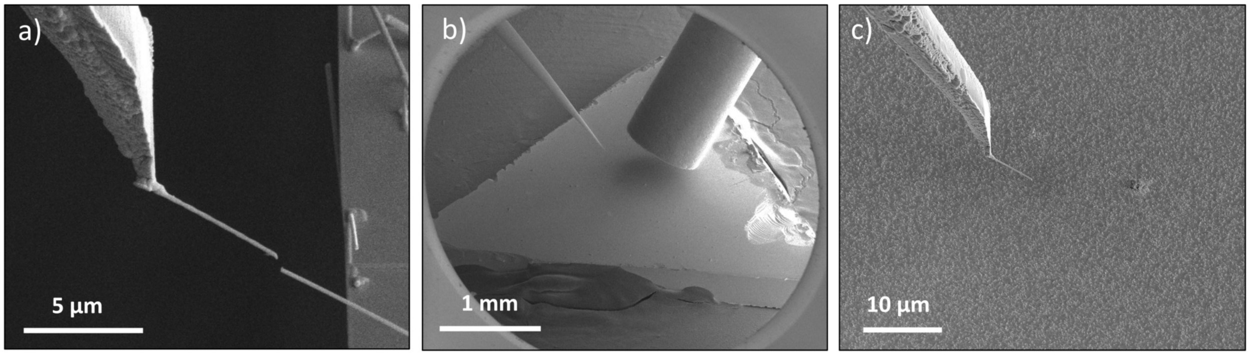

Figure 3.30: Tilted view SEM images (45°) of the micromanipulator tip etched with the FIB down to a 500 nm apex. a) Welding and cut-out of a 50 nm-diameter Ge NW at the apex of the micromanipulator tip. This whole system is then used as a *fishing rod* to grab the NW-QDs. b) Small pipe used to send tungsten precursor onto the sample to weld thanks to the electron beam and the precursor reaction, forming tungsten. c) Approach of the *fishing rod* toward the NW-QDs.

**Catching a single NW** Figure 3.31 highlights how a single NW-QDs was successfully caught. Figure 3.31a shows the Ge NW approaching a single ZnSe-CdSe NW-QDs. During the first tests, NW-QDs were caught by welding the Ge NW on the NW-QDs apex (not shown here). But when we moved the Ge NW to detach it, only the NW-QD apex was detached from the substrate.

To bypass this problem, the NWs were caught by *welding their base*, as displayed in Figure 3.31b. Then, the movement of the Ge NW was sufficient to break the NW-QD and efficiently extract it from its as-grown substrate, as displayed on 3.31c.

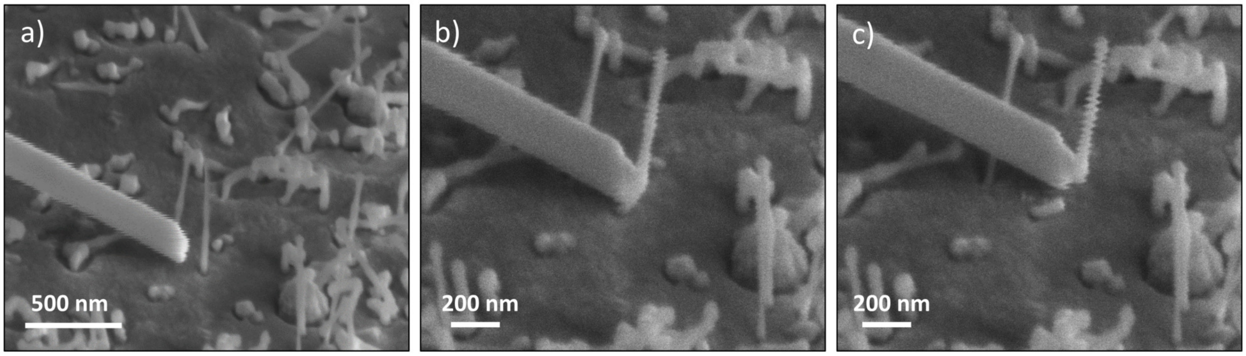

Figure 3.31: Tilted view SEM images (45°) of the Ge NW used as a *fishing rod* to extract single ZnSe-CdSe NW-QDs. a) Approach of the Ge NW toward the base of a single NW-QD. b) Welding of the NW-QD base on the Ge NW. c) Efficient extraction of the single NW-QD from the as-grown substrate.

**Fixing the NW at the apex of a tip** The next step consists in welding the NW-QDs at the apex of a TEM tip. First, the TEM tip was etched from 3 µm to 250 nm with the FIB. This etched tip is visible at the bottom of Figure 3.32a). Then, the NW-QD was welded at the apex of this TEM etched tip and the Ge NW was cut with the FIB. These two steps are visible in Figures 3.32b) and c). Note that the NW-QD visible in Figure 3.32c is the one characterized by EDX in section 3.3.1.

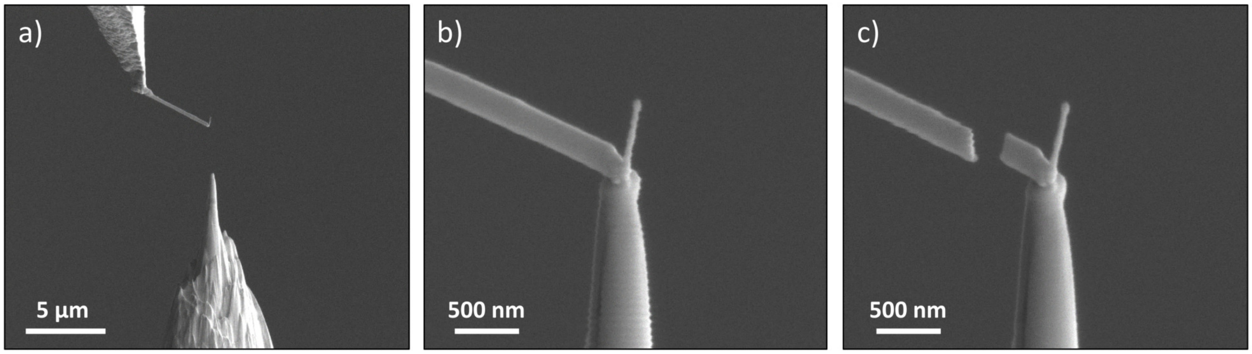

Figure 3.32: Sideview SEM images of a) a single ZnSe-CdSe NW-QD welded on a Ge NW which is fixed on a micromanipulator tip (top of the image) and an etched TEM tip (bottom of the image). b) Zoom on the NW-QD being welded at the apex of the TEM tip before and c) after the Ge NW as been cut by FIB.

A second NW-QD has been prepared with this technique and is visible in Figure 3.33. Isabelle Mouton and Pierre-Henri Jouneau from CEA-Grenoble/LEMMA will soon try to characterize this NW-QD by APT. This study will permit to further probe quantitatively the inner size and composition of our NW-QDs.

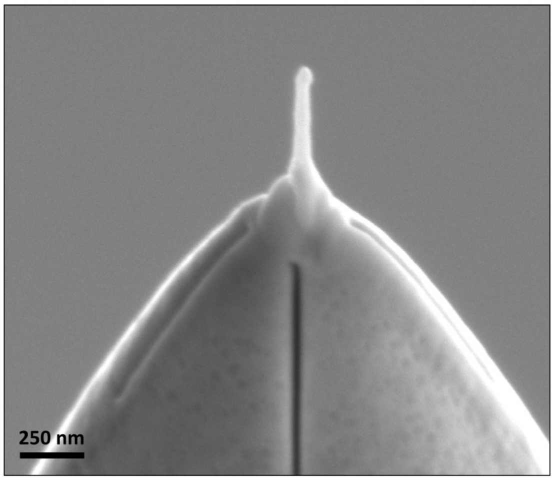

Figure 3.33: Sideview SEM image of a single ZnSe-CdSe NW-QD fixed at the apex of a TEM grid to be used for an APT characterization.

The nanomanipulation of such tiny 30 nm-diameter NW-QDs represents a feat of strength and goes beyond the scope of EDX or APT characterizations. It could be used for instance to precisely position such small nano-objects inside practical devices for quantum information applications.

## 3.4 Photoluminescence at cryogenic temperature

In this part, the NW-QDs optical properties are probed by PL measurements. The aim is to study the NW-QDs luminescence and correlate it to the previous structural and chemical characterizations. First, macroPL on the as-grown and µPL on single NW-QDs (along with polarization measurements) from $S_{2QDs}^{vacuum}$ and $S_{1QD}^{Se}$ will be presented at cryogenic temperature (5 to 10 K). Single NW-QDs will then be studied as a function of the temperature during PL and decay-time measurements to probe the QDs excitons dynamics.

### 3.4.1 QDs energy distributions of $S_{1QD}^{Se}$ and $S_{2QDs}^{vacuum}$

MacroPL measurements were performed on both $S_{2QDs}^{vacuum}$ and $S_{1QD}^{Se}$ with a 405 nm laser excitation (∼ 100 µW) at 10 K, as displayed in Figure 3.34. On both samples, the ZnSe emission is visible around 2.8 eV, along with a broad distribution ranging from 1.5 to 2.6 eV attributed to the emission of ZnSe defects (deep-level emission) within the 2D buffer layer. A sharper Gaussian distribution (well visible on $S_{1QD}^{Se}$) centered at 2.2 eV stands out and corresponds to the energy range of single NW-QDs emissions. For this reason, we attribute it to these CdSe QD emissions (highlighted by a semi-transparent orange strip on Figure 3.34). Moreover, a second Gaussian distribution is visible at higher energy only for $S_{2QDs}^{vacuum}$, centered around 2.55 eV. Since the NW of this sample are composed of two QDs inserted during 10 and 20 s, two size distributions are expected, resulting in two quantum confinement energies and consequently, two main Gaussian distributions. Therefore, for $S_{2QDs}^{vacuum}$, we attribute the low (2.2 eV) and high (2.55 eV) energy distributions to the emission of the QDs inserted during 20 and 10 s respectively.

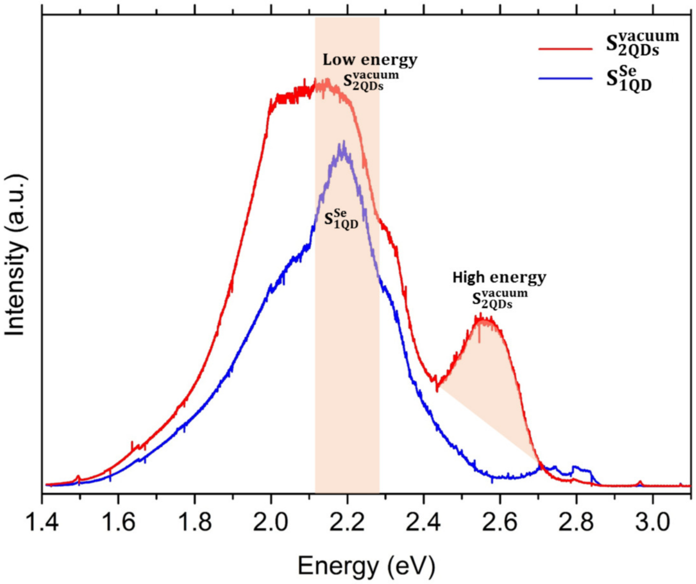

Figure 3.34: MacroPL spectra of the as-grown $S_{1QD}^{Se}$ and $S_{2QDs}^{vacuum}$ recorded at 10 K with a 405 nm laser excitation of ∼ 100 µW. The emerging part of the QDs emission distributions are highlighted by semi-transparent orange areas. For $S_{2QDs}^{vacuum}$, the two CdSe QDs emissions are visible at low (2.2 eV) and high (2.55 eV) energies.

### 3.4.2 Single NW-QDs emissions

As mentioned in Part 2.2.7, PL measurements on as-grown samples are practical ways to probe the samples luminescence but they also probe the 2D layers growing in between the NWs which can bias the results. To get a more quantitative study of the NWs luminescence, we carried out µPL measurements on single NW-QDs. To do so, the NW-QDs were gently deposited on a patterned substrate. To assure the study of single NW-QDs, we first precisely located by SEM more than a hundred well-isolated NW-QDs per sample at the surface of the pattern substrates. The aim of this method is to isolate bright NW-QDs and get a representative panel of the NW-QDs emission properties.

Due to difficulties to perform µPL on single NW-QDs using the 405 nm (3.06 eV) laser diode, we had to use the 488 nm (2.54 eV) laser (see Part 1.3.3) which cannot probe all the high energy QDs from $S_{2QDs}^{vacuum}$ . Consequently, on $S_{2QDs}^{vacuum}$ we always measured one clear QD emission (with its excitonic lines) and sometimes a second unidentified emission that might originate from the second high energy QD emission. Figure 3.35 provides an example of a single NW-QD emission from $S_{2QDs}^{vacuum}$. The *low energy* emission centered at 2.32 eV (called QD1 in the Figure) clearly corresponds to a QD emission, while the *high energy* emission (marked as QD2) might originate from a QD emission but does not provide a clear biexciton signature. Therefore, the results presented in this Chapter on $S_{2QDs}^{vacuum}$ correspond to the unique and clear QD emission from each studied NW-QDs.

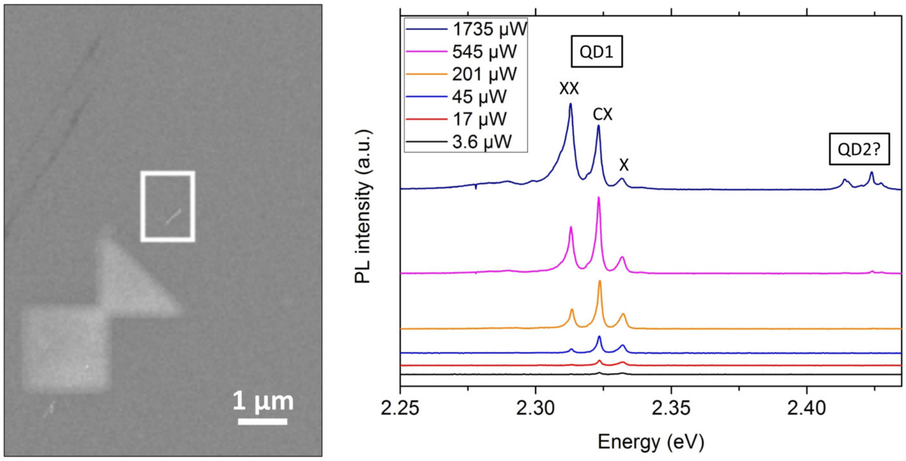

Figure 3.35: Top-view SEM image of a well-isolated single NW-QD from $S_{2QDs}^{vacuum}$ deposited on a patterned substrate and its PL spectra as a function of the 488 nm laser power.

For $S_{1QD}^{Se}$, Figure 3.36 shows an example of a single NW-QD and its typical multiexcitonic signature. The exciton (X) and biexciton (XX) lines increase linearly and quadratically with the laser power respectively, while the charged exciton (CX) stands in between.

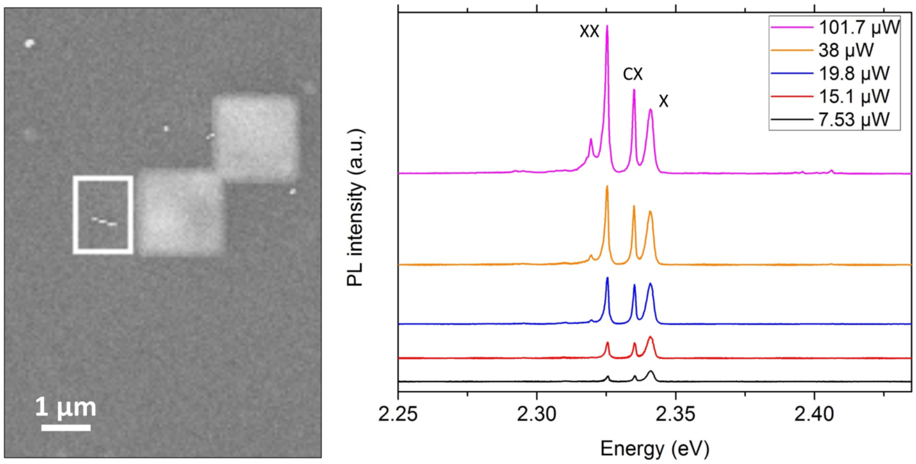

Figure 3.36: Top-view SEM image of a well-isolated single NW-QD from $S_{1QD}^{Se}$ deposited on a patterned substrate and its PL spectra as a function of the 488 nm laser power.

### 3.4.3 Polarization measurements and QDs dipoles orientations

After the identification of single and clear NW-QDs emissions, polarization measurements were carried out at cryogenic temperature with the 488 nm laser on 7 and 10 NW-QDs from $S_{2QDs}^{vacuum}$ and $S_{1QD}^{Se}$ respectively. The aim is to study the QDs dipole orientation which depends on the QD polarization in emission.

As mentioned in the Introduction Chapter Part 1.2.4, in *excitation*, the polarization is always parallel to the NW axis. This phenomenon is visible in Figure 3.37: the maximum of the polarization in excitation (in red) matches the NW axis (highlighted by a vertical blue line). In *emission*, three polarization behaviors were observed: perpendicular (radial), intermediate or parallel (longitudinal) to the NW axis, as shown in Figure 3.37.

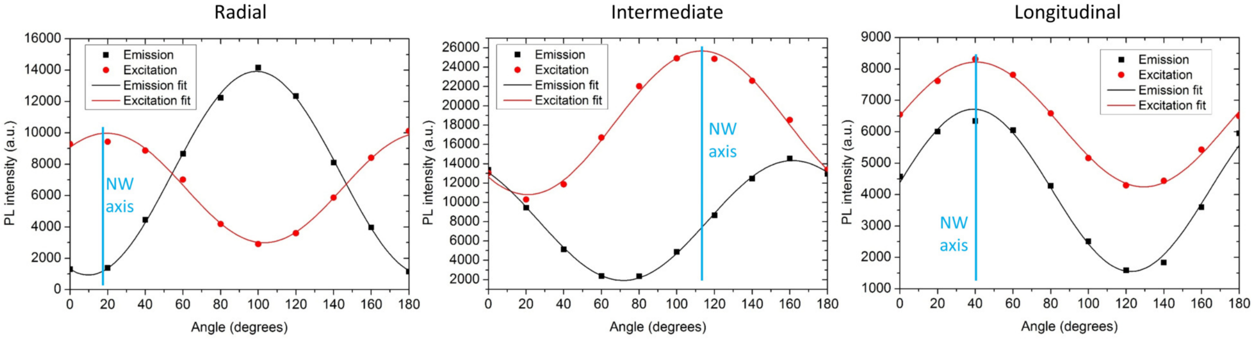

Figure 3.37: Polarization measurement in excitation (red) and emission (black) of ZnSe NWs showing three polarization behaviors: perpendicular, intermediate or parallel to the NW axis. The NWs axis have been highlighted by vertical blue line. The circles correspond to experimental points and the continuous lines to Malus law fittings of the NW polarizations.

To understand this polarization behavior, the optical selection rules and the QD aspect ratio have to be taken into account. According to the TEM studies in Part 3.2.2, the CdSe QD is composed of the ZB crystal phase. In a bulk ZB semiconductor, the HH and LH valence bands are degenerated at k = 0. When the dimensionality of the ZB material is reduced (like in a QD) the valence bands split. The HH band becomes the ground state while the LH is at a higher energy. According to Table 1.3 mentioned in Chapter 1, a HH-electron transition induces a dipole perpendicular to the z-axis. On the other hand, a LH-electron transition will induce a longitudinal polarization.

Moreover, the HH- or LH-electron transition depends on the QD aspect ratio (see Part 1.2.4), as reported by Alberto Artioli in his PhD [207] and others [45, 46]. According to our previous structural characterizations, we measured by TEM longitudinal QDs dimensions of 2-3 and 9 nm for $S_{2QDs}^{vacuum}$ and $S_{1QD}^{Se}$ respectively. In addition, EDX measurements permitted to estimate the radial QD size around 12 ± 2 nm. The aspect ratio (thickness/diameter) of the QDs from $S_{1QD}^{Se}$ and $S_{2QDs}^{vacuum}$ can be therefore approximated around 0.75 and 0.16-0.25.

The QDs from $S_{2QDs}^{vacuum}$ are thin along the NW axis, which favors a HH-electron transition and a radial dipole emission. This result is coherent with the polarization measurements reported in Table 3.3 (proportion of each polarization behavior in $S_{2QDs}^{vacuum}$ and $S_{1QD}^{Se}$) : over

7 NWs measured from $S_{2QDs}^{vacuum}$, one NW displayed an intermediate polarization and 6 NWs a polarization perpendicular to the NW axis. We can notice that no longitudinal emission was recorded for this sample.

| Sample \ Polarization | Radial | Intermediate | Longitudinal |
|---|---|---|---|
| $S_{2QDs}^{vacuum}$ (7 NW-QDs observed) | 6 | 1 | 0 |
| $S_{1QD}^{Se}$ (10 NW-QDs observed) | 2 | 6 | 2 |

Table 3.3: Number of NW-QDs grouped by polarization behavior (radial, intermediate or longitudinal compared to the NW axis) measured from $S_{2QDs}^{vacuum}$ and $S_{1QD}^{Se}$.

On the other hand, the 0.75 aspect ratio of $S_{1QD}^{Se}$ is closer to the aspect ratio of 1, which sets the limit of the HH- or LH-electron transition[16]. For this reason, a small variation of the aspect ratio could lead to a HH-electron (radial emission) or a LH-electron (longitudinal emission) transition, and various polarization measurements are expected to be observed from this sample. This result agrees with the polarization measurements reported in Table 3.3: over 10 NWs from $S_{1QD}^{Se}$, 6 displayed an intermediate polarization, 2 a radial and 2 a longitudinal polarization. Notice that the intermediate polarization is the result of the QD valence band mixing of the HH and the LH bands (see Part 1.2.4).

## 3.5 Temperature dependent photoluminescence

After the study of the samples at cryogenic temperature, we wanted to test the robustness of their luminescence as a function of the temperature. Indeed, during an increase of temperature, the carriers can escape towards nonradiative channels [208] and therefore, the PL intensity of the QDs drastically drops [209]. For single-photon applications like quantum cryptography [210], room temperature operations are desirable. These measurements have been carried out with Mathieu Jeannin from Néel Institute and Woojin Lee from Pusan University during his stay in our laboratory.

Among the many difficulties encountered during the temperature dependence measurements, the main one concerns the mechanical drift of the cryostat . The sample holder within this cryostat constantly drifts. This implies to properly refocus the laser on the studied NW every five minutes during the whole experiments to reoptimize the collected luminescence.

### 3.5.1 QDs luminescence up to room temperature

Figure 3.38 presents a µPL study of single NW-QDs from $S_{2QDs}^{vacuum}$ and $S_{1QD}^{Se}$ as a function of the temperature (5 to 300 K). At 5 K, the excitonic lines X, CX and XX are clearly visible.

---

[16] In a first approximation, the HH-LH bands splitting occurs for an aspect ratio of 1. A more detailed calculation including the QD quantum confinement and strain can shift this aspect ratio, as reported in Ref. [45, 46].

During the temperature increase, the phonons lines broadening is clearly visible [36] along with the expected red-shift of the bandgap[17] [211].

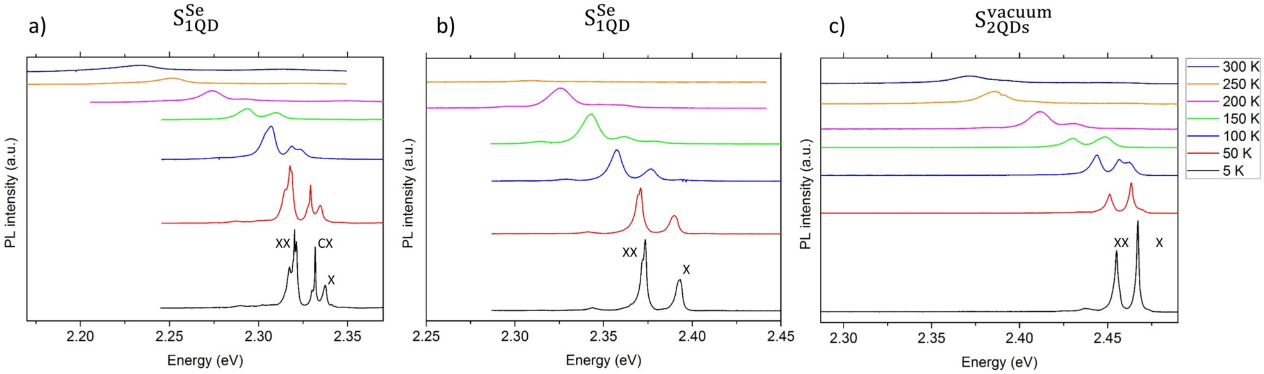

Figure 3.38: µPL measurements as a function of the temperature (from 5 to 300 K) of three NW-QDs deposited on a patterned substrate from $S^{Se}_{1QD}$ and $S^{vacuum}_{2QDs}$. Notice that for the two NW-QDs from $S^{Se}_{1QD}$, the first one in a) displays a charged-exciton while only the exciton/biexciton are visible for the NW-QD shown on b). The measurements were carried out with a 488 nm laser and a power excitation of 712 µW.

At 300 K, we have studied 7 NW-QDs from $S^{vacuum}_{2QDs}$, emitting from 1000 to 8000 counts/s and 9 NW-QDs from $S^{Se}_{1QD}$, emitting from 1000 to 11 000 counts/s. Figure 3.39 provides an example of two NW-QDs emissions at 300 K. Since the best luminescence obtained on (001)-oriented ZnSe-CdSe NW-QDs from Bounouar et *al.* in Ref.[23] was 8000 counts/s, our brightest NW-QDs is 37% brighter than previously reported by our group. Still, there is room for improvement and possibilities to further increase the NW-QDs photons emission and collection will be discussed in the Appendix.

From these µPL measurements, we observe that the NW-QDs integrated intensity is quite constant up to ∼200 K and then it decreases. The measure of the NW-QDs intensity with the CW laser is not very precise: it depends for instance on the setup optical alignment. However, the measure of the NW-QDs decay-time is more precise since it is independent of the laser intensity fluctuations and also permits to probe the NW-QDs optical properties as a function of the temperature.

---

[17] Attempts to fit the variation of the FWHM and bandgap as a function of the temperature have been made but are not presented. Indeed, the QDs are composed of a $Cd_xZn_{1-x}Se$ ternary alloy and the fitting coefficients are (supposedly) linear combinations of the pure CdSe and ZnSe fitting parameters. The large distribution of CdSe and ZnSe fitting parameters (for the FWHM and the bandgap as a function of the temperature) reported in the literature drastically increase the fitting uncertainty, making these fits sensless.

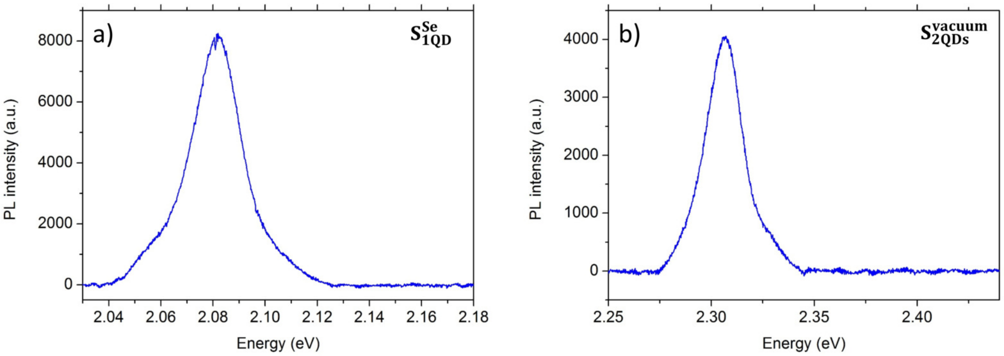

Figure 3.39: Room temperature PL of single NW-QDs from a) $S_{1QD}^{Se}$ and b) $S_{2QDs}^{vacuum}$ deposited on a patterned substrate (488 nm laser power of 700 µW and recorded during 5 s).

### 3.5.2 Temperature performance of single NW-QDs emissions

The decay-time of the NW-QDs has been measured as a function of the temperature for the X and XX lines, as shown in Figure 3.40. In most cases, we could follow the decay-time of both X and XX up to 300 K, except for some NW-QDs exciton for which: the exciton was drowned into the biexciton due to the temperature lines broadening or the exciton emission was hinders above a certain temperature. More precisely, the decay-time of 5 and 3 NW-QDs has been measured from 5 to 300 K for $S_{1QD}^{Se}$ and $S_{2QDs}^{vacuum}$ respectively.

Theoretically, the decay-time behavior as a function of the temperature $\tau(T)$ depends on the dimensionality of the studied nanostructure. When the temperature increases in a *2D quantum well*, phonons transfer energy to the excitons which populate high energy levels and relax down to the NBE. The relaxation procedure linearly increases $\tau$ as a function of the temperature [212]. In a 1D NW, $\tau(T)$ increases with the temperature as $T^{3/2}$ [213]. Finally in a QD (which corresponds to our system), $\tau(T)$ is expected to be constant as long as the electrons and hole remain in their fundamental state [209]. For all these systems, a decrease of $\tau(T)$ is expected above a certain temperature due to a coupling to non-radiative states.

For the excitons of $S_{1QD}^{Se}$, the NW-QDs labeled NW1, NW3 and NW5 have a similar behavior in temperature. From 5 to 200 K, their decay-time is a rather flat (with maybe two faint oscillations) and decreases above this temperature. NW2 and NW4 also show a similar behavior with first an increase of decay-time from 5 to 50 K, two oscillations and a decrease of the decay-time above 150 K.

For $S_{2QDs}^{vacuum}$, the three studied NW-QDs have a different behavior. NW1 and NW3 display a progressive increase of their decay-time (with different slops) up to 200 K and a decay-time decrease above this temperature, while NW2 shows a closer behavior than $S_{1QD}^{Se}$-NW2 and $S_{1QD}^{Se}$-NW4: an increase of its decay-time up to 50 K, a rather flat behavior up to 150 K and a decay-time decrease.

For both samples, the biexciton decay-time shows less variations in the whole temperature range with some fluctuations and quite similar $\tau_{XX}$ at 5 and 300 K. We can also note that at 5 K, $\tau_X$ is in some cases twice $\tau_{XX}$. Since the biexciton is always radiative, $\tau_X = 2\tau_{XX}$ corresponds to the ideal case of a radiatively limited X emission.

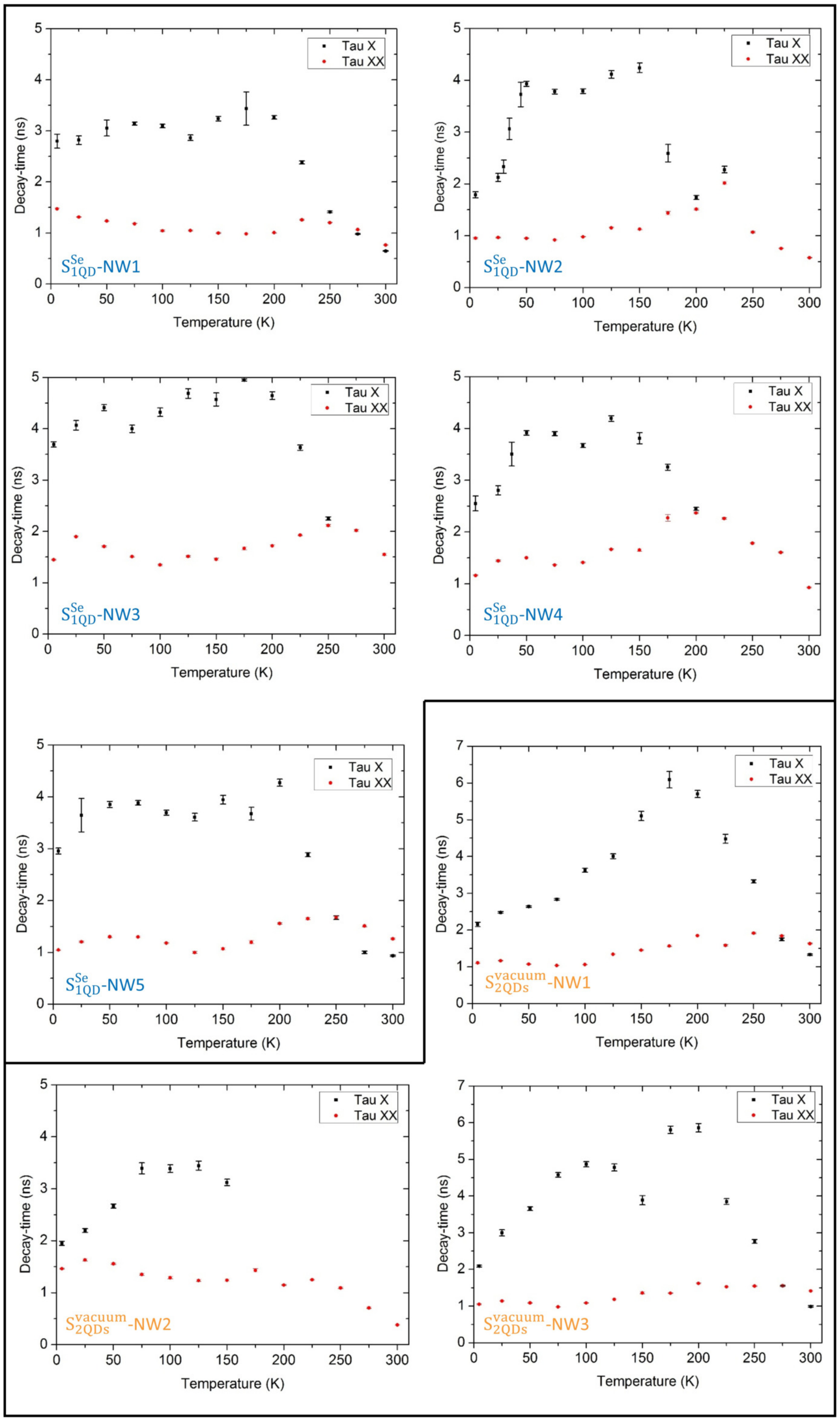

Figure 3.40: Decay-time of single ZnSe-CdSe NW-QDs as a function of the temperature from $S_{1QD}^{Se}$ (top part in blue) and $S_{2QDs}^{vacuum}$(bottom part in orange). The exciton and biexciton decay-times are displayed respectively in black and red.

To understand and model the excitons decay-time behaviors, we hypothesize that our CdSe QDs have a fundamental electron and hole state (s-state) and one excited electron and hole excited state (p-state, two times degenerated). The next excited state corresponds to a d-state (3 times degenerated) but it it not observed in our structures: the next excited state therefore corresponds to the ZnSe NW continuum of states (see Figure 3.41a).

In a QD, an increase of the decay-time as a function of the temperature can be explained by two phenomena:

1. a coupling to a dark-exciton [23], which gives a non-radiative exciton population decay. Indeed, when an exciton is trapped within a QD, the electron can have a total angular momentum $j_z^e = \pm\frac{1}{2}$ and for a HH $j_z^h = \pm\frac{3}{2}$ . Due to the conservation of the total angular momentum during the exciton recombination ($j_z^X = j_z^e + j_z^h$), the exciton has two energy levels: a first one with $j_z^X = \pm 1$ when the carriers $j_z$ have an opposite sign and a second one with $j_z^X = \pm 2$ when the carriers $j_z$ have the same sign. Since a photon has a ±1 total angular momentum, only $j_z^X = \pm 1$ is radiative: it is called *bright exciton*, in opposition to the non-radiative exciton called *dark exciton*.

2. a thermal distribution of the electron and hole to higher energy states [214, 215]. In this case, at low temperature, the carriers are in the fundamental *s*-state (even wavefunction) and can recombine. However, when the temperature increases, the hole has some probability to populate its excited *p*-state (odd wavefunction), though mainly occupying the s-state (Boltzmann distribution). The recombination of the electron in its s-state and a hole in its p-state (overlap of even and odd wavefunctions) is optically inactive (dark state). It prevents part of the electron-hole pairs to recombine and increases the excitons decay-time.

In the case (1), the coupling to a dark-exciton would result in a biexponential decay-time (short radiative and long non-radiative times) with a longer $\tau_X$ as a function of the temperature increase due to a repopulation of the bright X state by the dark X state [23]. In the case (2), a thermal coupling to electron-hole higher energy states would result in an increase of the decay-time with a monoexponential decay and this is what we observe experimentally (see Figure 3.41b).

According to these results, we used the case (2) to fit our data with a model illustrated in Figure 3.41. In this model (adapted from Ref.[209]), electrons and holes are thermally distributed on their fundamental $s$ and excited $p$ levels (electron and hole energy levels $\{E_e^s; E_h^s\}$, and $\{E_e^p; E_h^p\}$ in Figure 3.41). The QD energy levels are followed by a 1D (ZnSe NW) continuum of states $D^{1D}_{e(h)}(E) = \frac{m_{e(h)} L_{e(h)}}{\hbar\pi\sqrt{2m_{e(h)}E}}$ with $m_{e(h)}$ the electron (hole) effective mass, $L_{e(h)}$ the electron (hole) spatial extension of the wave-function describing a delocalized state and $E$ the energy. Since the exciton decay-time measurements were performed at low laser excitation power (only the exciton was visible), we consider that the QD is filled by one electron and one hole (one exciton). In this case, the sum over all the levels occupation probabilities for the electron (hole) must be unity:

$$\int D_{e(h)}(E)\,\mathcal{P}_{e(h)}(E)\,dE = 1 \tag{3.5.1}$$

with $D_{e(h)}$ the electron (hole) 1D density of states and $\mathcal{P}_{e(h)}(E) = \frac{1}{Z_{e(h)}} exp(\frac{-E}{k_B T})$ the canonical occupation probability.

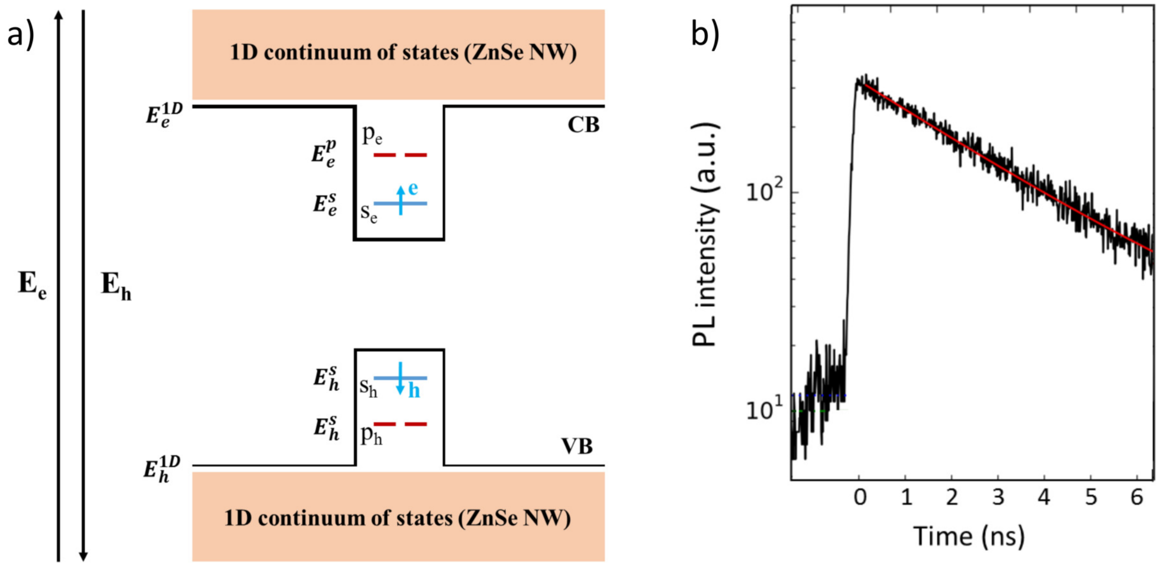

Figure 3.41: a) QD electronic structure described by two discrete levels: the fondamental $s$ (electron and hole energy levels $E_e^s$ and $E_h^s$) and excited $p$ (electron and hole energy levels $E_e^p$ and $E_h^p$) levels, surrounded by a 1D continuum of states (the ZnSe NW). b) Example of an exciton decay recorded at 75 K on NW1 from $\mathrm{S}_{1\mathrm{QD}}^{\mathrm{Se}}$ (same as in Figures 3.40 and 3.42). This decay shows a clear monoexponential behavior, representative of the measured NW-QDs decays.

By taking the QD s-state energy as the origin for both the electron and the hole, $E_{e(h)}^p$ the energy of the $p$ states and $E_{e(h)}^{1D}$ the lowest energy of the 1D continuum DOS, $D_{e(h)}(E)$ is written:

$$D_{e(h)}(E) = 2\delta(E) + 4\delta(E - E_{e(h)}^p) + D_{e(h)}^{1D}\Theta(E - E_{e(h)}^{1D}) \tag{3.5.2}$$

with $\Theta$ the Heaviside function and the factor 2 is introduced due to the spin degeneracy. Using both Equations 3.5.1 and 3.5.2, the partition function $Z_{e(h)}(T)$ is:

$$Z_{e(h)}(T) = \int D_{e(h)}(E)\, exp(\frac{-E}{k_B T})\, dE \tag{3.5.3}$$

In this model, the calculation yields:

$$Z_{e(h)}(T) = 2 + 4exp(\frac{-E_{e(h)}^p}{k_B T}) + \frac{L_{e(h)}}{\hbar}\sqrt{\frac{5m_{e(h)}k_B T}{\pi}} exp(\frac{-E_{e(h)}^{1D}}{k_B T}) \tag{3.5.4}$$

The occupation probabilities $e_s(h_s)$ and $e_p(h_p)$ of the $s$- and $p$-states respectively can be obtained:

$$e_s(h_s) = 2\mathcal{P}_{e(h)}(0) = \frac{2}{Z_{e(h)}(T)} \tag{3.5.5}$$

$$e_p(h_p) = 2\mathcal{P}_{e(h)}(E^p_{e(h)}) = \frac{2exp(-E^p_{e(h)}/k_BT)}{Z_{e(h)}(T)} \tag{3.5.6}$$

The probability for an electron (hole) to be in the 1D continuum of states is given by:

$$e_{1D}(h_{1D}) = \int_{E^{1D\,DOS}_{e(h)}}^{\infty} D^{1D}_{e(h)}\mathcal{P}_{e(h)}(E)dE = \frac{L_{e(h)}}{\hbar}\sqrt{\frac{5m_{e(h)}k_BT}{\pi}}exp(\frac{-E^{1D}_{e(h)}}{k_BT})\frac{1}{Z_{e(h)}(T)} \tag{3.5.7}$$

Then, three recombination channels are considered:

- electron-hole recombinations in a *s*- or a *p*-state with lifetimes of respectively $\tau_s$ and $\tau_p$ .
- non-radiative recombinations if the electron (hole) reaches the 1D continuum of state, with a lifetime $\tau_{nr}$.

Consequently, the decay-time is:

$$\frac{1}{\tau} = \frac{e_sh_s}{\tau_s} + 2\frac{e_ph_p}{\tau_p} + \frac{e_{1D}h_{1D}}{\tau_{nr}} \tag{3.5.8}$$

In the following, the impact of the fitting parameters is detailed. First of all, in the limit were the temperature tends toward 0 K, only the s-states are occupied. Consequently, the decay-time measured at the lowest temperature corresponds to $\tau_s$. When the temperature is increased, the *p*-states start to be populated and the decay-time $\tau$ increases due to the forbidden *s*-*p* recombinations.

In a CdSe-ZnSe type I heterostructure, the valence band offset is lower than the conduction band offset[18]. Therefore, the hole p-states will first be populated and the temperature at which $\tau$ starts to increase depends on $E^p_h$. Then, the electron p-states start to be occupied and the parameter $E^p_e$ defines the intermediate variation of $\tau$, which tends toward $\tau_p$. Notice that to get an increase of $\tau$, $\tau_p$ should not necessarily be longer than $\tau$ and an increase can be visible even if $\tau >> \tau_p$; this is due to the forbidden s-p recombinations.

At higher temperature, the holes start to couple to the 1D continuum of states (lower confinement), followed by the electrons (higher confinement): the exciton transitions are mainly provided by the confined electrons and delocalized holes; $E^{1D}_h$ and then $E^{1D}_e$ define the beginning of the second increase of $\tau$. Finally, $\tau_{nr}$ represents the asymptote of $\tau$ when the temperature tends toward infinity and the slope can be adjusted with $L_{e(h)}$. The fitted

---

[18] In a bulk CdSe-ZnSe heterostructure (type I), the conduction and valence band offset are 900 and 110 meV according to Ref. [216]

curves are displayed in Figure 3.42 and the corresponding parameters[19] are visible on Table 3.4.

By globally looking at these parameters, we can first notice that $L_h$ is always smaller than $L_e$. It indicates that the electron can be more easily delocalized than the hole. This easier delocalization of the electron can be understood by its lower mass ($\sim 0.1\ m_0$) compared to the hole ($\sim 1\ m_0$). Moreover, $E_h^p$ and $E_h^{1D}$ are smaller than $E_e^p$ and $E_e^{1D}$ respectively. This indicates that the hole excited state and coupling to the 1D continuum of states are smaller than for the electron. This results agrees with a valence band-offset smaller than the conduction band offset in the CdSe-ZnSe type I heterostructure.

The Fermi golden rule states that the exciton decay-time is inversely proportional to the overlap of the electron/hole wavefunctions:

$$\frac{1}{\tau} \propto |\,\langle \Phi_e | \Phi_h \rangle\,|^2$$

In $\mathrm{S}_{\mathrm{1QD}}^{\mathrm{Se}}$, we see that $\tau_s > \tau_p$. This indicates that the overlap of the electron/hole wavefunctions in the fundamental state is lower than in the excited state. This result can be understood with the EDX measurements which show that the CdSe QD is composed of a pure CdSe central part surrounded by a CdZnSe part. At low temperature, the hole is confined within the pure CdSe QD while the electron is delocalized in the CdZnSe part. However, when the temperature increases, the hole gets delocalized in the CdZnSe and the electron/hole wavefunction overlap increases.

On the other hand, for $\mathrm{S}_{\mathrm{2QDs}}^{\mathrm{vacuum}}$ we see that $\tau_s < \tau_p$, meaning that in this sample, we are in the opposite case: the overlap of the electron/hole wavefunctions in the fundamental state is higher than in the excited state. This result suggests that the Cd concentration in the CdSe QDs of $\mathrm{S}_{\mathrm{2QDs}}^{\mathrm{vacuum}}$ is more homogeneous (good overlap of the electron/hole wavefunctions at low temperature) than in $\mathrm{S}_{\mathrm{1QD}}^{\mathrm{Se}}$. An EDX measurement of the sample $\mathrm{S}_{\mathrm{2QDs}}^{\mathrm{vacuum}}$ is needed to confirm this hypothesis. This result also suggests that the coupling of the carriers to the 1D NW continuum is lower than in $\mathrm{S}_{\mathrm{1QD}}^{\mathrm{Se}}$ (hole or electron delocalization in the 1D continuum at higher temperature), which is indeed the case since the $\mathrm{S}_{\mathrm{2QDs}}^{\mathrm{vacuum}}$ QDs are smaller and therefore experience a higher quantum confinement. These results also agree with the higher value of $L_e$ and $L_h$ observed for $\mathrm{S}_{\mathrm{2QDs}}^{\mathrm{vacuum}}$ (higher delocalization of the carriers) compared to $\mathrm{S}_{\mathrm{1QD}}^{\mathrm{Se}}$.

---

[19] Notice that other similar models can be considered, using for instance only the electron fundamental level and the hole fundamental and excited states. In this case, less fitting parameters would be used, yielding potentially more accurate fittings. In addition, some fitting parameters obtained hereafter can be discussed, such as the rather long $\tau_{nr}$ which are expected to be experimentally shorter.

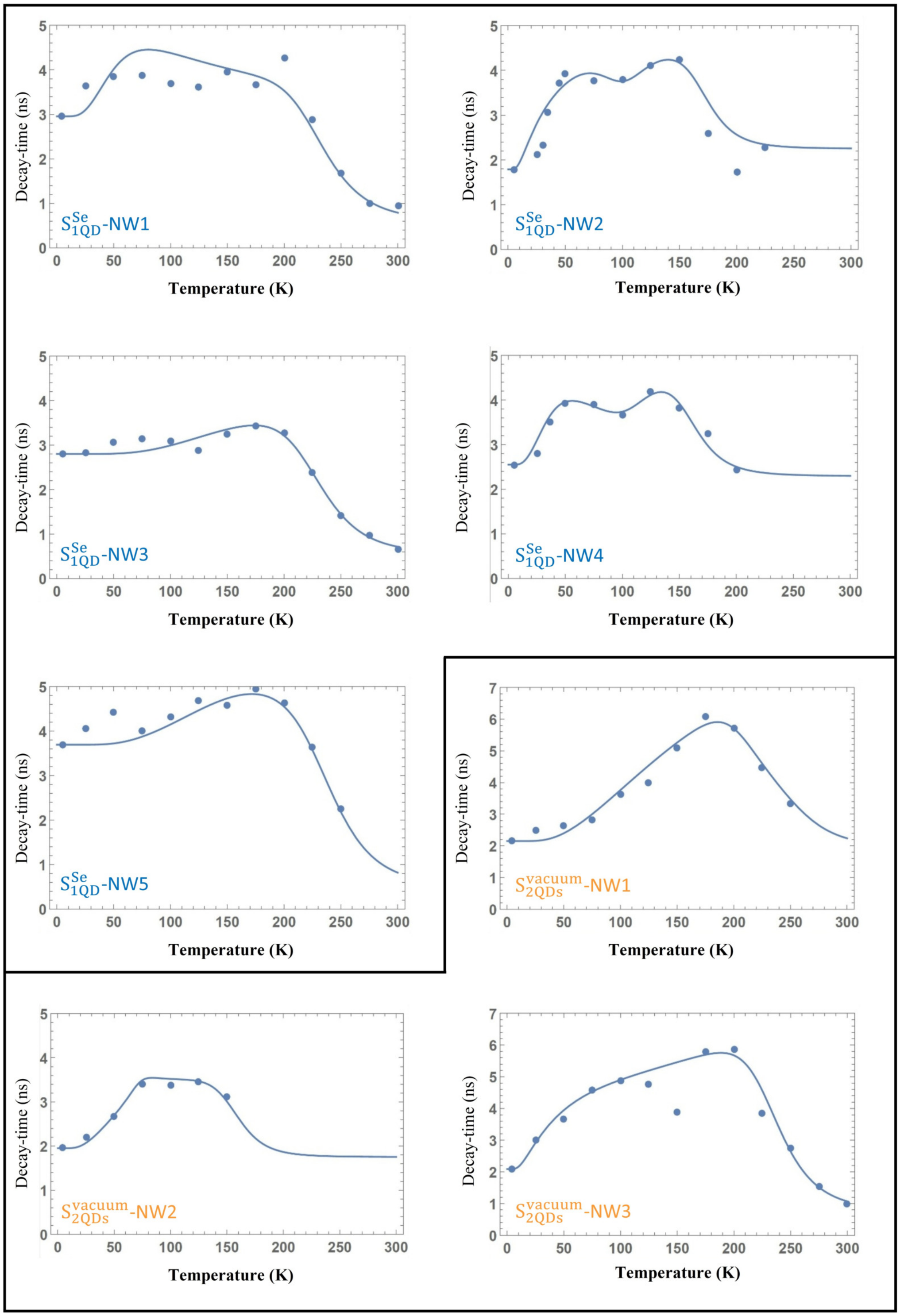

Figure 3.42: Decay-time of single ZnSe-CdSe NW-QDs from $S_{1QD}^{Se}$(top part in blue) and $S_{2QDs}^{vacuum}$ (bottom part in orange) as a function of the temperature. The dots correspond to experimental data and the continuous lines to the corresponding fitting curves.

| Sample | | $L_e$ (nm) | $L_h$ (nm) | $\tau_s$ (ns) | $\tau_p$ (ns) | $\tau_{nr}$ (ns) | $E_e^p$ (meV) | $E_h^p$ (meV) | $E_e^{1D}$ (meV) | $E_h^{1D}$ (meV) |
|---|---|---|---|---|---|---|---|---|---|---|
| $\mathrm{S}_{\mathrm{2QDs}}^{\mathrm{vacuum}}$ | NW1 | 30 | 12 | 2.15 | 9.9 | 3.9 | 16.5 | 14.5 | 310 | 255 |
| | NW2 | 24 | 14 | 1.95 | 8.8 | 3.5 | 19 | 7.5 | 185 | 84 |
| | NW3 | 8.8 | 8.6 | 2.09 | 7.65 | 1.55 | 49.5 | 3.5 | 310 | 290 |
| $\mathrm{S}_{\mathrm{1QD}}^{\mathrm{vacuum}}$ | NW1 | 3.4 | 1.2 | 2.80 | 0.25 | 1.1 | 53 | 29.5 | 275 | 255 |
| | NW2 | 6.7 | 4.7 | 1.79 | 0.15 | 4.5 | 35.5 | 2.7 | 205 | 110 |
| | NW3 | 2.5 | 1 | 3.69 | 0.15 | 1 | 71 | 24 | 288 | 273 |
| | NW4 | 2.1 | 1.9 | 2.55 | 0.65 | 4.52 | 9.5 | 5 | 155 | 110 |
| | NW5 | 8.6 | 5.2 | 2.95 | 0.75 | 1.2 | 9.5 | 9.5 | 290 | 275 |

Table 3.4: Parameters used to fit $\tau(T)$ in Figure 3.40. The interpretation of these parameters is provided in the text.

To summarize, these NW-QDs show good performances as a function of the temperature with a coupling to non-radiative channels only occurring above 200 K.

### 3.5.3 Summary of the NW-QDs optical properties

To summarize this part on the NW-QDs optical properties, the NW-QDs show at low temperature different polarization behavior: radial and longitudinal dipole orientations. These dipole orientations can be explained by the QD aspect ratio; flat or elongated (along the NW axis) QDs induce radial or longitudinal dipoles respectively. We showed the NW-QDs luminescence up to room temperature and carried out at the same time a decay-time analysis to probe the excitons dynamics. While the biexciton decay-time remains quite constant in temperature, in most cases the exciton decay-time increases at low temperature (∼ 30 K) due to a thermal coupling of the holes to excited states. The decay-time remains quite constant up above 200 K, a temperature at which it drops due to a coupling to non-radiative states.

## 3.6 Conclusion of the Chapter

In this Chapter, we demonstrated for the first time the possibility to insert one ($\mathrm{S}_{\mathrm{1QD}}^{\mathrm{Se}}$) and two ($\mathrm{S}_{\mathrm{2QDs}}^{\mathrm{vacuum}}$) CdSe QDs in ZnSe NWs grown on the (111)B surface orientation. TEM characterizations revealed that the CdSe QDs have thicknesses of 2-3 and 9 nm for $\mathrm{S}_{\mathrm{2QDs}}^{\mathrm{vacuum}}$ and $\mathrm{S}_{\mathrm{1QD}}^{\mathrm{Se}}$ respectively. Such a difference of thickness can be explained by the growth procedure of the insertion:

- for $\mathrm{S}_{\mathrm{2QDs}}^{\mathrm{vacuum}}$, the *Zn and Se fluxes are interrupted before the CdSe insertion.* During this interruption, the Au catalyst consumes its atomic elements and goes off the supersaturation needed for the growth. When the Cd and Se fluxes are sent back, a delay time is required for the Au catalyst to reach again the supersaturation and catalyze the CdSe QD growth. The resulting flat QDs (0.16-0.25 aspect ratio) agrees with PL polarization measurements in emission which mainly show radial dipole orientations.

- for $\mathrm{S}_{\mathrm{1QD}}^{\mathrm{Se}}$, the *Se flux remains before the CdSe insertion*. Our results suggest that this remaining flux permits to keep the Au catalyst in (or close to) the supersaturation regime. In this case, when the Cd and Se fluxes are sent, the QD growth can start directly without delay time, resulting in a longer QD size along the NW axis. Due to their longer size along the NW axis, these QDs showed a distribution of dipole orientations, in agreement with the QD aspect ratio of 0.75 close to the LH-HH crossing (see Figure 1.12).

A composition analysis revealed that the CdSe QD from $\mathrm{S}_{\mathrm{1QD}}^{\mathrm{Se}}$ are composed of a central pure CdSe zone surrounded by a CdZnSe area (with a decreasing Cd content). Decay-time measurements as a function of the temperature confirmed this observation, suggesting that at low temperature, the hole is trapped within the pure CdSe zone and gets delocalized in the CdZnSe area at higher temperature. These decay-time measurements also revealed that the exciton starts to couple to non-radiative channels above 200 K, showing the high temperature resistance of such NW-QDs. We can notice that a temperature around 200 K is easily reached by simple thermoelectric cooler using the Peltier effect. Since we also showed the NW-QDs luminescence up to room temperature, it positions these nano-objects has realistic candidates for applied SPS .

In the dynamics to develop and push characterization techniques to their limits, atom-probe tomography - another composition sensitive technique recently used for semiconductors - was calibrated for II-VI Se-based semiconductors by studying CdSe SK-QDs embedded in a ZnSe matrix. This technique represents a challenge for the characterization of our small (30 nm) NW-QDs and we showed the first step of this characterization by placing such a single NW-QD at the top of a TEM tip. This feat of strength goes beyond the scope of EDX or APT characterizations and could be used for instance to precisely position such small nano-objects inside practical devices for quantum information applications.

Chapter 4

# Enhancement of the light collection

## Contents

In the previous Chapter, we measured the decay-time of single NW-QDs which are surprisingly longer than SK-QDs decay-times [209]. To understand this result, we want to verify whether such a modification of the exciton decay-time is due to a difference of QD shape or dielectric environment. To clarify this point, we bury the NW-QDs in an homogeneous matrix, to recreate the SK-QDs environment with a NW-QD structure. In a second part, we address the problem of the photon collection. To be as efficient as possible and for realistic SPS applications, we want to collect a maximum of light emitted from the NW-QDs. Consequently, we demonstrate the possibility to form photonic wires by coating the NW-QDs with a thick dielectric shell. Using PL measurements and simulations, we show that these photonic wires clearly enhance the photon collection.

## 4.1 Modification of the QDs decay-time

In the previous Chapter, Part 3.5, the decay-time of our NW-QDs has been measured, ranging from 1.75 to 3.75 ns at 5 K. These values are substantially higher than the decay-time of CdSe SK-QDs buried in a ZnSe matrix, usually measured from 0.2 to 0.5 ns [209]. *Is it due to a difference of QDs shape or to their different dielectric environment?* A way to clarify this issue is to bury the NW-QDs in an homogeneous matrix, recreating the SK-QDs environment with a NW-QD structure. To do so, we grew the same NW-QDs sample as $S_{2QDs}^{vacuum}$ with the NW-QDs buried in a ZnMgSe matrix. The aim is to determine if the presence of such a ZnMgSe matrix lowers the NW-QDs decay-times.

### 4.1.1 ZnSe-CdSe NW-QDs buried in a ZnMgSe matrix

To grow NW-QDs buried in a ZnMgSe matrix, small NW-QDs[1] were first grown at 400°C with the same CdSe insertions as in sample $S_{2QDs}^{vacuum}$, followed by a long ZnMgSe deposition[2] at 220°C. At this temperature, the 2D growth in between the NWs in faster than the NWs (radial and longitudinal) growth. If the ZnMgSe shell is deposited during a sufficiently long time (here 30 min), it is possible to almost completely bury the NW-QDs in a ZnMgSe matrix. We successfully succeeded to grow such a structure visible in Figure 4.1 which provides a view of the sample and a zoom on a single NW-QD. The NW-QDs are almost completely buried: they can be recognized by their stone-like head composed of ZnMgSe (Figure 4.1b) and are surrounded by small craters. Figure 4.1c provides a side view illustration of the aimed structure.

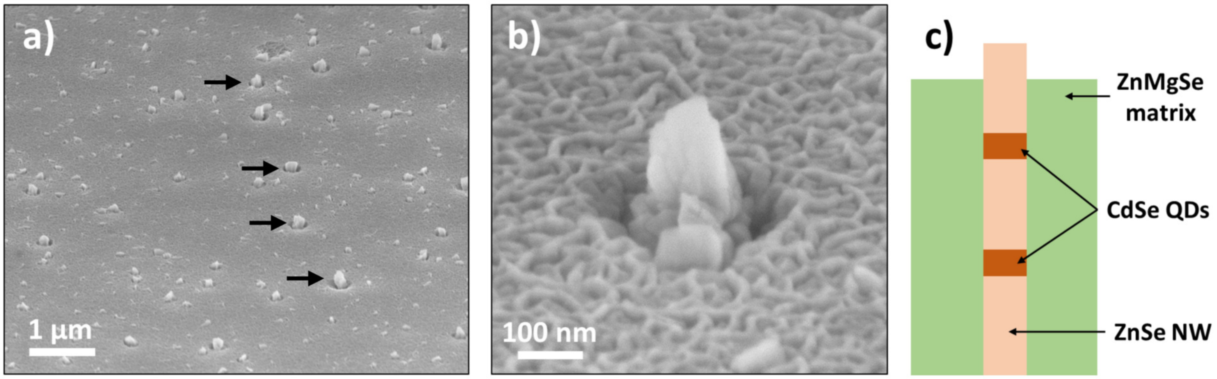

Figure 4.1: Tilted-view SEM images (65°) of the buried NW-QDs sample: ZnSe NWs with two CdSe QD insertions (10 and 20 s) grown at 400°C under Se-rich conditions and a nominal $Zn_{0.90}Mg_{0.10}Se$ shell deposited during 30 min at 220°C. The NW-QDs are almost completely buried and can be recognized thanks to their stone-like ZnMgSe shell head. a) Ensemble (black arrows show some well visible buried NW-QDs), b) zoom on the stone-like head of a single NW-QD and c) side view illustration of the aimed structure.

---

[1] 5 min of ZnSe (∼ 150 nm) + 10 s of CdSe (first CdSe insertion, under vacuum) + 3 min 30 s of ZnSe (∼ 100 nm) + 20 s of CdSe (second CdSe insertion, under vacuum) + 42 s of ZnSe (∼ 20 nm).

[2] 30 min of nominal $Zn_{0.90}Mg_{0.10}Se$ deposited at 220°C (∼ 260 nm-thick buffer).

### 4.1.2 Modification of the NW-QDs decay-time highlighted by TRPL

TRPL measurements were carried out on the buried NW-QDs at 10 K with the pulsed Fianium WhiteLase Supercontinuum fiber laser tuned at 485 nm (2.556 eV). Since the density of buried NW-QDs is low, single NW-QDs were probed on the as-grown sample by µPL. This was done by moving the laser beam at the surface until we could record clear X and XX emissions, confirmed by power dependence measurements and characteristic of the QDs emissions. Figure 4.2 presents the decay-time $\tau$ of X and XX of various buried NW-QDs at 5 K (Figure 4.2a), 200 K (Figure 4.2b) and 250 K (Figure 4.2c). Each temperature explores different QDs and statistical values are presented in Figure 4.2d.

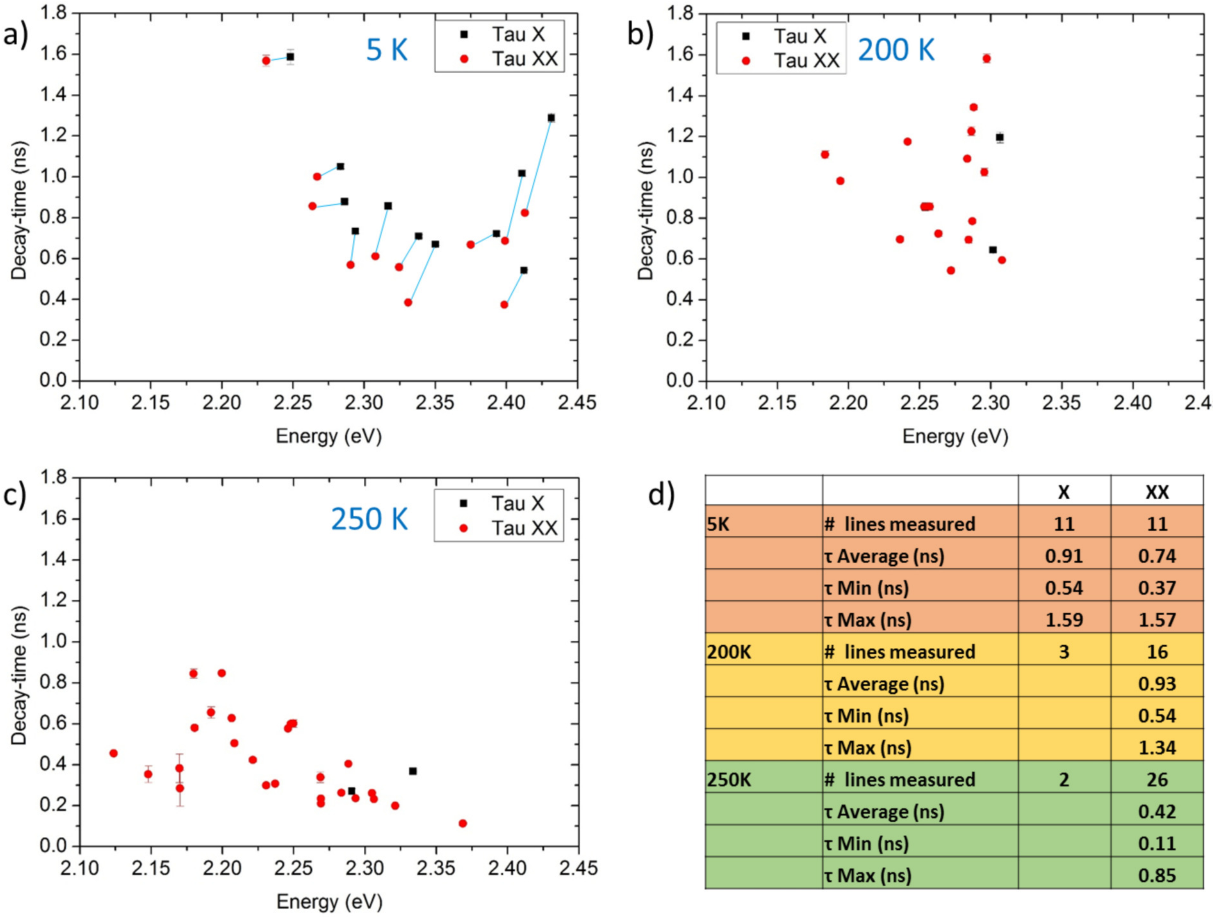

| | | X | XX |
|---|---|---|---|
| 5K | # lines measured | 11 | 11 |
| | τ Average (ns) | 0.91 | 0.74 |
| | τ Min (ns) | 0.54 | 0.37 |
| | τ Max (ns) | 1.59 | 1.57 |
| 200K | # lines measured | 3 | 16 |
| | τ Average (ns) | | 0.93 |
| | τ Min (ns) | | 0.54 |
| | τ Max (ns) | | 1.34 |
| 250K | # lines measured | 2 | 26 |
| | τ Average (ns) | | 0.42 |
| | τ Min (ns) | | 0.11 |
| | τ Max (ns) | | 0.85 |

Figure 4.2: Decay-time of the X and XX lines of buried NW-QDs recorded with a 485 nm-tuned Supercontinuum laser at a) 5 K (the X and XX lines are linked by a blue segment), b) 200 K and c) 250 K. d) Statistics on these decay-time measurements with the number of excitonic (X and XX) lines measured, $\tau$ average, min and max.

Statistically, a red-shift of the QDs emissions is observed as a function of the temperature, as expected [211]. The exciton decay-time was easily recorded at 5 K and difficult to record at 200 and 250 K due to its low intensity or because it was covered by the XX emission (due to the lines broadening in temperature [36]). On the other hand, the XX signal could be measured[3] up to 250 K: $\tau_{XX}$ remains quite constant (with a slight increase) from 5 K (0.74 ns) to 200 K (0.96 ns) and drops above this temperature (0.42 ns at 250 K). This result corresponds to what has been observed in the previous Chapter with $S^{Se}_{1QD}$ and $S^{vacuum}_{2QDs}$: a quite constant NW-QDs decay-time (with a slight increase) up to 200 K and a drop above this temperature due to a coupling to non-radiative channels. The key point is that the buried NW-QDs decay-time is lower than the NW-QDs decay-time measured in Chapter 3. *This result clearly shows the reduction of the NW-QDs decay-time due to the modification of the QD environment.*

However, one could argue that during these µPL measurements, we could have measured the decay-time of Cd composition fluctuations in between the NW-QDs. Indeed, during the CdSe QD insertion in the ZnSe NWs, the CdSe sent onto the sample also contributes to the substrate 2D growth (see Figure 1.21) and results in 2D Cd-rich zones in between the NW-QDs (similarly to what has been observed by APT in Part 3.3.2).

It has been observed that on a (001) surface [41], these Cd-rich zones emit light: their high density and size distribution gives rise to a Gaussian distribution on the PL spectra. When such a (001)-oriented sample is shined with a laser, the shape of the laser spot is uniformly bright whatever the laser position at the surface. On the other hand, on a (111) surface, these zones do not seem to emit light. When a laser is shined, only localized emission spots are visible, that we attribute to the NW-QDs emission.

Several arguments confirm that this emission indeed comes from the NW-QDs: in the case of 2D Cd-rich zones (like SK-QDs), the decay-time drop is expected to appear at temperatures ranging from 80 to 150 K [209] and here, we observe it above 200 K. In addition, decay-times of the 2D Cd-rich zones are expected to be lower (0.2 to 0.6 ns at 5 K) than our values (see Figure 4.2d). To confirm that the decay-time measured in this section originate from buried NW-QDs, we carried out Time-Resolved CathodoLuminescence (TRCL) measurements.

### 4.1.3 Time-resolved cathodoluminescence on buried NW-QDs

As mentioned in the Chapter 1, CL measurements are carried out at 5K in a SEM. An electron beam (e-beam) is used to visualize and excite (with a nanometric precision) a sample of interest. The emitted light is then collected with a parabolic mirror and analyzed (more details in Part 1.3.3).

Recently, a TRCL setup has been implemented in our laboratory by Fabrice Donatini - who helped us to perform these measurements - and very few TRCL measurements have been carried out due to the complexity of the setup. Indeed, to give some examples, an additional electronic part (not detailed here) needs to be connected and manually configured for time-resolved measurements (at least 3h to mount it), the luminescence (emitted and

---

[3] Since both X and XX could be probed at 5 K (linked by a blue segment in Figure 4.2a), we can also get a statistical value of the biexciton binding energy (exciton minus biexciton energy) of 17 meV, with minimum and maximum values of 12 and 23 meV respectively. Such high biexciton binding energies is a key parameter for room temperature single-photon emission, as discussed in Part 1.1.1.

collected) is lower compared to µPL measurements and thermal drifts are experienced during the measurements along with charging effects of the samples, which also induce drifts. Consequently, a constant realignment of the setup is needed.

This fantastic method permits to record the decay-time of single emitters with a nanometric spatial resolution. It consists in focusing the e-beam on a light emitter and to deflect the e-beam periodically (similarly to a pulsed laser excitation for TRPL measurements). This e-beam is controlled by an external voltage. In our case, when the voltage is set to 0.03 V or - 0.03 V, the e-beam excites a buried NW-QDs or is deflected far away (see Figure 4.3a). Small voltage fluctuations can occur, slightly deflecting the e-beam which excites less the QD. This phenomenon is visible around 12 ns in Figure 4.3a and explains the corresponding drop of the buried NW-QD emission in Figure 4.3b.

The relevant information is obtained when the e-beam is deflected from the QDs (from 25 to 50 ns in Figure 4.3). In this case, the QD is no longer excited and the recorded CL intensity decreases, allowing to measure the QD decay-time.

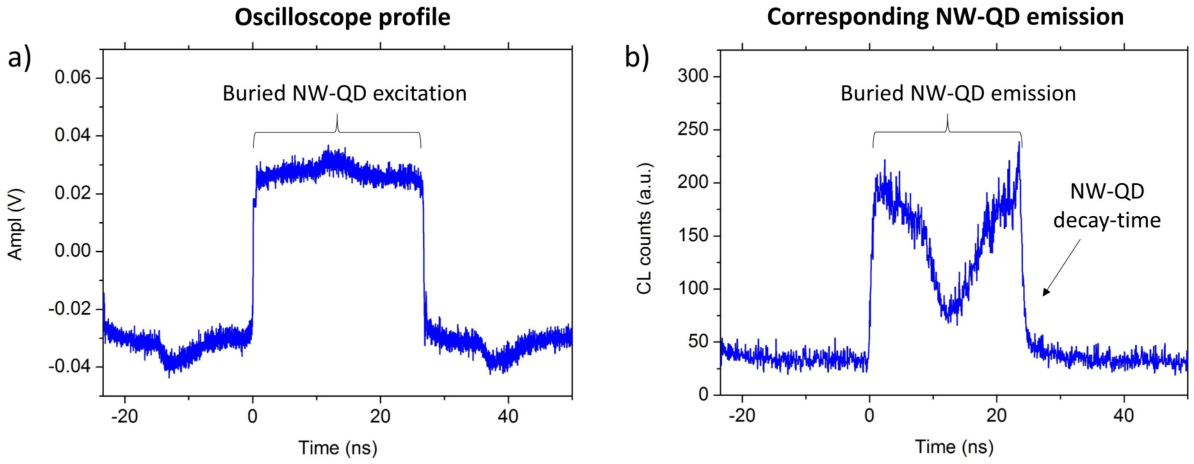

Figure 4.3: Comparison between a) the external voltage controlling the periodic e-beam deflection and b) the corresponding buried NW-QD emission.

Figure 4.4 presents two examples of buried NW-QDs decay-times (fitted with monoexponential curves) recorded by TRCL and Table 4.1 summarizes all the decay-time measurements of $\tau_X$ and $\tau_{XX}$. These TRCL decay-times values are comprised within the TRPL decay-times reported in Figure 4.2d, confirming the efficient reduction of the NW-QDs decay-time due to the QD environment modification.

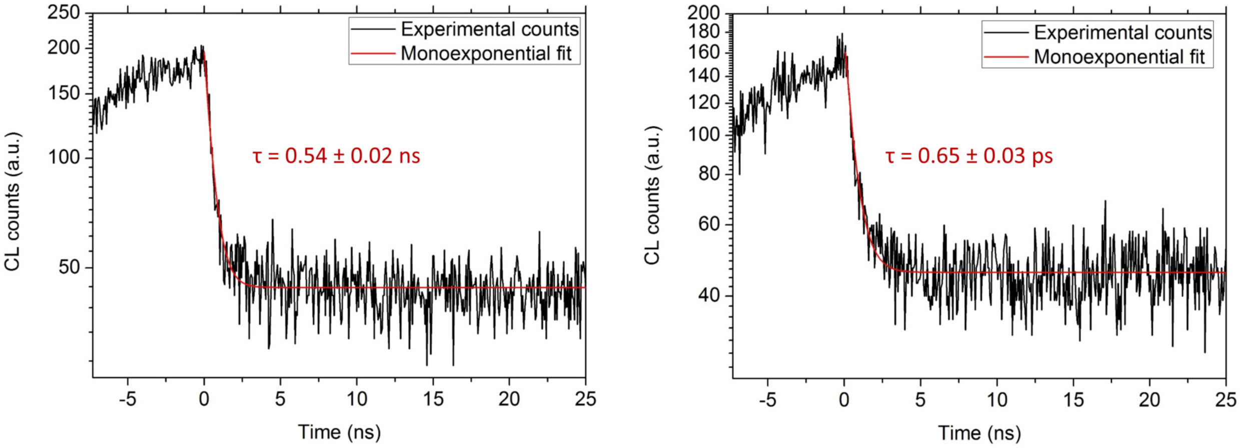

Figure 4.4: Decay-times recorded by TRCL at 5K on two buried NW-QDs. The experimental signal and the fitted curves are displayed in black and red respectively.

| | $\tau_X$ (ns) | $\tau_{XX}$ (ns) |
|---|---|---|
| TRCL | 0.70 ± 0.04 | 0.64 ± 0.06 |
| TRCL | 0.62 ± 0.04 | 0.45 ± 0.03 |
| TRCL | | 0.65 ± 0.03 |
| TRCL | | 0.54 ± 0.02 |
| min TRPL | 0.54 | 0.37 |
| max TRPL | 1.59 | 1.57 |

Table 4.1: Summary of the decay-times $\tau_X$ and $\tau_{XX}$ recorded on the X and XX lines of four buried NW-QDs by TRCL measurements. These decay-times are compared to the min and max $\tau_X$ and $\tau_{XX}$ values obtained by TRPL, showing that the TRCL decay-times are comprised in the TRPL interval.

### 4.1.4 Analysis of the NW-QDs decay-time modification by the dielectric environment

The TRPL and TRCL measurements clearly show a reduction of the NW-QDs decay-time when these NW-QDs are embedded in a ZnMgSe matrix. To the best of our knowledge, this is the first time that such a decay-time modification of quantum emitters by the dielectric environment is reported for NW-QDs. It has been reported for other systems like molecules [217], colloidal QDs [218, 219], doped insulators [220, 221] and also through the so-called Purcell effect [222].

When we look at the radiative spontaneous emission rate (the inverse of the decay-time) of an emitter, it can be described by the Fermi's golden rule which states in the dipole approximation that:

$$\frac{1}{\tau} \propto \rho(\omega) |\left\langle i|\overrightarrow{d}.\overrightarrow{\epsilon}|f\right\rangle|^2 \tag{4.1.1}$$

with $\tau$ the emitter decay-time, $\rho(\omega)$ the density of final states and $\left\langle i|\overrightarrow{d}.\overrightarrow{\epsilon}|f\right\rangle$ the dipole matrix element with $\overrightarrow{d}$ the dipole displacement vector and $\overrightarrow{\epsilon}$ the vacuum electromagnetic field inducing the dipole's spontaneous emission. When the emitter is placed inside a material of refractive index $n$, the electromagnetic modes proportionally tighten along the three spatial dimensions[4]: $\rho(\omega)$ is therefore proportional to $n^3$.

Moreover, in a dielectric, the vacuum energy is equal to:

$$E_{vacuum} = \frac{\hbar\omega}{2} = \frac{1}{2} n^2 \epsilon_0 ||\overrightarrow{\epsilon}||^2 V \tag{4.1.2}$$

From Equation 4.1.2, we deduce that $\epsilon \propto \frac{1}{n}$, meaning that in dielectric medium, the vacuum electric field is divided by a factor $n$ compared to the vacuum case. Consequently, we deduce that: $|\left\langle i|\overrightarrow{d}.\overrightarrow{\epsilon}|f\right\rangle|^2 \propto \frac{1}{n^2}$ and $\frac{1}{\tau} \propto n$.

More quantitatively, in the dipole approximation and a homogeneous medium, the spontaneous emission rate is :

$$\Gamma_{rad}(\omega) = \frac{1}{\tau_{rad}} = \frac{\omega^3 n |\mu_{12}|^2}{3\pi\epsilon_0\hbar c^3} = \frac{4\alpha\omega^3 \boldsymbol{n} | < i|r|f > |^2}{3c^3} = n\Gamma_{vacuum}(\omega) \tag{4.1.3}$$

with $\omega$ the emission frequency, $\tau_{rad}$ the radiative decay-time, $\mu_{12}$ the transition dipole moment, $\epsilon_0$ the vacuum permittivity, $\hbar$ the reduced Planck constant, $c$ the speed of light in vacuum and $\alpha$ the fine structure constant. In this equation, $\Gamma_{rad}$ is indeed proportional to $n$ (or $\tau_{rad}$ is inversely proportional to $n$). Let us take an example and consider a QD with a decay-time $\tau^{vacuum}$ in vacuum (refractive index of 1). If this same QD is placed in a medium of refractive index $n$, its decay-time $\tau^{medium}$ will be:

$$\tau^{medium} = \frac{\tau^{vacuum}}{n} \tag{4.1.4}$$

This equation clearly highlights that the QD (in our case, the CdSe QD) environment modifies the QD decay-time. To calculate the expected value of $\tau^{medium}$, we need the reference decay-time of our emitters in vacuum ($\tau_X^{vacuum}$) and the refractive index of the ZnMgSe medium.

$\tau_X^{vacuum}$ can be estimated from the decay-time measurements carried out in the previous Chapter on single NW-QDs from $\mathrm{S}_{\mathrm{1QD}}^{\mathrm{Se}}$ and $\mathrm{S}_{\mathrm{2QDs}}^{\mathrm{vacuum}}$ (see Part 3.5.2). These NW-QDs can be considered to emit in vacuum if they have a longitudinal dipole orientation. In the case of a radial dipole orientation, the electromagnetic screening effect induced by the NW geometry increases the decay-time (see Part 1.2.4). For this reason, only the decay-time of

---

[4] See the calculation of $\rho(\omega)$ in the Black Body theory (for instance in Ref.[223]) and with $c = v/n$.

longitudinal and intermediate[5] dipole orientations measured from $S^{Se}_{1QD}$ and $S^{vacuum}_{2QDs}$ are used for the calculation. Notice that the dipole orientation in the buried NW-QDs does not play any role since both dipoles experience the same refractive index environment by symmetry.

For the refractive index of $Zn_{1-x}Mg_xSe$, we can use Ref. [224] which provides the following Sellmeier-type relation:

$$n^2(\lambda) = A + \frac{B\lambda^2}{\lambda^2 - C} \tag{4.1.5}$$

with A, B and C constants. For a Mg composition of 10% which corresponds to our nominal value: A = 3.949, B = 1.719 and C = 0.115. Note that by convention, this formula uses the wavelength in units of µm. At 550 nm (average CdSe emission wavelength), we obtain $n_{Zn_{90}Mg_{10}Se}(550\,nm) = 2.63$.

Using Equation 4.1.4, we can extract the theoretical value of $\tau^{medium}$:

$$\tau^{medium}_{theoretical} = \frac{\tau^{vacuum}}{n_{Zn_{0.90}Mg_{0.10}Se}} = \frac{2.54}{2.63} = 0.96\,\text{ns} \tag{4.1.6}$$

Compared to the experimental value $\tau^{medium}_{experimental}$ of 0.91 ns, we have a deviation of 5.2 %. A larger deviation could have been expected since the NW-QDs decay-times $\tau^{vacuum}_X$ were measured on NW-QDs deposited on the $Al_2O_3$ spacer of the patterned substrates: consequently, the NW-QDs are not strictly speaking in vacuum and this $Al_2O_3$ spacer is expected to changes the NW-QD environment. However, it might be possible that we measured some radial dipole contributions from the intermediate dipole orientations, which would increase the NW-QDs decay-times due to the screening effect: therefore, both effects could have canceled each other.

Nevertheless, despite the approximations made in this model, the theoretical and experimental values are in a good agreement: *the decay-time of the dipole has been successfully reduced by inserting the NW-QDs into a higher refractive index medium.*

### 4.1.5 Conclusion

To summarize this part, we compared the decay-time of two samples: ZnSe-CdSe NW-QDs *in vacuum* (measured in the previous Chapter) and buried *in a ZnMgSe medium* by using PL and CL measurements. A modification of the NW-QDs decay-time has been observed, resulting from the different NW-QDs environment. This modification can be quantified using the Fermi's golden rule. It states that the NW-QDs decay-time is inversely proportional to its surrounding refractive index $n$ and the calculated decay-time modification is in good agreement with the experimental value. This reduction of the emitters decay-time could be used to higher its decay-rate in the GHz regime for quantum information applications, increasing the number of emitted (and collected) photons per second.

---

[5] with an absolute angular difference from the longitudinal dipole below 45°, indicating that the longitudinal dipole has a stronger effect than the radial dipole on the polarization.

## 4.2 Photonic wires to increase of the photon collection

In the previous section, we showed a modification of the NW-QDs decay-time. It is induced by a modification of the NW-QDs refractive index environment which modifies the density of accessible electromagnetic modes $\rho(\omega)$ (see Equation 4.1.1), similarly to the Purcell effect. One difference [6] is that the Purcell effect (taking place in a cavity) only increases $\rho(\omega)$ in a certain direction ($\vec{k} \perp$ to the cavity) while we increased $\rho(\omega)$ isotropically.

To efficiently exploit the NW-QDs photon collection, the increase of $\rho(\omega)$ should no longer be isotropic: we need to favor the increase of $\rho(\omega)$ in the photon collection orientation. This is what happens in a photonic wire which guides the photons along its axis. In such a photonic wire, the dipole orientation plays a key role that we discuss in the next parts.

### 4.2.1 Guided modes in a wire

**Dipole emission**

In the simple case of a dipole in vacuum oscillating along the z-axis , the dipole time-averaged Poynting vector is given by:

$$\langle S \rangle = \frac{\mu_0 p_0^2 \omega^4}{32\pi^2 c} \frac{sin^2\theta}{r^2} \overrightarrow{r} \qquad (4.2.1)$$

with $\mu_0$ the vacuum permeability, $p_0$ the dipole moment, $\omega$ the dipole's angular frequency, $c$ the speed of light in vacuum, $\theta$ the angle according to the z-axis, $r$ the distance from the dipole and $\overrightarrow{r}$ the unit vector in the direction of $r$. The collected emission in a certain direction (fixed by $\theta$) is proportional to the time-averaged Poynting vector (proportional to $sin^2\theta$). Therefore, the dipole radiation pattern is not isotropic but shows a toroidal shape with a maximal emission perpendicular to the dipole axis (see Figure 4.5). The same discussion is true in an homogeneous medium. **Consequently, the photon collection depends on the dipole's orientation.**

Figure 4.5 illustrates this point for a radial and a longitudinal dipole orientation (according to the z vertical axis) and we can see that more light is collected in the microscope objective (sketched in blue) for a radial dipole orientation.

---

[6] In the Purcell effect, the emitter needs to be in resonance with the cavity mode and at its position, $\epsilon$ is high. In our case, $\epsilon$ decreases compared to the vacuum case ($\epsilon \propto \frac{1}{n}$ and $n$ increases).

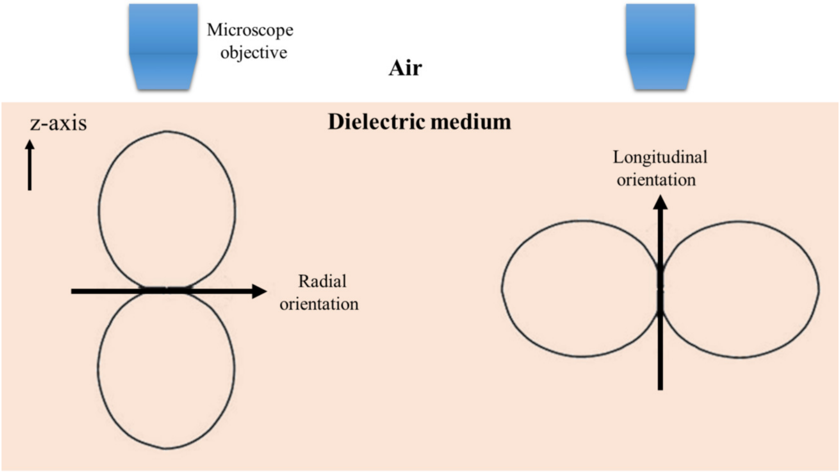

Figure 4.5: Illustration of dipole emissions in an homogeneous dielectric medium. The radial and longitudinal (according to the z-axis) dipole orientations and there radiation pattern in vacuum are sketched to highlight their difference for the photon collection in a microscope objective. Indeed, more light is expected to be collected from the radial dipole.

### Coupling of a dipole to an infinite wire

Henderson et *al.* [225] studied the dipole emission in an infinite wire. They expressed the total electric field emitted by a dipole as a sum of guided and radiative modes, and studied the effect for a dipole at the center (red) or at the interface (blue) of the wire. They show that the emitted light is guided differently depending if the dipole is radial (perpendicular to the wire axis, Figure 4.6a) or longitudinal (along the wire axis, Figure 4.6b).

In Figures 4.6a and b, let us only focus on the case of a dipole centered in the wire (red curves). We can see that the radial dipole emission is more guided than the longitudinal dipole emission (60% compared to 42%). This effect can be physically understood by looking at Figures 4.6c and d which show the emission of a radial and a longitudinal dipole in vacuum superimposed to a wire. From these illustrations, we can see that the radial dipole emission is naturally directed toward the wire axis (to the contrary of the longitudinal dipole).

For the very small wire diameters, the radial dipole guided power gradually increases while the core diameter increases, meaning that this dipole progressively starts to couple to the wire guided modes. On the other hand, the longitudinal dipole guided power is null until the wire diameter reaches approximately 0.3 µm (normalized threshold diameter of $rn/\lambda \sim 0.43$), meaning that this dipole is uncoupled to the wire guided modes if the wire diameter is below the diameter's threshold.

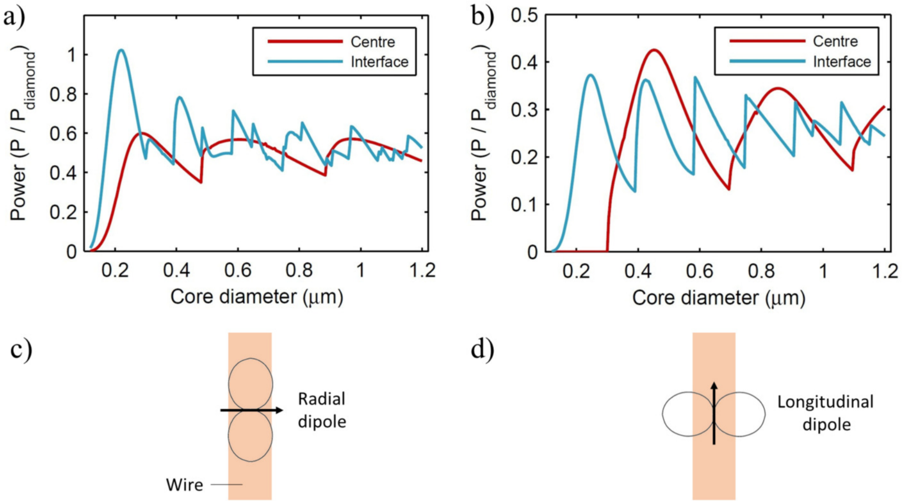

Figure 4.6: Top part: power captured into a fiber guided modes vs. core diameter from a dipole placed at the center (red) and on the wire side (blue). The power is normalized to the total power emitted by the dipole in a bulk (homogeneous) diamond material. a) Radial and b) longitudinal dipole orientations. Figure extracted from Ref.[225]. Bottom part: emission of c) a radial and d) a longitudinal dipole in vacuum superimposed to a wire, showed for visualization purpose.

### Radial dipole guided modes

The results of Henderson et *al.* show that a radial dipole orientation is favorable to efficiently guide the photon along an infinite wire axis. This paragraph focuses on this radial orientation. In this part, we describe the first guided modes which propagate in an infinite wire of diameter $d$ oriented along the z-axis. In the cylindrical basis $(r,\, \theta,\, z)$, the electromagnetic field of the guided modes can be written in the following form (more details can be found in Ref.[226]):

$$\left\{\begin{array}{c} E(r,t)\\ H(r,t)\end{array}\right\} = \left\{\begin{array}{c} E_{l,m}(r,t)\\ H_{l,m}(r,t)\end{array}\right\} e^{jl\theta}e^{j(\omega t-k_z z)} \tag{4.2.2}$$

with $l \in \mathbb{N}$ and $m \in \mathbb{N}^\star$. Such a waveguide generally supports hybrid modes (see Figure 4.7 for a representation of the first guided modes) that are a combination of Transverse Electric (TE; $\mathrm{E_z} = 0$) and Transverse Magnetic (TM; $\mathrm{H_z} = 0$): if $\mathrm{E_z}$ dominates, the mode is called $\mathrm{EH_{lm}}$(TM-like mode) and if $\mathrm{H_z}$ dominates, it is called $\mathrm{HE_{lm}}$ (TE-like mode). The fundamental guided mode $\mathrm{HE_{11}}$ is always supported by the waveguide without any cutoff. Ref.[227] - which considers photonic wire-like structures composed of GaAs ($n_{GaAs} = 3.45$) - mentions that for an on-axis emitters (which is our case), the wire remains single mode for $r \cdot n/\lambda = 0.63$ (cutoff of $\mathrm{HE_{12}}$[7]). It also mentions that an optimal transverse confinement (radial dipole) is obtained for $r \cdot n/\lambda = 0.405$, which is still in the single mode regime.

---

[7] Off-axis emitters only remain in the monomode regime for $d/\lambda < 0.23$ which corresponds to the cutoff of $\mathrm{TE_{01}}$ and $\mathrm{TM_{01}}$.

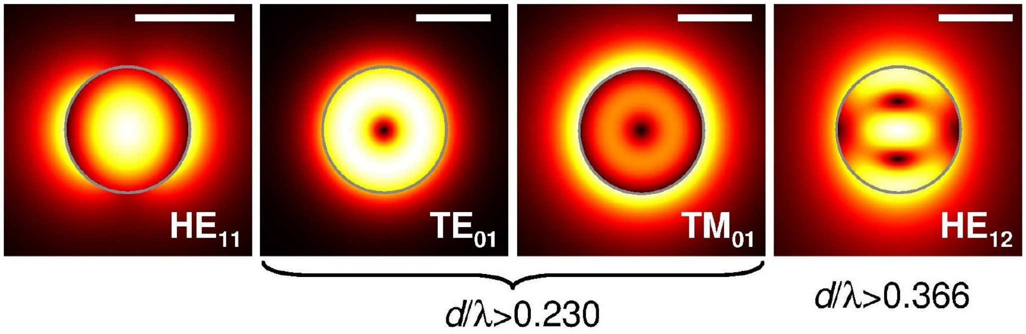

Figure 4.7: Representative map of the in-plane electrical field amplitude associated with the first guided modes in an infinitely-long wire having a circular section. The profile of $HE_{11}$ is calculated for $d/\lambda = 0.25$, for the other modes $d/\lambda = 0.37$. The scale bars represent 200 nm. Note that off-axis emitters only remain in the monomode regime for $d/\lambda < 0.23$ which corresponds to the cutoff of $TE_{01}$ and $TM_{01}$, while on-axis emitters remain in the monomode regime for $d/\lambda < 0.366$ (cut-off of $HE_{12}$). This Figure is extracted from Ref.[227].

These results apply to infinite wires. However, in our case, we would like to cover our NW-QDs with a thick dielectric shell to create photonic wires, efficiently guide the photons along the wire axis and increase the photon collection. How can we deposit such a thick dielectric shell experimentally?

### 4.2.2 Possibility to form photonic wires from thin NW-QDs

In the previous paragraphs, we have seen that an optimal guiding of the photons along a wire axis is reached for $r \cdot n/\lambda = 0.405$. We would like to reach such an optimal diameter by covering our NW-QDs with a thick shell. To minimize the shell deposition, a high refractive index material should be used. In an ideal case, we could have deposited a thick ZnMgSe shell after the NW-QD growth. However, its low deposition speed on the NWs sidewalls and the high 2D growth in between the NWs (see Part 2.2.7) does not permit to grow such a large ZnMgSe shell without burying the NWs. To overcome this limitation, we deposited dielectric shells around the passivated NW-QDs by atomic layer deposition.

#### Deposition of a dielectric shell by atomic layer deposition around the NW-QDs

To create photonic wires out of our nanostructures, we first had to find a way to experimentally deposit a dielectric shell around the NW-QDs. We used Atomic Layer Deposition (ALD) which is a ML by ML deposition technique. It consists in sequential self-limiting surface reactions and is ideal to deposit materials with a high conformality and an atomic layer control. In a typical ALD process for a binary compound like $Al_2O_3$, two gas phase molecules are alternatively exposed to a substrate in an ABAB sequence. First, the (A) precursor reacts with the surface atoms until it saturates, then the reaction chamber is purged to remove the (A) gas. Next, the (B) precursor is introduced in the chamber to react with the new surface groups to form a ML of the desired material. Again, the chamber is purged.

The AB cycle can be reproduced to deposit a precise number of atomic layers in order to reach the desired layer thickness. For instance, $Al_2O_3$ ALD[8] is carried out using alternating $Al(CH_3)_3$ and $H_2O$ exposures [228]:

$$\begin{aligned} A) \quad & AlOH^\star + Al(CH_3)_3 \rightarrow AlOAl(CH_3)_2^\star + CH_4 \\ B) \quad & AlCH_3^\star + H_2O \rightarrow AlOH^\star + CH_4 \end{aligned} \tag{4.2.3}$$

The deposition of several materials was performed in a Cambridge Nanotech Savannah S100 deposition machine:

- $TiO_2$(precursor: TTIP[9] ),
- $ZrO_2$(precursor: TDMAZr[10]),
- $HfO_2$(precursor: TDMAHf[11]) ,
- $Al_2O_3$(precursor: TMA[12]).

Table 4.2 summarizes the conditions of these depositions with the precursors, temperature, deposition speed (maximum variations of 10 %), the aimed thickness of each deposition and the refractive index of the materials at 550 nm. We wanted to favor the deposition of high refractive index materials since in this case, a smaller shell thickness is needed to guide the photons [13]

| | $TiO_2$ | $ZrO_2$ | $HfO_2$ | $Al_2O_3$ |
|---|---|---|---|---|
| Precursors | TTIP | TDMAZr | TDMAHf | TMA |
| Temperature (°C) | 260 | 250 | 250 | 250 |
| Experimental deposition speed (nm/cycle) | 0.028 | 0.076 | 0.1 | 0.09 |
| Number of cycles | 1857 | 829 | 780 | 855 |
| Deposited thickness (nm) | 52 | 63 | 78 | 77 |
| Refractive index (at λ= 550 nm) | 2.65 [229] | 2.17 [230] | 2.12 [231] | 1.77 [232] |

Table 4.2: Summary of the ALDs carried out to deposit $TiO_2$, $ZrO_2$, $HfO_2$ and $Al_2O_3$ on the NWs. For all the depositions: the pressure was $4.10^{-1}$ Torr, each pulse lasted 15 ms and the purge 5 s.

Figure 4.8 shows SEM images of ZnSe NWs grown at 350°C under Se-rich conditions (presented in Part 2.2.2, average height: ∼ 400 µm, base and top diameter: ∼ 20 and ∼ 11

---

[8] The overall reaction is $2Al(CH_3)_3 + 3H_2O \rightarrow Al_2O_3 + 3CH_4$

[9] Titanium(IV) isopropoxide: $C_{12}H_{28}O_4Ti$

[10] Tetrakis(ethylmethylamido)zirconium(IV): $C_{12}H_{32}N_4Zr$

[11] Tetrakis(dimethylamino)hafnium: $C_8H_{24}HfN_4$

[12] Trimethylaluminum: $C_6H_{18}Al_2$

[13] The normalized diameter is $d_{normalized} = r \cdot n/\lambda$ so for a fixed $d_{normalized}$, if $n$ increases, $r$ decreases.

nm) before (Figure 4.8a) and after the deposition of a dielectric shell of $TiO_2$ (Figure 4.8b), $ZrO_2$ (Figure 4.8c), $HfO_2$ (Figure 4.8d) and $Al_2O_3$ (Figure 4.8e). All the NWs coated with a dielectric material are ZnSe NWs, except for the $TiO_2$ deposition which has been carried out on a ZnTe NW (height: 1.4 µm, base and top diameter: 140 and 10 nm). These coated NWs are sorted out according to the roughness of their shell: $TiO_2$ displays the highest shell roughness while $Al_2O_3$ shows a very conformal and smooth deposition around the NW. For these later reasons, we chose to keep $Al_2O_3$ for future ALD to create conformal photonic wires. This result shows the possibility to create photonic wire from thin NW-QDs with a QD deterministically positioned along the NW axis.

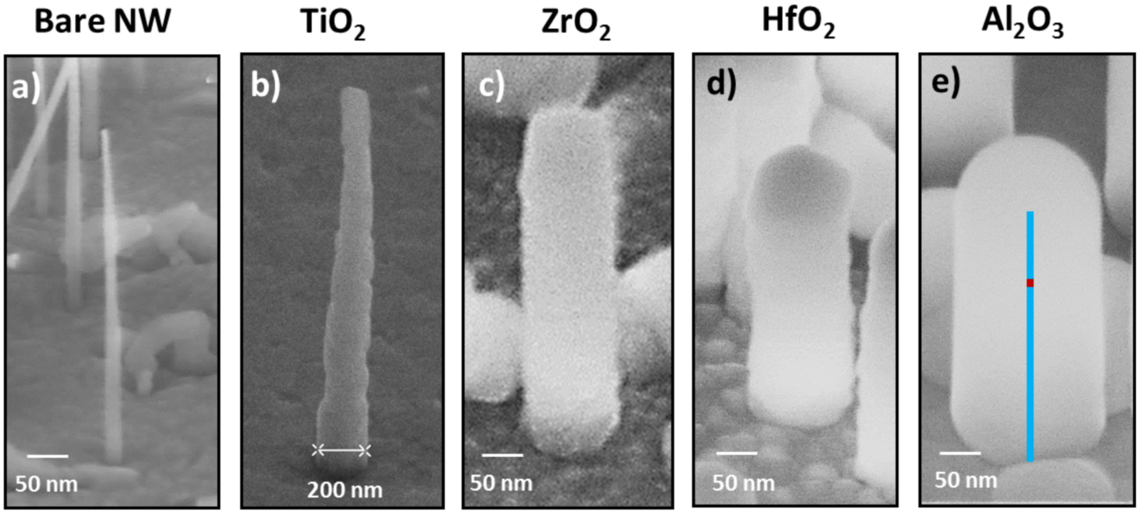

Figure 4.8: a) Bare ZnSe NWs. b) NW covered with a dielectric shell of $TiO_2$, c) $ZrO_2$, d) $HfO_2$ and e) $Al_2O_3$ (the NW and QD are sketched respectively in blue and red for visualization purpose). Note that all the coated NWs are similar to the bare ZnSe NW displayed in a), except for the $TiO_2$ deposition displayed on b) which has been carried out on a ZnTe NW (height: 1.4 µm, base and top diameter: 140 and 10 nm).

These results apply to infinite wires. However, in our case, we would like to cover our NW-QDs with a thick dielectric shell to create photonic wires to efficiently guide the photon along the wire axis and increase the photon collection. The photons guiding in such a structure cannot be solved analytically; for this reason, we used simulation tools presented in the next part.

### 4.2.3 Photons guiding in photonic wires: FDTD simulations

In this part, we are interested in the guiding of photons emitted from a ZnSe-CdSe NW-QD covered with a thick dielectric shell, creating a photonic wire. Such a photonic wire would be able to efficiently guide along its axis the photons emitted by the NW-QD. For vertically oriented photonic wires, the guided photons will therefore be collected more efficiently by our microscope objective during µPL experiments, as illustrated in Figure 4.9. The possibility to create such photonic wires experimentally will be later demonstrated in Part 4.2.2.

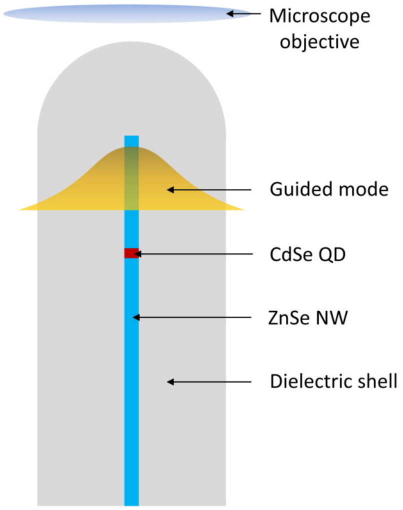

Figure 4.9: Illustration of a our NW-QDs covered by a thick dielectric shell to create a photonic wire. Guided modes can propagate along the photonic wire axis. These guided modes would be more efficiently collected by the microscope objective used during the µPL measurements.

In a first approximation, the optical properties of such a photonic wire can be studied via a dipole placed within a wire of finite dimensions. As previously mentioned, a similar problem of a dipole emitting in an infinite optical fiber has been treated analytically by Henderson et *al.* and their study reveals that the power emitted by a dipole in a fiber strongly depends on the dipole orientation: for this reason, we studied both cases. Note that our photonic wire is quite different from Henderson's model due to its finite dimension and its different edges (a spherical dome and a flat tip, see Figure 4.10). Thus, we need to implement a more precise numerical analysis and used Finite Difference Time Domain (FDTD) simulations which discretizes space and time to solve Maxwell equations. More information about the working principle of this simulation technique can be found in Refs.[233, 234].

### Simulation geometry

We carried out 3D FDTD calculations using the simulation package MEEP (MIT Electromagnetic Equation Propagation) [235]. This study has been the result of a paper [236] in Physica Status Solidi (C). The simulated NW-QD has a typical length of 500 nm and a 10 nm-diameter with a QD positioned 100 nm below its apex, as displayed in Figure 4.10a. The influence of the photonic wire diameter on the emitted power has been studied. The QD is approximated by a dipole with a free-space wavelength of 550 nm (CdSe QDs mean emission) defined as the distance unit. The ZnSe-CdSe NW-QD has been neglected since it represents less than 1% of the total photonic wire volume for a 50 nm shell. The photonic wire is a thick free standing photonic wire with a shape similar to the experimentally coated NWs (Figure 4.10a). To simulate an open boundary problem, we defined perfectly matched absorbing layers with a thickness of 1 unit at the boundaries of the computational space. Each time-dependent simulation was carried out during 20 time units to reach the stationary regime with a grid resolution of 20 (number of points per unit distance). The emitted power and radiation pattern of this photonic structure has been calculated.

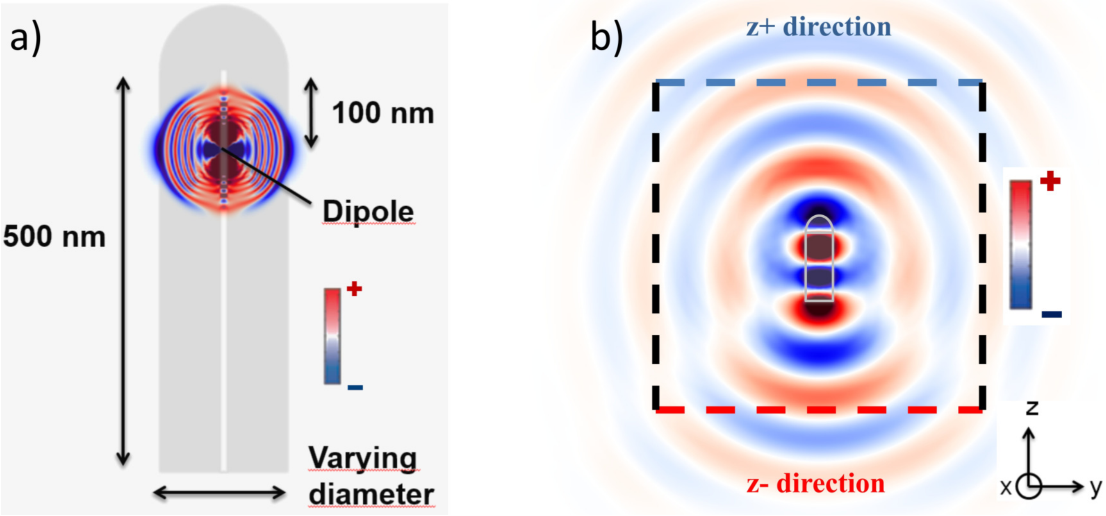

Figure 4.10: a) Illustration of the geometry used for the FDTD simulations. The bare free-standing photonic wire with its top spherical dome is displayed in grey. The dipole is set to a free-space wavelength of 550 nm (CdSe photon emission) and its electromagnetic field's color scale goes from dark blue (negative) to white (zero) to dark red (positive). The ZnSe/CdSe/ZnSe NW-QD (displayed in white at the center of the photonic wire for visualization purpose) is neglected. b) Propagation of the dipole's electric field (stationary regime) through the faces of the square box (dashed lines) used to calculate the radiated power. The faces of the box corresponding to the blue and red dashed lines are used to calculate the power emitted along the z+ and z- directions, respectively. The photonic wire is sketched in grey at the center of the image and the dipole is oriented along x (radial).

The flux of electromagnetic energy $E_i$ has been computed through the six surfaces $\sigma_i$ of a square box during a time interval [0 ; 20] (in MEEP time units) as :

$$E_i = \int_0^{20} \int_{\sigma_i} S(r,t) \cdot d\sigma_i \, dt \tag{4.2.4}$$

with $S(r,t)$ the Poynting vector and $\sigma_i$ the outward-facing normal surface vectors (see Figure 4.10b). The power flowing through each surface can be calculated as $p_i = E_i / \sum_j E_j$.

The simulations were carried out with a photonic wire refractive index of 2. This refractive index is a good compromise to study the effect of $Al_2O_3$ (n=1.77), $ZrO_2$ (n=2.17) and $HfO_2$ (n=2.12), materials we will experimentally deposit in Part 4.2.2. To make the results more general and independent of the refractive index, they will be displayed in the normalized and dimensionless unit $r \cdot n/\lambda$.

### Power guided in the photonic wires

Figure 4.11 displays the normalized power emitted along the photonic wire axis (z direction) as a function of its radius. The z+ and z- directions are respectively directed toward the top and the base of the photonic wire. The total emitted power along the z axis (sum of the power emitted along z+ and z-) can reach maxima of 74% (radial dipole and $r \cdot n/\lambda$ ∼0.42) and 52% (radial dipole and $r \cdot n/\lambda$ ∼0.85) of the total emitted power. The radial orientation of the dipole is more favorable to collect the photons along the photonic wire axis and its optimal normalized diameter of $r \cdot n/\lambda$ ∼0.42 is in good agreement with the analytical calculation of guided modes in an infinite wire treated in Part 4.2.1 ($r \cdot n/\lambda = 0.405$, relative difference ∼ 3%). Note that for this geometry, more power is emitted toward the bottom of the wire (toward z-, Figure 4.11). To collect these photons in the z+ direction, a mirror could be deposited at the base of the wire to reflect this downward emission upwards, increasing the extraction efficiency as designed by Claudon et *al.* [25]. This possibility will be later discussed in Parts 4.3 and 4.3.

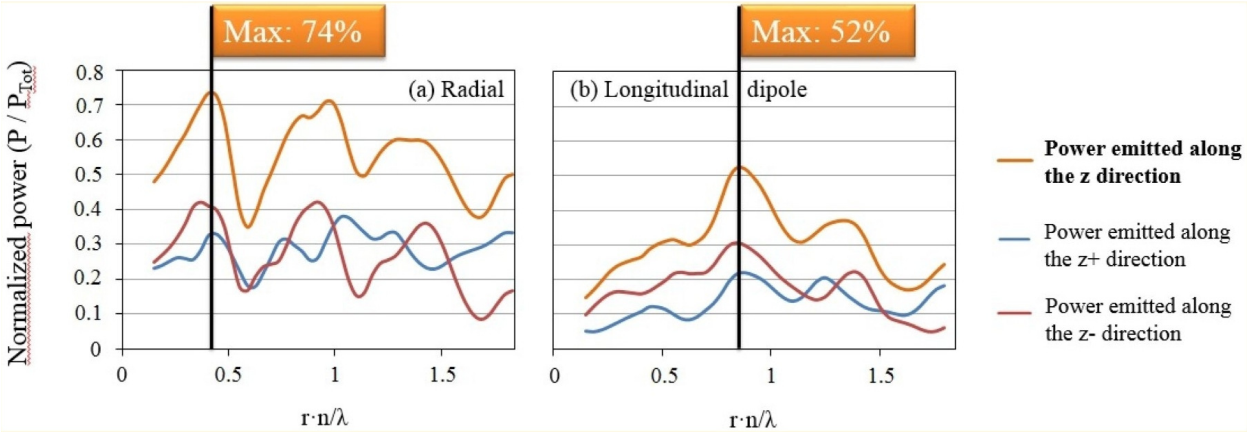

Figure 4.11: Normalized power emitted along the wire axis as a function of the dimensionless parameter parameter $r \cdot n/\lambda$ (with $r$ the photonic wire radius) in the case of a) a radial and b) a longitudinal dipole. The z+ and z- directions are respectively directed toward the top and the base of the photonic wire.

### Radiation patterns

In a second step, the radiation pattern of the optimal photonic wires (with a maximum on-axis emitted power) has been calculated. Similarly to the previous paragraph, the total dipole's radiated power can be computed by integrating the time-average Poynting vector over a closed spherical surface in the far-field:

$$P_{rad} = \frac{1}{2} Re\{[E(\theta,\phi) \times H^{\star}(\theta,\phi)] \cdot dS\} \tag{4.2.5}$$

with E and H the electric and magnetic fields. Upon reaching the steady-state, the time-average radial component of the Poynting vector was determined for the spherical surface in the far-field. The radius of such a sphere must be superior to $\lambda/(2\pi)$ since the dimension of the photonic wire is smaller or of the order of $\lambda$. Figure 4.12 shows the calculated radiation pattern of our photonic wires (with optimal diameters) for radial and longitudinal dipoles. We can see that the longitudinal dipole emission is less guided than for the radial dipole. The radial dipole's emission is clearly directional and could mainly be collected with a NA of 0.6 (compared to 0.7 for the longitudinal dipole), and mainly directed toward the photonic wire base.

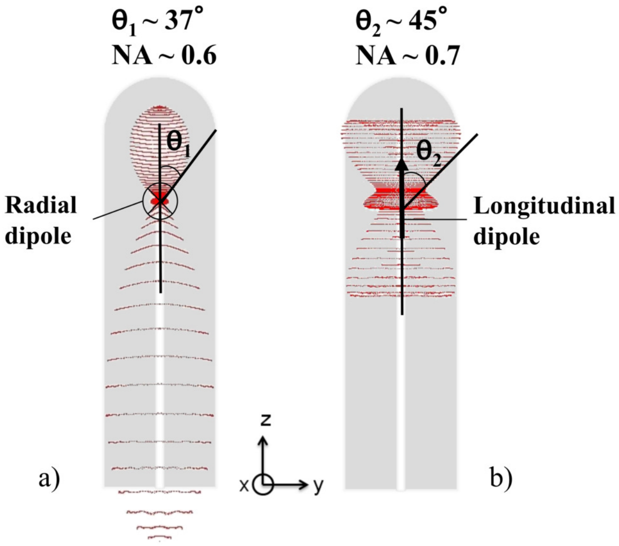

Figure 4.12: Radiation pattern of a) a radial and b) a longitudinal dipole in a photonic wire (refractive index of 2) with a diameter optimized to funnel the maximum power along its axis. The photonic wire is sketched approximately for visualization purpose.

### Summary of the ALD and FDTD simulations

We have shown the possibility to form photonic wires by covering the NW-QDs with a thick dielectric shell using ALD. Using FDTD simulations, the optimal diameter of a free-standing photonic wire used for an efficient photons extraction has been calculated, along with the corresponding radiation patterns. The radial dipole orientation is favorable (compared to the longitudinal dipole) due to its high directionality and higher maximum on-axis guided power. The position of the QD along the NW axis is another parameter to be optimized and will be discussed in Part 4.3.

In the next part, we experimentally investigate the effect of the photonic wire geometry on the light collection.

### 4.2.4 Effect of the dipole orientation on the light collection

#### PL investigation of the photonic wires

For quantum information applications, the single mode regime is ideal[14] [237]. In Part 4.2.1, we have seen that a wire remains single mode for $r \cdot n/\lambda = 0.63$ and the FDTD simulations showed that an optimal confinement (for a radial dipole) is obtained for $r \cdot n/\lambda = 0.42$, which is still in the single mode regime. For an $Al_2O_3$ coating of the NW-QDs, this normalized diameter corresponds to a total diameter around 260 nm: 120 nm of $Al_2O_3$ deposited around the 10 nm-radius NW-QDs from sample $S_{1QD}^{vacuum}$ used for the ALD depositions treated in this Part. The growth procedure of $S_{1QD}^{vacuum}$ is detailed in Part 3.1.2: it consists in one QD of CdSe inserted in a ZnSe NW (400°C under Se-rich conditions) with a $Zn_{0.83}Mg_{0.17}Se$ shell deposition at 220°C during 5 min. An important parameter is that the NW-QDs density has been reduced to probe individual NW-QDs at the surface of the as-grown sample.

After carefully splitting several pieces of the $S_{1QD}^{vacuum}$, we carried out ALD depositions on each piece with various $Al_2O_3$ shell thicknesses ranging[15] from 20 to 110 nm in radius. The result is displayed in the upper part of Figure 4.13. Then, µPL has been performed at 10 K with a pulsed Fianium WhiteLase Supercontinuum fiber laser tuned at 485 nm (2.556 eV). By performing power dependence measurements, we could obtain every time clear excitonic signatures (X, CX and XX) from the NW-QD emissions (Figure 4.13 bottom part).

We wanted to study quantitatively the collection efficiency as a function of the $Al_2O_3$ shell radius by µPL. This procedure could not be performed with a CW laser, since the collected intensities would depend on the PL experimental conditions. For instance, with a CW laser the NW-QDs are very sensitive to laser power fluctuations which are linear for the exciton and quadratic for the biexciton. To be insensitive to these effects, we carried out the µPL measurements using a pulsed laser at saturation. In pulsed excitation, the intensity of X and XX increase with the laser power (see Figure 4.14a). At a high enough excitation power, one exciton (biexciton) per pulse can be emitted (see the radiative cascade in Part 1.1.1): this is the saturation regime - visible in Figure 4.14b - which is insensitive to the laser power fluctuations.

In this regime, one exciton is recorded at each laser pulse (in the ideal case). An experimental saturation phenomenon is displayed in Figure 4.14. During the increase of the pulsed laser excitation power, the exciton intensity also increases until it reaches a plateau: this is the saturation regime. To compare the intensity of the photonic wires as a function of their radius, all the measurements were carried out at saturation.

---

[14] In this regime, the $HE_{11}$ (fundamental) mode has a field distribution very close to that of an ideal Gaussian mode necessary for quantum information applications

[15] We aimed a maximum thickness of 120 nm and obtained 110 nm experimentally.

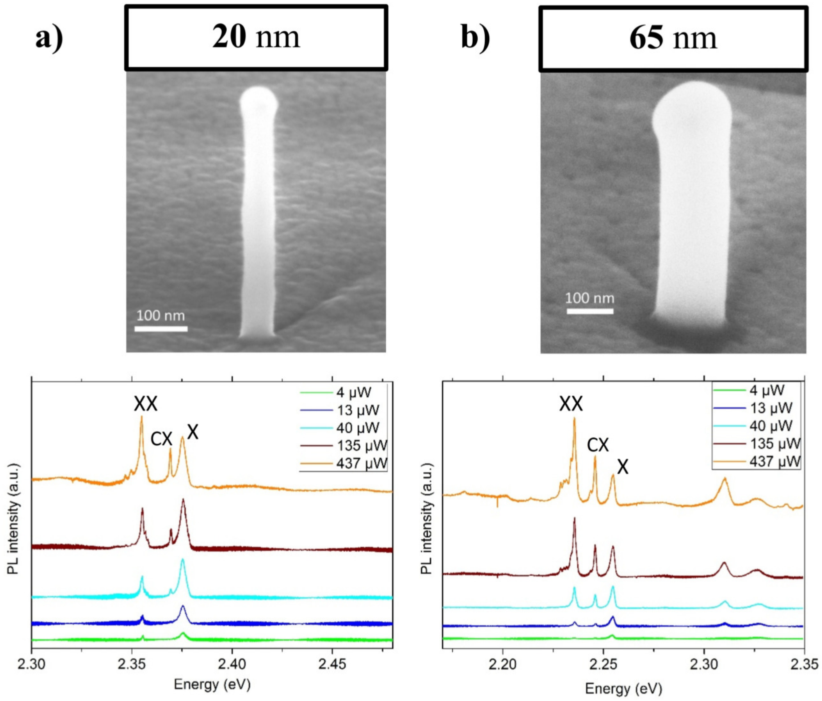

Figure 4.13: (Upper part) Tilted-view SEM images (65°) of photonic wires coated with an $Al_2O_3$ radius of a) 20 nm, b) 65 nm and c) 110 nm. (Bottom part) Corresponding power dependence µPL spectra with a clear excitonic (X, CX and XX) signature of the NW-QD emission. The excitation was carried out at 10 K with a pulsed Fianium WhiteLase Supercontinuum fiber laser tuned at 485 nm (2.556 eV).

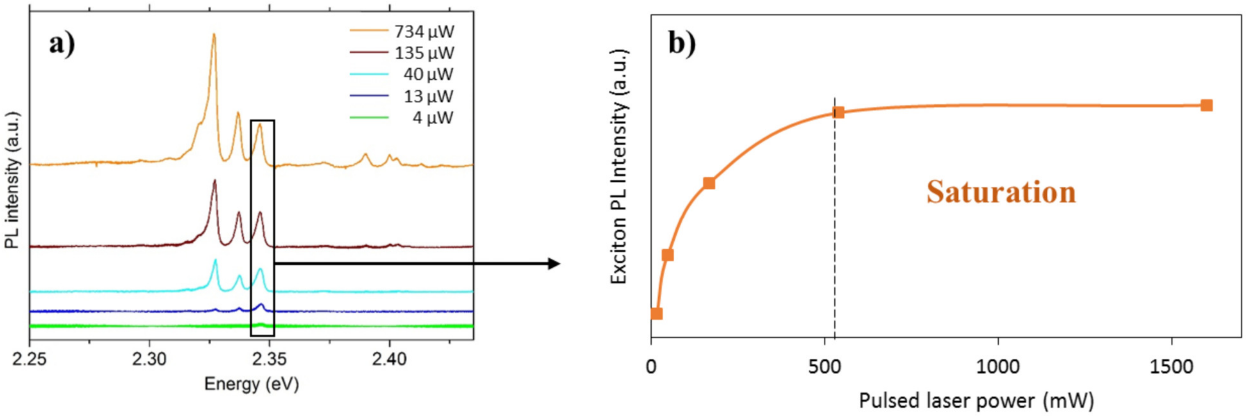

Figure 4.14: a) Power measurement carried out on a photonic wire ($Al_2O_3$ radius of 110 nm) at 10 K with a pulsed Fianium WhiteLase Supercontinuum fiber laser tuned at 485 nm (2.556 eV) and b) exciton intensity as a function of the pulsed laser power. Above a laser excitation of ∼500 µW, the saturation of the exciton is observed.

To ensure that the collected emission originates from vertically oriented photonic wires, we etched the sample composed of 110 nm $Al_2O_3$ shell radius by FIB. This etching technique permitted to create regular squared patterns of 2.5 µm x 2.5 µm crosses separated by 10 µm. The position of the collected PL emission with a clear excitonic signature was recorded and later compared to the corresponding SEM image, as displayed in Figure 4.15. We can clearly see that these positions (labeled in red in Figure 4.15b) correspond to vertically oriented photonic wires (circular white dots which correspond to the photonic wire top spherical dome[16]).

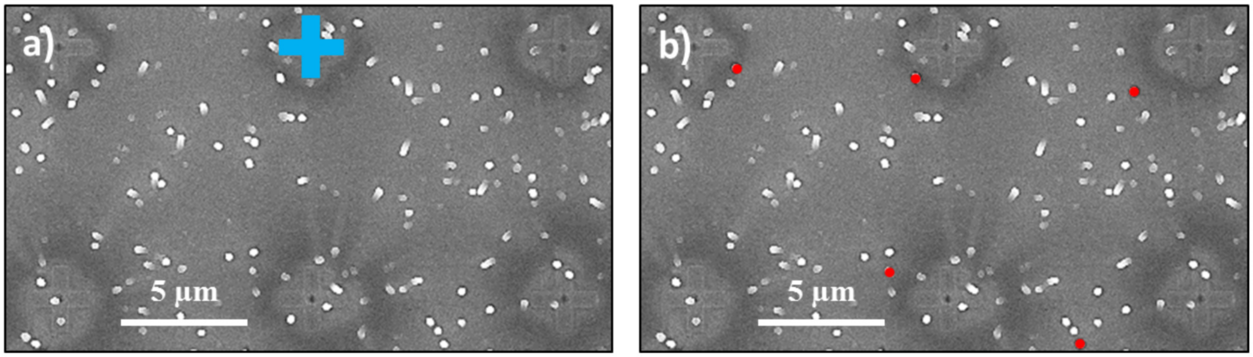

Figure 4.15: Top-view SEM images of the sample composed of 110 nm $Al_2O_3$ shell radius photonic wires. This sample has been etched by FIB to create regular squared patterns of 2.5 µm x 2.5 µm crosses (a single cross is colored in blue for visualization purpose) separated by 10 µm. The SEM images are displayed a) before and b) after the localization of photonic wires emitting a clear excitonic signature, labeled by red circles on the image.

Due to their low light intensity, the saturation regime could not be observe on NW-QDs uncoated by $Al_2O_3$(0 nm $Al_2O_3$ radius). For this reason, the PL intensity of photonic wires of 20 and 110 nm-radii were statistically compared and averaged over 20 photonic wires. We observe an experimental intensity increase of 3.9 for 110 nm compared to 20 nm-radii.

Since the quantum emitters (NW-QDs) originate from the same $S_{1QD}^{vacuum}$, this difference of intensity is the result of a *more efficient guiding of the photons along the photonic wire axis.* These results show that the photonic wire geometry clearly increases the photon collection from our nanostructures and we will better understand the origin of this intensity increase in the next part.

### COMSOL simulations

To quantitatively understand this intensity increase, we simulated the amount of power: emitted by these photonic wires and collected in a microscope objective. We worked with COMSOL Multiphysics[17] which uses finite element simulations (more details about this simulation technique can be found in Ref.[238]). Figure 4.16 illustrates the geometry used for the

---

[16] The number of recorded bright photonic wires is not aimed at being exhaustive

[17] We used the Radio Frequency/Electromagnetic Waves module in the Frequency domain.

simulation based on the experimentally studied NW-QDs from $S_{1QD}^{vacuum}$. More precisely, we approximate the ZnSe/ZnMgSe NW by a single ZnSe NW due to the similar ZnSe-ZnMgSe refractive indexes (2.66 and 2.63). Taking into account the ZnMgSe shell would have drastically increased the computational time needed to run the simulation, which is already long for 3D simulations (up to one day). The parameters of the simulations are the following:

- The ZnSe NW is 550 nm long, 20 nm in diameter (to include the ZnMgSe shell) and vertically oriented (as experimentally shown in Figure 4.15).
- A ZnSe buffer has been placed below the NW which are covered with an $Al_2O_3$ coating of varying thickness labeled $R_{shell}$.
- Simulations were made for both radial and longitudinal orientations.
- Since we experimentally use a microscope objective with a 0.6 NA, we calculated the power emitted from the photonic wires in such a solid angle.

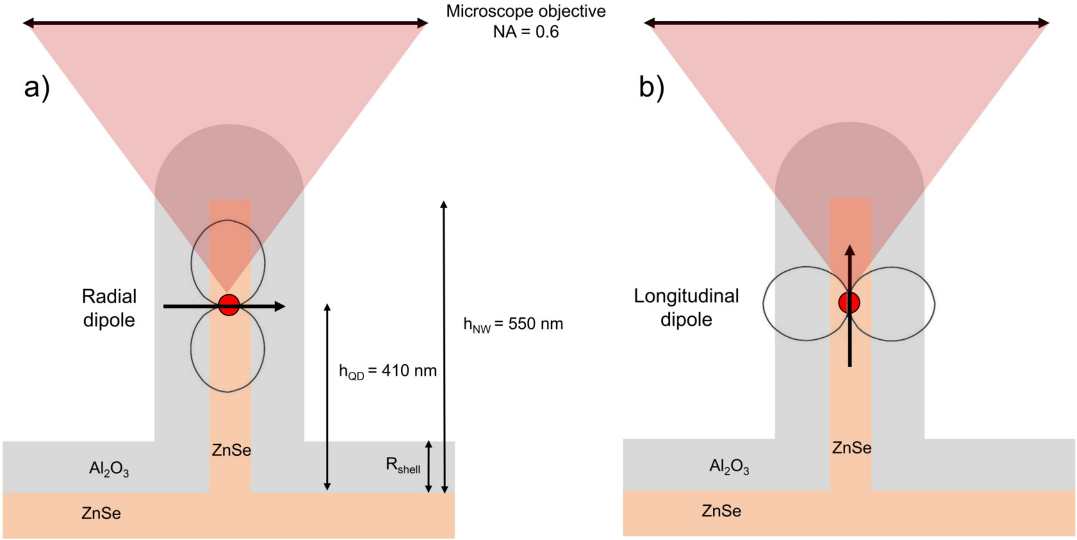

Figure 4.16: Illustration of the photonic wire geometry used to run COMSOL simulations. Both a) radial and b) longitudinal dipole orientations have been simulated. The radiation patterns of these dipoles in vacuum has been sketched in black for visualization purpose.

The results of the simulations are visible in Figure 4.17. We can see that the collected power increases with the photonic wire radius. As compared to a 20 nm-radius wire, the power collected from a 110 nm-radius wire is increased by a factor 1.6 and 4.0 for a longitudinal and a radial dipole respectively. This later result is in agreement with the experimentally measured intensity increase of 3.9, suggesting that the dipole orientation in these NW-QDs is radial. Such a dipole orientation is expected in this sample $S_{1QD}^{vacuum}$ since its CdSe QD growth procedure is the same as in $S_{2QDs}^{vacuum}$, which showed flat QD along the NW axis (see Part 3.2.1) and radial dipole orientations (see the discussion in Part 3.4.3).

Moreover, the collected power enhancement from an uncoated NW-QD (0 nm $Al_2O_3$ radius) and a 110 nm-$Al_2O_3$-radius is $\sim 7$ for a radial dipole orientation (see Table 4.3). *This result clearly highlights the interest of such a photonic wire geometry to increase the photon collection by almost one order of magnitude.*

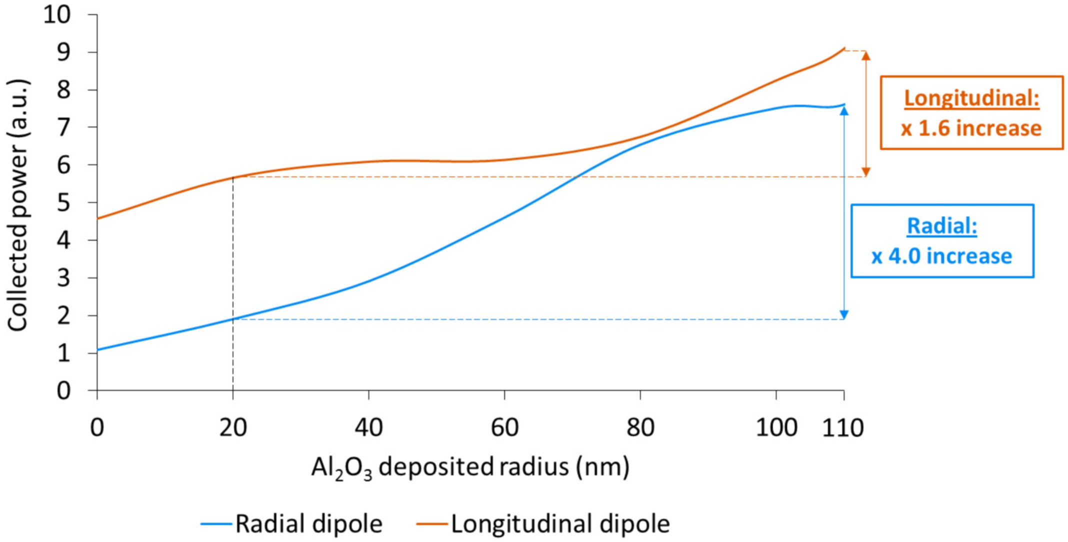

Figure 4.17: Collected power in a 0.6 NA microscope objective from a vertically oriented photonic wire (illustrated in Figure 4.16) for radial and longitudinal dipole orientations. On the right of the Figure, the collected power enhancement between 20 and 110 nm $Al_2O_3$ deposited radii are displayed, with values of 4.0 and 1.6 for the radial and longitudinal dipoles respectively.

| Ratio of deposited $Al_2O_3$ radii | Collected power enhancement | | |
|---|---|---|---|
| | Simulation: radial dipole | Simulation: longitudinal dipole | Experimentally |
| 110 nm / 20 nm | 3.99 | 1.61 | 3.89 |
| 110 nm / 0 nm | 6.99 | 1.99 | Not measurable |

Table 4.3: Collected power enhancement determined from COMSOL simulations (radial and longitudinal dipoles) and experimental PL measurements, comparing the emission of 20 nm with 110 nm and 0 nm with 110 nm-radii $Al_2O_3$ photonic wires.

In Figure 4.17, we can notice that the longitudinal dipole orientation shows a stronger absolute collected intensity compared to the radial dipole orientation. This counter-intuitive result contrasts with the previously obtained FDTD results, for which we obtained the opposite.

In the FDTD simulations, the ZnSe-CdSe NW-QD structure has been neglected since it represents a negligible volume within the photonic wires. Such an approximation is only valid if the core (ZnSe NW + ZnMgSe shell) and the dielectric shell refractive indices are similar.

However, the difference of refractive indices ($n_{core} \sim n_{ZnSe} = 2.66$ and $n_{dielectric\,shell} \sim 1.77$) induces a dielectric screening (see Part 1.2.4). This dielectric screening has a strong impact on the dipole and reduces its emission: the longitudinal dipole is in this case brighter than the radial dipole. This effect is particularly visible for $r_{Al_2O_3} = 0$. In this case, the screening is maximum due to a higher dielectric contrast between the NW and the air (compared to the $Al_2O_3$ shell).

A way to reduce this dielectric screening is to deposit a dielectric shell with a similar refractive index than ZnSe. For instance, a $TiO_2$ deposition (already carried out by ALD in Figure 4.8) with a refractive index of 2.65 would drastically reduce the screening effect; the FDTD results would be valid and in this case, the radial dipole orientation would be optically more favorable.

### 4.2.5 Decay-time measurements to confirm the dipole orientation

A way to confirm the dipole orientation can be provided by decay-time measurements. To do so, we carried out exciton decay-time measurements as a function of the photonic wire $Al_2O_3$ radius. In this context, different $Al_2O_3$ radii of 20, 35, 55, 65, 100 and 110 nm were deposited by ALD on several pieces of $S_{1QD}^{vacuum}$. After these depositions, the decay-time of single NW-QDs (photonic wires) from each sample was measured with Mathieu Jeannin from Néel Institute, with a total of 95 NW-QDs to get a statistical distribution. These results are visible in Figure 4.18.

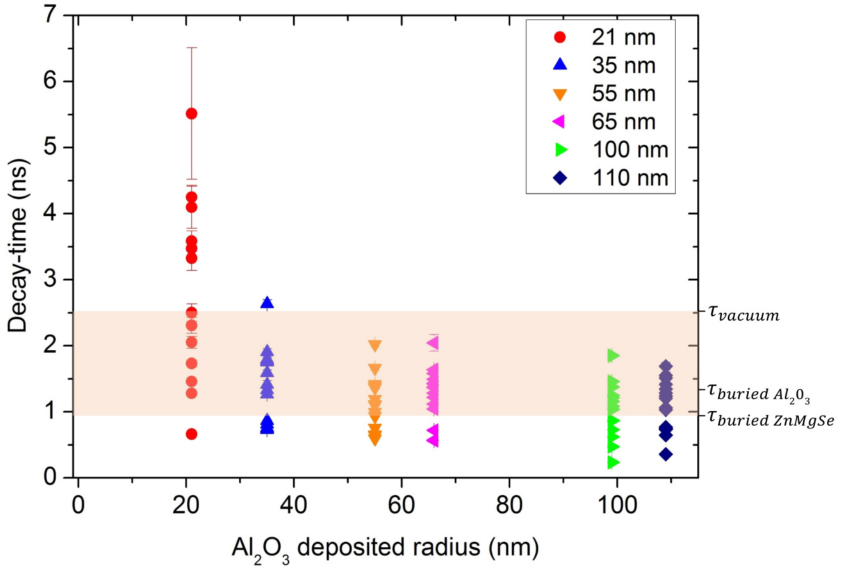

Figure 4.18: Experimental exciton decay-times of single NW-QDs from $S_{1QD}^{vacuum}$ covered by different $Al_2O_3$ shell radii ranging from 20 to 110 nm. The transparent strip vertically ranges from $\tau_{buried\,ZnMgSe}$ (average decay-time of the NW-QDs buried in a ZnMgSe matrix of 0.92 ns) to $\tau_{vacuum}$ (average decay-time of the NW-QDs in vacuum of 2.54 ns) and is a guide for the eyes. The expected decay-time of NW-QDs buried in $Al_2O_3$ matrix $\tau_{buried\,Al_2O_3}$ is also provided (1.35 ns, using Equation 4.1.4).

In Figure 4.18, we first see that there is a decay-times distribution within the same $Al_2O_3$ deposited radius. Moreover, the maxima decay-times progressively decreases when the $Al_2O_3$ deposited radius increases, with a drastic drop of $\tau_{max}$ from 20 to 35 nm. In the limit $r \to \infty$, the decay-times should tend toward the decay-times of NW-QDs buried in an $Al_2O_3$ matrix $\tau_{buried\,Al_2O_3}$. We do not have the experimental value of $\tau_{buried\,Al_2O_3}$ but we can calculate it with Equation 4.1.4. Using the experimentally measured average decay-time of NW-QDs buried in a ZnMgSe matrix $\tau_{buried\,ZnMgSe}$ (see Part 4.1) of 0.92 ns, we calculate $\tau_{buried\,Al_2O_3} = 1.35\,\text{ns}$. The values reported in Figure 4.18 can also be compared to the decay-time of the NW-QDs in vacuum $\tau_{vacuum}$ (from longitudinal dipoles measured in Part 3.5.2) of 2.54 ns.

In Figure 4.18, a guide for the eyes (transparent strip) ranges from $\tau_{buried\,ZnMgSe}$ to $\tau_{vacuum}$. We can see that the maxima decay-times of NW-QDs covered by 20 and 35 nm of $Al_2O_3$ in radius are above $\tau_{vacuum}$. Since $\tau > \tau_{vacuum}$, this is an indication that the NW-QDs experience a dielectric screening, which is induced by a radial dipole orientation.

To further determine if these recorded decay-times originate from radial or longitudinal dipoles, theoretical calculations have been carried out by Niels Gregersen and Teppo Häyrynen from DTU Fotoniks (Denmark) using the analytical Modal method. Briefly, this method consists in decomposing the guided and radiation modes (which form together a complete basis set) in the studied structure. This structure is geometrically composed of adjacent objects of homogeneous refractive index. For an object with a homogeneous refractive index along the $z$ direction, the solutions of Maxwell's equations can be expressed as a superimposition of forward and backward propagating modes:

$$\begin{aligned} E(x,y,z) &= \textstyle\sum_{k=1}^{M}(a_k e^{i\beta_k z} + b_k e^{-i\beta_k z})E_k(x,y) \\ H(x,y,z) &= \textstyle\sum_{k=1}^{M}(a_k e^{i\beta_k z} + b_k e^{-i\beta_k z})H_k(x,y) \end{aligned} \tag{4.2.6}$$

When there is a change of refractive index along the z direction (change of object), a coupling between the different objects can be formalized in a scattering matrix by using the boundary conditions of Maxwell's equations at the interface. More information about this method can be found in Ref.[239].

By applying this modal method to our system (same experimental geometry, already used for COMSOL simulations in Figure 4.16), the theoretical decay-times of radial and longitudinal dipoles as a function of the $Al_2O_3$ shell radii was calculated. The results are displayed in Figure 4.19.

In Figure 4.19, the longitudinal dipole decay-time only shows small variations as a function of the photonic wire radius. This result comes from the lower coupling of this dipole to guided modes (as already discussed in Part 4.2.1). However, since the radial dipole couples to guided modes depending on the photonic wire radius, this dipole displays more decay-time variations. Notice that the decay-time of this radial dipole only starts above 20 nm due to convergence issues at lower radii. Above 20 nm, this dipole starts to couple to the photonic wire modes and the corresponding decay-time decreases until the $Al_2O_3$ radius of 120 nm is reached, with a small oscillation from 40 to 80 nm.

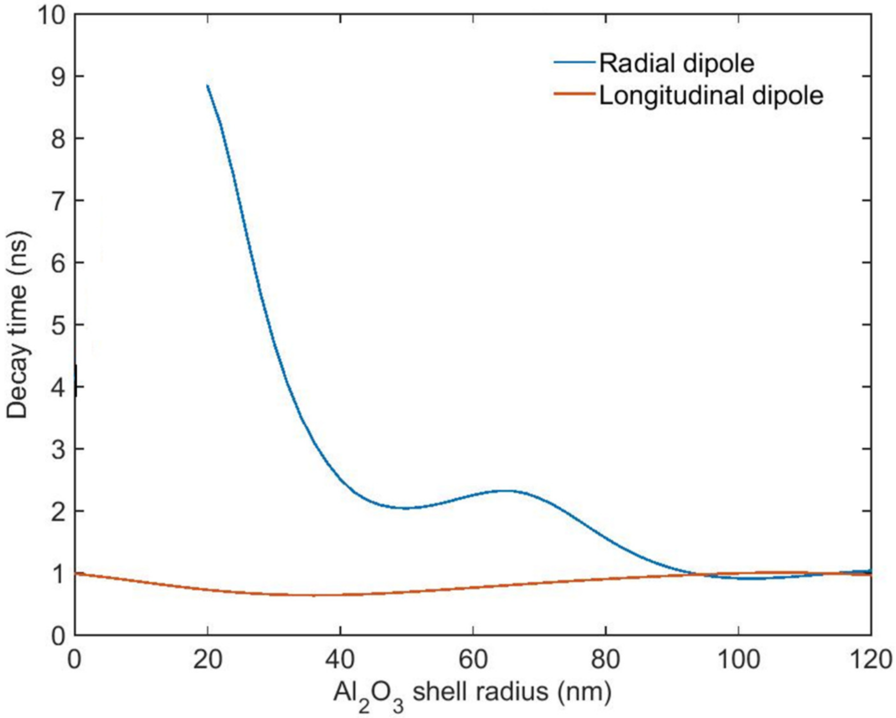

Figure 4.19: Calculated exciton decay-times of radial (blue) and longitudinal (red) dipoles as a function of the $Al_2O_3$ shell radius. These results have been calculated using the analytical Modal method technique.

To compare the experimental decay-times to this theoretical expectation, both Figures 4.18 and 4.19 have been merged in Figure 4.20.

We can notice that the experimental decay-time maxima follow the theoretical radial blue curve quite well for $Al_2O_3$ radii from 20 to 65 nm; this is a second indication that the NW-QDs dipoles of $S_{1QD}^{vacuum}$ are radially oriented. Besides, deviations from the theoretical values observed for $Al_2O_3$ radii of 100 and 110 nm can be originate from geometrical differences between the model used for the calculation and the real experimental geometry of the NW-QD (for instance: larger ZnMgSe shell or different QD position along the NW axis).

In addition, the vertical distribution visible for each $Al_2O_3$ radius can be due to a mixing of radial and longitudinal dipoles. It can also be due to non-radiative channels which can lower the total decay-time of the emitter ($1/\tau = 1/\tau_{rad} + 1/\tau_{non\,rad}$). In this case, the maxima experimental decay-times have the lowest coupling to non-radiative channels and consequently the highest quantum efficiency. These assumptions could be verified with further experiments highlighting the values of $\tau_{rad}$ and $\tau_{non\,rad}$ .

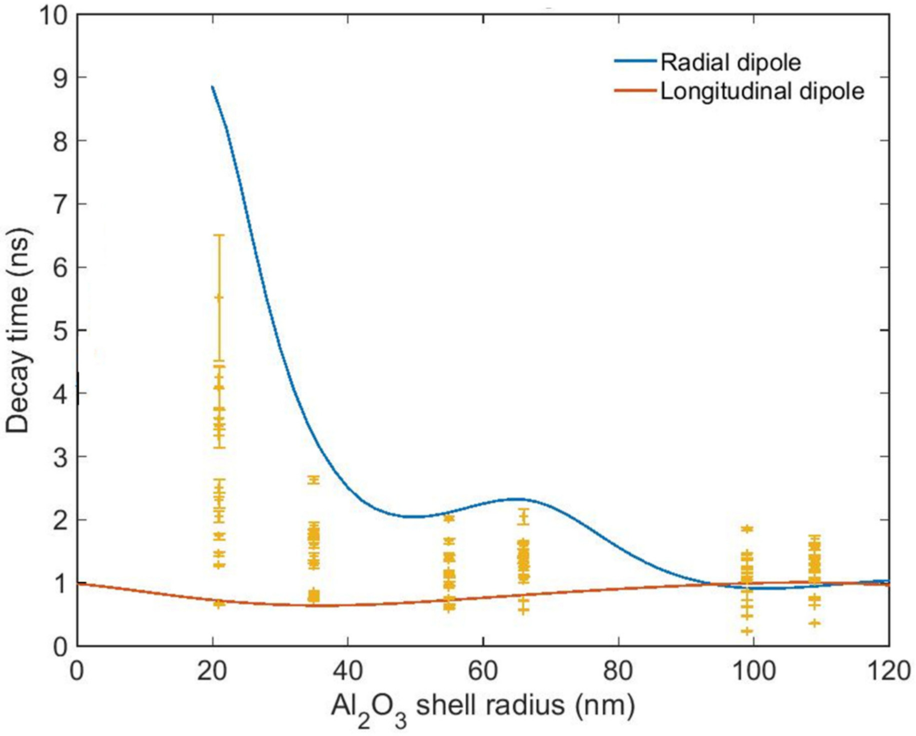

Figure 4.20: Merging of the experimental points (orange) from Figure 4.18 with the theoretical exciton decay-times of radial (blue) and longitudinal (red) dipoles as a function of the $Al_2O_3$ shell radius from Figure 4.19.

## 4.3 Conclusion of the Chapter

In this Chapter, the photons enhancement from the ZnSe-CdSe NW-QDs was investigated. In a first part, we compared the decay-time of two samples: ZnSe-CdSe NW-QDs *in vacuum* (measured in the previous Chapter) and buried *in a ZnMgSe medium* by using PL and CL measurements. A modification of the NW-QDs decay-time has been observed, resulting from the different NW-QDs environment. This modification can be quantified using the Fermi's golden rule. It states that the NW-QDs decay-time is inversely proportional to its surrounding refractive index $n$ and the calculated decay-time modification is in good agreement with the experimental value. This reduction of the emitters decay-time could be used to higher the QDs decay-rate in the GHz regime for quantum information applications, increasing the number of emitted (and collected) photons per second.

In the second part of this Chapter, we studied the coupling of ZnSe-CdSe NW-QDs to photonic structures formed by coating the NWs with a dielectric shell. We show the possibility to deposit several dielectric materials: $Al_2O_3$ , $ZrO_2$, $HfO_2$ and $TiO_2$: $Al_2O_3$ was chosen since it provides a conformal material deposition with the smoothest surface. To model the photonic properties of these wires, FDTD simulations were carried out. These simulations concluded that a radial dipole orientation is favorable to efficiently guide the photons along the photonic wire axis. This approximation is true for a bare $Al_2O_3$ photonic wire. However, a more complete simulation using a NW-QD surrounded by an $Al_2O_3$ shell shows that the radial dipole emission is less collected than a longitudinal dipole. This is due to the screening effect induced by the difference of refractive index between the NW-QDs and the dielectric shell and it needs to be taken into account to fully describe our structure.

Moreover, the luminescence of single photonic wires with 20 and 110 nm $Al_2O_3$ radii was experimentally compared, yielding a collected photons intensity increase of almost a factor four. COMSOL simulations show that this intensity increase originates from a radial dipole orientation and show that the photonic wire geometry permits to increase the photon collection by almost one order of magnitude compared to bare NW-QDs.

In addition, the decay-times of single photonic wires were recorded as a function of their radius. These experimental results show a dispersion of decay-times for each radius as a function of the photonic wire radius, along with a sharp decrease of the mean decay-time while increasing the photonic wire radius. This decrease results from a better coupling of the NW-QDs to the photonic wire modes. These experimental results were compared to analytical calculations performed using the Modal method and also agree with a radial dipole orientation.

To conclude, the photonic wire geometry offers the possibility to increase the collected photons intensity from the NW-QDs by almost one order of magnitude. Moreover, the modification of the refractive index surrounding the photons emitter permits to reduce its decay-time. This reduction of the emitters decay-time could be used to higher the decay rate of these emitters in the GHz regime for quantum information applications.

# General conclusion and perspectives

The aim of this work was: (1) to develop the growth of vertically oriented ZnSe-CdSe NW-QDs on the (111)B surface orientation, (2) to characterize their optical properties up to room temperature and (3) to study the possibility of enhancing their photon collection.

**In the first part**, we determined the best growth conditions to obtain high quality and vertically oriented NWs on (111)-oriented surfaces. The deposition of a ZnMgSe shell around the NWs revealed an impressive passivation effect, showing on single NWs a PL intensity increase of more than two orders of magnitude.

**In the second part**, we demonstrated for the first time the possibility to insert CdSe NW-QDs in ZnSe NWs grown on (111)B-oriented surfaces. We tested the effect of two CdSe QDs growth procedures, with - before and after the QD insertions - growth interruptions:

- *under vacuum.* In this case, the QDs are flat and show radial dipole orientations, coherent with mainly HH excitons states.
- *under a Se flux.* In this case, the QDs are longer, with an aspect ratio (thickness/diameter) of 0.75. Theoretical calculations have shown that such an aspect ratio corresponds to an important HH-LH mixing and consequently, a distribution of dipole orientations is observed.

These NW-QDs show luminescence up to room temperature. The temperature performance was assessed by performing decay-time measurements on single NW-QDs as a function of the temperature. This study revealed that the exciton starts to couple to non-radiative channels above 200 K. Such a temperature can be easily reached by simple thermoelectric coolers using the Peltier effect, positioning these nano-objects has realistic candidates for applied SPS.

For the QD inserted *under vacuum* conditions, a composition analysis revealed that the QDs are composed of a central pure CdSe zone surrounded by a CdZnSe area (with a decreasing Cd content). This result helps to explain the decay-time temperature behavior which suggests that at low temperature, the hole is trapped within the pure CdSe zone and gets delocalized in the CdZnSe area at higher temperature.

**In the third part**, the photon collection enhancement from the NW-QDs was investigated. First, we showed that by placing these NW-QDs in a high refractive index material, the NW-QDs decay-rate can be increased in the GHz regime. This feature can be used to increase the number of emitted (and collected) photons per second from the NW-QDs, which is beneficial for quantum information applications.

Then, by coating the NW-QDs with a thick dielectric shell, we demonstrate the possibility to create photonic wires. Our experimental results and simulations suggest that the dipole orientation in our nanostructures is radial. Such a radial dipole experiences a dielectric screening which reduces its emission. However, for such a radial dipole orientation, the photonic wire geometry still permits to increase the photon collection by almost one order of magnitude compared to bare NW-QDs.

To reach the objectives of this PhD project, a lot of work has been carried out on the NW growth and characterizations. Still, there is room for improvement and two main points can be developed :

**1) The NW-QDs emission**. This part can be developed in three steps. First, a *thicker ZnMgSe shell* could potentially be deposited around the NW-QDs to induce a better passivation and increase the luminescence. To reach this aim, a possibility would be to grow longer (∼2-3 µm) NW-QDs. In this case, the ZnMgSe deposition time can be increased without burying the NW-QDs, resulting in thicker ZnMgSe shells. Secondly, the *QD-shell interface can be improved.* The Mg cells are not as pure (99.999% purity, 5 nines or 5N) as the Zn and Se cells (6 to 7N). To avoid the deposition of impurities close to the QD due to the Mg cells, the passivating shell could consist in a first a ZnSe shell, surrounded by a higher bandgap ZnMgSe shell. Thirdly, the *QDs growth conditions can be further explored*: for instance, in this work, we used Se-rich conditions for the QDs insertion and the effect of Cd-rich conditions could be tested to see its impact on the QDs luminescence.

**2) The light collection.** In this project, we mainly developed radial dipole orientations on purpose, thinking about coupling such a dipole to photonic wires guided modes. However, this dipole orientation experiences a dielectric screening due to the difference of refractive index between the NW-QD and the surrounding environment. This screening is maximum when the NW-QD is in vacuum and is reduced when the NW-QD is coated with $Al_2O_3$ (to create photonic wires). A way to hinder the screening effect (and increase the radial dipole emission) is to deposit a dielectric shell with a similar refractive index than the ZnSe-CdSe NW-QD, like $TiO_2$.

According to COMSOL simulations (Part 143), a longitudinal dipole is brighter than a radial dipole experiencing a ZnSe-CdSe/$Al_2O_3$ dielectric screening. Since the QD aspect ratio permits to control the dipole orientation, we recently grew ZnSe NWs with two QDs of different aspect ratio. The aim is to demonstrate the full control of the dipole orientation by measuring the two main dipole orientations (radial and longitudinal) on the same NW-QD.

In photonic wires, even if the photons are efficiently guided along the wire axis, a substantial amount of photons is lost in the substrate. A way to solve this issue is to grow the NW-QDs on distributed Bragg reflectors or through an aluminum mirror to reflect and collect the light emitted toward the substrate. Preliminary results using these growth techniques are presented in the Appendix A and B.

Another way to collect the photons emitted in the substrate is to deposit the NW-QDs on a high refractive index and transparent material. In this case, most of the light will be direct toward the transparent substrate and can be collected underneath. Corresponding simulations have been carried out by Flora Gautheron during her L3 internship and are presented in the Appendix A.

Finally, the constant effort we made to **push the characterization techniques to their limits** is beneficial to our research group and permits deeper analyzes of other semiconductor materials, going beyond the scope of this PhD project.

# Appendix A. Further increase of the photon collection

In the Chapter 4, we showed the possibility to enhance the photon collection by using a photonic wire geometry. However, even if the photons are efficiently guided along the wire axis, a substantial amount of photons are emitted in the substrate and are not collected. In this Appendix, we propose three approaches to collect the photons lost in the substrate with NW-QDs grown on distributed Bragg reflectors, the use of a bottom aluminum mirror and the NW-QDs deposition on transparent high refractive index materials.

## NW-QDs grown on Distributed Bragg Reflectors

A way to collect the photons emitted in the substrate is to grow the NW-QDs on Distributed Bragg Reflectors (DBRs). A DBR is a succession of planes which have different refractive indices. It permits to reflects incident light with a high reflectivity by constructive interferences. The DBR's reflectivity $R_{DBR}$ is given by:

$$R_{DBR} = \left[\frac{n_0(n_2)^{2N} - n_s(n_1)^{2N}}{n_0(n_2)^{2N} + n_s(n_1)^{2N}}\right]^2 \tag{4.3.1}$$

with $n_0$, $n_1$, $n_2$ and $n_s$ the refractive indices of the originating medium, the two alternating materials and the substrate; and $N$ is the number of repeated pairs of low/high refractive index materials.

Since our ZnSe-CdSe NW-QDs have an average emission around 550 nm, the DBRs have been optimized to reflect a maximum of light at this wavelength. These DBRs have been grown by the group of Wojciech Pacuski (University of Warsaw in Poland) on GaAs (111)B and (001). As displayed in Figure 4.21a, they are composed of 15 pairs of $ZnSe_{0.9}Te_{0.1}$ (53 nm-thick) and $Zn_{1\text{-}x}Mg_xSe$ (with x ranging from 30 to 60 according to the samples) grown on a 54 nm-thick ZnSe buffer layer and covered by an additional 53 nm-thick $ZnSe_{0.9}Te_{0.1}$ layer. This last layer protects the Mg from oxidizing by a contact with the air. Figure 4.21b presents pictures of some of these DBRs. Notice that some of them have been covered by an additional amorphous Se layer, which are mentioned on the images. Figures Figure 4.21c and d provide the calculated reflectivities of some samples grown on the (111)B and (001) surfaces. From sample to sample and at the wavelength of interest (550 nm), the reflectivity ranges from 80 to 96%. Such high reflectivities would drastically improve the collected luminescence from the NW-QDs.

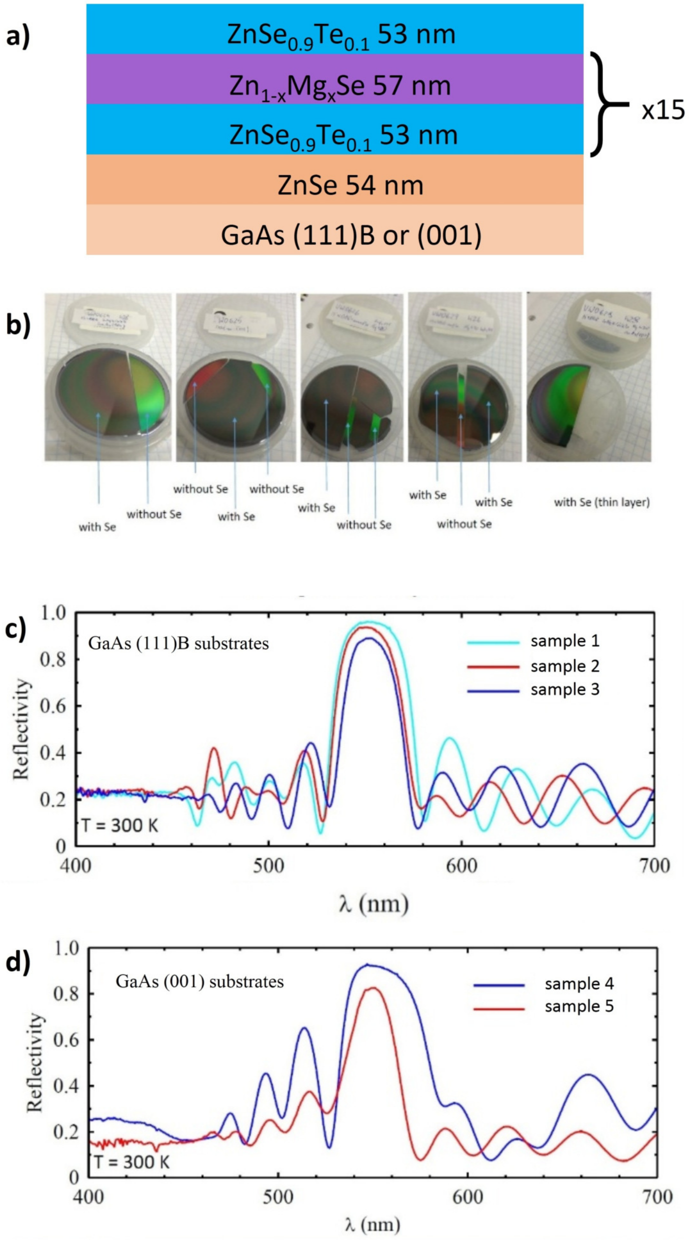

Figure 4.21: a) Sketch of the grown DBR (with x in $Zn_{1-x}Mg_xSe$ ranging from 30 to 60 according to the samples). b) Picture of some of the grown DBR. The zones protected by a Se layer are mentioned. c) and d) Calculated reflectivity of some of these DBR structures grown on the (111)B and (001) surface orientations.

Preliminary trials are soon to be carry out to determine the best NW-QDs growth conditions on these DBRs.

## Use of a bottom mirror

Another way to collect the light emitted in the substrate is to growth the NW-QDs through an aluminum mirror. The corresponding growth procedure is detailed in the Appendix B, page 173, along with preliminary results.

To quantify the enhancement of the light collection induced by the aluminum mirror, COMSOL simulations have been achieved by using the same structure already displayed in Figure 4.16. This structure corresponds to our experimental growth of a 550 nm-long ZnSe NW (30 nm-diameter with the ZnMgSe shell) with a CdSe QD inserted at 1/3 of the NW top, a radial dipole. In the following, all the intensities are normalized to this system (value of 1 in Table 4.4).

To explore the emission properties of our NW-QDs, we varied both the $Al_2O_3$ dielectric shell radius (0 to 200 nm) and the QD position (along the NW axis). The optimal values are reported in Table 4.4 in the case of longitudinal and radial dipoles, with and without a mirror.

| Dipole orientation: Radial (R) or Longitudinal (L) | R | R | L | L |
|---|---|---|---|---|
| Al mirror: Yes (Y) or No (N) | N | Y | N | Y |
| QD position from the top of the 550 nm-long NW (nm) | 250 | 100 | 130 | 130 |
| $Al_2O_3$ shell radius (nm) | 140 | 140 | 200 | 180 |
| Normalized collected intensity enhancement | 13 | 35 | 23 | 67 |

Table 4.4: Collected intensity enhancement normalized (reference value of 1) to the experimental NW-QD emission of this PhD (550 nm-long and 30 nm-diameter ZnSe NW with a CdSe QD inserted at 1/3 of the NW top and a radial dipole, calculated in Part 4.2.4). In the simulations, the $Al_2O_3$ dielectric shell radius was varied from 0 to 200 nm, the QD position was varied along the NW axis, in the case of a radial and a longitudinal dipole, with and without an Al-mirror below the NW-QD. The optimal values are reported in this table.

First, we can notice that a factor two of intensity enhancement can be obtained by using a longitudinal dipole instead of a radial dipole. As previously mentioned, this phenomenon is due to the dielectric screening induced by the difference of refractive index between the $Al_2O_3$ shell and the NW-QD. The deposition of a dielectric shell with a refractive index close to ZnSe value of 2.66 would hinder the dielectric screening and increase the QD spontaneous emission rate (as discussed in Part 3.5.2), resulting in a brighter QD emission. Experimentally, this could be achieved by depositing a thick $TiO_2$ shell by ALD (already achieved and seen in Figure 4.8) which has a 2.65 refractive index at 550 nm. Moreover, the maxima intensity enhancements of 13 and 35 for a radial dipole with and without an Al mirror, and of 23 and 67 for a longitudinal dipole with and without an Al mirror show that there is still room for improvement to enhance the collected luminescence from the NW-QDs studied during this PhD.

## Deposition of the NW-QDs on a high refractive index and transparent substrate

Another possibility to enhance the light collection from the NW-QDs is to deposit them on a *high refractive index and transparent substrate*, as illustrated in Figure 4.22a. Indeed, in this case, the NW-QDs are laying on the substrate and most of the luminescence is directed toward this substrate. Figure 4.22b shows the three dipole orientations (longitudinal, radial parallel and perpendicular to the substrate surface) used to calculate the power emitted by a NW-QD as a function of the substrate refractive index (Figure 4.22c), emitting upward (apart from the substrate) and downward (into the substrate).

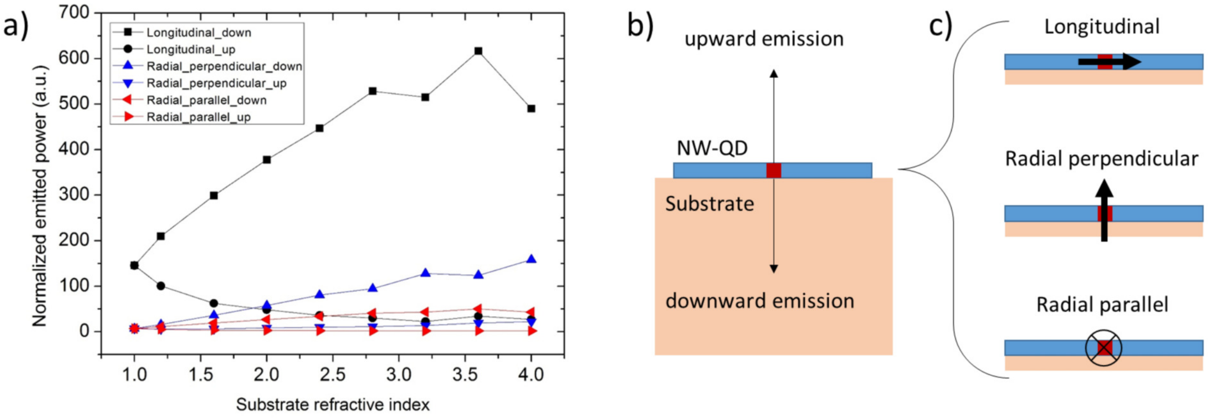

Figure 4.22: a) Scheme of the geometry and b) the three dipole orientations (longitudinal, radial parallel and perpendicular to the substrate surface) used to calculate c) the power emitted by a ZnSe-CdSe NW-QD (30 nm in diameter and 600 nm long) as a function of the refractive index of the substrate it is deposited on. The dipoles emitted power has been calculated according to their emission upward (apart from the substrate) and downward (into the substrate). This power has been normalized to the emission of a dipole in vacuum (here 100%). Courtesy of Flora Gautheron (L3 internship).

Clearly, the longitudinal dipole orientation emits more than the two radial orientations, especially toward a substrate of high refractive index. Compared to a radial dipole deposited on $Al_2O_3$ (our patterned substrates, $n = 1.77$), the light collected from a longitudinal dipole deposited on a 2.6 refractive index material is expected to be increased by one order of magnitude. Experimentally, the NW-QDs could be deposited on high bandgap semiconductors (their bandgap needs to be higher than the CdSe QDs emissions around 2.5 eV to be transparent) of high refractive index. Examples of such semiconductors are provided in Table 4.5.

| Material | Refractive index | Bandgap (eV) |
|---|---|---|
| GaN | 2.41 | 3.4 |
| AlN | 2.15 | 6 |
| SiC | 2.66 | 2.36 (3C phase)<br>3.23 (4H phase)<br>3.05 (6H phase) |
| Diamond | 2.42 | 5.5 |
| ZnSe(001) | 2.66 | 2.8 |
| $TiO_2$ | 2.65 | 3.2 |

Table 4.5: List of high bandgap materials with their corresponding refractive index.

Note that for epitaxially grown semiconductors, a sacrificial layer of AlAs (III-V semiconductors) or MgTe (II-VI semiconductors) can be inserted between the layer of interest and the substrate. This sacrificial layer is consumed by oxidization when the sample is exposed to the air and permits to efficiently extract the layer of interest: for instance a 500 µm thick ZnSe(001) layer grown on top of a GaAs(001) substrate, to later deposit and efficiently collect the light emitted by the NW-QDs.

# Appendix B. Recipe to grow localized NWs through an Al mirror

## Preliminary reflection

A way to increase the photon collection from our nanostructures is to grow the NW-QDs through a metal-dielectric mirror. This approach - visible in Figure 4.23 - has been proposed by Claudon et *al.* [227]. In this paper, they suggest to deposit a $SiO_2$-Au mirror on top of a semiconductor substrate, to create a hole in the mirror and to grow the NW-QDs through this hole with an epitaxial link with the substrate underneath. They propose afterwards to deposit a tapered shell around the NW-QD to favor the photons outcoupling toward the microscope objective (adiabatic expansion of the mode thanks to the tapered geometry), which is carried out in our case by the dome-like shape dielectric shell of our photonic wires.

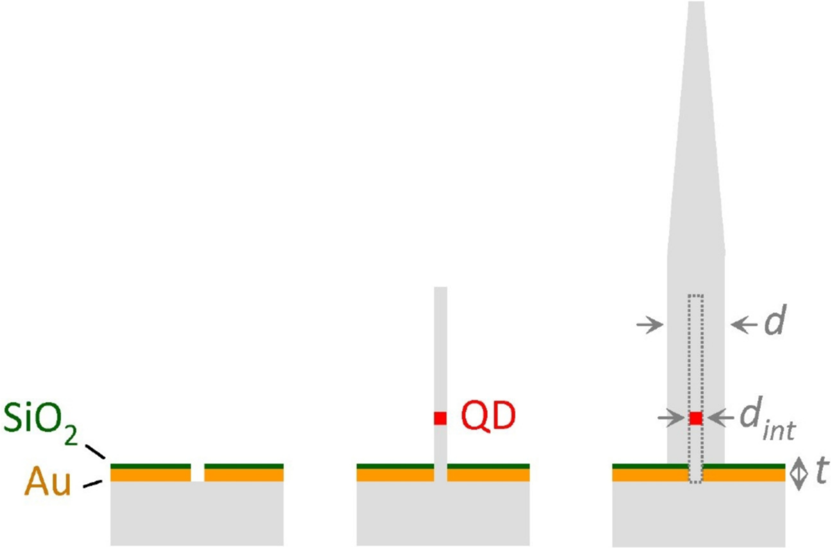

Figure 4.23: Proposed strategy to realize directly a tapered wire supported by a metal-dielectric mirror. Figure extracted from Ref.[227].

Since gold is used in the form of droplets to catalyze the growth of our NW-QDs, it cannot be used as a mirror, otherwise the gold droplets would mix with such a gold mirror during the annealing process. Let us look at Figure 4.24[18] which provides the metals reflectivities at our mean CdSe QD emission wavelength of 550 nm. At this wavelength, the two highest reflectivities are 90 and 97% for Al and Ag respectively. Experimentally, Ag is tricky to use due to its fast oxidation. Consequently, Al is the metal we consider in the rest of this discussion.

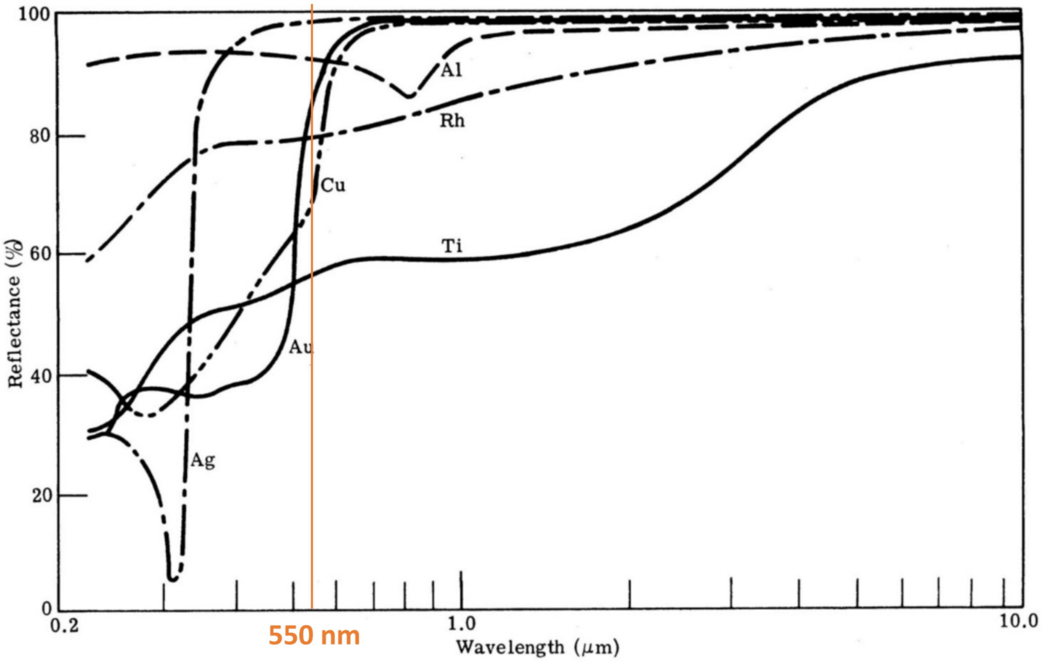

Figure 4.24: Reflectivity of several materials as a function of the reflected wavelength. The mean CdSe QD emission wavelength of 550 nm is highlighted in orange.

Technologically, Al is a difficult metal is etch (this is why it is often used as a mask in lithography). For this reason, we will try to deposit the thinest Al thickness possible while keeping a reasonable reflectivity. The reflectivity of a thin aluminum film deposited on a ZnSe substrate can be analytically calculated by using the matrix formulation for isotropic layered media [240] and is visible in Figure 4.25.

---

[18] Extracted from http://www.tvu.com/metalreflectivityLR.jpg

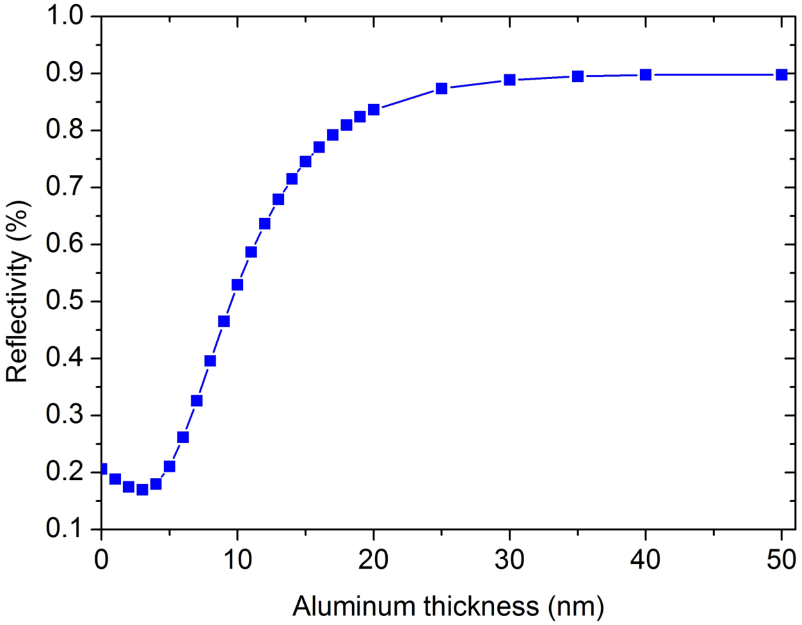

Figure 4.25: Reflectivity of an Al thin film as a function of its thickness. The Al film is deposited on a ZnSe substrate. The Al and ZnSe refractive indexes used are 0.965 +j 6.3996 and 2.6628 respectively. This calculation is in good agreement with similar calculations carried out by only considering a layer of Al in Refs. [241, 242].

This Figure indicates that below an Al thickness of 20 nm, the reflectivity drastically drops down to 20% approximately. It then reaches the bulk value around 90% for a thickness above 30 nm that we choose to deposit experimentally.

The melting point of metals depends on their dimensions, especially at the nanoscale. During our gold dewetting, the temperature is increased to 510°C and the Al melting point should be higher than this value to avoid any Au-Al mixing. The following Ref. [243, 244] report that the melting point of thin Al film with thicknesses above 10 nm correspond to the bulk Al melting point of 660°C and consequently, a 30 nm-thick Al film can be used in our system.

## First steps to develop the structure

### Creation of the etched Al mirror

The creation of the etched mirror can be carried out with different techniques depending on:

- the type of resist used (positive: the insulated resist becomes soluble; negative: the insulated resist becomes insoluble)
- the type of etching used (wet or physical etchings).

A possible roadmap is displayed in Figure 4.26. To give an overview of the main steps involved: a positive resist is insolated by an electron-beam. Then the resist is developed and

Al is etched by Ion Beam Etching (IBE) with an argon plasma. Finally, the resist is cleaned by wet etching and Reactive Ion Etching (RIE) with an oxygen plasma to reveal the etched aluminum mirror.

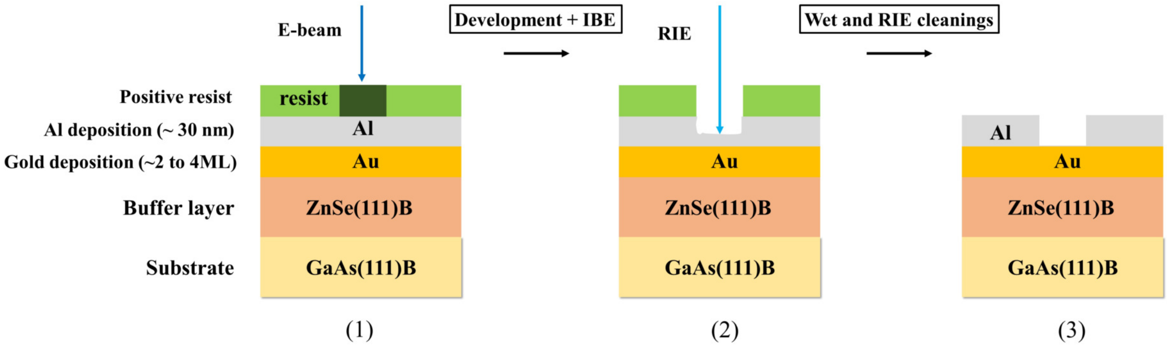

Figure 4.26: Steps involved in the creation of an etched aluminum mirror deposited on top of a thin gold layer, above ZnSe-GaAs(111)B epitaxial layers.

In the light of Figure 4.26, our experimental trials are detailed hereafter.

### Gold-Al depositions and lithography mask

After the deposition of a ZnSe buffer layer on top of a GaAs(111)B substrate and prior to the 30 nm-thick Al deposition[19], gold depositions of 2 and 4 ML were carried out on two different substrates[20]. The aim of these two depositions is to test the effect of the Au thickness on the Au dewetting properties at the bottom of the Al etched hole. Indeed, during the annealing procedure, the Au layer will form half-spheres (Au catalysts). The formation of these half-Au-spheres depends on the initial Au layer thickness and on the size of the holes etched in the Al mirror. Consequently, we created an e-beam mask consisting of a 50 µm x 50 µm frame with inside a 7 x 7 matrix of etched points (holes). These holes have a variable diameter from 5 (top left) to 250 nm (bottom right) with an incremental diameter increase of 5 nm. A SEM image of the resulting structure is visible in Figure 4.27a. Moreover, to test the effect of the e-beam dose on the resist, the structure presented in Figure 4.27a has been reproduced and each structure exposed to doses from 240 to 510 µC/cm$^2$ (with an increment of 20 µC/cm$^2$), resulting in a total of 16 structures distributed in a 4 x 4 matrix visible in Figure 4.27b.

---

[19] Deposited by Joule deposition in the metal deposition MBE chamber at a slow deposition rate of 3 $\mathring{A}/s$ calibrated using a quartz resonator along with SEM observations of the deposited layers.

[20] Note that all these depositions were carefully performed under UHV inside the MBE machine, in the II-VI, III-V and metallic chamber to prevent any deposition of impurities at the interfaces (due to an exposure to the air).

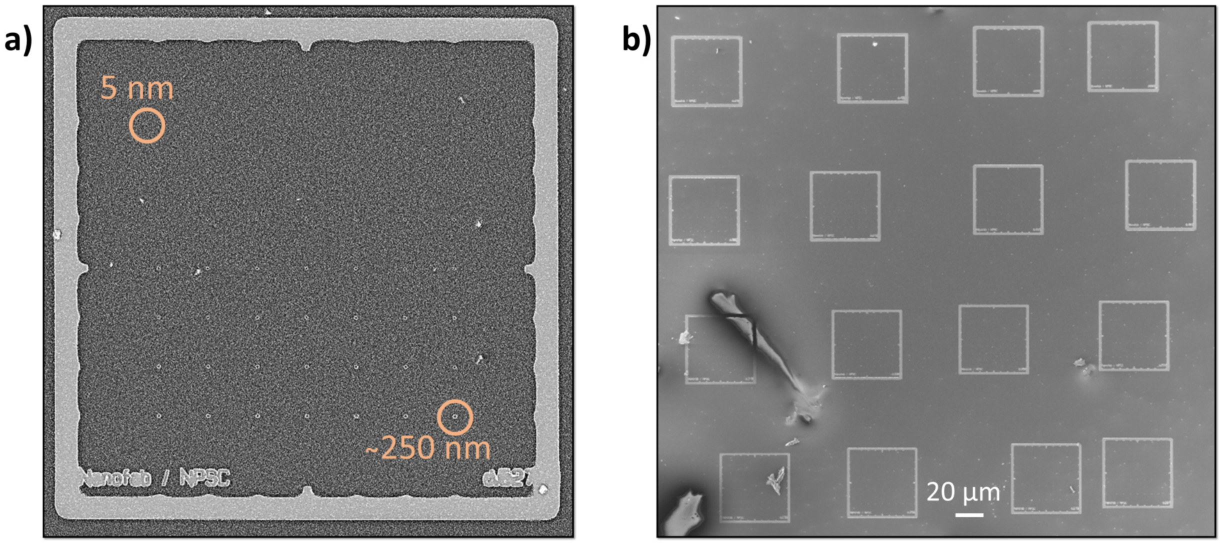

Figure 4.27: Top-view SEM pictures of our sample after the development of the positive resist insolated by e-beam following a lithography mask. a) Zoom on the structure of the mask composed of a 50 x 50 $\mu m^2$ frame with inside a 7 x 7 matrix of etched holes. These holes have an increasing diameter from 5 nm (top left) to 250 nm (bottom right) with an incremental diameter increase of 5 nm. The dark-grey part is the positive resist and the light-grey part is the Al layer. b) Overview of the 16 structures used to test the effect of the e-beam dose on the resist (doses from 240 to 510 $\mu C/cm^2$ with an increment of 20 $\mu C/cm^2$).

## Steps performed in the clean-room

### E-beam positive resist

The e-beam lithography, resist development and Al etchings have been carried out in the Néel Institute Nanofab clean-room. First, for the e-beam lithography, the positive resist PMMA 4% has been deposited at 4000 rotations/min (rpm) during 30 s to get the thinest uniform resist deposition possible at this time (260 nm). After the e-beam exposure, the resist development has been performed using the standard MIBK developer process, followed by an isopropanol rinsing. These two steps need a vigorous agitation of the sample to properly remove the resist due to the nanometric size of the exposed parts, from 5 to 250 nm in diameter.

### Ion Beam Etching (IBE)

After the cautious removal of the resist, the Al etching procedure had to be determined: wet (chemical) or physical etching. The main difference between the two approaches is that the wet etching induces a more isotropic etching, while it is more anisotropic for the physical etching. This effect is visible in Figure 4.28a and b. Since we want to keep the size of the Al hole close to the size of the hole in the resist, we used a mixed approach: first a physical etching of 20 nm by IBE, followed by a 10 nm wet etching. This mixed approach is visible in Figure 4.28c. The interest of this approach is also to finish the etching by a selective wet etching which preserves the gold layer. In the case of a completely physical etching, the gold layer is also etched, which is highly undesirable.

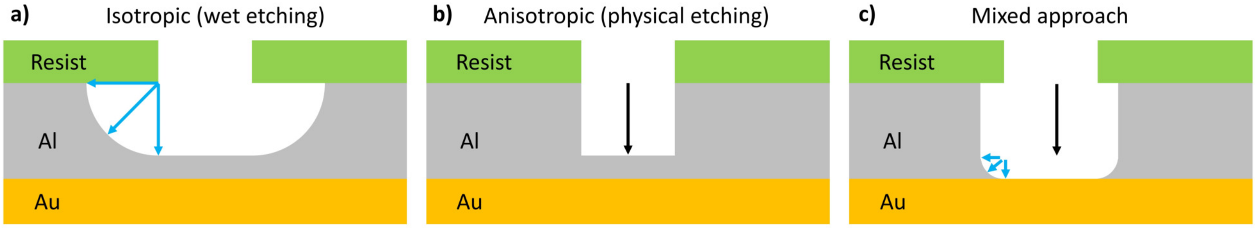

Figure 4.28: Difference between a) an isotropic wet etching and b) an anisotropic physical etching. c) Mixed approach used in this work, which consists in a first physical etching of 20 nm followed by a 10 nm wet etching.

We first calibrated the speed of the etching on a 100 nm-thick Al layer (measured with a profilometer after 10 min of etching), which is 0.1 nm/s at 400W. To avoid the removal of the whole resist during the etching, it has been carried out in a pulsed mode with 30 s of etching followed by 1 min without etching, for a total etching time of 200 s (20 nm of etching) and a rotation of the sample of 6 rpm. The result is visible in Figure 4.27a. The resist is still visible after the IBE etching: the pulsed mode was therefore efficient at keeping it. Besides, the mask visible in Figure 4.27a has been exposed to the smallest e-beam dose. This mask has the smallest number of opened holes in the resist: 35. Since we have 16 masks, at least 35 x 16 = 560 holes have been opened, which should be sufficient to warranty the growth of some NW-QDs.

After this physical etching by IBE, the wet etching has been performed (vigorous agitation) during 6 s using the MF319 solution (Al etching speed of 100 nm/min). After this wet etching, the Au layer starts to be visible (brighter than Al) as displayed in Figure 4.29. Figure 4.29a presents the name of our laboratory (NPSC for NanoPhysics and SemiConductors) etched through the Al layer, with the gold visible at the bottom. Underneath this very thin Au film of 4 ML, the ZnSe buffer layer is visible and recognizable due to the small ZnSe triangles induced at its surface by the (111)B crystalline orientation. Finally, Figure 4.29c reveals the presence of gold at the bottom of a hole through the surrounding resist.

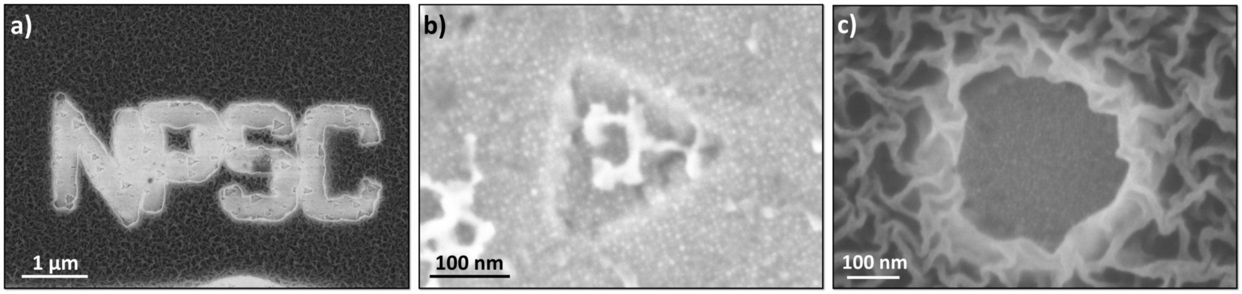

Figure 4.29: Top-view SEM images of a) our laboratory acronym etched through the resist with the gold visible. b) Zoom on the thin 4 ML gold film, revealing triangles from the ZnSe(111)B layer. c) Zoom on a hole etched through the resist with the gold visible.

The final step consists in removing the resist with an oxygen plasma by RIE. This step was rendered difficult by the hardening of the resist during the IBE etching. Several trials have be performed and the resist is still attached onto the sample surface. A possibility would be to carry out an ultrasonification of the sample in a solvent to ease the detachment of the resist. Next, this cleaned sample will be ready to be used in the MBE chamber.

# Publication/Scientific Events

This work gave rise to the following publications/presentations (by chronological order):

## Peer review publications

- T. Cremel, M. Elouneg-Jamroz, E. Bellet-Amalric, L. Cagnon, S. Tatarenko, and K. Kheng, *Bottom-up approach to control the photon outcoupling of a II-VI quantum dot with a photonic wire.* Phys. Status Solidi C, 11: 1263–1266 (2014).
- H. Benallali, T. Cremel, K. Hoummada, D. Mangelinck, R. André, S. Tatarenko and K. Kheng, *Atomic scale investigations on* $Cd_xZn_{1-x}Se$ *quantum dots: Correlation between the composition and emission properties*, Appl. Phys. Lett. 105, 053103 (2014)
- V. Zannier, T. Cremel, A. Artioli, D. Ferrand, K. Kheng, V. Grillo and S. Rubini, *Optical properties of single wurtzite/zinc blende ZnSe nanowires grown at low temperature*, J. Appli. Phys. 118, 095702 (2015).
- T. Cremel, E. Bellet-Amalric, and K. Kheng, *Homoepitaxial growth and optical properties of ZnSe nanowires on (111) substrates*, to be published.
- T. Cremel, M. Jeannin, E. Bellet-Amalric, W. Lee, K. Kyhm, G. Nogues and K. Kheng, *Structural, chemical and optical properties of ZnSe-CdSe nanowire quantum dots grown along (111)B,* to be published.
- T. Cremel, M. Jeannin, E. Bellet-Amalric, G. Nogues and K. Kheng, *Optical studies of ZnSe-CdSe(111)B nanowire quantum dots insered in photonic wires,* to be published.

## Presentations that I attended

- Fifth International Conference on One Dimensional Nanomaterials (ICON) in Annecy (2013): poster presentation.
- Fifth International Conference on Nanostructures SElf-Assembly (NanoSEA) in Marseille (2014): poster presentation.
- Condensed Matter (CMD-JMC) in Paris (2014): poster presentation.
- Scientific Exchange in Stanford and Berkeley (2014) and at the EPFL in Lausanne (2015): oral presentations.
- Journées boîtes quantiques in Grenoble (2015): poster presentation.
- 17th International Conference on II-VI Compounds and Related Materials in Paris (2015): poster presentation + **best oral presentation award.**
- RAFALD (Réseau des Acteurs Français ALD) workshop in Grenoble (2015): **best oral presentation award.**
- Dautreppe Photonics in Grenoble (2015): poster presentation.
- French-German-Korean (FKG) workshop on nanophotonics in Würzburg (2015): poster + mixed oral presentation with Mathieu Jeannin.
- Young Physicists Meeting in Grenoble (2015): **best oral presentation award.**
- International Summer School and workshop "Nanostructures for Photonics" in Saint-Petersburg: poster presentation.

# Bibliography

[1] R. S. Wagner and W. C. Ellis. Vapor-liquid-solid mechanism of single crystal growth. *Applied Physics Letters*, 4(5):89–90, March 1964.

[2] F. Glas. Critical dimensions for the plastic relaxation of strained axial heterostructures in free-standing nanowires. *Physical Review B*, 74(12):121302, September 2006.

[3] G. Priante, G. Patriarche, F. Oehler, F. Glas, and J.-C. Harmand. Abrupt GaP/GaAs Interfaces in Self-Catalyzed Nanowires. *Nano Letters*, 15(9):6036–6041, September 2015.

[4] M. D. Eisaman, J. Fan, A. Migdall, and S. V. Polyakov. Invited Review Article: Single-photon sources and detectors. *Review of Scientific Instruments*, 82(7):071101, 2011.

[5] C. H. Bennett and G. Brassard. A Quantum Information Science and Technology Roadmap. *Part*, 2:12, 2004.

[6] J. L. O'Brien. Optical Quantum Computing. *Science*, 318(5856):1567–1570, December 2007.

[7] A. Beveratos, R. Brouri, T. Gacoin, A. Villing, J.-P. Poizat, and P. Grangier. Single Photon Quantum Cryptography. *Physical Review Letters*, 89(18):187901, October 2002.

[8] A. J. Shields. Semiconductor quantum light sources. *Nature Photonics*, 1(4):215–223, April 2007.

[9] S. Buckley, K. Rivoire, and J. Vučković. Engineered quantum dot single-photon sources. *Reports on Progress in Physics*, 75(12):126503, 2012.

[10] S. Bounouar, M. Elouneg-Jamroz, M. den Hertog, C. Morchutt, E. Bellet-Amalric, R. André, C. Bougerol, Y. Genuist, J.-Ph. Poizat, S. Tatarenko, and K. Kheng. Ultrafast Room Temperature Single-Photon Source from Nanowire-Quantum Dots. *Nano Letters*, 12(6):2977–2981, June 2012.

[11] T. Akiyama, K. Sano, K. Nakamura, and T. Ito. An empirical interatomic potential approach to structural stability of ZnS and ZnSe nanowires. *Japanese journal of applied physics*, 46(4R):1783, 2007.

[12] Frank Glas, Jean-Christophe Harmand, and Gilles Patriarche. Why Does Wurtzite Form in Nanowires of III-V Zinc Blende Semiconductors? *Physical Review Letters*, 99(14):146101, October 2007.

[13] N. Sangouard and H. Zbinden. What are single photons good for? *Journal of Modern Optics*, 59(17):1458–1464, October 2012.

[14] M. Hennrich, T. Legero, A. Kuhn, and G. Rempe. Photon statistics of a non-stationary periodically driven single-photon source. *New Journal of Physics*, 6(1):86, 2004.

[15] Christian Maurer, Christoph Becher, Carlos Russo, Jürgen Eschner, and Rainer Blatt. A single-photon source based on a single Ca + ion. *New Journal of Physics*, 6(1):94, 2004.

[16] Mathias Steiner, Achim Hartschuh, Rafał Korlacki, and Alfred Johann Meixner. Highly efficient, tunable single photon source based on single molecules. *Applied Physics Letters*, (18), 2007.

[17] Shuai Chen, Yu-Ao Chen, Thorsten Strassel, Zhen-Sheng Yuan, Bo Zhao, Jörg Schmiedmayer, and Jian-Wei Pan. Deterministic and Storable Single-Photon Source Based on a Quantum Memory. *Physical Review Letters*, 97(17):173004, October 2006.

[18] O. Alibart, D. B. Ostrowsky, P. Baldi, and S. Tanzilli. High-performance guided-wave asynchronous heralded single-photon source. *Optics Letters*, 30(12):1539–1541, June 2005.

[19] S. Castelletto, B. C. Johnson, V. Ivády, N. Stavrias, T. Umeda, A. Gali, and T. Ohshima. A silicon carbide room-temperature single-photon source. *Nature Materials*, 13(2):151–156, February 2014.

[20] R. Brouri, A. Beveratos, J.-P. Poizat, and P. Grangier. Photon antibunching in the fluorescence of individual color centers in diamond. *Optics Letters*, 25(17):1294–1296, September 2000.

[21] G. Messin, J. P. Hermier, E. Giacobino, P. Desbiolles, and M. Dahan. Bunching and antibunching in the fluorescence of semiconductor nanocrystals. *Optics Letters*, 26(23):1891–1893, December 2001.

[22] O. Fedorych, C. Kruse, A. Ruban, D. Hommel, G. Bacher, and T. Kümmell. Room temperature single photon emission from an epitaxially grown quantum dot. *Applied Physics Letters*, 100(6):061114, February 2012.

[23] S. Bounouar. *Corrélation de photons sur un émetteur de photons uniques semi-conducteur à température ambiante*. PhD thesis, Grenoble, 2012.

[24] L. Besombes, K. Kheng, L. Marsal, and H. Mariette. Excited states and multi-exciton complexes in single CdTe quantum dots. *EPL (Europhysics Letters)*, 65(1):144, January 2004.

[25] J. Claudon, J. Bleuse, N. S. Malik, M. Bazin, P. Jaffrennou, N. Gregersen, C. Sauvan, P. Lalanne, and J.-M. Gerard. A highly efficient single-photon source based on a quantum dot in a photonic nanowire. *Nat Photon*, 4(3):174–177, March 2010.

[26] Léonard Monniello, Antoine Reigue, Richard Hostein, Aristide Lemaitre, Anthony Martinez, Roger Grousson, and Valia Voliotis. Indistinguishable single photons generated by a quantum dot under resonant excitation observable without postselection. *Physical Review B*, 90(4):041303, July 2014.

[27] Satoshi Kako, Charles Santori, Katsuyuki Hoshino, Stephan Götzinger, Yoshihisa Yamamoto, and Yasuhiko Arakawa. A gallium nitride single-photon source operating at 200 K. *Nature Materials*, 5(11):887–892, November 2006.

[28] M. J. Holmes, K. Choi, S. Kako, M. Arita, and Y. Arakawa. Room-Temperature Triggered Single Photon Emission from a III-Nitride Site-Controlled Nanowire Quantum Dot. *Nano Letters*, 14(2):982–986, February 2014.

[29] M. J. Holmes, S. Kako, K. Choi, M. Arita, and Y. Arakawa. Single Photons from a Hot Solid-State Emitter at 350 K. *ACS Photonics*, 3(4):543–546, April 2016.

[30] Yu-Ming He, Yu He, Yu-Jia Wei, Dian Wu, Mete Atatüre, Christian Schneider, Sven Höfling, Martin Kamp, Chao-Yang Lu, and Jian-Wei Pan. On-demand semiconductor single-photon source with near-unity indistinguishability. *Nature Nanotechnology*, 8(3):213–217, March 2013.

[31] N. Somaschi, V. Giesz, L. De Santis, J. C. Loredo, M. P. Almeida, G. Hornecker, S. L. Portalupi, T. Grange, C. Antón, J. Demory, C. Gómez, I. Sagnes, N. D. Lanzillotti-Kimura, A. Lemaítre, A. Auffeves, A. G. White, L. Lanco, and P. Senellart. Near-optimal single-photon sources in the solid state. *Nature Photonics*, 10(5):340–345, May 2016.

[32] Mohamed Benyoucef, Hong Seok Lee, Juliane Gabel, Tae Whan Kim, Hong Lee Park, Armando Rastelli, and Oliver G. Schmidt. Wavelength tunable triggered single-photon source from a single CdTe quantum dot on silicon substrate. *Nano Letters*, 9(1):304–307, January 2009.

[33] Wei Geng, Mathieu Manceau, Nancy Rahbany, Vincent Sallet, Massimo De Vittorio, Luigi Carbone, Quentin Glorieux, Alberto Bramati, and Christophe Couteau. Localised excitation of a single photon source by a nanowaveguide. *Scientific Reports*, 6:19721, January 2016.

[34] Xing Ding, Yu He, Z.-C. Duan, Niels Gregersen, M.-C. Chen, S. Unsleber, S. Maier, Christian Schneider, Martin Kamp, Sven Höfling, Chao-Yang Lu, and Jian-Wei Pan. On-Demand Single Photons with High Extraction Efficiency and Near-Unity Indistinguishability from a Resonantly Driven Quantum Dot in a Micropillar. *Physical Review Letters*, 116(2):020401, January 2016.

[35] E. Knill, R. Laflamme, R. Martinez, and C.-H. Tseng. An algorithmic benchmark for quantum information processing. *Nature*, 404(6776):368–370, March 2000.

[36] L. Besombes, K. Kheng, L. Marsal, and H. Mariette. Acoustic phonon broadening mechanism in single quantum dot emission. *Physical Review B*, 63(15), March 2001.

[37] Tom Beer. *The Aerospace Environment.* Wykeham Publications, 1976.

[38] N. Mizuochi, T. Makino, H. Kato, D. Takeuchi, M. Ogura, H. Okushi, M. Nothaft, P. Neumann, A. Gali, F. Jelezko, J. Wrachtrup, and S. Yamasaki. Electrically driven single-photon source at room temperature in diamond. *Nature Photonics*, 6(5):299–303, May 2012.

[39] Michel Nasilowski, Piernicola Spinicelli, Gilles Patriarche, and Benoît Dubertret. Gradient CdSe/CdS Quantum Dots with Room Temperature Biexciton Unity Quantum Yield. *Nano Letters*, 15(6):3953–3958, June 2015.

[40] T. Aichele, A. Tribu, G. Sallen, J. Bocquel, E. Bellet-Amalric, C. Bougerol, J.-P. Poizat, K. Kheng, R. André, S. Tatarenko, and H. Mariette. CdSe quantum dots in ZnSe nanowires as efficient source for single photons up to 220K. *Journal of Crystal Growth*, 311(7):2123–2127, March 2009.

[41] M. Elouneg-Jamroz. *Croissance catalysée de nanofils de ZnSe avec boîtes quantiques de CdSe.* phdthesis, Université de Grenoble, October 2013.

[42] Sebastian Moehl, Laurent Maingault, Kuntheak Kheng, and Henri Mariette. Enhanced carrier confinement in quantum dots by raising wetting layer state energy. *Applied Physics Letters*, 87(3):033111, July 2005.

[43] Sebastian Unsleber, Yu-Ming He, Stefan Gerhardt, Sebastian Maier, Chao-Yang Lu, Jian-Wei Pan, Niels Gregersen, Martin Kamp, Christian Schneider, and Sven Höfling. Highly indistinguishable on-demand resonance fluorescence photons from a deterministic quantum dot micropillar device with 74% extraction efficiency. *Optics Express*, 24(8):8539–8546, April 2016.

[44] M. Gschrey, A. Thoma, P. Schnauber, M. Seifried, R. Schmidt, B. Wohlfeil, L. Krüger, J.-H. Schulze, T. Heindel, S. Burger, F. Schmidt, A. Strittmatter, S. Rodt, and S. Reitzenstein. Highly indistinguishable photons from deterministic quantum-dot microlenses utilizing three-dimensional in situ electron-beam lithography. *Nature Communications*, 6:7662, July 2015.

[45] Y.-M. Niquet and D. C. Mojica. Quantum dots and tunnel barriers in InAs - InP nanowire heterostructures. Electronic and optical properties. *Physical Review B*, 77(11):115316, March 2008.

[46] M. Zieliński. Fine structure of light-hole excitons in nanowire quantum dots. *Physical Review B*, 88(11):115424, September 2013.

[47] N. Akopian, G. Patriarche, L. Liu, J.-C. Harmand, and V. Zwiller. Crystal Phase Quantum Dots. *Nano Letters*, 10(4):1198–1201, April 2010.

[48] V. Zannier, T. Cremel, A. Artioli, D. Ferrand, K. Kheng, V. Grillo, and S. Rubini. Optical properties of single wurtzite/zinc-blende ZnSe nanowires grown at low temperature. *Journal of Applied Physics*, 118(9):095702, September 2015.

[49] Springer Materials, the Landolt-Börnstein Database.

[50] L. Vegard. Die Konstitution der Mischkristalle und die Raumfüllung der Atome. *Zeitschrift für Physik*, 5(1):17–26, January 1921.

[51] H. Benallali, K. Hoummada, M. Descoins, P. Rueda-Fonseca, L. Gerard, E. Bellet-Amalric, S. Tatarenko, K. Kheng, and D. Mangelinck. Nature of the ZnSe/GaAs interface investigated by atom probe tomography. *Scripta Materialia*, 69(7):505–508, October 2013.

[52] P. Stepanov. *Magneto-optical spectroscopy of semiconductor magnetic quantum dots.* PhD thesis, Université de Grenoble, 2013.

[53] Claus F. Klingshirn. *Semiconductor Optics*. Springer, New York, 4th ed. 2012 edition edition, January 2012.

[54] S. L. Chuang and C. S. Chang. k. p method for strained wurtzite semiconductors. *Physical Review B*, 54(4):2491, 1996.

[55] G. Bastard. *Wave mechanics applied to semiconductor heterostructures.* EDP Sciences, Les Ulis Cedex, France : New York, N.Y, January 1992.

[56] N. S. Malik. *Les fils photoniques : une géométrie innovante pour la réalisation de sources de lumière quantique brillantes.* phdthesis, Université de Grenoble, November 2011.

[57] A. F. Moodie, J. M. Cowley, and P. Goodman. Dynamical theory of electron diffraction. In U. Shmueli, editor, *International Tables for Crystallography Volume B: Reciprocal space*, number B in International Tables for Crystallography, pages 552–556. Springer Netherlands, 2006.

[58] E. Hilner, A. Mikkelsen, J. Eriksson, J. N. Andersen, E. Lundgren, A. Zakharov, H. Yi, and P. Kratzer. Au wetting and nanoparticle stability on GaAs(111)B. *Applied Physics Letters*, 89(25):251912, 2006.

[59] H. Yi and P. Kratzer. Gold-induced surface reconstruction on GaAs(111) *B* surface. *Molecular Simulation*, 35(3):258–261, March 2009.

[60] M. A. Van Hove and G. A. Somorjai. Adsorption and adsorbate-induced restructuring: a LEED perspective. *Surface Science*, 299:487–501, January 1994.

[61] J. C. Harmand, M. Tchernycheva, G. Patriarche, L. Travers, F. Glas, and G. Cirlin. GaAs nanowires formed by Au-assisted molecular beam epitaxy: Effect of growth temperature. *Journal of Crystal Growth*, 301–302:853–856, April 2007.

[62] Ph. Buffat and J-P. Borel. Size effect on the melting temperature of gold particles. *Physical Review A*, 13(6):2287–2298, June 1976.

[63] M. Tchernycheva, J. C. Harmand, G. Patriarche, L. Travers, and G. E. Cirlin. Temperature conditions for GaAs nanowire formation by Au-assisted molecular beam epitaxy. *Nanotechnology*, 17(16):4025, 2006.

[64] J. C. Harmand, G. Patriarche, N. Péré-Laperne, M.-N. Mérat-Combes, L. Travers, and F. Glas. Analysis of vapor-liquid-solid mechanism in Au-assisted GaAs nanowire growth. *Applied Physics Letters*, 87(20):203101, November 2005.

[65] T. B. Massalski and etc. *Binary Alloy Phase Diagrams*. ASM International, Materials Park, Ohio, 2nd revised edition edition, 1990.

[66] C.-Y. Wen, J. Tersoff, M. C. Reuter, E. A. Stach, and F. M. Ross. Step-Flow Kinetics in Nanowire Growth. *Physical Review Letters*, 105(19), November 2010.

[67] C.-Y. Wen, M. C. Reuter, J. Bruley, J. Tersoff, S. Kodambaka, E. A. Stach, and F. M. Ross. Formation of Compositionally Abrupt Axial Heterojunctions in Silicon-Germanium Nanowires. *Science*, 326(5957):1247–1250, November 2009.

[68] H. Benallali. *Étude de nanostructures de semiconducteurs II-VI par sonde atomique tomographique*. Aix-Marseille, April 2015.

[69] F. Donatini and L. S. Dang. A single-step electron beam lithography of buried nanostructures using cathodoluminescence imaging and low temperature. *Nanotechnology*, 21(37):375303, September 2010.

[70] L. Polerecký, J. Hamrle, and B. D. MacCraith. Theory of the radiation of dipoles placed within a multilayer system. *Applied Optics*, 39(22):3968–3977, August 2000.

[71] T. J. Kempa, R. W. Day, S. Kim, H. Park, and C. M. Lieber. Semiconductor nanowires: a platform for exploring limits and concepts for nano-enabled solar cells. *Energy & Environmental Science*, 6(3):719, 2013.

[72] P. B. Sorokin, P. V. Avramov, V. A. Demin, and L. A. Chernozatonskii. Metallic beta-phase silicon nanowires: Structure and electronic properties. *JETP Letters*, 92(5):352–355, September 2010.

[73] P. Kusch, E. Grelich, C. Somaschini, E. Luna, M. Ramsteiner, L. Geelhaar, H. Riechert, and S. Reich. Type-II band alignment of zinc-blende and wurtzite segments in GaAs nanowires: A combined photoluminescence and resonant Raman scattering study. *Physical Review B*, 89(4), January 2014.

[74] P. Rueda-Fonseca, E. Bellet-Amalric, R. Vigliaturo, M. den Hertog, Y. Genuist, R. André, E. Robin, A. Artioli, P. Stepanov, D. Ferrand, K. Kheng, S. Tatarenko, and J. Cibert. Structure and Morphology in Diffusion-Driven Growth of Nanowires: The Case of ZnTe. *Nano Letters*, 14(4):1877–1883, April 2014.

[75] Y. Liang, Y. Tao, and S. K. Hark. Fabrication and optical properties of vertically aligned ZnSe nanowire arrays catalyzed by Ga and Ag. *CrystEngComm*, 13(19):5751, 2011.

[76] X. T. Zhang, Z. Liu, Y. P. Leung, Quan Li, and S. K. Hark. Growth and luminescence of zinc-blende-structured ZnSe nanowires by metal-organic chemical vapor deposition. *Applied Physics Letters*, 83(26):5533, 2003.

[77] X. Zhang, Z. Liu, Q. Li, Y. Leung, K. Ip, and S. Hark. Routes to Grow Well-Aligned Arrays of ZnSe Nanowires and Nanorods. *Advanced Materials*, 17(11):1405–1410, June 2005.

[78] C. X. Shan, Z. Liu, X. T. Zhang, C. C. Wong, and S. K. Hark. Wurtzite ZnSe nanowires: growth, photoluminescence, and single-wire Raman properties. *Nanotechnology*, 17(22):5561–5564, November 2006.

[79] C. X. Shan, Z. Liu, C. M. Ng, and S. K. Hark. ZnxCd1-xSe alloy nanowires covering the entire compositional range grown by metalorganic chemical vapor deposition. *Applied Physics Letters*, 87(3):033108, 2005.

[80] K. B. Kahen, I. A. Goldthorpe, and M. Holland. II–VI nanowire radial heterostructures. *Nanotechnology*, 24(45):455603, November 2013.

[81] C. Lee, S. Park, and J. Jun. Enhanced Photoluminescence of ZnSe Nanowires with Branches. *Journal of the Korean Physical Society*, 55(2):554–557, 2009.

[82] J. Xu, A. Lu, C. Wang, R. Zou, X. Liu, X. Wu, Y. Wang, S. Li, L. Sun, X. Chen, H. Oh, H. Baek, G.-C. Yi, and J. Chu. ZnSe-Based Longitudinal Twinning Nanowires: ZnSe-Based Longitudinal Twinning Nanowires. *Advanced Engineering Materials*, 16(4):459–465, April 2014.

[83] B. Xiang, H. Z. Zhang, G. H. Li, F. H. Yang, F. H. Su, R. M. Wang, J. Xu, G. W. Lu, X. C. Sun, Q. Zhao, and D. P. Yu. Green-light-emitting ZnSe nanowires fabricated via vapor phase growth. *Applied Physics Letters*, 82(19):3330, 2003.

[84] C. Ye, X. Fang, Y. Wang, P. Yan, J. Zhao, and L. Zhang. Structural characterization of long ZnSe nanowires. *Applied Physics A: Materials Science & Processing*, 79(1):113–115, June 2004.

[85] L. Shi, Y. Xu, and Q. Li. Controlled Fabrication of ZnSe Arrays of Well-Aligned Nanorods, Nanowires, and Nanobelts with a Facile Template-Free Route. *The Journal of Physical Chemistry C*, 113(5):1795–1799, February 2009.

[86] T. Zhang, Y. Shen, W. Hu, J. Sun, J. Wu, Z. Ying, and N. Xu. Growth of ZnSe nanowires by pulsed-laser deposition. *Journal of Vacuum Science & Technology B: Microelectronics and Nanometer Structures*, 25(6):1823, 2007.

[87] S.J. Chang, C.H. Hsiao, B.W. Lan, S.C. Hung, B.R. Huang, S.J. Young, Y.C. Cheng, and S.H. Chih. Growth of ternary ZnCdSe nanowires and the fabrication of ZnCdSe nanowire photodetectors. *Superlattices and Microstructures*, 48(1):50–57, July 2010.

[88] A. Colli, F. Martell, Stephane Rubini, C. Ducati, S. Hofmann, A. C. Ferrari, J. Robertson, and A. Franciosi. Growth of ZnSe nanowires by molecular beam epitaxy. In *Nanotechnology, 2004. 4th IEEE Conference on*, pages 177–179. IEEE, 2004.

[89] A. Colli, S. Hofmann, A. C. Ferrari, C. Ducati, F. Martelli, S. Rubini, S. Cabrini, A. Franciosi, and J. Robertson. Low-temperature synthesis of ZnSe nanowires and nanosaws by catalyst-assisted molecular-beam epitaxy. *Applied Physics Letters*, 86(15):153103, 2005.

[90] A. Colli, S. Hofmann, A. C. Ferrari, F. Martelli, S. Rubini, C. Ducati, A. Franciosi, and J. Robertson. Selective growth of ZnSe and ZnCdSe nanowires by molecular beam epitaxy. *Nanotechnology*, 16(5):S139–S142, May 2005.

[91] C. H. Hsiao, S. J. Chang, S. B. Wang, S. P. Chang, T. C. Li, W. J. Lin, C. H. Ko, T. M. Kuan, and B. R. Huang. ZnSe Nanowire Photodetector Prepared on Oxidized Silicon Substrate by Molecular-Beam Epitaxy. *Journal of The Electrochemical Society*, 156(4):J73, 2009.

[92] Y. Cai, T. L. Wong, S. K. Chan, I. K. Sou, D. S. Su, and N. Wang. Growth behaviors of ultrathin ZnSe nanowires by Au-catalyzed molecular-beam epitaxy. *Applied Physics Letters*, 93(23):233107, 2008.

[93] S.K. Chan, Y. Cai, I.K. Sou, and N. Wang. MBE-grown Au-island-catalyzed ZnSe nanowires. *Journal of Crystal Growth*, 278(1-4):146–150, May 2005.

[94] S. K. Chan, N. Liu, Y. Cai, N. Wang, G. K. L. Wong, and I. K. Sou. Molecular beam epitaxy—Grown ZnSe nanowires. *Journal of electronic materials*, 35(6):1246–1250, 2006.

[95] V. Zannier, F. Martelli, V. Grillo, J. R. Plaisier, A. Lausi, and S. Rubini. Strong blue emission from ZnSe nanowires grown at low temperature: Strong blue emission from ZnSe nanowires grown at low temperature. *physica status solidi (RRL) - Rapid Research Letters*, 8(2):182–186, February 2014.

[96] Y. Cai, S. K. Chan, I. K. Sou, Y. F. Chan, Dang Sheng Su, and N. Wang. TEM investigation of nucleation and initial growth of ZnSe nanowires. In *MRS Proceedings*, volume 838, pages O14–11. Cambridge Univ Press, 2004.

[97] Y. Cai, S. K. Chan, I. K. Sou, Y. F. Chan, D. S. Su, and N. Wang. Temperature-Dependent Growth Direction of Ultrathin ZnSe Nanowires. *Small*, 3(1):111–115, January 2007.

[98] Y. Cai, S. K. Chan, I. K. Sou, Y. F. Chan, D. S. Su, and N. Wang. The Size-Dependent Growth Direction of ZnSe Nanowires. *Advanced Materials*, 18(1):109–114, January 2006.

[99] Y. G. Wang, B. S. Zou, T. H. Wang, N. Wang, Y. Cai, Y. F. Chan, and S. X. Zhou. $I-V$ characteristics of Schottky contacts of semiconducting ZnSe nanowires and gold electrodes. *Nanotechnology*, 17(9):2420–2423, May 2006.

[100] Y. F. Chan, X. F. Duan, S. K. Chan, I. K. Sou, X. X. Zhang, and N. Wang. ZnSe nanowires epitaxially grown on GaP(111) substrates by molecular-beam epitaxy. *Applied Physics Letters*, 83(13):2665, 2003.

[101] J. Basu, R. Divakar, J. Nowak, S. Hofmann, A. Colli, A. Franciosi, and C. B. Carter. Structure and growth mechanism of ZnSe nanowires. *Journal of Applied Physics*, 104(6):064302, 2008.

[102] X. Fang, S. Xiong, T. Zhai, Y. Bando, M. Liao, U. K. Gautam, Y. Koide, X. Zhang, Y. Qian, and D. Golberg. High-Performance Blue/Ultraviolet-Light-Sensitive ZnSe-Nanobelt Photodetectors. *Advanced Materials*, 21(48):5016–5021, December 2009.

[103] Y. P. Leung, W. C. H. Choy, and T. I. Yuk. Linearly resistive humidity sensor based on quasi one-dimensional ZnSe nanostructures. *Chemical Physics Letters*, 457(1–3):198–201, May 2008.

[104] G. Xing, J. Luo, H. Li, B. Wu, X. Liu, C. H. A. Huan, H. J. Fan, and T. C. Sum. Ultrafast Exciton Dynamics and Two-Photon Pumped Lasing from ZnSe Nanowires. *Advanced Optical Materials*, 1(4):319–326, April 2013.

[105] C. Fernandes, H. Ruda, A. Saxena, and C. de Souza. Preparation of high quality ZnSe nanowires dominated by excitonic emission. *physica status solidi (c)*, 9(12):2460–2464, December 2012.

[106] A. Saxena, Q. Pan, and H. E Ruda. Unambiguous identification of recombination lines in single zinc-blende ZnSe nanowires in direct relation to their microstructure. *Nanotechnology*, 24(10):105701, March 2013.

[107] X. Fan, X. M. Meng, X. H. Zhang, M. L. Zhang, J. S. Jie, W. J. Zhang, C. S. Lee, and S. T. Lee. Formation and Photoelectric Properties of Periodically Twinned ZnSe/SiO2 Nanocables. *The Journal of Physical Chemistry C*, 113(3):834–838, January 2009.

[108] Y. Q. Wang, U. Philipose, T. Xu, H. E. Ruda, and K. L. Kavanagh. Twinning modulation in ZnSe nanowires. *Semiconductor Science and Technology*, 22(3):175, 2007.

[109] T. Aichele, A. Tribu, C. Bougerol, K. Kheng, R. André, and S. Tatarenko. Defect-free ZnSe nanowire and nanoneedle nanostructures. *Applied Physics Letters*, 93(14):143106, 2008.

[110] K.B. Kahen, I. A. Goldthorpe, and J. Minter. Low temperature II–VI nanowire growth using Au–Sn catalysts. *Journal of Crystal Growth*, 322(1):57–62, May 2011.

[111] V. Zannier, V. Grillo, F. Martelli, J. R. Plaisier, A. Lausi, and S. Rubini. Tuning the growth mode of nanowires via the interaction among seeds, substrates and beam fluxes. *Nanoscale*, 6(14):8392, 2014.

[112] E. Carlino, F. Martelli, S. Rubini, and A. Franciosi. Catalyst incorporation in ZnSe nanowires. *Philosophical Magazine Letters*, 86(4):261–266, April 2006.

[113] E. Bellet-Amalric, M. Elouneg-Jamroz, P. Rueda-Fonseca, S. Bounouar, M. Den Hertog, C. Bougerol, R. André, Y. Genuist, J. P. Poizat, K. Kheng, J. Cibert, and S. Tatarenko. Growth of II-VI ZnSe/CdSe nanowires for quantum dot luminescence. *Journal of Crystal Growth*, 378:233–237, September 2013.

[114] V. Zannier, V. Grillo, and S. Rubini. Diameter-dependent morphology of vapour–solid–solid grown ZnSe nanowires. *Journal of Physics D: Applied Physics*, 47(39):394005, 2014.

[115] A. Artioli, P. Rueda-Fonseca, P. Stepanov, E. Bellet-Amalric, M. Den Hertog, C. Bougerol, Y. Genuist, F. Donatini, R. André, G. Nogues, K. Kheng, S. Tatarenko, D. Ferrand, and J. Cibert. Optical properties of single ZnTe nanowires grown at low temperature. *Applied Physics Letters*, 103(22):222106, November 2013.

[116] M. Yamaguchi, A. Yamamoto, and M. Kondo. Photoluminescence of ZnSe single crystals diffused with a group-III element. *Journal of Applied Physics*, 48(12):5237–5244, December 1977.

[117] P. J. Dean, D. C. Herbert, C. J. Werkhoven, B. J. Fitzpatrick, and R. N. Bhargava. Donor bound-exciton excited states in zinc selenide. *Physical Review B*, 23(10):4888–4901, May 1981.

[118] A. D. Raisanen, L. J. Brillson, L. Vanzetti, A. Bonanni, and A. Franciosi. Atomic diffusion-induced deep levels near ZnSe/GaAs(100) interfaces. *Applied Physics Letters*, 66(24):3301, 1995.

[119] T. Taguchi, T. Kusao, and A. Hiraki. Growth of high-purity ZnSe by sublimation THM and the characteristics of the Y and Z deep-level emission lines. *Journal of Crystal Growth*, 72(1):46–50, July 1985.

[120] W. Y. Liang and A. D. Yoffe. Luminescence in hexagonal zinc selenide crystals. *Philosophical Magazine*, 16(144):1153–1166, December 1967.

[121] Y.-C. Zhu and Y. Bando. Preparation and photoluminescence of single-crystal zinc selenide nanowires. *Chemical Physics Letters*, 377(3-4):367–370, August 2003.

[122] U. Philipose, S. Yang, T. Xu, and H. E. Ruda. Origin of the red luminescence band in photoluminescence spectra of ZnSe nanowires. *Applied Physics Letters*, 90(6):063103, 2007.

[123] U. Philipose, A. Saxena, H. E. Ruda, P. J. Simpson, Y. Q. Wang, and K. L. Kavanagh. Defect studies of ZnSe nanowires. *Nanotechnology*, 19(21):215715, May 2008.

[124] A. Saxena, S. Yang, U. Philipose, and H. E. Ruda. Excitonic and pair-related photoluminescence in ZnSe nanowires. *Journal of Applied Physics*, 103(5):053109, 2008.

[125] A. Saxena, Q. Pan, and H. E. Ruda. Radiative recombination mechanisms in individual wurtzite ZnSe nanowires with a defect-free single-crystalline microstructure. *Nanoscale*, 5(7):2875, 2013.

[126] A. Mishra, L. V. Titova, T. B. Hoang, H. E. Jackson, L. M. Smith, J. M. Yarrison-Rice, Y. Kim, H. J. Joyce, Q. Gao, H. H. Tan, and C. Jagadish. Polarization and temperature dependence of photoluminescence from zincblende and wurtzite InP nanowires. *Applied Physics Letters*, 91(26):263104, 2007.

[127] Y. Masumoto, Y. Hirata, P. Mohan, J. Motohisa, and T. Fukui. Polarized photoluminescence from single wurtzite InP/InAs/InP core-multishell nanowires. *Applied Physics Letters*, 98(21):211902, May 2011.

[128] T. Ba Hoang, A. F. Moses, L. Ahtapodov, H. Zhou, D. L. Dheeraj, A. T. J. van Helvoort, B.-O. Fimland, and H. Weman. Engineering Parallel and Perpendicular Polarized Photoluminescence from a Single Semiconductor Nanowire by Crystal Phase Control. *Nano Letters*, 10(8):2927–2933, August 2010.

[129] H. E. Ruda and A. Shik. Polarization-sensitive optical phenomena in thick semiconducting nanowires. *Journal of Applied Physics*, 100(2):024314, 2006.

[130] M. Murayama and T. Nakayama. Chemical trend of band offsets at wurtzite/zinc-blende heterocrystalline semiconductor interfaces. *Physical Review B*, 49(7):4710, 1994.

[131] D. Spirkoska, J. Arbiol, A. Gustafsson, S. Conesa-Boj, F. Glas, I. Zardo, M. Heigoldt, M. H. Gass, A. L. Bleloch, S. Estrade, M. Kaniber, J. Rossler, F. Peiro, J. R. Morante, G. Abstreiter, L. Samuelson, and A. Fontcuberta i Morral. Structural and optical properties of high quality zinc-blende/wurtzite GaAs nanowire heterostructures. *Physical Review B*, 80(24), December 2009.

[132] J. Bao, D. C. Bell, F. Capasso, J. B. Wagner, T. Mårtensson, J. Trägårdh, and L. Samuelson. Optical Properties of Rotationally Twinned InP Nanowire Heterostructures. *Nano Letters*, 8(3):836–841, March 2008.

[133] P. Caroff, K. A. Dick, J. Johansson, M. E. Messing, K. Deppert, and L. Samuelson. Controlled polytypic and twin-plane superlattices in iii–v nanowires. *Nature Nanotechnology*, 4(1):50–55, January 2009.

[134] P. Rueda-Fonseca. *Magnetic quantum dots in II-VI semiconductor nanowires.* PhD thesis, Grenoble, 2015.

[135] S. Ambrosini, M. Fanetti, V. Grillo, A. Franciosi, and S. Rubini. Self-catalyzed GaAs nanowire growth on Si-treated GaAs(100) substrates. *Journal of Applied Physics*, 109(9):094306, 2011.

[136] S. Ambrosini, M. Fanetti, V. Grillo, A. Franciosi, and S. Rubini. Vapor-liquid-solid and vapor-solid growth of self-catalyzed GaAs nanowires. *AIP Advances*, 1(4):042142, 2011.

[137] A. Y. Cho. Morphology of Epitaxial Growth of GaAs by a Molecular Beam Method: The Observation of Surface Structures. *Journal of Applied Physics*, 41(7):2780–2786, June 1970.

[138] A. Ohtake, J. Nakamura, T. Komura, T. Hanada, T. Yao, H. Kuramochi, and M. Ozeki. Surface structures of GaAs {111} A , B - (2×2). *Physical Review B*, 64(4), June 2001.

[139] A. Ohtake, S. Miwa, L.-H. Kuo, K. Kimura, T. Yasuda, C. Jin, and T. Yao. Surface processes during heteroepitaxy of ZnSe on $\mathrm{GaAs}(111)A$ as observed by reflection high-energy electron diffraction. *Physical Review B*, 56(23):14909–14912, December 1997.

[140] D. A. Woolf, D. I. Westwood, and R. H. Williams. The homoepitaxial growth of GaAs (111) A and (111) B by molecular beam epitaxy: an investigation of the temperature-dependent surface reconstructions and bulk electrical conductivity transitions. *Semiconductor science and technology*, 8(6):1075, 1993.

[141] F. S. Gard, J. D. Riley, R. Leckey, and B. F. Usher. Comparison studies on growth modes of MBE grown ZnSe on GaAs [111] A and GaAs [111] B, using RHEED. In *Proceedings Conference on Optoelectronic and Microelectronic Materials and Devices, 2000. COMMAD 2000*, pages 475–478, 2000.

[142] F. S. Gard, J. D. Riley, R. Leckey, and B. F. Usher. Reflection high-energy electron diffraction (RHEED) study of MBE growth of ZnSe on GaAs (111) B surfaces. *Applied surface science*, 181(1):94–102, 2001.

[143] F. S. Gard, M. May, D. James, J. D. Riley, R. Leckey, and B. F. Usher. RHEED investigation of MBE growth of ZnSe epilayer on GaAs (111) B. In *Semiconducting and Insulating Materials Conference, 2000. SIMC-XI. International*, pages 322–325. IEEE, 2000.

[144] I. C. Robin, R. André, H. Mariette, S. Tatarenko, L. S. Dang, J. Bleuse, E. Bellet-Amalric, and J.-M. Gérard. Control of the two-dimensional–three-dimensional transition of self-organized CdSe/ZnSe quantum dots. *Nanotechnology*, 16(8):1116–1118, August 2005.

[145] A. Krost, W. Richter, D. R. T. Zahn, K. Hingerl, and H. Sitter. Chemical reaction at the ZnSe/GaAs interface detected by Raman spectroscopy. *Applied Physics Letters*, 57(19):1981, 1990.

[146] E. Kurtz, T. Sekiguchi, Z. Zhu, T. Yao, J. X. Shen, Y. Oka, M. Y. Shen, and T. Goto. Growth and time-resolved photoluminescence study of self-organized CdSe quantum dots in ZnSe. *Superlattices and microstructures*, 25(1):119–125, 1999.

[147] P. R. Kratzert, M. Rabe, and F. Henneberger. Formation and stability of II–VI self-assembled quantum dots revealed by in situ atomic force microscopy. *Applied Surface Science*, 166(1–4):332–335, October 2000.

[148] X. Liu, A. M. Mintairov, J. Herzog, F. Vietmeyer, R. E. Pimpinella, M. Kuno, J. L. Merz, T. H. Kosel, M. Dobrowolska, and J. K. Furdyna. II-VI heterostructures obtained by encapsulation of colloidal CdSe nanowires by molecular beam epitaxy deposition of ZnSe. *Journal of Vacuum Science & Technology B: Microelectronics and Nanometer Structures*, 29(3):03C102, 2011.

[149] Y. Park, M. J. Cich, R. Zhao, P. Specht, E. R. Weber, E. Stach, and S. Nozaki. Analysis of twin defects in GaAs(111)B molecular beam epitaxy growth. *Journal of Vacuum Science & Technology B*, 18(3):1566–1571, May 2000.

[150] A. Roy, K. Bhattacharjee, J. Ghatak, and B. N. Dev. Growth of epitaxially oriented Ag nanoislands on air-oxidized Si(1 1 1)-(7 × 7) surfaces: Influence of short-range order on the substrate. *Applied Surface Science*, 258(7):2255–2265, January 2012.

[151] C. B. Alcock, V. P. Itkin, and M. K. Horrigan. Vapour Pressure Equations for the Metallic Elements: 298–2500K. *Canadian Metallurgical Quarterly*, 23(3):309–313, July 1984.

[152] T. Hasegawa, K. Takata, S. Hosaka, and S. Hosoki. Au-induced reconstructions of the Si(111) surface. *Journal of Vacuum Science & Technology A*, 8(1):241–244, January 1990.

[153] D. J. Chadi. Doping in ZnSe, ZnTe, MgSe, and MgTe wide-band-gap semiconductors. *Physical review letters*, 72(4):534, 1994.

[154] A. Fleszar. LDA, GW, and exact-exchange Kohn-Sham scheme calculations of the electronic structure of sp semiconductors. *Physical Review B*, 64(24), November 2001.

[155] U. Lunz, C. Schumacher, J. Nürnberger, K. Schüll, A. Gerhard, U. Schüssler, B. Jobst, W. Faschinger, and G. Landwehr. The energy gap of epitaxial layers as a function of composition and temperature. *Semiconductor science and technology*, 12(8):970, 1997.

[156] H. Okuyama, K. Nakano, T. Miyajima, and K. Akimoto. Epitaxial growth of ZnMgSSe on GaAs substrate by molecular beam epitaxy. *Japanese Journal of Applied Physics*, 30:L1620–L1623, September 1991.

[157] C. A. Madu and B. N. Onwuagba. Electronic and Structural Properties of MgSe, CaSe, SrSe, and BaSe. *The African Review of Physics*, 7, 2012.

[158] G. A. Saum and E. B. Hensley. Fundamental Optical Absorption in the IIA-VIB Compounds. *Physical Review*, 113(4):1019, 1959.

[159] W. H. Strehlow and E. L. Cook. Compilation of Energy Band Gaps in Elemental and Binary Compound Semiconductors and Insulators. *Journal of Physical and Chemical Reference Data*, 2(1):163–200, January 1973.

[160] H. Li, H. L. Xin, D. A. Muller, and L. A. Estroff. Visualizing the 3D Internal Structure of Calcite Single Crystals Grown in Agarose Hydrogels. *Science*, 326(5957):1244–1247, November 2009.

[161] L. J. Brillson, X. Yang, A. D. Raisanen, A. Franciosi, L. Vanzetti, and L. Sorba. Deep level formation and heterojunction band offsets at ZnSe/GaAs interfaces. *Applied Surface Science*, 123:289–293, January 1998.

[162] P. J. Dean, B. J. Fitzpatrick, and R. N. Bhargava. Optical properties of ZnSe doped with Ag and Au. *Physical Review B*, 26(4):2016–2035, August 1982.

[163] R. Songmuang, L. T. T. Giang, J. Bleuse, M. Den Hertog, Y. M. Niquet, L. S. Dang, and H. Mariette. Determination of the Optimal Shell Thickness for Self-Catalyzed GaAs/AlGaAs Core–Shell Nanowires on Silicon. *Nano Letters*, April 2016.

[164] P. V. Kamat, N. M. Dimitrijevic, and A. J. Nozik. Dynamic Burstein-Moss shift in semiconductor colloids. *The Journal of Physical Chemistry*, 93(8):2873–2875, April 1989.

[165] I. L. Kuskovsky, C. Tian, G. F. Neumark, J. E. Spanier, Irving P. Herman, W.-C. Lin, S. P. Guo, and M. C. Tamargo. Optical properties of $\delta$ -doped ZnSe:Te grown by molecular beam epitaxy: The role of tellurium. *Physical Review B*, 63(15), March 2001.

[166] D. Ferrand and J. Cibert. Strain in crystalline core-shell nanowires. *European Physical Journal: Applied Physics*, 67:30403, August 2014.

[167] G. L. Bir and G. E. Pikus. *Symmetry and Strain-induced Effects in Semiconductors.* Wiley, 1974.

[168] Frances M. Ross. Controlling nanowire structures through real time growth studies. *Reports on Progress in Physics*, 73(11):114501, 2010.

[169] Bozhi Tian, Ping Xie, Thomas J. Kempa, David C. Bell, and Charles M. Lieber. Single-crystalline kinked semiconductor nanowire superstructures. *Nature Nanotechnology*, 4(12):824–829, December 2009.

[170] J. M. Gaines, J. Petruzzello, and B. Greenberg. Structural properties of ZnSe films grown by migration enhanced epitaxy. *Journal of Applied Physics*, 73(6):2835–2840, March 1993.

[171] S. Duman, S. Bağcı, H. M. Tütüncü, and G. P. Srivastava. First-principles studies of ground-state and dynamical properties of MgS, MgSe, and MgTe in the rocksalt, zinc blende, wurtzite, and nickel arsenide phases. *Physical Review B*, 73(20):205201, May 2006.

[172] Young-Il Kim, Katharine Page, and Ram Seshadri. Synchrotron x-ray study of polycrystalline wurtzite Zn[sub 1-x]Mg[sub x]O (0<=x<=0.15): Evolution of crystal structure and polarization. *Applied Physics Letters*, 90(10):101904, 2007.

[173] L. J. Lauhon, M. S. Gudiksen, D. Wang, and C. M. Lieber. Epitaxial core–shell and core–multishell nanowire heterostructures. *Nature*, 420(6911):57–61, 2002.

[174] Peter Krogstrup, Henrik I. Jørgensen, Erik Johnson, Morten Hannibal Madsen, Claus B. Sørensen, Anna Fontcuberta i Morral, Martin Aagesen, Jesper Nygård, and Frank Glas. Advances in the theory of III–V nanowire growth dynamics. *Journal of Physics D: Applied Physics*, 46(31):313001, 2013.

[175] Toru Akiyama, Kosuke Sano, Kohji Nakamura, and Tomonori Ito. An empirical potential approach to wurtzite–zinc-blende polytypism in group III–V semiconductor nanowires. *Japanese journal of applied physics*, 45(3L):L275, 2006.

[176] P. Rueda-Fonseca, E. Robin, E. Bellet-Amalric, M. Lopez-Haro, M. Den Hertog, Y. Genuist, R. André, A. Artioli, S. Tatarenko, D. Ferrand, and J. Cibert. Quantitative Reconstructions of 3D Chemical Nanostructures in Nanowires. *Nano Letters*, 16(3):1637–1642, March 2016.

[177] M. Watanabe and D. B. Williams. The quantitative analysis of thin specimens: a review of progress from the Cliff-Lorimer to the new $\zeta$-factor methods. *Journal of Microscopy*, 221(2):89–109, February 2006.

[178] M. K. Miller, T. F. Kelly, K. Rajan, and S. P. Ringer. The future of atom probe tomography. *Materials Today*, 15(4):158–165, April 2012.

[179] E. A. Marquis, N. A. Yahya, D. J. Larson, M. K. Miller, and R. I. Todd. Probing the improbable: imaging C atoms in alumina. *Materials Today*, 13(10):34–36, October 2010.

[180] K. Inoue, F. Yano, A. Nishida, H. Takamizawa, T. Tsunomura, Y. Nagai, and M. Hasegawa. Dopant distributions in n-MOSFET structure observed by atom probe tomography. *Ultramicroscopy*, 109(12):1479–1484, November 2009.

[181] M. J. Galtrey, R. A. Oliver, M. J. Kappers, C. McAleese, D. Zhu, C. J. Humphreys, P. H. Clifton, D. Larsen, and A. Cerezo. Atom probe reveals the structure of Inx Ga1–xN based quantum wells in three dimensions. *physica status solidi (b)*, 245(5):861–867, May 2008.

[182] A. D. Giddings, J. G. Keizer, M. Hara, G. J. Hamhuis, H. Yuasa, H. Fukuzawa, and P. M. Koenraad. Composition profiling of InAs quantum dots and wetting layers by atom probe tomography and cross-sectional scanning tunneling microscopy. *Physical Review B*, 83(20):205308, May 2011.

[183] J. Hernández-Saz, M. Herrera, S. I. Molina, C. R. Stanley, and S. Duguay. Atom probe tomography analysis of InAlGaAs capped InAs/GaAs stacked quantum dots with variable barrier layer thickness. *Acta Materialia*, 103:651–657, January 2016.

[184] M. Müller, A. Cerezo, G. D. W. Smith, L. Chang, and S. S. A. Gerstl. Atomic scale characterization of buried InxGa1-xAs quantum dots using pulsed laser atom probe tomography. *Applied Physics Letters*, 92(23):233115, June 2008.

[185] H. Benallali, T. Cremel, K. Hoummada, D. Mangelinck, R. André, S. Tatarenko, and K. Kheng. Atomic scale investigations on CdxZn1-xSe quantum dots: Correlation between the composition and emission properties. *Applied Physics Letters*, 105(5):053103, August 2014.

[186] D. Litvinov, A. Rosenauer, D. Gerthsen, P. Kratzert, M. Rabe, and F. Henneberger. Influence of the growth procedure on the Cd distribution in CdSe/ZnSe heterostructures: Stranski–Krastanov versus two-dimensional islands. *Applied Physics Letters*, 81(4):640–642, July 2002.

[187] T. Passow, H. Heinke, T. Schmidt, J. Falta, A. Stockmann, H. Selke, P. L. Ryder, K. Leonardi, and D. Hommel. Segregation-enhanced etching of Cd during Zn deposition on CdSe quantum dots. *Physical Review B*, 64(19):193311, October 2001.

[188] T. Passow, K. Leonardi, H. Heinke, D. Hommel, D. Litvinov, A. Rosenauer, D. Gerthsen, J. Seufert, G. Bacher, and A. Forchel. Quantum dot formation by segregation enhanced CdSe reorganization. *Journal of Applied Physics*, 92(11):6546–6552, December 2002.

[189] E. A. Marquis, B. P. Geiser, T. J. Prosa, and D. J. Larson. Evolution of tip shape during field evaporation of complex multilayer structures. *Journal of Microscopy*, 241(3):225–233, March 2011.

[190] M. K. Miller and M. G. Hetherington. Local magnification effects in the atom probe. *Surface Science*, 246(1):442–449, April 1991.

[191] F. Vurpillot, B. Gault, B. P. Geiser, and D. J. Larson. Reconstructing atom probe data: A review. *Ultramicroscopy*, 132:19–30, September 2013.

[192] D. J. BenDaniel and C. B. Duke. Space-Charge Effects on Electron Tunneling. *Physical Review*, 152(2):683–692, December 1966.

[193] J. W. Conley, C. B. Duke, G. D. Mahan, and J. J. Tiemann. Electron Tunneling in Metal-Semiconductor Barriers. *Physical Review*, 150(2):466–469, October 1966.

[194] A.G. Areshkin, G.S. Pecar, G.N. Polisskii, T.B. Popova, L.G. Suslina, and D.L. Fedorov. Composition dependence of the band gap of ZnxCd1-xSe semiconductor solutions having different crystal structures. *Sov. Phys. Solid State*, 28:2109–2111, 1986.

[195] H. C. Poon, Z. C. Feng, Y. P. Feng, and M. F. Li. Relativistic band structure of ternary II-VI semiconductor alloys containing Cd, Zn, Se and Te. *Journal of Physics: Condensed Matter*, 7(14):2783, 1995.

[196] W. Shan, J. J. Song, H. Luo, and J. K. Furdyna. Determination of the fundamental and split-off band gaps in zinc-blende CdSe by photomodulation spectroscopy. *Physical Review B*, 50(11):8012–8015, September 1994.

[197] Y. D. Kim, M. V. Klein, S. F. Ren, Y. C. Chang, H. Luo, N. Samarth, and J. K. Furdyna. Optical properties of zinc-blende CdSe and ZnxCd1-xSe films grown on GaAs. *Physical Review B*, 49(11):7262–7270, March 1994.

[198] M. Isshiki. Photoluminescence and cyclotron resonance studies on highly purified ZnSe single crystals. *Journal of Crystal Growth*, 86(1–4):615–624, January 1988.

[199] N. C. Constantinou and B. K. Ridley. Effects of finite well depth on polar optical phonon scattering rates in cylindrical quantum well wires. *Journal of Physics: Condensed Matter*, 1(12):2283, 1989.

[200] S. Birner, T. Zibold, T. Andlauer, T. Kubis, M. Sabathil, A. Trellakis, and P. Vogl. nextnano: General Purpose 3-D Simulations. *IEEE Transactions on Electron Devices*, 54(9):2137–2142, September 2007.

[201] Nari Jeon and Lincoln J. Lauhon. Atom Probe Tomography of Nanowires. In *Semiconductors and Semimetals*, volume 93, pages 249–278. Elsevier, 2015.

[202] D. P. Burt, N. R. Wilson, J. M. R. Weaver, P. S. Dobson, and J. V. Macpherson. Nanowire Probes for High Resolution Combined Scanning Electrochemical Microscopy - Atomic Force Microscopy. *Nano Letters*, 5(4):639–643, April 2005.

[203] J. E. Allen, E. R. Hemesath, D. E. Perea, J. L. Lensch-Falk, Z. Y. Li, F. Yin, M. H. Gass, P. Wang, A. L. Bleloch, R. E. Palmer, and L. J. Lauhon. High-resolution detection of Au catalyst atoms in Si nanowires. *Nature Nanotechnology*, 3(3):168–173, March 2008.

[204] D. E. Perea, E. R. Hemesath, E. J. Schwalbach, J. L. Lensch-Falk, P. W. Voorhees, and L. J. Lauhon. Direct measurement of dopant distribution in an individual vapour–liquid–solid nanowire. *Nature Nanotechnology*, 4(5):315–319, May 2009.

[205] R. Agrawal, R. A. Bernal, D. Isheim, and H. D. Espinosa. Characterizing Atomic Composition and Dopant Distribution in Wide Band Gap Semiconductor Nanowires Using Laser-Assisted Atom Probe Tomography. *The Journal of Physical Chemistry C*, 115(36):17688–17694, September 2011.

[206] D.E. Perea, J.L. Lensch, S.J. May, B.W. Wessels, and L.J. Lauhon. Composition analysis of single semiconductor nanowires using pulsed-laser atom probe tomography. *Applied Physics A*, 85(3):271–275, October 2006.

[207] A. Artioli. *Formation de Polarons Magnétiques dans des boites quantiques de (Cd,Mn)Te insérées dans des nanofils de ZnTe.* PhD thesis, June 2016.

[208] C. Hauswald, P. Corfdir, J. K. Zettler, V. M. Kaganer, K. K. Sabelfeld, S. Fernández-Garrido, T. Flissikowski, V. Consonni, T. Gotschke, H. T. Grahn, L. Geelhaar, and O. Brandt. Origin of the nonradiative decay of bound excitons in GaN nanowires. *Physical Review B*, 90(16), October 2014.

[209] I.-C. Robin, R. André, and J.-M. Gérard. Relation between growth procedure and confinement properties of Cd Se / Zn Se quantum dots. *Physical Review B*, 74(15), October 2006.

[210] B. Lounis and W. E. Moerner. Single photons on demand from a single molecule at room temperature. *Nature*, 407(6803):491–493, September 2000.

[211] K. P. O'Donnell and X. Chen. Temperature dependence of semiconductor band gaps. *Applied Physics Letters*, 58(25):2924–2926, 1991.

[212] M.O. Manasreh. *Optoelectronic properties of semiconductors and superlattices.*, volume Vol 13. 2002.

[213] W. Lee, T. Kiba, A. Murayama, C. Sartel, V. Sallet, I. Kim, R. A. Taylor, Y. D. Jho, and K. Kyhm. Temperature dependence of the radiative recombination time in ZnO nanorods under an external magnetic field of 6T. *Optics Express*, 22(15):17959, July 2014.

[214] M. Gurioli, A. Vinattieri, M. Zamfirescu, M. Colocci, S. Sanguinetti, and R. Nötzel. Recombination kinetics of InAs quantum dots: Role of thermalization in dark states. *Physical Review B*, 73(8), February 2006.

[215] E. Harbord, P. Spencer, E. Clarke, and R. Murray. Radiative lifetimes in undoped and p -doped InAs/GaAs quantum dots. *Physical Review B*, 80(19), November 2009.

[216] C. G. Van de Walle and J. Neugebauer. Universal alignment of hydrogen levels in semiconductors, insulators and solutions. *Nature*, 423(6940):626–628, 2003.

[217] G. Lamouche, P. Lavallard, and T. Gacoin. Optical properties of dye molecules as a function of the surrounding dielectric medium. *Physical Review A*, 59(6):4668–4674, June 1999.

[218] X. Brokmann, L. Coolen, M. Dahan, and J. P. Hermier. Measurement of the Radiative and Nonradiative Decay Rates of Single CdSe Nanocrystals through a Controlled Modification of their Spontaneous Emission. *Physical Review Letters*, 93(10):107403, September 2004.

[219] S. F. Wuister, C. de M. Donegá, and A. Meijerink. Local-field effects on the spontaneous emission rate of CdTe and CdSe quantum dots in dielectric media. *The Journal of Chemical Physics*, 121(9):4310–4315, September 2004.

[220] D. W. Cooke, J.-K. Lee, B. L. Bennett, J. R. Groves, L. G. Jacobsohn, E. A. McKigney, R. E. Muenchausen, M. Nastasi, K. E. Sickafus, M. Tang, J. A. Valdez, J.-Y. Kim, and K. S. Hong. Luminescent properties and reduced dimensional behavior of hydrothermally prepared Y[sub 2]SiO[sub 5]:Ce nanophosphors. *Applied Physics Letters*, 88(10):103108, 2006.

[221] H. Schniepp and V. Sandoghdar. Spontaneous Emission of Europium Ions Embedded in Dielectric Nanospheres. *Physical Review Letters*, 89(25):257403, December 2002.

[222] E. M. Purcell. Spontaneous emission probabilities at radio frequencies. In *Physical Review*, volume 69, page 681, 1946.

[223] A. F. J. Levi. *Applied Quantum Mechanics.* Cambridge University Press, June 2006.

[224] F. C. Peiris, S. Lee, U. Bindley, and J. K. Furdyna. Wavelength dependence of the indices of refraction of molecular beam epitaxy-grown ZnMgSe and ZnCdSe thin films measured by two complementary techniques. *Journal of Applied Physics*, 86:918–922, July 1999.

[225] M. R. Henderson, S. Afshar V, A. D. Greentree, and T. M. Monro. Dipole emitters in fiber: interface effects, collection efficiency and optimization. *Optics Express*, 19(17):16182–16194, 2011.

[226] E. Snitzer. Cylindrical Dielectric Waveguide Modes. *Journal of the Optical Society of America*, 51(5):491, May 1961.

[227] J. Claudon, N. Gregersen, P. Lalanne, and J.-M. Gérard. Harnessing Light with Photonic Nanowires: Fundamentals and Applications to Quantum Optics. *ChemPhysChem*, 14(11):2393–2402, August 2013.

[228] A.W. Ott, K.C. McCarley, J.W. Klaus, J.D. Way, and S.M. George. Atomic layer controlled deposition of Al2O3 films using binary reaction sequence chemistry. *Applied Surface Science*, 107:128–136, November 1996.

[229] J. R. DeVore. Refractive Indices of Rutile and Sphalerite. *JOSA*, 41(6):416–419, June 1951.

[230] D. L. Wood, Kurt Nassau, T. Y. Kometani, and D. L. Nash. Optical properties of cubic hafnia stabilized with yttria. *Applied Optics*, 29(4):604–607, February 1990.

[231] D. L. Wood and K. Nassau. Refractive index of cubic zirconia stabilized with yttria. *Applied Optics*, 21(16):2978–2981, August 1982.

[232] M. J. Weber. *Handbook of Optical Materials.* CRC Press, September 2002.

[233] S. G. Garcıa, A. R. Bretones, B. G. Olmedo, and R. G. Martın. Finite difference time domain methods. *Time Domain Techniques in Computational Electromagnetics*, 2003.

[234] J. B. Schneider. *Understanding the finite-difference time-domain method.* 2010.

[235] A. F. Oskooi, D. Roundy, M. Ibanescu, P. Bermel, J. D. Joannopoulos, and S. G. Johnson. Meep: A flexible free-software package for electromagnetic simulations by the FDTD method. *Computer Physics Communications*, 181(3):687–702, March 2010.

[236] T. Cremel, M. Elouneg-Jamroz, E. Bellet-Amalric, L. Cagnon, S. Tatarenko, and K. Kheng. Bottom-up approach to control the photon outcoupling of a II-VI quantum dot with a photonic wire. *physica status solidi (c)*, 11(7-8):1263–1266, July 2014.

[237] Christian Weedbrook, Stefano Pirandola, Raúl García-Patrón, Nicolas J. Cerf, Timothy C. Ralph, Jeffrey H. Shapiro, and Seth Lloyd. Gaussian quantum information. *Reviews of Modern Physics*, 84(2):621–669, May 2012.

[238] D. W. Pepper and J. C. Heinrich. *The Finite Element Method: Basic Concepts and Applications.* Taylor & Francis, October 2005.

[239] *Numerical Methods in Photonics.* Boca R., 2014.

[240] Pochi Yeh. *Optical Waves in Layered Media.* Wiley, March 2005.

[241] H. Ehrenreich, H. R. Philipp, and B. Segall. Optical Properties of Aluminum. *Physical Review*, 132(5):1918–1928, December 1963.

[242] G. Hass and J. E. Waylonis. Optical Constants and Reflectance and Transmittance of Evaporated Aluminum in the Visible and Ultraviolet. *JOSA*, 51(7):719–722, July 1961.

[243] F. O. Jones and K. O. Wood. The melting point of thin aluminium films. *British Journal of Applied Physics*, 15(2):185, 1964.

[244] P. Puri and V. Yang. Effect of Particle Size on Melting of Aluminum at Nano Scales. *The Journal of Physical Chemistry C*, 111(32):11776–11783, August 2007.